NASA CONTRACTOR REPORT

NASA CR-1290

NASA CR-1290

HIGH-PERFORMANCE TURBOALTERNATOR AND ASSOCIATED HARDWARE

I — DESIGN OF TURBOALTERNATOR

by R. Cohen, W. K. Gilroy, and W. B. Spencer

Prepared by
UNITED AIRCRAFT CORPORATION
East Hartford, Conn.
for Lewis Research Center

NATIONAL AERONAUTICS AND SPACE ADMINISTRATION • WASHINGTON, D. C. • MARCH 1969

NASA CR-1290

HIGH-PERFORMANCE TURBOALTERNATOR AND ASSOCIATED HARDWARE

I - DESIGN OF TURBOALTERNATOR

By R. Cohen, W. K. Gilroy, and W. B. Spencer

Prepared under Contract No. NAS 3-6013 by
PRATT & WHITNEY AIRCRAFT
Division of United Aircraft Corporation
East Hartford, Conn.

for Lewis Research Center

NATIONAL AERONAUTICS AND SPACE ADMINISTRATION

For sale by the Clearinghouse for Federal Scientific and Technical Information
Springfield, Virginia 22151 – CFSTI price $3.00

ABSTRACT

The National Aeronautics and Space Administration is conducting an evaluation of candidate Brayton-cycle turbomachinery configurations. As part of this program, Pratt & Whitney Aircraft has designed a turboalternator incorporating a two-stage axial-flow turbine driving an inductor alternator supported on gas bearings. The gas bearing rotor support system was successfully tested in a gas bearing dynamic simulator and in the turboalternator under electrical load and fault conditions to impose magnetic unbalance forces. A total of about 300 hours of operation was accumulated on the gas bearings with about 200 hours under electrical load. A backup gas bearing system was designed and various experimental investigations were conducted to verify certain areas of the turboalternator design in addition to the gas bearing testing. Two turboalternators were delivered to NASA in addition to a turbine rig, an alternator rig and two flight-type voltage regulator exciters. The turboalternator was successfully tested at design conditions in a high temperature loop at the NASA Lewis Research Center.

FOREWORD

The research described herein, which was conducted by Pratt & Whitney Aircraft, Division of United Aircraft Corporation, was performed under NASA Contract NAS 3-6013. The project was managed by Mr. Henry B. Tryon, Space Power Systems Division, NASA-Lewis Research Center. The report was originally issued as Pratt & Whitney PWA-3070, volume 1.

Page Intentionally Left Blank

TABLE OF CONTENTS

LIST OF ILLUSTRATIONS

LIST OF ILLUSTRATIONS (Cont'd)

LIST OF ILLUSTRATIONS (Cont'd)

LIST OF ILLUSTRATIONS (Cont'd)

LIST OF ILLUSTRATIONS (Cont'd)

LIST OF ILLUSTRATIONS (Cont'd)

LIST OF ILLUSTRATIONS (Cont'd)

LIST OF ILLUSTRATIONS (Cont'd)

LIST OF ILLUSTRATIONS (Cont'd)

LIST OF ILLUSTRATIONS (Cont'd)

LIST OF ILLUSTRATIONS (Cont'd)

LIST OF ILLUSTRATIONS (Cont'd)

LIST OF TABLES

LIST OF TABLES (Cont'd)

I. SUMMARY

The National Aeronautics and Space Administration is conducting an evaluation of candidate Brayton Cycle turbomachinery to supply electrical power for extended space missions. As part of this program, Pratt & Whitney Aircraft has designed a turboalternator using a two-stage axial flow turbine to drive a four pole, brushless, solid rotor alternator rated at 12 KW, 120/208 volts, 400 cps. The rotor is supported on gas lubricated bearings. The alternator and its voltage regulator-exciter were designed by the General Electric Company; the gas bearings were designed by Mechanical Technology Incorporated. Two turboalternators, two flyable voltage regulator-exciters, a turbine research package, and an alternator research package and breadboard voltage regulator-exciter were constructed and delivered to NASA. A back-up turboalternator configuration was prepared by Pratt & Whitney Aircraft incorporating gas bearings designed by the Franklin Institute Research Laboratories.

A gas bearing rotor dynamics simulator was constructed to verify bearing performance of the primary design under various turboalternator operating conditions. Tests were conducted at bearing ambient pressure levels from 14.7 psia to 6.7 psia and at various electrical loads, including design power, single phase operation and single and three phase short circuits. Hydrodynamic performance of the main thrust bearing was tested at loads up to 85 pounds. Hydrostatic performance of the main and reverse thrust bearings was tested at loads up to 250 and 100 pounds respectively. A total of 111 hours operation was accumulated on the simulator and satisfactory bearing performance was demonstrated under all test conditions.

Alternator and voltage regulator-exciter tests conducted by the General Electric Company and by NASA demonstrated predicted electrical and thermal performance. Measured efficiency was over 90% over the power output range between 4.5 and 17 KW at 0.8 power factor. These tests indicate that the alternator should have the capability to operate continuously at 200% of rated power.

The turbine research package demonstrated close to design aerodynamic efficiency in performance evaluation tests at NASA.

Satisfactory operation of the turboalternators was demonstrated throughout the test program. A total of 140 hours of test time, including 113 hours on electrical load, was accumulated by the two turboalternators. Rotor speeds up to 16,000 rpm (133% of design) and power levels up to 9.3 KW were demonstrated.

The turboalternator was successfully tested at design power output and full turbine temperature in a loop at the NASA Lewis Research Center. Satisfactory hydrodynamic and hydrostatic gas bearing operation was demonstrated.

II. INTRODUCTION

The National Aeronautics and Space Administration has embarked on the Apollo program to put man on the moon. Because this mission is of relatively short duration, the electrical power requirements of the spacecraft can be met with three 2-kilowatt fuel cells. Future space missions now being planned may last as long as a year, and power requirements will be in the tens of kilowatts. For these longer missions, nuclear and solar heat sources are being considered for electrical power, together with a variety of power-conversion systems, both static and dynamic. One of these systems is the Brayton cycle, which offers a potential of high efficiency with a well-developed technology based on aircraft gas turbines. As part of the continuing research activity of the National Aeronautics and Space Administration, Pratt & Whitney Aircraft designed a Brayton-cycle, axial-flow turboalternator as a potential power source for extended missions in space.

The objective of the turboalternator program was to evaluate two basic areas of technical uncertainty:

- Since efficiency of the turbomachinery in a Brayton-cycle powerplant affects overall system characteristics in a high degree, it was imperative to achieve high aerodynamic efficiency; also, the efficiency of small solid-rotor alternators is inadequately documented.

- Gas bearings appeared to be desirable to eliminate possible contamination of the cycle gas with oil, but the technology of gas bearings in this type of environment is limited.

The investigation was, therefore, based on as much well-documented technology as possible in all areas of turboalternator design, and conservative engineering practice was utilized in extrapolating known technology in the least-documented areas.

The turboalternator and voltage regulator-exciter were designed to provide a high-performance unit suitable for use in a long-life Brayton-cycle powerplant. The axial-flow turbine design is described in Reference 1 and the inductor-alternator in Reference 2. The rotating system, supported on gas bearings, is described in Volume II of this report, and a back-up system for gas-bearing rotor support is described in Volume III. A description of the integration of the back-up bearings in the turboalternator will be found in Appendix I of this volume.

The turbine, alternator, and bearings operate on argon. The mechanical design of the turboalternator (Figure 1) provides a unit which will meet the environmental conditions specified in Contract NAS3-6013 when used with the turbine-compressor (also shown in Figure 1) designed under Contract NAS3-4179. The unit was designed to be capable of more than 10,000 hours operating life and provides a versatile arrangement for ease of assembly and disassembly. The following conditions were used in the design of the turboalternator package:

Turbine

Working fluid, including bearings	Argon
Weight flow	0.611 lb/sec
Inlet total temperature	1685°R
Inlet total pressure	8.45 psia
Pressure ratio, total to static	1.26
Rotative speed	12,000 rpm
Speed capability, percent of design	120%

Alternator

Design power, maximum	15kva at 0.8 power factor
Number of phases	3
Voltage	120/208 volts
Frequency	400 cps
Stator hot spot temperature, maximum	356°F
Coolant	Liquid
Coolant temperature	200°F

See Reference 3 for detailed discussion of the turbine-compressor, which is designed for 50,000 rpm. The six-stage compressor has a blade tip diameter approximating 3.5 inches. The single-stage turbine diameter is about 5.1 inches. Compressor gas inlet temperature is 536°R, and turbine inlet temperature is 1950°R.

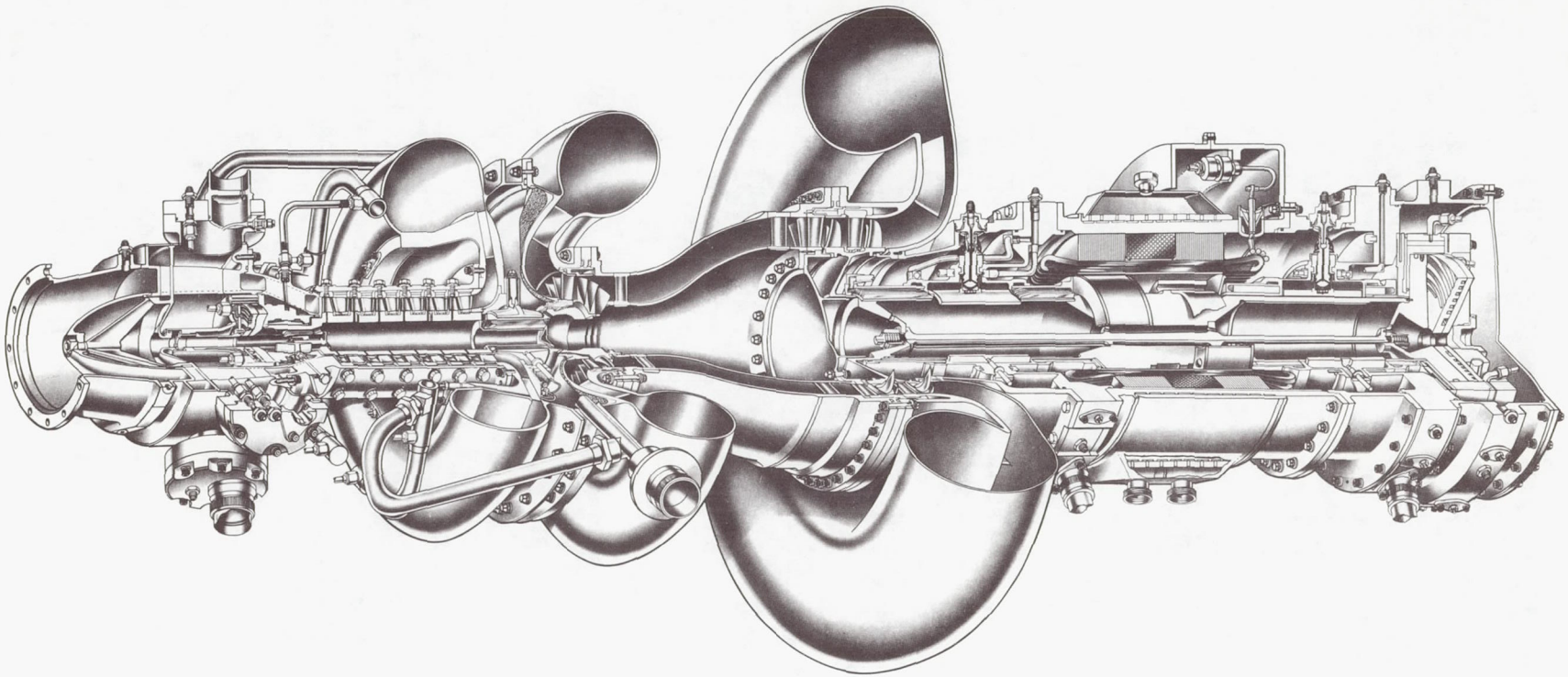

Figure 1 Brayton-Cycle Turbomachinery

III. DESCRIPTION OF TURBOALTERNATOR DESIGN

The turboalternator package design is shown in Figure 2, and the complete assembly is shown in Figures 3 and 4. The basic cycle flow enters the axial turbine inlet and flows through the two-stage axial-flow turbine, which drives the alternator directly. The argon then exhausts through the exit scroll and ducting.

The turbine inlet cone (Figure 5) is designed with vanes to impart swirl to the argon, simulating the characteristics of the turbine exit gas of the turbine-compressor designed under Contract NAS3-4179 and described in Reference 3. The turboalternator, with the inlet duct removed, is designed to mate with the exit duct of the turbine-compressor. The inlet duct assembly (Figure 6) is located by a bolted flange which incorporates a composite metal seal to prevent gas leakage (Figure 7). Individual first-stage nozzle vanes (Figure 8) are located axially by a ring in the turbine case, restricted circumferentially by slots and pins, and retained by the front cover (Figure 9). The second-stage vane assembly, split for assembly purposes, consists of two rigid half rings with brazed-on vanes (Figure 10). The turbine nozzle vanes are airfoils as defined in Reference 1.

The turbine exit diffuser and scroll (Figure 11) is bolted to the flange of the front No. 1 bearing support (Figure 12). A conical support extends from the back of the diffuser wall to the front bearing support flange, providing ample stiffness and effective thermal resistance consistent with the structural integrity of the part. Access is provided in the conical support for radial bearing adjustment, instrumentation, and hydrostatic jacking-gas supply.

The rotor of the turboalternator (Figures 13 and 14) consists of a two-stage turbine (Figures 15 and 16) and a thrust runner, (Figure 17) bolted to shaft extensions on the alternator rotor (Figure 18) by a center tierod (Figure 19). This configuration provides a rigid rotor for good balancing, dimensional accuracy, and rotor dynamics. The turbine blades defined in Reference 1 are machined integrally with the disk which connects with the alternator shaft extension through a cone. The cone design, in addition to providing long-life structural integrity, provides an effective thermal dam to minimize turbine heat conduction into the front radial bearing. The outer surfaces of the shaft extensions are coated with chrome oxide, based on the work described in Reference 3, to serve as bearing journals. Copper, 0.125 inch thick, is plated on the inside of the shaft extensions to conduct heat, generated in the radial gas bearings, away from the bearings with a minimum thermal gradient and hence minimum distortion in the bearing. An investigation of thick copper plating is discussed in Appendix II. Cooling rings located on both axial ends of the radial

bearings and separated from the shaft by a 0.005-inch gas gap remove heat from the shaft. Six teeth in the outer periphery of the thrust runner provide a speed signal to three magnetic pickups (Figure 20).

The turbine wheel and the shaft are individually balanced prior to rotor assembly, and correction is by material removal at flanges provided for that purpose. The turbine wheel is balanced on rolling contact bearings, as shown in Figure 21. The shaft and rotor assembly are balanced at about 2,000 rpm on oil-lubricated hydrostatic half bearings, as shown in Figures 22 and 23. Balance correction of the rotor assembly is by the addition of counterweights. For field balancing, the counterweight rivets in the turbine wheel (Figure 24) and the screws in the thrust runner rim (Figure 25) can be added without disturbing the gas bearings.

The two radial bearing assemblies (Figures 26 and 27) are essentially the same construction and design. Each consists of four tilting pads with flexible mounts, a bearing support ring, two liquid-cooled heat exchangers or cooling rings, cylindrical supports, and an outer flange which is bolted to the outer case of the turboalternator (Figure 28). The two heat exchangers are fed coolant independently through tubes from fittings on the outer flange. The bearing support ring also has coolant provisions for temperature control. Thin cylindrical supports are used to join the heat exchangers to the bearing support ring and join the bearing support ring to the outer flange to uncouple the thermal growth of the heat exchangers and bearing support ring from each other and from the outer flange. The rigid construction of the type 347 stainless steel heat exchangers and the bearing support ring minimize restraint from the thin support cylinders so that each can accommodate a different temperature without significant distortion. Thermal tests of the journal bearing mounts are discussed in Appendix III. Instrumentation feed-throughs are provided on the outer flange for thermocouples, pressure taps, and bearing proximity probes. Mount provisions are also on the outer flange of each radial bearing support assembly from which the turboalternator is affixed to the turboalternator mount and base plate.

The turboalternator rear compartment contains the thrust bearing assembly, cooling lines, jacking gas lines, and instrumentation leads (Figure 29). The rear case (Figure 30) is bolted to the rear No. 2 radial bearing outer flange. Type 347 stainless steel is used extensively throughout the rear compartment as well as in the radial bearing supports because of its nonmagnetic property, compatibility with the liquid coolant (glycol or Versilube F-50), and good corrosion resistance. Also, the thermal growth of the radial bearing mount ring matches the journal growth at the respective operating temperatures. Located on the outside case of the rear compartment is a thickened ring which contains instrumentation feed-throughs. The thrust bearing consists of a hydrostatic bearing for reverse thrust (Figure 31) mounted to the outer flange of the No. 2 radial bearing. Bolted to the reverse thrust plate is the support ring (Figure 32)

for the main thrust bearing. The main thrust bearing stator (Figure 33) is supported from the support ring by four tangential rods which provide the required stiffness for bearing performance. The main thrust stator is a welded aluminum plate and includes Whipple grooves for hydrodynamic bearing action during steady-state operation at design speed and orifices for hydrostatic bearing action for transient operation. The main thrust plate is cooled by liquid to minimize thermal distortion.

The alternator, fully described in Reference 2, Volume I, is a four-pole inductor consisting of a one-piece rotor (Figure 18) and a liquid cooled stator (Figure 34). The rotor pole tips are laminated, and copper amortisseur bars are mounted close to the pole faces. Aerodynamic baffles are welded and riveted to the ends of the alternator rotor to reduce windage power loss. The rotor pole diameter is 5.2 inches. Each pole is contoured at the shaft interface for maximum saliency. The stator consists of stacks of laminations at each of the two pole locations. A wound field coil is located axially between the stator stacks to supply the required magnetic flux from direct current supplied by the voltage regulator-exciter. Copper coils for the three phases are mounted in axial slots on the inside diameter of the stator. Electrical insulation is provided between the coils and the slots. The two stator stacks and field coil are shrunk-fit into the stator frame and welded in place. The steel frame provides a conduction path for the magnetic flux, provides structural support, and contains liquid cooling provisions. Circumferential slots near the outside surface of the frame contain liquid coolant. Hermetic terminals are mounted on the frame for instrumentation, power leads, and the field connection.

The turboalternator mount supports the unit at the radial bearing planes (Figure 35). The front mount supports the turboalternator in the axial and vertical directions and provides for radial thermal growth of the turboalternator. The rear mount retains the unit in the horizontal direction and provides for radial and axial thermal growth of the unit.

Compressor exit gas is bled from the compressor discharge of the turbine-compressor, cooled, and fed through a fitting on the rear radial bearing outer flange of the turboalternator. About 0.5 percent of the cycle flow, cooled to 100°F, is required at the fitting at a pressure of 12.75 psia. This gas divides into two approximately equal streams after entering the turboalternator. One stream flows through the radial bearings and alternator. It then flows through the gap at the front heat exchanger of the front radial bearing and enters the turbine flow after the second-stage blades. The other stream flows through the thrust bearing compartment, through the inside of the rotor, and enters the turbine flow before the first-stage blades. Both streams are metered to prevent circulation of hot turbine gas into the front radial bearing and provide the desired ambient pressure in the bearing and alternator areas.

Turbine inlet and exhaust flanges (Figures 36 and 37) are supplied for test facility installation.

The voltage regulator-exciter, described in Reference 2, consists of two units, each sealed in hard epoxy to withstand space vacuum conditions, and uses simple circuitry, component derating, and redundancy to achieve the high reliability required for 10,000 hours operating life. The voltage regulator unit is shown in Figures 38 and 39 and the exciter in Figures 40 and 41. The parasitic power loss in the voltage regulator-exciter is 94 watts at design power and is conducted through the epoxy "potting" to cold plates maintained at 150°F and 250°F for the regulator and exciter respectively. The overall circuit diagram is shown in Figure 42. Referring to the block diagram (Figure 43) the voltage regulator functions as follows:

A reference voltage is supplied by the reference circuit to the comparison circuit. A signal voltage is supplied to the comparison circuit by the voltage sensing circuit. The reference and signal voltages are compared, and the error current, which indicates that a change in voltage is necessary, is amplified by a transistor and magnetic amplifier. The output current, supplied by the magnetic amplifier to the control winding of the exciter, changes the exciter output so that line voltage is restored to the correct value. The stabilizing circuit provides for fast response while preventing oscillation. A separate high phase take-over circuit limits the maximum voltage on any phase to approximately 110 percent of normal during single-phase short or open circuits.

The voltage regulator-exciter includes revisions as a result of testing a breadboard voltage regulator-exciter with the alternator research package described in Reference 2.

The total weight of the hardware is 633 pounds broken down as follows:

- Turboalternator: 530 pounds (Not including the mount)
- Voltage regulator: 57 pounds
- Exciter: 46 pounds

A. Aerodynamic Design

The turbine blading for the Brayton-cycle turboalternator was selected with the objective of producing high efficiency and high reliability. Since the speed and temperature in the turboalternator are relatively low, the mechanical design of the turbine can incorporate large design margins to provide high reliability po-

tential. A high-velocity-ratio* turbine was selected to provide high efficiency potential. Rather than using a large-diameter single-stage turbine with short blades, a two-stage turbine was chosen to maintain a reasonable blade height to reduce tip clearance and end losses. The effort to maintain reasonable blade heights coupled with low gas flow in the Brayton cycle led to a low axial-velocity-to-wheel-speed ratio. This design results in a turbine with high reaction, which is consistent with the high velocity ratio selected. The aerodynamic design is fully described in Reference 1.

The thermodynamic design parameters of the turbine are presented in Table 1. The predicted overall performance of the turbine is given in Figures 44 and 45.

TABLE 1

TURBINE THERMODYNAMIC DESIGN

	First Stage	Second Stage	Overall
Work, Btu/lb	7.52	7.52	15.04
Rotational Speed, rpm	12,000	12,000	12,000
Pressure ratio across turbine			
Total to total	1.1144	1.1190	1.2469
Total to static	------	------	1.2542
Pressure ratio, flange to flange			
Total to total	------	------	1.2495
Total to static	------	------	1.2540
Mean velocity ratio (actual)	0.726	0.724	0.725
Axial gas velocity to mean blade velocity	0.334	0.3375	------
Stage exit axial Mach number	0.0809	0.0833	------
Total-to-total efficiency	0.8473	0.8472	0.8501
Total-to-static efficiency	0.8050	0.8026	0.8254
Exit swirl angle (mean), degrees	-4.61	-4.56	------
Hub-to-tip ratio	0.746	0.730	------
Blade root static pressure ratio	1.0363	1.0356	------
Flange-to-flange, total-to-total efficiency	------	------	0.8428
Flange-to-flange, total-to-static efficiency	------	------	0.8264

*Velocity ratio (υ) is defined as the ratio of mean wheel linear speed (U) to the square root of twice the actual turbine work. Hence, $\upsilon = U/\sqrt{2\Delta h_o}$. For multi-stage turbines, the overall velocity ratio is defined as $\upsilon = \sqrt{\Sigma U^2/2\Delta h_o}$, where Δh_o is the actual overall turbine work.

The turbine rig discussed in Reference 1 and shown here in Figure 46 was tested at the Lewis Research Center of the National Aeronautics and Space Administration. Testing was conducted with low-temperature gas on the two-stage configuration and also on the first stage only. The comparison of measured and predicted efficiencies (Table 2) shows performance to be essentially as predicted except for total pressure recovery in the exit diffuser. Turbine flow for both the single-stage and two-stage configurations was about 4 percent below the prediction, and subsequent gaging of the turbine indicated the first-stage nozzle flow area to be low by about the same amount.

TABLE 2

TURBINE AERODYNAMIC EFFICIENCY

	Predicted Efficiency, %	Measured Efficiency, %	
	Small Clearance	Small Clearance	Large Clearance
Stage exit			
Total to total	85.01	84.5	
Total to static	82.54	82.5	
Flange to flange			
Total to total	84.28	83.5	79.2
Total to static	82.64	82.6	78.5

The radial blade tip clearances in the turbine research package, 0.0095 and 0.0105 inch in the first and second stages, respectively, were left small to permit testing at various tip clearances. The predicted operating radial blade tip clearances for the turboalternator turbine are 0.030 and 0.032 inch for the first and second stages, respectively. The increased turboalternator clearances were conservatively established to prevent possible blade tip rub during the maximum expected transient thermal conditions which are discussed later in this report. Reduction of turboalternator blade tip clearances may be possible using experimental data on the actual transient behavior of the turbine.

B. Electrical Design

The selection of an inductor alternator for the Brayton-cycle turboalternator was based on the following order of priority: 1) reliability, 2) efficiency, 3) power quality, 4) radial bearing force, and 5) weight. This alternator has an unwound rotor with both the field and power windings stationary. Reliability is further enhanced through use of derated state-of-the-art materials and components.

Several design techniques were employed to obtain a high degree of efficiency. Both stationary and rotating baffles were used to decrease the windage loss. Laminated pole tips were electron beam welded to a solid rotor hub to reduce pole face losses. Copper and core losses were held to a minimum through use of low current and flux densities. Using multiple strands in the stator conductors and placing them flat in the slots reduced deep bar losses.

Good power quality was obtained through use of an amortisseur winding to improve the voltage unbalance under unbalanced load conditions. The third harmonic was eliminated through use of a 2/3 pitch in the coil winding. However, no attempt was made to reduce the stator slot harmonics, since skewing of either the rotor or stator might decrease the reliability. The voltage overshoot, or dip, on the removal or application of one per unit load current was purposely designed to be just within the specification (1.364 per unit volts), and it, along with the other power quality parameters, represents the best overall design.

Since the alternator is to operate on gas bearings, it was necessary to minimize radial forces on the bearings, and thus a relatively large air gap and low gap flux density have been used.

Table 3 summarizes the final design of the alternator which is described in Reference 2.

TABLE 3

ALTERNATOR DESIGN PARAMETERS

A. Stator

Turns per coil	4
Effective turns	26.55
Strands per turn	2
Circuits	2
Coil pitch	0.667
Resistance at 160°C	0.0183 ohms per unit

TABLE 3 (Cont'd)

Length	4.0 in.
Slot pitch	0.346 in.
Outside diameter	8.68 in.
Inside diameter	5.28 in.
Slots skewed	0
Yoke thickness	1.1 in.
Slot Width	0.171 in.
Stack separation	2.2 in.
Slots	48

B. Rotor

Outside diameter	5.2 in.
Hub diameter	3.6 in.
Tooth thickness	2.1 in.
Length	3.9 in.
Tooth axial length	1.95 in.
Tooth axial separation	2.2 in.
Pole arc	2.86 in.

C. Field

Outside diameter	8.68 in.
Inside diameter	6.48 in.
Turns	515
Resistance at 160°C	4.97 ohms
Current (I_f) at 15 kva	6.29 amp

D. Gap — 0.040 in.

E. Materials

Rotor	AISI 4620
Pole tips	AISI M-19 (0.014 in)
Stator laminations	0.007 in. silicon steel
Frame	Ingot iron
Frame flanges	AISI 4140
Frame shroud	72%Ni - 15%Cr - 8%Fe
Windage baffles	AISI 321
Conductors	Tough pitch copper
Conductor insulation	Polyimide enamel

Impregnant	Epoxide compound
Amortisseur bars	Zirconium copper
Connection insulation	Polytetrafluoroethylene glass
Slot liner	Polyimide film
Separator	Silicone glass cloth
Topstick	Molded polyimide resin

In order to obtain electrical performance data, an alternator research package (Figure 47) was fabricated. This machine was an electrical and thermal equivalent of the alternator used in the turboalternator except that ball bearings were utilized. Figure 48 is a cross-sectional view of the alternator research package.

Table 4 is a comparison of the computed and measured losses and efficiency (the design efficiency was 91.66 percent, and the test efficiency was 91.74 percent). Although there are significant differences in the loss distribution, the efficiency was as predicted. The plot of measured efficiency versus load shown in Figure 49 indicates good efficiency over a wide range of load.

Test data indicated that the degree of electromagnetic and thermal conservatism designed into the alternator would permit continuous operation at 100 percent overload with a small loss in efficiency and life.

TABLE 4

ALTERNATOR LOSS SUMMARY, 12-KILOWATT LOAD

(Including Voltage Regulator-Exciter Losses)

	Design Loss, Watts	Test Loss, Watts
Stator copper	276	277
Field copper	206	135
Core	200	320
Stray (includes pole face)	190	270
Total electrical loss	872	1,002
Windage	220	78
Total loss	1,092	1,080

When an alternator is operating under either a no-load or loaded condition, radial magnetic forces occur between the rotor and stator. If the rotor is perfectly concentric with the stator, the forces cancel and no net force exists on the rotor. However, due to manufacturing tolerances, this condition rarely occurs, and some net magnetic force usually is present. Since gas bearings are employed in the turboalternator, it became important that the nature and magnitude of the force be determined to check the load capability and stability of the bearings. To accomplish these aims, both an analytical and experimental study were initiated.

The goal of the analytical study was to determine analytical expressions describing the force which could serve as input to a gas bearing stability analysis. The basic equation for radial magnetic force is:

$$F = K \int B^2 dA$$

where

K is a constant

B is the flux density in the air gap

dA is the differential area of the air gap

Flux density was determined by multiplying the air gap permeance by the magnetomotive force (m.m.f.) existing across it. Permeance included the effects of stator, rotor, and amortisseur slotting, and the m.m.f. included both the d.c. and armature reaction components. Fourier series, truncated at realistic harmonics, were used to describe the permeances and m.m.f. and several computer programs were written to handle the large number of terms resulting from the multiplication. Uniform saturation was assumed around the stator circumference and was factored into the calculation by adjusting the coefficients of the rotor permeance terms.

In the experimental study, the alternator research package was equipped with specially designed endshields and antifriction bearings so that the bearing reactions could be measured.

The endshields had necked-down supports for the bearing housings. Strain gages mounted on these supports gave an electrical readout of instantaneous bearing reactions. Four sets of bearing housings were made. By changing bearing housings, the eccentricity of rotor with respect to stator could be varied from essentially zero to 0.006 inch (out of 0.040-inch nominal air gap). Tests were

staged by loading the alternator at different power outputs, different power factors, and with balanced and unbalanced loads and shorts.

Table 5 shows comparative measured and calculated bearing forces for several load conditions with a rotor-to-stator eccentricity of 0.006 inch. Both the analytical and test data indicated the major portion of the magnetic forces occurred at a frequency of two times the rotor speed and equal to the pole or electrical frequency.

TABLE 5

NET BEARING FORCE SUMMARY FOR 0.006-INCH ECCENTRICITY

Load Condition	Experimental Force, lb.	Analytical Force, lb.
No load (2.7 amp excitation)	9.0	32.0
15 kva, 0.8 power factor	14.2	47.4
3.3 kva, single phase	9.1	40.0

C. Stress and Deflection Analyses

The design of the turboalternator is based on conservative stresses and deflections in both the rotating and stationary parts to provide a machine with long life potential and with the ability to operate at the small clearances necessary for high aerodynamic efficiency and proper bearing performance. The turboalternator is designed to withstand the environments defined by NASA Specification P005-1 dated June 19, 1964 with ample margin.

The natural frequencies of the turbine blades and disk are summarized in Table 6.

TABLE 6

TURBINE BLADE NATURAL FREQUENCIES

	Natural Frequency First Stage, cps	Natural Frequency Second Stage, cps
First bending	3300	3300
Second bending	6100	6100
First torsion	9700	9100

The turbine blade bending natural frequencies are removed from the probable sources of excitation which are associated with the inlet ducting and nozzle wakes: 600, 7200, 8000, and 8800 cps. Torsional resonances at both turbine stages may occur at operating speed due to variations from nominal thickness. Excitation associated with these modes and its response is expected to be small.

The turbine disk has been designed to provide overspeed margin. The turbine disk is expected to yield at a rotational speed above 25,000 rpm and to burst at a speed above 26,000 rpm. An operational condition which might lead to overspeeding of the turbine has been examined to determine the possibility of a disk failure. If the load were removed from the alternator due to a three-phase short, loss of alternator excitation, or circuit breaker action, the unloaded turbine would probably accelerate in approximately 15 seconds to a possible bearing rub, as indicated in Figure 50. Actually, the bearing should not rub, since the flexure will allow the bearing pads to move outward. The overspeed margin is substantially higher than the 20 percent specified, and 15 seconds appears to be a reasonable time interval to apply corrective action.

The turbine blades and disk are designed to provide low creep rates. In 10,000 hours, less than 0.2 percent creep is predicted. Figures 51 and 52 show the anticipated blade stress distributions. The possibility of unsymmetric creep exists, and a pessimistic estimate of the resulting unbalance indicates that it should be less than 0.005 oz-in. at the completion of 10,000 hours operation. The design of the rotor forging requires radial grain orientation in the turbine, which should minimize unsymmetric creep and provide significantly less turbine unbalance at the end of 10,000 hours.

The turbine wheel cone between the No. 1 bearing journal and the turbine disk is designed to limit turbine heat flow into the bearing area and to cause as little centrifugal growth in the journal as possible. Distortion at the bearing end of the cone is negligible. The maximum steady-state stress in the turbine rotor occurs in the cone at the disk (see location No. 7 on Figure 53) as a radial stress of 43,000 psi at 14,400 rpm. The 0.2-percent yield strength of the turbine rotor material (Inconel 718) is 126,000 psi at the local temperature of 1000°F occurring at this location. The maximum transient thermal stress occurs at this location at a stress of 61,000 psi at 12,000 rpm. An additional high stress occurs in the turbine hub (see location 8 on Figure 53) due to the tiebolt load during transient thermal conditions at a stress of 69,000 psi. The 0.2-percent yield strength of the turbine hub at 300°F is 144,000 psi.

Shaft journal growth for the No. 1 and No. 2 radial bearings is given in Tables 7 and 8.

TABLE 7

NUMBER 1 BEARING JOURNAL GROWTH
(DIAMETRAL)

	12,000 rpm Growth, in.	14,400 rpm Growth, in.
Centrifugal	0.00030	0.00043
Thermal (70-290°F)	0.00430	0.00430
Total	0.00460	0.00473

TABLE 8

NUMBER 2 BEARING JOURNAL GROWTH
(DIAMETRAL)

	12,000 rpm Growth, in.	14,400 rpm Growth, in.
Centrifugal	0.00030	0.00043
Thermal (70-300°F)	0.00550	0.00550
Total	0.00580	0.00593

The nominal bearing gas film clearances in both radial bearings is 0.00088 inch (radial) at design conditions. Matched thermal expansion of the bearing support and journal and adjustment of the cold initial clearance provide substantially the nominal gas film clearances at design conditions.

The titanium tiebolt is preloaded to retain the turbine and thrust runner under all operating and transient thermal conditions. The maximum stress of 75,000 psi in the tiebolt occurs at the flange mating with the alternator rotor bore (see location 9 on Figure 53) during a thermal transient. The 0.2-percent yield strength of titanium (AMS 4928) is 88,000 psi at 300°F. The maximum steady-state stress occurs in the flange at 46,000 psi. Other significant transient stresses in the tiebolt are 54,300 psi and 38,000 psi at locations 10 and 11, respectively.

The unit construction rotor design is a stiff configuration, and, with proper balancing, rotor deflections will have negligible effect on blade, seal, bearing heat exchanger, and bearing film clearances. Rotor dynamic analysis (see the following section, paragraph III. D, Rotor Dynamics and Gas Bearing Design) indicates that rotor deflections will be less than 0.00005 inch at the bearings. Figure 54 presents the predicted rotor deflection at design speed, assuming 0.005 oz-in. unbalance due to turbine creep after 10,000 hours operation.

The thrust bearing runner located at the rear end of the turboalternator rotor is designed and supported to minimize distortion. The runner was made heavy to lower the rotor rigid body critical speeds below the operating range. The runner is positioned by a light "press fit" and a butting face, indexed by a dowel, and retained by the center tiebolt. The tiebolt is more flexible than the runner and will absorb the axial stretch caused by assembly and thermal transient loads.

Stresses induced by temperature, pressure and assembly loads throughout the static structure are designed at an acceptable level in order to assure the integrity of the turboalternator and provide sufficient rigidity to the bearing supports and seals. All steady-state and transient thermal stresses are significantly below the 0.2 -percent yield strength of the materials used in the static structure. Figure 53 shows the locations of significant transient stresses in the static structure. These locations are listed in Table 9.

TABLE 9
SIGNIFICANT STRESSES IN THE TURBOALTERNATOR STATIC STRUCTURE

Location	Stress, psi	Material	0.2-Percent Yield Strength, psi
1. Inlet bullet	34,000	Hastelloy X	42,000
2. 1st-stage turbine shroud	83,000	Inconel 718	126,000
3. 2nd-stage turbine shroud	92,000	Inconel 718	126,000
4. Turbine diffuser support cone	51,000	Inconel 718	121,000
5. Bearing heat Exchanger supports	20,000	Type 347 stainless steel	26,000
6. Bearing ring support	16,000	Type 347 stainless steel	26,000

Thermal bowing of the alternator frame due to a circumferential 10°F coolant temperature difference causes a radial displacement of the bearing centerline from the alternator stator centerline of 0.0001 inch. It is predicted that this displacement will cause a magnetic unbalance force of about 0.5 pounds on the bearing which is acceptable.

The turboalternator will not have any case-bending frequencies below the 12,000 rpm operating speed because the cases are relatively stiff. Vibratory amplitudes at design speed will be negligible because rotor unbalance loads are small.

The turboalternator is designed to withstand the required launch environmental conditions. However little data is available on the ability of the gas bearings to survive the shock and vibration environments. The launch, lift-off, and boost conditions represent the most severe shock and vibration conditions. A test program is recommended to determine the capability of the gas bearings under the anticipated environments. If the bearings prove to be unsatisfactory when subjected to these conditions, one of two approaches can be taken: 1) shock-mount the machinery, or 2) restrain the rotor in the inoperative condition. The rest of the static and rotating structure is designed to be capable of meeting the requirements. Therefore, shock mounts do not appear necessary. A special shipping container and fixtures which restrain the rotor to prevent bearing damage during shipping were designed and used. Preparation of the turboalternators for shipment is discussed in Appendix IV.

D. Rotor Dynamics and Gas Bearing Designs

The rotor of the turboalternator weighs 57.5 pounds with the center of gravity located 7.40 inches from the front radial bearing centerline. The rotor mass distribution is shown in Figure 55. The total polar moment of inertia is 0.6268 in-lb-sec^2 with the distribution shown in Figure 56. The transverse moment of inertia about the center of gravity is 9.656 in-lb-sec^2.

The "free-shaft" critical speed of the rotor is calculated to be 33,000 rpm, which is sufficient to provide ample margin over the design speed of 12,000 rpm and the overspeed of 14,400 rpm to limit the shaft distortion due to dynamic forces. Also, the free-shaft critical speed is above the expected two-per-revolution electrical excitation. The rotor must pass through two rigid-body critical speeds in the 6500-to 8500-rpm range when accelerating to design conditions. Since these two critical speeds are primarily dependent on the gas bearing characteristics, they are discussed in Volume 2 of this report. The critical speed of the rotor tie-rod is over 30,000 rpm with minimum preload.

The detailed gas bearing designs and simulator test program are presented in Volume 2 of this report. Volume 2 also includes the determination of the radial bearing loads experienced in supporting the rotor weight of 57.5 pounds, both in the rotor vertical position (zero g condition for the journal bearings) and in

one horizontal attitude, as well as the analysis and experimental determination of the effect of radial magnetic forces on gas bearing performance. The calcution and experimental measurement of the magnitude of radial magnetic forces due to rotor-stator eccentricity were conducted by the General Electric Company and were reported in Reference 2, Volume II.

The aerodynamic thrust load when the unit is operating at the design point in the horizontal attitude (zero g condition for the thrust bearing) is 30 pounds in the direction of gas flow through the turbine. The unit is also required to operate vertically with the turbine inlet up, in which case the net rotor thrust at the design point is approximately 87 pounds in the direction of turbine gas flow. The maximum anticipated axial misalignment between the alternator rotor and stator (0.010 inch) results in an insignificant magnetic thrust force, as shown in Figure 57.

The aerodynamic thrust during startup and shutdown is difficult to predict accurately. In fact, the thrust direction may be reversed during part of the acceleration, depending on the method of starting. Transient thrust loads of up to 250 pounds in the normal thrust direction and 100 pounds in the reverse thrust direction were selected as design requirements. Additional design requirements for the bearings were:

- Stable operation at any ambient pressure above 7.2 psia
- Stable operation with an unbalance of 0.005 ounce-inch in the plane of the turbine wheel
- Ability to withstand vibrational and thermal transients during startup and shutdown.

Pivoted-pad flexure-mounted journal bearings and a spiral-groove main thrust bearing were selected. All bearings utilize hydrostatic lift-off to reduce starting torque and eliminate rubbing during startup and shutdown. A hydrostatic reverse thrust bearing is provided for startup and shutdown. The bearing designs, the data for which is listed in Table 10, include the following features:

- Four 80°-arc pads with provisions to adjust pivot radial position
- Each pad mounted on a flexible beam
- Chrome oxide surfacing material, selected as a result of material tests reported in Reference 3, Volume II.
- Startup thrust loads supported by a hydrostatic bearing built into a spiral-groove self-acting thrust bearing
- Plated copper heat shunts to minimize thermal gradients in the bearing journals

- Liquid-cooled aluminum thrust stator
- Miniaturized capacitance probes embedded near the pivot to measure journal pad-to-shaft film thickness
- Capacitance probes to measure pad dynamic behavior

Each journal bearing is made up of four pads like that shown in Figures 58 and 59. Each pad is mounted on a pivot (Figure 60) which is radially adjustable by screwing it in or out of its flexure. The lower pad pivots have drilled passages to carry the hydrostatic jacking gas into the lower pads. The terms "lower pads" and "lower pivots" refer to the two pads and two pivots in each journal bearing which carry the rotor weight when the rotor is horizontally oriented in a 1-g acceleration field.

Figure 61 shows the high-spring-rate flexures used at the lower pad locations and the low-spring-rate flexures used at the upper pad locations of both journal bearings. The flexures provide extra softness in the bearing mount system to allow the pads to move radially outward under extreme thermal transient or load conditions. The two upper and two lower pivot-support flexures in each journal bearing have measured spring rates of 34,800 and 84,000 pounds per inch, respectively. The upper flexures provide most of the accommodation of differential thermal expansions which would otherwise be directly reflected as a change in bearing clearance. In addition to accommodation of thermal expansions, the use of flexures results in a desirable reduction of the rigid-body critical speeds of the rotor-bearing system. Without the flexures, the first two critical speeds would occur between 9,500 and 11,000 rpm, rather than in the range of 6,500 to 8,500 rpm. The journal bearing film clearance is affected by the piston area of the center section of the flexure which is acted upon by the pressure difference between adjacent compartments. For instance, the top flexures in the front bearing will deflect outward 0.0001 inch due to the 3.8-psi differential acting against the 34,800 pound-per-inch spring. This motion is acceptable and is considered in establishing the cold set-up clearance.

During hydrostatic operation, gas is fed through the two lower pivots, metered through an orifice in each of the lower pads, and distributed across the journal by a recess in the pad surface. Rubber O-rings are used as seals and check valves to prevent backflow from the bearing gas film during hydrodynamic operation.

The thrust bearings consist of a thrust runner (Figure 62) turning between the reverse-thrust stator and the flexibly supported liquid-cooled main thrust stator (Figure 63). Figure 64 shows the capacitance probe readout equipment set up for gas bearing adjustment at assembly.

TABLE 10

TURBOALTERNATOR GAS BEARING DESIGN PARAMETERS AND CALCULATED PERFORMANCE CHARACTERISTICS

All data given in this table is based on the following gas bearing operating conditions:

Rotor speed: 12,000 prm
Lubricant gas: argon
Lubricant viscosity: 4.2×10^{-9} lb-sec/inch^2

JOURNAL BEARINGS

Configuration	Pivoted pad with hydrostatic lift-off
Journal diameter	3.4962 in.
Bearing length-to-diameter ratio (L/D)	1.0
Number of pads per bearing	4
Pad orientation (with reference to horizontal orientation of the rotor)	Rotor weight between pivots
Arc length (θ) of pads	80.0°
Pivot location (β / θ) from leading edge	0.65
Pad clearance ratio (C_p/R)	0.00128
Preload	0.612
Pivot ball diameter	0.625 in.
Pivot socket diameter	0.812 in.
Hydrostatic orifice diameter	0.0135 in.
Recess axial length	1.500 in.
Recess circumferential width	0.500 in.
Recess depth	0.0002 in.
Hydrostatic gas supply pressure at startup	65 psia (horizontal orientation)
Hydrostatic gas flow per pad	0.65×10^{-4} lb/sec
Pivot support radial stiffness	
Upper pads	34,800 lb/in.
Lower pads	84,000 lb/in.
Bearing load (rotor weight), horizontal orientation in 1g field	
No. 1 bearing	29.3 lb
No. 2 bearing	28.2 lb
Space operation (due only to 0.005 oz-in. of mass unbalance in turbine plane)	
No. 1 bearing	2.8 lb
No. 2 bearing	0.85 lb

TABLE 10 (Cont'd)

Operating radial clearance at pivot, horizontal orientation (loaded pads) in a 1 g field	
No. 1 bearing	0.0006 in.
No. 2 bearing	0.0006 in.
Space operation (all pads)	
No. 1 bearing	0.0009 in.
No. 2 bearing	0.0009 in.
Friction loss per journal, horizontal orientation in 1 g field	
No. 1 bearing	89.5 watts
No. 2 bearing	90.2 watts
Space operation	
No. 1 bearing	83.9 watts
No. 2 bearing	84.5 watts
Radial gas film stiffness, horizontal operation in 1g field	
No. 1 bearing	1.4×10^5 lb/in.
No. 2 bearing	1.45×10^5 lb/in.
Space operation	
No. 1 bearing	1.14×10^5 lb/in.
No. 2 bearing	1.24×10^5 lb/in.
Shaft temperature	
No. 1 bearing	288°F
No. 2 bearing	296°F
Pad temperature	
No. 1 bearing	292°F
No. 2 bearing	299°F
Shaft material	AMS 6294 low alloy steel
Pad material	M-1 tool steel
Pivot material	M-1 tool steel
Journal and pad surfacing material	Chrome Oxide

MAIN THRUST BEARING

Configuration	Spiral groove with hydrostatic lift-off
Thrust plate diameter	7.0 in.
Spiral groove bearing O.D.	7.0 in.
Spiral groove bearing I.D.	3.92 in.
Groove depth	0.0022 in.
Number of grooves	12
Design load (aerodynamic) for spiral groove bearing	30 lb.
Operating clearance of spiral groove bearing	0.0018 in.
Friction loss at design load (space operation)	59.0 watts
Friction loss, vertical operation in a 1 g field	97.0 watts

TABLE 10 (Cont'd.)

Orifice diameter	0.028 in.
Number of orifices	16
Hydrostatic gas supply pressure at startup	100 psia
Hydrostatic gas flow	0.0058 lb./sec
Hydrostatic bearing load at startup	250 lb.
Hydrostatic film clearance at startup	0.0014 in.
Stator support stiffness in axial direction	33,100 lb/in.
Stator support stiffness in tilt direction	99,000 in-lb/radian
Stator temperature at design load	210°F
Runner temperature at design load	220°F
Runner material	AMS 6415 low alloy steel
Stator material	AMS 4027 aluminum
Stator and runner surfacing material	Chrome oxide

REVERSE THRUST BEARING

Configuration	Hydrostatic
Orifice diameter	0.028 in.
Number of orifices	16
Supply gas pressure	100 psia
Gas flow	0.0063 lb/sec
Design load	100 lb
Hydrostatic clearance at startup	0.0015 in.
Stator surfacing material	AMS 5646 Type 347 stainless steel
Stator and runner surfacing material	Chrome oxide

E. Thermal Analysis

The turboalternator design is based on steady-state and transient thermal analyses of critical areas. The thermal conditions within the unit determine the basic clearances of blade tips, seals, and bearings as well as provide a basis for material selection. The overall thermal map of the turboalternator for design operating conditions is presented in Figure 65.

At the design operating condition the various heat losses to be removed by the coolant are tabulated below.

Journal bearing loss (each bearing)	90 watts
Thrust bearing loss	59 watts
Alternator stator electrical loss	962 watts
Alternator rotor electrical loss	40 watts
Alternator rotor windage loss	78 watts
Heat conducted from the turbine	170 watts

The results of initial studies, using gas cooling, showed that higher cycle bleed flows were required. Liquid coolant is available for alternator stator cooling, and its use in the bearings results in an acceptable solution for rotor heat removal. With liquid cooling, an argon gas bleed flow rate of 0.5 percent of the cycle flow is required to maintain thrust balance pressures and gas bearing ambient pressures and to ensure that high-temperature turbine gas does not leak through the turbine seals into the bearings and alternator. Figure 66 shows the routing of the argon bleed flow through the turboalternator. Also included are the ambient pressure levels in the various compartments. Argon (0.5 percent of the cycle flow) is introduced at the thrust bearing end of the unit at 12 psia and 100°F. Half of this flow proceeds through the rotor and re-enters the mainstream at the turbine front seal. The remaining half of the flow passes over the No. 2 journal bearing, is reduced to 10.5 psia through the No. 2 bearing front cooling ring gap, passes over the alternator rotor and the No. 1 journal bearing, is reduced to 6.73 psia through the No. 1 bearing front cooling ring gap, and re-enters the mainstream through the turbine rear seal. The pressure levels throughout the machine and the aerodynamic thrust of the turbine result in a thrust load of 30 pounds rearward at design conditions.

Cooling rings located on each side of the radial bearings remove the rotor heat generated in the journal bearings and the alternator rotor and the heat conducted from the turbine. Heat is conducted away from the journal bearings and alternator rotor through 0.125-inch-thick copper plate in the bore of the shaft. The heat is then conducted to the liquid-cooled rings across a 0.005-inch gas gap. Figure 67 shows the rotor temperatures from the alternator rotor through the No. 1 bearing area and the turbine. The resulting maximum bearing temperature is 292°F. The axial temperature gradients within the No. 1 bearing result in 5.75°F crowning distortion and 0.5°F coning distortion, as shown in Figure 68. Figure 69 is the thermal map of the alternator rotor through the No. 2 bearing to the thrust bearing. The maximum bearing temperature in the No. 2 bearing is 299°F. Crowning and coning distortions shown in Figure 70 are 6.5° and 0.75°F, respectively. This configuration meets the design objective, which is to limit bearing temperatures to about 400°F and to limit the distortion in the film clearance to a maximum of 0.0001 inch. This design criteria corresponds to a maximum axial temperature difference of 10°F in the journal.

Additional thermal maps of the No. 1 bearing area (between the turbine and the alternator) were prepared to check the adequacy of the system at various operating conditions. Figure 71 presents a thermal map for the case where there are no electrical losses, which corresponds to open-circuit conditions, and Figure 72 presents the temperature distribution in the bearing and pad. The turboalternator will at times be run with low-temperature gas. Figures 73 and 74 present the thermal map of the No. 1 area with low-temperature turbine inlet gas and no losses in the alternator. The thermal conditions were examined with no windage losses for the two cases discussed above, and the results are presented in Figures 75 through 78. The effect of higher-than-anticipated heat generation rates in the bearings and in the alternator were reviewed. Bearing temperature levels and profiles were acceptable with higher heat generation rates of 50% in the bearings and 100% in the alternator. The purpose of examining these extreme conditions was to determine whether a design margin exists. The results of the thermal analyses indicate that the crowning is within the 10°F maximum temperature difference in the journal indicated previously as a design criterion. Coning of the journal is evident in some of these cases because of the variation in axial heat input at these extreme conditions. However, the pivoted pads are normally able to follow a moderate amount of coning. These studies were based on the use of 0.060-inch-thick heat shunts inside the journals. The final design thickness of 0.125 inch results in lower axial temperature gradients than shown.

The various thermal conditions studied have resulted in various temperature levels, and, therefore, the basic bearing clearance is affected. To provide the design operating radial clearance of 0.0009 inch, the No. 1 bearing will be adjusted to have a 0.0017-inch diametral clearance in the cold static condition. In the most extreme case studied here, the operating bearing clearance will be 0.0015 inch, which corresponds to a reduction in the preload from a design value of 0.6 to 0.2. This is the case with no electrical load, no windage loss, and cold gas driving the turbine. The turboalternator was tested at these off-design bearing clearances, and acceptable operation was demonstrated.

Liquid cooling has been selected for the main thrust bearing to minimize thermal distortions. Coolant performance at a thrust load consistent with space operation is shown in Figure 79, with Versilube F-50 as the coolant. As shown in Figure 80 the liquid enters the thrust bearing stator at 200°F through one inlet and flows in two streams circumferentially 180° where the two streams combine. The flow travels again in circumferential grooves 360° and exits from the stator at an outlet located diametrically opposite to the inlet. The inlet and outlet coolant fittings are located opposite each other to prevent unsymmetrical restraint of the thrust stator by the coolant tubes. The reverse thrust face is designed to act hydrostatically during start and shutdown sequences and requires no liquid cooling during operation.

The alternator rotor is cooled by transferring heat to the bearing cooling rings. The alternator stator is cooled by liquid coolant flow in the frame. The stator operating temperatures, based on the use of Versilube F-50 as the coolant, are listed in Table 11. The location numbers are identified in Figure 81. During the alternator research package tests with a coolant inlet temperature of 200°F, the highest temperature measured in the stator occurred at the end windings and was 255°F at design power level, well below the maximum allowable stator hot spot temperature of 356°F. This conservatism should permit steady-state alternator operation at 100% over rated power.

TABLE 11
STATOR OPERATING TEMPERATURES AT 12 KW

Location	Temperature, °F	
	Predicted	Measured
T1, slot copper	287	
T2, conductor under coil can	288	
T3, end winding	291	255
T4, tooth	285	243
T5, yoke	266	
T6, field coil	277	248

TABLE 11 (Cont'd)

Location	Temperature, °F	
	Predicted	Measured
T7, frame	237	
T8, frame	243	240
TG, tooth surface at air gap	288	–
T9, average coolant	220	–
Coolant rise	15.1	5.4

Studies have been conducted to determine journal bearing clearances during transient thermal conditions. Gas bearing clearances are small (0.0009 inch) and require careful control of the journal and bearing support thermal expansion rates to avoid rubbing when the clearance becomes too low and instability when the clearance becomes too high. In the interest of designing a versatile machine to accommodate a variety of transient conditions, the analysis was conducted for the extreme condition of an instantaneous startup to ensure an ample design margin for other transient startup situations. Figure 82 shows the transient response of the shaft (journal) and the No. 1 bearing mount ring for an assumed step change in speed from zero to 12,000 rpm with no liquid coolant flow in the bearing area. The results of this study indicate that the bearing clearance may not remain within acceptable limits, conservatively set as 0.0004 inch from the nominal gap. No credit was taken for the motion of the flexible pad support, which would double the width of the allowable bearing mount ring temperature band shown in the figure. Introduction of liquid coolant at design temperature and flow rate into the No. 1 bearing heat exchangers at the same time the unit is brought up to speed results in an acceptable transient bearing clearance (Figure 83). The No. 2 journal bearing thermal response was also analyzed; the results are shown in Figure 84. The method of analysis, bearing clearances, and conclusions are essentially the same as those for the No. 1 journal bearing.

Figures 83 and 84 show the transient temperature change of the shaft and bearing support rings for a rapid startup with 200°F coolant supplied only to the bearing cooling rings. Although the predicted transient bearing clearance is satisfactory, changes in the startup procedure or inaccuracy in the predictions make it desirable to provide adjustment of the bearing clearance during the transient for test flexibility. Liquid coolant passages are provided in the journal bearing support rings to permit the flow of coolant in the bearing support ring independent of the coolant flow to the bearing cooling rings. Introduction of 200°F coolant into the bearing support ring at any time during the transient would increase the rate of temperature rise in the bearing support ring shown in Figures 83 and 84 by a factor between 2 and 3. Testing of the turboalternator indicated that this thermal control of bearing clearance was not required for the transient conditions encountered and probably would not be needed for the step start-up assumed in the analysis.

Transient thermal analyses were conducted in the turbine to determine thermal stresses and blade and seal clearances. The studies were conducted assuming a step change in turbine inlet gas flow, pressure, and temperature to full design conditions. Figures 85 and 86 show the metal temperatures at several locations in the first stage, and Figures 87 and 88 show similar results for the second stage. The curves indicate that a more rapid temperature rise occurs in the airfoils than in the turbine case. A turbine operating blade tip clearance of 0.030 inch and a vane seal clearance of 0.048 inch provide a margin of 0.004 to 0.008 inch clearance during the most severe thermal transients. Thermal stresses have been determined, and anticipated transient stresses are below the yield strength of the material indicated in paragraph III. C, Stress and Deflection Analyses.

In the design of the thrust bearing, the distortion of the thrust runner during a rapid startup was examined, both with and without coolant flow during startup. A rapid start was assumed as a step change from zero to 12,000 rpm for conservative results. Also, the orientation which resulted in the smallest thrust bearing clearance and, therefore, the highest heat generation rate was selected. The time at which coolant flow is initiated was examined to evaluate the influence of the coolant temperature. Figure 89 shows the thermal transients at various points in the thrust bearing area with coolant flow in the thrust stator at startup. Figure 90 shows the same temperature curves with no coolant flow in the thrust stator. The resulting deflection of the thrust runner due to temperature gradients across the thrust runner are 0.00024 inch and 0.00007 inch for the cooled and uncooled conditions, respectively. Both deflections are the axial motion of the outer tip of the thrust runner and are small compared to the 0.0011 inch running clearance with the turboalternator in the vertical orientation with the thrust bearing on the bottom. Initiating coolant flow at startup increases the heat flow into the rear face of the thrust runner due to the elevated temperature of the coolant (200°F). This heat flow added to the heat generated in the bearing clearance causes the rear face of the thrust runner to increase in temperature at a faster rate than the forward face, thus causing a small amount of deflection. This analysis indicates that the thrust bearing coolant flow can be initiated at any convenient time after starting up to the time that the thrust stator temperature reaches the coolant temperature.

F. Materials Selection

The turboalternator materials were selected to provide high integrity for a mission duration of at least 10,000 hours and to withstand the handling and storage environments. Materials which have long and successful records in aircraft gas turbine service are employed. Also, to prevent corrosion in storage and handling, stainless materials are included where possible.

PWA 1010 (Inconel 718) nickel-base alloy has been selected for the turbine wheel. Inconel 718 is a heat-treatable nickel-base alloy which has good strength at temperatures up to 1300°F and good oxidation and corrosion resistance in gas turbine engine atmospheres up to approximately 1800°F. The alloy is eminently suitable for use at the design turbine inlet temperature of 1225°F. The specification values have been met consistently by the ingot and forging suppliers. The general industry level of 170,000 psi tensile strength and 130,000 psi 0.2 percent yield strength has been upgraded to 185,000 psi ultimate tensile strength and 150,000 psi yield strength in Pratt & Whitney Aircraft specifications for bars and forgings. Of equal importance are P&WA-initiated requirements for 1300°F notched and smooth bar stress-rupture testing, finer grain size, and vacuum melting practices. In the direction of more uniform properties, composition ranges have been restricted, and permissible amounts of such deleterious elements as manganese, silicon, phosphorus, and sulfur have been reduced significantly.

AMS 5382 (X-40) cobalt-base alloy has been chosen as the turbine vane material. In addition to its heat and corrosion resistance, the alloy was selected for its extremely good castability, permitting better control of trailing edge thicknesses. Pratt & Whitney Aircraft has used this alloy successfully as a turbine blade and vane material for over 12 years.

The inlet case, swirl vanes, struts and nose cone are of AMS 5754 and 5536 (Hastelloy X), a nickel-base metal richly alloyed, primarily with chromium. Because it is nonhardenable by precipitation heat-treatment, it is usually used in the solution-heat-treated condition. It is readily fabricated and welded, and oxidation resistance is excellent at temperatures to 2200°F.

The turbine exhaust diffuser and scroll is a welded assembly fabricated of Inconel 718 and Hastelloy X nickel-base alloys.

AMS 5645 (AISI 347) austenitic stainless steel has been selected for the bearing supports. The alloy has excellent corrosion resistance and is readily brazed. Its high coefficient of thermal expansion is desirable for bearing clearance control. The material has fair machinability, is nonhardenable by heat treatment, and has relatively low strength. The material is not subjected to high stresses in this application, however.

AMS 6294 (AISI 4620) low alloy steel was chosen for the alternator rotor by the General Electric Company because of its combination of desirable electrical properties, weldability, and strength. Although not a deep hardening grade of steel, the requirements of RC30 minimum at the surface of the hardened and tempered rotor adequately define the strength requirements.

The rotor center tiebolt is made of AMS 7460 (Ti-6Al-4V) heat treated and roll threaded titanium alloy. Titanium was selected for its low weight and low modulus of elasticity. Fabrication of parts by this processing specification results in high-quality high-strength lightweight threaded hardware for use up to 600°F. Pratt & Whitney Aircraft and the aerospace industry in general have made extensive use of Ti-6Al-4V processed in this manner for fasteners and related hardware.

G. Instrumentation

Chromel-alumel thermocouples are located at various points of the static structure where variation from the calculated thermal map could affect bearing operation, running clearances, or internal stresses. At the front bearing location, one 10-pin (5 thermocouples) and three 16-pin (8 thermocouples each) hermetic connectors (Figure 91) have been included for measurement of temperatures in the front journal bearing and turbine areas. At the rear bearing location, four more 16-pin connectors have been incorporated. Internal thermocouple locations are given in Table 12. External thermocouples are attached to nonhermetic connectors and are located as stated in Table 13.

Location of 21 capacitance probes for monitoring gas bearing performance are given in Table 14. The probes are illustrated in Figures 31, 33, 58, 101, 102, and 103, as indicated in the table.

Fittings are available for measurement of static pressure in the following compartments:

- Rear face of turbine wheel
- No. 1 journal bearing and alternator
- No. 2 journal and thrust bearings

Three magnetic speed pickups are mounted radially in the reverse thrust stator and receive their signals from six teeth on the thrust runner rim.

TABLE 12

INTERNAL THERMOCOUPLES

Quantity, thermocouples	Location
5	Inside turbine scroll conical section (Figure 92)
8	No. 1 journal bearing pads (Figure 93)
4	No. 1 journal bearing mount ring (Figure 94)
8	No. 2 journal bearing pads
4	No. 2 journal bearing mount ring
3	Main thrust stator (Figure 95)
2	Main thrust stator support (Figure 95)
10	Alternator stator (Figure 96)

TABLE 13

EXTERNAL THERMOCOUPLES

Quantity, thermocouples	Location
8	Axial and circumferential gradient on turbine inlet case (Figure 97)
4	Circumferential gradient on first stage rotor shroud (Figure 98)
8	Radial and circumferential gradient on turbine scroll rear wall (Figure 99)
4	Alternator stator coolant-in and coolant-out temperatures (Figure 100)

TABLE 14

GAS BEARING PERFORMANCE CAPACITANCE PROBES

Location	Purpose	Number of Probes
Thrust Bearing		
Ground* to main thrust plate (Figure 101)	Measurement of movement of thrust plate and net thrust load	1
Main thrust plate to thrust runner (Figure 33)	Measurement of film thickness of main thrust bearing	3
Reverse thrust plate to thrust runner (Figure 31)	Measurement of film thickness of reverse thrust bearing	1
Journal Bearings		
Ground to shaft (Figure 102)	Set-up of bearings and measurement of dynamic motion of shaft relative to ground	2 at 90° per bearing (total of 4)
Pad to shaft (Figure 58)	Measurement of film thickness between each pad and shaft at pivot	4 at 90° per bearing (total of 8)
Ground to back of pad (Similar to that shown in Figure 102)	Measurement of pad flutter in pitch direction (unloaded pad)	1 per bearing (total of 2)
Pad to shaft (Figure 103)	Measurement of pad flutter in roll direction (unloaded pad)	1 per bearing (total of 2)

* The term "ground" refers to any static portion of the structure to which a probe is rigidly attached.

H. Recommendations for Provisions to Install Additional Instrumentation

The recommended aerodynamic instrumentation for the turboalternator package is essentially the same as that suggested for the inlet and exit of the turbine research package so that performance figures will be comparable. Interstage instrumentation, scroll static pressure taps, traverse bosses, and other internal aerodynamic instrumentation are not suggested for the turboalternator. Recommended instrumentation at the turbine inlet (upstream of the flange) is as follows:

- Three total pressure rakes with three taps per rake
- Three total temperature rakes with three thermocouples per rake
- Three static pressure taps

Recommended instrumentation at the turbine scroll exit (upstream of flange) are the following:

- Two total pressure rakes with three taps per rake
- One total temperature rake with three thermocouples per rake
- Four static pressure taps

It is recommended that various pressures and temperatures of coolant flows, bearing compartments, and areas critical to the thrust balance be measured. Thermocouples or pressure taps at the locations in the following list are recommended. Unless otherwise specified, the instrumentation is located in plumbing external to the turboalternator.

- Temperature of liquid coolant to each radial bearing heat exchanger, total of four
- Pressure of liquid coolant to each radial bearing heat exchanger, total of four
- Temperature of liquid coolant from each radial bearing heat exchanger, total of four
- Pressure of liquid coolant from each radial bearing heat exchanger, total of four
- Temperature of liquid coolant to each radial bearing support ring, total of two

- Pressure of liquid coolant to each radial bearing support ring, total of two
- Temperature of liquid coolant from each radial bearing support ring, total of two
- Pressure of liquid coolant from each radial bearing support ring, total of two
- Temperature of liquid coolant to thrust bearing
- Pressure of liquid coolant to thrust bearing
- Temperature of liquid coolant from thrust bearing
- Pressure of liquid coolant from thrust bearing
- Pressure of liquid coolant to alternator
- Pressure of liquid coolant from alternator
- Pressure in the turbine case in front of cone, fitting on one of three inlet struts (see Figure 6)

IV. SUMMARY OF GAS BEARING DYNAMIC SIMULATOR TESTING

A. Objectives

A test program was set up with the following objectives:

- To evaluate the rotor-bearing system under the anticipated turbo-alternator operating conditions with no electrical load and under various electrical loads which impose magnetic unbalance forces on the rotor support system.

- To identify any problems and recommend corrective action.

A rotor system dynamic simulator was built to duplicate the turboalternator rotor mass, distribution of mass and stiffness, and the transverse and polar moments of inertia of the rotor. The bearings and method of support were substantially the same as those designed for the turboalternator package. Figure 104 shows the simulator mounted in the two attitudes tested. Figure 105 shows the internal configuration of the simulator for the first test program, which did not include electrical generating capability.

Figure 106 shows the simulator control panel instrumentation readout equipment and electrical load bank setup for the magnetic unbalance tests. Shop air was used to drive the turbine. A vacuum pump was used to reduce bearing ambient pressures to the test levels. Filtered shop air or argon was used to supply the bearings and the thrust loading chambers. Speed was controlled by turbine inlet pressure and measured by a magnetic speed pickup, which received its input from the six slots machined in the thrust runner.

Thermocouples on the bearings and bearing mounts were recorded sequentially on a strip chart recorder. Signals from the capacitance proximity probes were displayed on oscilloscopes after being conditioned in Wayne Kerr or Microdyne distance-measuring equipment. The Microdyne console, three of which can be seen in Figure 106, is an integrated system including improved stability, switching, and readout equipment to facilitate data presentation in various forms. The ground-to-shaft probes, spaced 90° apart at each journal, are displayed on the X and Y axes of an oscilloscope, as shown in part B Figure 107. The large square represents the maximum displacement of the journal when rotated manually against the pads. The corners of the square are located between adjacent pivots. All probes are displayed versus a time scale in parts A and C of Figure 107.

The bearing design was tested in the simulator as outlined in Table 15. The bearing system operated satisfactorily over the entire test range and met all operating requirements.

TABLE 15

SUMMARY OF TESTS CONDUCTED ON
TURBOALTERNATOR GAS BEARING DYNAMIC SIMULATOR,
First Test Program

Speed rpm	Ambient Air Pressure, psia	Thrust Bearing Load, pounds			Journal Bearings Test Conditions			
		Hydrostatic		Hydrodynamic	Residual Unbalance		0.005 oz-in. Unbalance in Turbine Plane	
		Forward	Reverse	Forward	Hor.	Vert.	Hor.	Vert.
12,000	10.5	250	100	85, 55, 30	X	X	X	X
14,400	10.5	0	0	55,0	X	X	X	X

From the inception of the program, there was concern about the adverse effects that unbalanced alternator magnetic forces might have on the load capacity and stability of the rotor-bearing system. Under idealized conditions of manufacture and operation, the radial magnetic forces in a four-pole inductor alternator would cancel (i.e., the resultant radial force and transverse moment acting on the rotor would be zero). In practice, however, unavoidable variations in material and geometry of the rotor and stator, and deviations of the rotor from the exact magnetic centerline of the stator, will result in unbalanced magnetic forces (and, to a lesser extent, moments) acting on the rotor. These forces act to increase eccentricity of the rotor which in turn results in further increase in the forces. An unstable condition may thus exist if the journal bearings lack sufficient restorative force capability. Although the alternator magnetic forces were known to exist, their dynamic magnitudes and characteristics had not been investigated in detail. Accordingly, conservative procedures were used to size the turboalternator bearings for magnetic loading, and every effort was made during the alternator design to minimize the unbalanced magnetic force gradient.

In 1965, testing of a high-speed motor-driven gas-bearing compressor (by Mechanical Technology Incorporated) identified a severe condition of rotor disturbance (perhaps instability). The disturbance arose only during excitation of the motor. Similar effects, some quite severe, had also been observed on other developments of motor-driven gas-bearing machines. As a result of these experiences, the turboalternator program was expanded to include a detailed

investigation of the interactions between the alternator and rotor-bearing system due to electromagnetic coupling. The objectives of the investigation were first to determine the magnitudes and characteristics of the electromagnetic rotor forces as a function of eccentricity of the rotor from the magnetic centerline of the stator and, second, to determine whether or not these forces would create any rotor-dynamic problems during operation of the turboalternator. The investigation was carried out in four phases as follows:

- Analysis and prediction of the magnitudes and characteristics of the unbalanced magnetic forces as functions of rotor eccentricity and various electrical load conditions

- Measurement of these forces using a duplicate alternator supported by rolling-element bearings and mounted on a specially designed force-measuring test stand

- Analytical investigation of the response of the gas-lubricated turboalternator rotor-bearing system to the predicted electromagnetic forces.

- Experimental substantiation of the predicted rotor-bearing system performance using a turboalternator gas-bearing simulator equipped with the prototype alternator and operating under various power generating conditions.

The first two phases were performed by the General Electric Company and are discussed in Reference 2, Volume II.

A number of calculations were performed to ascertain dynamic response of the rotor-bearing system for combinations of the mechanical variables listed in Table 16 and the electrical load conditions of Table 17. Calculated responses for two mechanical conditions of operation are given in Table 18. In addition to the journal and pad-pitch amplitudes in the table, the amplitudes of pad motion in the roll and radial directions were also calculated. Amplitudes in these directions were insignificant and hence are not listed.

It is seen from Table 18 that the calculated dynamic amplitudes were very small for all the electrical cases with a mechanically balanced rotor in the vertical position. For the case of an unbalanced horizontal rotor, the calculated amplitudes, while considerably larger, were still quite acceptable for reliable operation. The rotor amplitudes were, in fact, of the same magnitude as the expected out-of-roundness of the rotor journals.

TABLE 16

MECHANICAL VARIABLES OF SIMULATOR TEST PROGRAM

1.	Rotor orientation	Horizontal and vertical
2.	Rotor speed	10,800, 12,000 and 14,400 rpm
3.	Bearing ambient pressure	7.2 and 10.5 psia
4.	Bearing preload ratio	0.35 (or less) and 0.5 (or greater)
5.	Rotor mass unbalance	Residual and residual plus 0.005 oz-in. unbalance added to the turbine plane
6.	Alternator rotor eccentricity	Concentric (within ±0.5 mil) and eccentric (from 2.0 to 4.0 mils)

TABLE 17

ELECTRICAL LOAD CONDITIONS OF SIMULATOR TEST PROGRAMS

1. 3-phase balanced load: 0, 3, 6, 9, and 12 kw
2. Single-phase load (2 phases open): 3.33 kw
3. Power factor: 1.0 and 0.8 lagging
4. 3-phase short circuit
5. Single-phase short circuit
6. No-load condition, but with field excitation applied.

The highest calculated value of static magnetic force given in Table 19 occurs at the single-phase short circuit condition. The predicted force (per pole pair) is 33.4 pounds at a 2.0-mil rotor eccentricity. Although the journal bearings could handle this load under steady-state conditions, there was concern that initiation of the short circuit might induce sudden application of the load, in which case the resulting rotor transient might cause a bearing contact. (The transient response condition was not included in the analytical investigation.) However, based on prior experience, it was felt that, should a bearing contact occur, it would be momentary in nature and the bearing surfacing materials would be capable of enduring the contact without failure or degradation of bearing performance.

In addition to performing the response calculations described in the preceding paragraphs, the effect of alternator magnetic force gradient on rotor stability was also investigated. A multi-degree-of-freedom Mathieu-type stability analysis, including the effects of bearing damping, was programmed for computer solution. The resulting stability map for the turboalternator is plotted in Figure 108, together with the point corresponding to 15 kva (at 0.8 lagging power factor) operation of the turboalternator, this being the point which was found to lie

TABLE 18
CALCULATED RESPONSE OF JOURNAL BEARINGS TO VARIOUS CONDITIONS OF ALTERNATOR OPERATION AND ROTOR MECHANICAL UNBALANCE

Rotor Eccentricity and Mechanical Balance Condition	Rotor Orientation	Alternator Oper. Cond.	Bearing Preload Ratio	Amplitude of Journal Motion, microinches		Pitch Amplitude of Pads microradians			
				Thrust Brg. End	Turbine End	Thrust Bearing End		Turbine Bearing End	
						Top Pad	Bottom Pad	Top Pad	Bottom Pad
Rotor eccentric by 0.002 inch, both pole planes; no mechanical unbalance.	Vertical	1	0.5	5.1	6.2	4.2	8.8	5.4	11.1
		2	0.5	3.3	3.9	2.3	5.7	3.0	7.1
		3	0.5	3.0	3.6	2.4	5.1	3.1	6.4
		4	0.5	0.3	0.3	0.3	0.3	0.4	0.5
		5	0.5	2.5	2.3	5.1	3.5	4.0	2.7
		6	0.5	2.3	2.8	3.0	3.5	3.7	4.4
		7	0.5	1.8	1.8	2.5	3.1	2.9	2.8
Rotor eccentric by 0.002 inch, both pole planes; 0.005 oz-in. unbalance in plane of turbine wheel	Horizontal	1	0.35	28.6	67.7	23.7	41.8	78.1	97.4
		2	0.35	18.8	53.0	14.1	27.9	51.4	76.4
		2	0.50	19.5	55.7	20.3	27.8	42.7	80.1
		3	0.35	17.1	50.4	14.1	25.0	64.7	71.9
		3	0.50	17.8	63.1	19.8	24.8	41.9	75.5
		6	0.35	13.4	43.7	16.4	16.9	66.1	59.4
		7	0.50	14.0	47.1	20.1	16.1	42.4	62.5

Note: Response amplitudes in the above table are peak single-amplitude values measured from the static eccentricity position of the rotor due to the static component of electromagnetic force (F_o) and, in the case of horizontal orientation, rotor weight.

TABLE 19
CALCULATED STATIC ELECTROMAGNETIC FORCE
FOR ALTERNATOR AT 2.0-MIL ROTOR ECCENTRICITY

F_o, pounds	KW	Power Factor	Load	Other
11.25	12	0.8	Balanced	No saturation effects
11.44	12	0.8	Balanced	Including saturation effects
10.01	9	0.8	Balanced	-
13.09	12	0.8	Balanced	Three-phase short circuit
33.4	12	0.8	Balanced	Single-phase short circuit
7.64	0	-		Alternator field excited
7.86	3.33	1.0	Single phase	Two phases open

closest to the unstable region. It is seen that this "closest" point is well removed from the unstable region, indicating that turboalternator operation should be stable.

The rotor system dynamic simulator was revised to include the turboalternator shaft and stator (Figure 109). The drive turbine was replaced with a unit capable of driving the alternator at full power as well as supplying the bearing and windage losses. Thermocouples in the stator and its coolant lines were used in addition to the instrumentation described for the first test program. Independent control of electrical load and power factor for each phase of the alternator was possible with the load bank, which is shown in Figure 106. In addition, both single-phase and three-phase short circuits could be applied via the load bank at any condition of output load.

A total of over 250 test points was recorded during the second simulator test program. Each point corresponded to a different condition of simulator operation. The conditions of simulator operation were uniquely defined by a particular combination of six mechanical variables and one of six possible electrical load conditions. The six mechanical variables, and the values of each variable used during the test, are identified in Table 16. The six electrical load conditions, and the values of each load condition used during the test, are identified in Table 17. It will be recognized that there are considerably more than 250 combinations of simulator test conditions based upon the conditions of Tables 16 and 17. Most of the additional points, however, were eliminated by conduct-

ing all the power generation tests at 12,000 rpm only and by performing most of the short-circuit tests at the 12-kw power level. During all of the tests the simulator journal bearings were operated in the normal self-acting mode (i.e. without any external pressurization). The thrust bearings were operated hydrostatically.

B. Simulator Test Results

Oscilloscope photographs of the turbine bearing performance taken during test of the simulator with the rotor vertical, eccentric, and with residual mechanical unbalance are shown in Figures 110 and 111. Figure 110 shows the effect on the journal, and on the pivoted-pad film thickness, of applying alternator field excitation at no-load conditions of operation. Figure 111 shows the effect of imposing both single-phase and 3-phase short circuits on the alternator when operating at a 12-kw balanced load condition.

The upper traces on the photographs in Figures 110 and 111 indicate that journal vibration is largely synchronous and that the amplitude is virtually unaffected by the various conditions of alternator electrical load and short circuit. The cause of this synchronous vibration, the peak-to-peak amplitude of which is approximately 0.14 mil, is attributed primarily to residual unbalance and, to a lesser extent, to out-of-roundness of the journal. There is no evidence in these traces of any two-per-rev or higher harmonic response due to electromagnetic forces. It should be noted, however, that the predicted amplitude of journal vibration at the higher harmonics was, as shown in Table 18, in the order of a few microinches with the rotor vertical and mechanically balanced. Under such small amplitude conditions, the associated instrumentation signals would be masked by the residual electrical noise level which is present on all channels of instrumentation.

The lower traces on the photographs in Figure 110 and 111 show the film thickness of one of the lower bearing pads and indicate an increase in dynamic film variation when an electrical load is applied. The largest peak-to-peak variation in the pad film thickness, approximately 0.16 mil, occurred during the single-phase short, as shown in Figure 111. As noted above, the amplitude of journal vibration was essentially unaffected by the electrical conditions of alternator operation. Consequently, the apparent increase in dynamic variation of film thickness must have been due to vibration of the pad-flexure assembly relative to the journal.

The high-frequency content of the lower (film thickness) traces seen in Figures 110 and 111 is attributed to electrical noise in the particular channel of instrumentation. However, during single-phase shorting of the alternator (while operating under conditions of 12-kw load) a clear indication of two-per-rev varia-

tion in film thickness did emerge from the background noise level as shown in Figure 111.

Oscilloscope photographs of the turbine bearing performance taken during test of the simulator with the rotor horizontal, eccentric, and mechanically unbalanced by 0.005 oz-in. in the plane of the turbine wheel, are shown in Figures 107, 112, and 113. Figure 107 shows the effect on bearing performance of applying the alternator field excitation at no-load conditions of operation. Figure 112 shows the effect of 12-kw balanced load and single-phase short circuit conditions. The effect of a 3-phase short-circuit condition, and a resulting labyrinth rub due to excessive rotor eccentricity, is shown in Figure 113. The upper traces on the photographs of Figures 107 and 112 indicate that the journal vibration is again synchronous. The peak-to-peak amplitude is approximately 0.16 mil for alternator operation without excitation, as shown in Figure 107. The peak-to-peak amplitude increases to 0.25 mil under the single-phase short condition shown in Figure 112. Again, it is not possible to detect with any certainty the presence of the predicted higher harmonics.

The lower traces in Figures 107 and 112, showing pad film thickness, have characteristics similar to those described for vertical operation with residual unbalance. The peak-to-peak amplitudes of vibration of both the journal and the pad film thickness, however, are seen to be somewhat larger in the case of horizontal and unbalanced operation. This trend was predicted by analysis, as is shown in Table 18.

During the 3-phase short circuit tests on the horizontal rotor, the turbine wheel rubbed on a labyrinth when the short was initiated. This incident is clearly seen from the bearing orbit photographs of Figure 113. The right-hand orbit was photographed immediately prior to the short being applied. On applying the short, the rotor moved vertically downward, causing contact with the labyrinth. The rotor then bounced vertically upward. The situation returned to normal on removal of the short condition. Figure 113 (A) shows time-base traces from the X and Y journal probes during the labyrinth rub, while Figure 113(C) shows simultaneous traces from the X journal probe and the loaded-pad film-thickness probe.

The rub, which occurred on the large-diameter turbine wheel labyrinth seal, was the result of operating at alternator eccentricities in excess of 4 mils at the alternator pole plane adjacent to the turbine bearing and 3.5 mils at the pole plane adjacent to the thrust-end bearing. The eccentricity at the plane of the turbine was calculated to be in excess of 6 mils. During assembly of the simulator the clearance at this plane was checked, with shim stock, to be 7 mils. From these figures it can be seen that the small increase in eccentricity which resulted from initiating the 3-phase short circuit was sufficient to cause the rub. This short-circuit test was repeated several times, and on each occasion a labyrinth rub occurred. However, no bearing rubs were detected, and, as can be seen from

the lower trace on Figure 113, adequate film thickness between the journal and the pad was retained throughout the incident.

The effect of the static electromagnetic force, F_o, on journal position and pad film thickness can also be clearly seen on Figures 107, 110, 111, and 112. In Figure 110 the vertical distance of 0.6 mil separating the two orbits indicates the movement of the journal resulting from switching on the alternator excitation with the rotor in a vertical position. The lower traces on Figures 110 and 110 show the effect on the pad film thickness.

Figure 107 also shows the effect of switching on the excitation. In this case the rotor was horizontal. As a result of the increased stiffness of the loaded bearings, the journal movement is considerably reduced. The reduction in pad film thickness is, for the same reason, also less. Similar trends can be seen as a consequence of initiating both the single-and three-phase shorts (Figures 112 and 113).

From the observed steady-state movements of the journal and changes in pad film thickness which resulted from each change in the condition of alternator operation, it is possible to estimate the static electromagnetic force which caused these changes. In order to make such estimates it is necessary to have experimental data showing the pad film thickness for each of the four pads in the bearing, and also experimental data showing the eccentricity of the rotor pole-planes relative to the bore of the alternator stator. As described previously, the simulator was equipped with the instrumentation required to make these measurements.

Following acquisition of the experimental data, the recorded probe readings were corrected for thermal expansion and instrumentation calibration effects. The data were then superimposed on plots of calculated bearing performance. The calculated bearing performance was plotted as curves of film thickness versus bearing preload ratio for various values of bearing load. In order to plot the experimental data, the value of bearing preload ratio (m) was calculated using the following equation:

$$m = 1 - h_{p(avg)} / C_p$$

where $h_{p(avg)}$ is the average of four film thickness measurements taken at the pivot locations of one journal bearing, and

C_p is the pad radius minus the journal radius

The value of static magnetic load was then obtained by linear interpolation of the experimental points relative to the two adjacent calculated load curves.

Three representative curves are shown in Figures 114 through 116. The experimental data plotted in Figures 114 and 115 are for the journal bearing located adjacent to the thrust bearing. The rotor is vertically oriented with residual mechanical unbalance. The experimental data plotted in Figure 116 is likewise for the same bearing. In this case, however, the rotor is horizontal and also unbalanced by 0.005 oz-in. in the plane of the turbine wheel.

Under alternator operating conditions of no excitation (and hence no load), the electromagnetic force is zero and the corresponding experimental data point should fall on the zero load line for vertical operation and on the load line representing 1-g bearing load for horizontal operation (which, in this case, is 28 pounds). The fact that the experimental data points for zero excitation condition are not coincident with the appropriate load lines is attributed to radial forces on the rotor resulting from eccentric operation of the turbine labyrinth seals and also to variations in bearing geometry. For example, the analysis of bearing performance does not take into account the effect of the 0.2-mil-deep pocket which is cut into the surface of each of the loaded pads for the purposes of hydrostatic lift-off. A further potential loss in film thickness for a given load exists as a consequence of back leakage from the bearing film through the lift-off bearing orifice in the loaded pads. Although check valves were used to limit this backflow, some leakage was nonetheless detected with a flowmeter during the tests.

Examination of the calculated bearing performance plotted in Figures 114 and 116 shows that the load change associated with a given change in film thickness is greater in the regions of high loads than it is for the same film thickness change in the regions of low loads. Considering, then, the experimental data obtained during alternator operation in a vertical orientation, it is reasonable to describe the zero excitation test point as the zero load point. The bearing loads at other conditions of alternator electrical operation can then be determined.

If it is assumed that the electromagnetic force gradients are the same for each of the two alternator pole pairs and that for small eccentricities the force gradients are linear, then the calculated and experimental bearing performance data can be used to calculate the static electromagnetic gradients. The change in radial force on the rotor which results from a change in eccentricity at the turbine labyrinth is accounted for in the calculations of the electromagnetic gradients. Values of bearing load and pole-plane eccentricity under various conditions of alternator operation are given in Table 20 together with values of the experimentally determined and analytically predicted average static force gradient for each pole pair. From examination of the force gradient values, it is

TABLE 20

CALCULATED AND EXPERIMENTALLY-DETERMINED STATIC ELECTROMAGNETIC FORCE GRADIENT PER ALTERNATOR POLE PAIR

Alternator Operating Condition	Turbine Journal Bearing and Adjacent Pole Pair		Thrust-End Journal Bearing and Adjacent Pole Pair		Average Static Force Gradient Per Pole Pair, lb/mil	
	*Force on Brg. Due to F_o, lb	*Eccentricity of Poles, mils	*Force on Brg. Due to F_o, lb	*Eccentricity of Poles, mils	*From Test Results	Predicted by Analysis
No Excitation	0	2.64	0	2.30	0	0
No Excitation	0	2.81	0	2.42	0	0
Excitation only	8.0	2.84	4.6	2.46	2.01	3.82
Excitation only	10.0	3.16	4.0	2.67	1.82	3.82
3 kw, 3-phase, 0.8 p.f.	11.0	2.87	4.4	2.47	2.19	----
3 kw, 3-phase, 0.8 p.f.	13.5	3.22	5.5	2.70	2.45	----
6 kw, 3-phase, 0.8 p.f.	11.0	2.88	6.6	2.46	2.83	----
6 kw, 3-phase, 0.8 p.f.	16.5	3.23	5.5	2.71	2.67	----
12 kw, 3-phase, 0.8 p.f.	17.0	3.01	7.5	2.56	3.44	5.625
12 kw, 3-phase, 0.8 p.f.	16.0	3.00	6.4	2.57	3.05	5.625
12 kw, 3-phase, 0.8 p.f.	22.0	3.45	6.8	2.87	3.22	5.625
12 kw, 3-phase, 0.8 p.f.	22.0	3.42	7.7	2.83	3.48	5.625
3.33 kv-a, 1-phase, 1.0 p.f.	8.0	2.73	4.1	2.28	1.98	3.93
3.33 kv-a, 1-phase, 1.0 p.f.	11.0	3.23	3.4	2.73	1.70	3.93

* The experimental data was obtained during test with the rotor oriented vertically and rotating at 12,000 rpm.

seen that those obtained from experimental data are lower than the predicted values. The spread in the experimentally determined gradient values at any given alternator operating condition is due to (1) experimental error and (2) small viscosity changes due to 30° to 40°F variations in temperature from the 110°F value used for the bearing performance calculations.

The experimentally determined gradients for zero load and for 3.33-kva alternator operation are approximately 50 percent of the predicted values, whereas the gradients at 12 kw alternator output are 55 to 65 percent of the predicted values.

The results of the analytical and experimental rotor-response studies can be summarized as follows:

1. Operation of the rotor-bearing system was analytically predicted to be stable under various conditions of electrical power generation. Test operation of the simulator was stable under all electrical output conditions imposed during the test program.

2. Calculated forced vibration amplitudes due to electromagnetic excitation of the rotor-bearing system were found to be so small as to be of no practical consequence. Test operation of the simulator indicated no detectable vibration response of the rotor due to electromagnetic forces. Definite two-per-revolution vibration of one of the pad-flexure assemblies was observed under single-phase short circuit conditions. However, amplitude of this vibration was of no practical concern.

3. Experimentally determined alternator electromagnetic static force gradients were smaller than the predicted gradients. The General Electric Company (Reference 2, Volume II) using a different experimental technique also indicated significantly lower measured gradients.

4. The large static alternator force predicted by analysis for the single-phase short circuit condition was not confirmed by the simulator test data. GE test data also shows the single-phase short circuit force to be considerably smaller than predicted.

5. Under all imposed conditions of mechanical and electrical simulator operation, including an unintentional labyrinth rub, operation of the rotor-bearing system was excellent. No condition of actual or imminent bearing contact or instability was detected.

6. The electromagnetic force gradient was experimentally determined to be about 3 pounds per 0.001 inch of rotor-stator eccentricity. The tur-

boalternator design tolerances should control the eccentricity to within 0.0015 inch.

7. A check of bearing system performance was made with each of the two journal bearings approximately 0.001 inch eccentric in opposite directions, that is, with the rotor cocked rather than just laterally displaced. Bearing performance was excellent, including that of the hydrodynamic thrust bearing, which had been adjusted parallel to the thrust runner with the rotor in the concentric position. The thrust stator flexure-mount system apparently permitted sufficient self-alignment of the bearing so that performance was not seriously affected.

V. TURBOALTERNATOR TEST PROGRAM

A. Introduction

A test program was conducted at Pratt & Whitney Aircraft to verify the mechanical design of the turboalternator. The test program consisted of three phases:

- Testing of the gas bearing dynamic simulator under the same conditions used at Mechanical Technology Incorporated. This phase will not be described.
- Developmental testing of the turboalternator.
- Acceptance test of each turboalternator.

B. Test Facility

The test stand used for testing the turboalternator packages and some of the instrumentation readout equipment are shown in Figure 117. Turbine drive air was supplied by diesel-driven positive displacement compressors through the system shown in part (a) of Figure 118. Valves V-4 and V-5 are fine and coarse manual throttle controls. The check valve at the turbine inlet prevented excessively low turbine inlet pressure when the turbine drive air was abruptly stopped and the unit was at speed. Nitrogen or argon for the hydrostatic jacking of the bearings was supplied from the facility tank farm through the system shown in part (c) of Figure 118. The hydrostatic gas pressure to the bearings was set as necessary by adjusting valves V-8, V-9, and V-10. The turbine throttle controls were opened manually when nonautomatic start was desired.

An interlock system between the turbine drive and jacking gas systems permitted:

- Semi-automatic startup by closing two switches
- Automatic shutdown by opening one switch
- Automatic hydrostatic pressurization of the appropriate bearings in the event of accidental loss of turbine drive air.

Startup using the interlocks shown in part (b) of Figure 118 was as follows: Hydrostatic gas supply valves V-8, V-9, and V-10 were preset to supply the desired pressure levels at the respective bearings. Pressure-sensitive switches PT-3, PT-4, and PT-5 were closed by their respective hydrostatic jacking gas pressures. The turbine throttle valves V-4 and/or V-5 were preset for the desired turboalternator rotor speed. The "start" switch was closed to energize solenoid S-1 which opened valve V-2 and supplied drive air to the

turbine. Pressure at the turbine inlet closed switches PT-1 and PT-2 so that when the desired speed was reached, the hydrostatic gas supply could be shut off by closing the run switch to energize solenoids S-2 and S-3.

Normal shutdown was achieved by opening the "run" switch which turned on the hydrostatic gas by opening solenoid valves S-2 and S-3. The "start" switch was then opened to de-energize solenoid S-1, close valve V-2, and shut off the turbine drive air.

Rapid shutdown was possible by opening the "start" switch, which shut off the turbine drive air. This intentional loss of turbine inlet air pressure or any accidental loss of turbine inlet air pressure opened switch PT-2, which in turn opened solenoid valves S-2 and S-3 to provide hydrostatic jacking gas to the bearings. For vertical operation, the position switch was closed to bypass PT-3 and prevent hydrostatic gas flow to the journal bearings.

Case pressurization or bleed flow was required to maintain bearing cavity pressure and to prevent entry of turbine drive air into the bearing compartments. This flow was supplied through the reverse thrust stator by valves V-6 and S-2 or through the case pressure supply fitting.

The water circulating system (Figure 119) supplied water at the design temperature of 200°F±15°F to the journal bearing heat exchangers, the alternator stator, and the main thrust stator in amounts thermally equivalent to the design flows for Versilube F-50 coolant.

An oil circulating system (Figure 120) permitted journal bearing clearance control. The temperature of each bearing mount ring, and thus its size, could be changed by varying the temperature of the oil circulating in the mount ring. An increase in oil temperature resulted in increased journal bearing clearance.

The General Electric Company engineering breadboard voltage regulator-exciter (Figure 121) and load bank (Figure 122), described in Reference 2, were available for energizing the field and loading the alternator.

Signals from the 21 capacitance proximity probes were displayed on oscilloscopes as described in Section IV. Twelve of the more significant capacitance probes could also be recorded on a Precision Industries Model PS-214A tape recorder with an Industry Standard 14-channel head for 1-inch wide magnetic tape. The two remaining channels recorded rotor speed and vocal commentary.

Rotor speed was sensed by the bill-of-material magnetic speed pickups receiving their signal from six teeth on the thrust runner periphery. Readout was on Hewlett-Packard counters.

Vibration pickups (Consolidated Electrodynamics Corporation Type 4-118-0001) were used to measure the vibration of the static cases in the axial direction and in horizontal and vertical planes at each mount plane. Signals from the pickups were read on meters designed by Pratt & Whitney Aircraft and capable of measuring vibrations with amplitudes up to 0.0025 inch.

C. Developmental Tests

No. 1 Turboalternator Package

Both turboalternator packages were mounted with the shaft centerline 45° from horizontal, as shown in Figures 123 and 124, to permit loading of both the main thrust and the journal bearings. The first run of the first turboalternator consisted of bringing the unit to design speed (12,000 rpm), shutting off the nitrogen hydrostatic gas supply, checking hydrodynamic bearing operation, and shut-down with hydrostatic gas supplied to all bearings. Shaft orbits, measured by the ground-to-shaft probes in each journal bearing were about 0.0001 inch in diameter. Pitch and roll motion of the journal pads was minimal, consistent with the 0.00005 inch total out-of-roundness of the journals. Dynamic motion of the main thrust stator was also minimal, consistent with the 0.0001 inch total runout of the seven-inch-diameter thrust runner with respect to the shaft centerline.

Additional testing was performed to verify bearing operation 1) with design temperature coolant flowing in all loops, 2) under 7KW of electrical load, 3) at 20% over design speed, and 4) using argon as the lubricant. All testing was conducted with the hydrodynamic bearings except during startup and shutdown. Satisfactory shaft orbits or bearing dynamics were observed during the 21 hours of testing. Adjustment of the journal bearing clearance, using the thermal control provisions in the bearing mount rings, was demonstrated. Upon removal of the electrical load, the rotor speed increased temporarily to 16,000 rpm, and the bearings, operating hydrodynamically, performed satisfactorily.

No. 2 Turboalternator Package

The first run of the second turboalternator consisted of bringing the unit to design speed and achieving hydrodynamic operation of the bearings. The speed was increased to 14,400 rpm (120% of design speed) and a balanced electrical load was applied to lower the rotor speed to 12,000 rpm for the same turbine throttle setting. This load was 3.6 KW at unity power factor.

Figures 125 through 129 show the gas bearing performance with the bearings operating hydrodynamically at 14,400 rpm. Journal orbits, measured by the ground-to-shaft probes, were less than 0.0001 inch in diameter. Journal and thrust bearing film thicknesses proved to be as anticipated. Pitch and roll motion of the journal-bearing pads was minimal, consistent with the 0.00005 inch total out-of-roundness of the journals. Figure 128 indicates axial oscillation of the rotor. This oscillation was detected on both turboalternators and was caused by the turbine drive air system. Figure 129 indicates that the main thrust stator moves with the rotor and the rotor amplitude is 0.0003-0.0004 inches.

On starts after the initial testing, the front journal bearing exhibited an increased orbit which quickly reduced in size. This initial increase in orbit was caused by oil from the drive compressors accumulating in the turbine wheel during the shutdown. Figure 130 shows the front journal bearing orbit at various speeds up to 12,000 rpm; the increased orbit at design speed due to this accumulation of oil is evident. Figure 131 shows the orbit during a coasting deceleration and indicates the predicted critical speed range from 8000 to 10,000 rpm. The bearings were operating hydrostatically for these low speed tests. The rear journal bearing indicated smaller orbit diameters than the front journal bearing.

An endurance test was run at 12,000 rpm, with the journal and main thrust bearings operating hydrodynamically on argon, an electrical load of 3.6 kw at unity power factor, and with the cooling provisions at design temperature. Figures 132 and 133 are graphic plots of significant data such as bearing clearances, temperatures, and temperature differentials. Of particular interest are the facility coolant-water thermostat failures which occurred at 31 hours, 68 hours, and 81 hours. The consequent coolant stoppage in each case caused a slow (1°-2°F per minute) temperature rise, but no significant thermal gradients were produced in the bearings. Satisfactory turboalternator operation was indicated during the 100-hour test.

D. Acceptance Test

An acceptance test of each turboalternator package to demonstrate the mechanical integrity of the unit was required. The specified acceptance test consisted of acceleration to design speed (12,000 rpm), operation at this speed for five (5) hours, and deceleration. The test was specified as a free spin-up using any convenient cold gas. A record of gas bearing performance during acceleration and deceleration was required.

No. 1 Turboalternator Package

The first turboalternator package successfully completed its acceptance test on 13 September 1967. Argon was used for hydrostatic bearing operation and bearing cavity pressurization. The unit was started with hydrostatic gas to all bearings. At 12,000 rpm the hydrostatic gas was shut off with a solenoid valve and the bearings operated hydrodynamically. After about an hour a load of 7 kw was applied to the alternator at unity power factor. The load, limited by the facility turbine drive airflow capacity was carried for 15 minutes. After four hours running had been completed, the thermal control of the journal bearing radial clearance was demonstrated although bearing clearance during the test did not require adjustment. After the five hours had been completed the hydrostatic jacking gas was supplied to the bearings by opening the solenoid valve, the turbine throttle was closed, and the rotor coasted to a stop. Terminal voltage was maintained throughout the acceptance test by the voltage regulator-exciter.

Total accumulated running time on the first turboalternator package was 26 hours including 5 hours on electrical load.

Photographs of oscilloscope traces taken when the turboalternator bearings were operating hydrodynamically at 12,000 rpm are presented in Figures 134 through 137. The shaft orbits remained essentially the same as shown in Figure 134 (less than 0.0001" diameter) for all test conditions including the electrical load. Journal bearing film thicknesses remained within the allowable operating range of 0.0005-0.0015 inches as shown on Figure 135 without use of the thermal control system. The amplitude of the journal bearing pad dynamic motion in both the roll and pitch modes shown in Figure 136 was consistent with the shaft orbit diameter and the 0.00005 inch measured out-of-roundness of the shaft journals. The main thrust bearing film thickness shown in Figure 137 is as predicted for the running condition and the sum of the film thicknesses for the two thrust bearings is consistent with the 0.004 inch measured thrust bearing axial clearance.

No. 2 Turboalternator Package

The second turboalternator package successfully completed its acceptance test on 21 November 1967. This test was essentially the same as the acceptance test of the first turboalternator package except for the following items:

- A DC variable power supply was used to energize the alternator in place of the engineering breadboard voltage regulator-exciter which had given indications of failure during previous tests on the second turboalternator.
- An electrical load of 3.6 kw at unit power factor was carried during the acceptance test.
- An electrical load of 9.3 kw at unit power factor was carried for about 30 minutes.

Bearing performance data during this acceptance test are shown in Figures 138 through 141.

Total accumulated running time on the second turboalternator package was 114 hours including 108 hours on electrical load.

E. Test Results

The turboalternators performed satisfactorily under all conditions. The major design operating conditions to which the unit was not subjected were design turbine inlet temperature and design bearing cavity pressure level. Bearing clearances were satisfactory and required no adjustment after assembly.

Thermal control of the journal bearing mount ring was not required during the testing; however, the journal clearance can be varied over a wide range with reasonable response.

No bearing instability was detected during the test program and rotor motion due to magnetic forces was negligible.

The cooling system maintained acceptable temperature levels with very low bearing gradients during all testing. Accidental loss of liquid coolant flow resulted in a temperature rise in the machine, but the rise was slow enough to permit corrective action or safe shutdown. No significant thermal gradients developed in the bearings as a result of the coolant stoppage.

No degradation of bearing performance was detected during the 114 hours of operation on the second turboalternator.

REFERENCES

1. Turbine Research Package for Research and Development of High-Performance Turboalternator. Report PWA-2796, NASA CR-54885, Contract NAS3-6013, January 1967.

2. Alternator and Voltage Regulator-Exciter for a Brayton Cycle Space Power System. General Electric Report, Contract NAS3-6013.

   Volume I. Alternator and Voltage Regulator - Exciter Design and Development,

   Volume II. Unbalanced Electromagnetic Forces Investigation

3. Research and Development of High Performance Axial Flow Turbomachinery. Report PWA-2977, Contract NAS3-4179.

   Volume I. NASA CR 800, Design of Turbine Compressor, March 1967.

   Volume II. NASA CR 801, Design of Gas Bearings, March 1967.

   Volume III. NASA CR 802, Design of Back-Up Gas Bearings, December 1966.

APPENDIX I

Back-up Gas Bearing Design

The purpose of the back-up-gas-bearing effort was to design a rotor support system that could be incorporated into the turboalternator if the initial gas bearing system proved unsatisfactory upon testing. Therefore, as much as possible of the turboalternator design was maintained to provide an economical substitution of bearing systems. The Franklin Institute Research Laboratories provided the gas-bearing performance and dynamic analyses and furnished design requirements for the back-up bearings during design investigation. The gas-bearing design and analysis is presented as Volume 3 of this report, which was prepared by the Franklin Institute Research Laboratories. The major areas of design integration included bearing performance, thermal control, and bearing mechanical support design. This appendix deals with the thermal and mechanical design of the back-up bearing system.

The Franklin Institute Research Laboratories selected hybrid journal bearings, a dead-ended, spiral-groove, inward-pumping hybrid main thrust bearing and a hydrostatic reverse thrust bearing for the turboalternator (Figure 142). The journal diameter is the same as for the primary bearing design, so the alternator rotor is interchangeable. Each journal bearing (Figure 143) is a full sleeve, with a gas supply orifice feeding each of six axial recesses. The sleeve is supported on a flexible diaphragm. The thrust bearings (Figure 144) are similar in appearance to the primary design.

Each bearing is pressurized by argon bled from the compressor discharge. The bearing cavity is maintained at low pressure, slightly above the turbine discharge pressure. In order to maintain the argon flow into the turbine, the bearing cavity pressure will be about 7 psia at design conditions, and the pressure drop across the bearings will be about 2 psi. The resulting low pressure in the No. 2 bearing and thrust area results in an aerodynamic thrust load of about 79 pounds. In operation on the ground in the vertical position, the weight of the rotor, 56 pounds, is added to the aerodynamic thrust. The hybrid thrust bearing diameter of seven inches results in the following thrust bearing performance:

Rotor Position	Vertical (Turbine Up)	Horizontal
Thrust	135	79
Clearance - inch	0.0020	0.0027
Friction power loss - watts	80	60

The hybrid thrust bearing requires a flow of 0.0013 lb/sec during horizontal or zero g operation. Each radial hybrid bearing requires 0.0034 lb/sec of argon flow. An additional 0.0012 lb/sec of gas is used to prevent leakage of hot mainstream gas through the front turbine seal. The total of these bleed flows is about 1.5 percent of the system flow. The total friction loss for both journal and thrust bearings is 160 watts during space operation.

The requirement to maintain low radial-bearing-flexure stiffness necessitates careful routing of the gas-supply tubing to the bearing to limit restraint of the bearing. The sum of the tube restraint and support stiffness is designed at 15,000 inch-pounds per radian. The corresponding support diaphragm thickness is 0.035 inch with 50 percent of the area removed. The thrust-bearing coolant and hydrostatic-gas tubing also required additional routing study to limit restraint of the thrust stator. The support of the thrust stator is a diaphragm similar to that for the radial bearing. The thrust stator support has a thickness of 0.036 inch with 60 percent of the area removed. The torsional stiffness of the support and the tube restraint is 20,000 inch-pounds per radian.

Natural frequencies and deflections of the bearings and support system of the hybrid bearings have been calculated with the following results for the thrust bearing:

	Axial	Radial	Pitch
Bearing Support Spring Rate	5000 to 17,000 lb/in	1,500,000 lb/in	6000 to 20,000 in-lb/rad
Natural Frequency (RPM)	30,000 to 54,000	154,000	32,000 to 33,000
Bearing Support Deformation	0.028 in	--	--

A range of values is indicated to correspond to the range of temperatures anticipated. The natural frequencies of the thrust bearing support system are well removed from the operating speeds. The calculated values for the radial

bearings are listed below:

	Axial	Radial	Pitch
Bearing Support Spring Rate	1300 to 2800 lb/in	3,000,000 lb/in	9000 to 20,000 lb-in/rad
Natural Frequency (RPM)	3000 to 4300	145,000	8300 to 9700
Bearing Support Deformation	0.047 in	--	--

The operating speed of the turboalternator is 24 percent higher than the highest predicted natural frequency in roll. Therefore, the rotor will be required to pass through this resonance as it accelerates to design speed. The flutter natural frequencies of the thrust- and radial-bearing support diaphragms were computed and are over ten times the operating speed of the turboalternator.

Three bearing cooling methods have been examined: gas cooling, liquid cooling in the bearing, and the cooling rings employed in the primary design.

The first cooling system consisted of supplying coolant gas at 100°F to the hydrostatic portion of the hybrid bearings. This system did not lower temperature levels in the turboalternator rotor, shown in Figures 145 and 146, enough. They were about 480°F in the No. 1 bearing, and about 540°F in the copper amortisseur bars in the pole tips of the alternator.

The second configuration incorporated 200°F liquid cooling in the radial bearings. The resultant temperature map and temperature distribution for the No. 1 bearing area are shown in Figures 147 and 148. As can be seen in these figures, there is 23°F of crowning and 48°F of coning for this geometry, due to excessive heat conducted from the turbine. Therefore, the copper heat shunt inside the shaft between the bearing and the turbine was removed and the results are presented in Figures 149 and 150. The crowning was reduced to 19°F and the coning to 11°F. By adding a static cooling ring between the turbine and the No. 1 bearing, similar to the cooling ring employed in the tilting pad configuration, the crowning was reduced to 11°F and the coning to 4°F as shown in Figure 151. Thermal studies of the No. 2 bearing with liquid coolant in the stationary portion of the thrust bearing indicated an influence of the thrust bearing coolant temperature on the No. 2 radial bearing temperature map. Figures 152 and 153 present the temperature map and the temperature gradients with the thrust

bearing stator liquid-cooled with 200°F coolant. The resultant crowning in the radial bearing is about 5°F and the coning is 19°F. The coning is due to the low thrust-runner temperature. By increasing the thrust-bearing stator-coolant temperature from 200°F to 240°F, the crowning temperature was increased slightly to 7°F and the coning reduced to 13°F, as shown in Figure 154. These investigations demonstrate that liquid cooling directly in the radial bearings provides acceptable bearing temperatures and temperature gradients.

Further studies were conducted using the cooling rings employed in the tilting pad bearing configuration. The resulting temperature maps and bearing temperature gradients are shown in Figure 155 and 156 for the No. 1 bearing and in Figures 157 and 158 for the No. 2 bearing. The resulting temperature distributions are nearly isothermal; therefore the cooling-ring system employed with the tilting-pad bearings was selected as the cooling system for the hybrid bearings.

Twelve thermocouples and six capacitance probes are incorporated in each of the hybrid radial bearings. Nine thermocouples on each bearing sleeve located at three axial planes and at three circumferential locations will measure bearing temperature and temperature gradients. Three thermocouples mounted on the outer rim of each support diaphragm will measure the radial gradient across the diaphragm. The proximity probes will be mounted on each bearing sleeve and located 90° apart circumferentially to measure the journal position in relation to the bearing. Two capacitance probes mounted on the outer support at each end of the sleeve 90° apart circumferentially will determine the bearing sleeve motion relative to the outer case. The thrust bearing instrumentation will be similar to the corresponding instrumentation in the primary design. One proximity probe in the forward thrust stator and three probes in the rearward thrust stator will measure the thrust-bearing-gas-film thickness. These probes will also be used to determine parallelism and axial gaps during the bearing assembly. One proximity probe will be mounted on the fixed structure and will measure the axial motion of the flexible-support-thrust-bearing stator.

TABLE 21

TURBOALTERNATOR BACK-UP GAS BEARING DESIGN PARAMETERS

Journal Bearings

Configuration	360° sleeve, hybrid
Journal diameter, inches	3.4962
Bearing diameter, inches	3.5000
Bearing length-to-diameter ratio (L/D)	1.0
Bearing number (Λ)	4.0
Number of orifices per journal	6
Orifice diameter, inches	0.021
Number of recesses per journal	6
Axial length of recess, inches	0.625
Width of recess, inches	0.125
Depth of recess, inches	0.005
Gas supply pressure, psia	12.0
Gas flow, pounds per second	0.0071
Bearing support stiffness	
axial, pounds per inch	1,300-2,800
radial, pounds per inch	3,000,000
roll, inch-pounds per radiam	9,000-20,000
Bearing load, pounds	
horizontal orientation (rotor weight)	
No. 1 bearing	28.12
No. 2 bearing	26.46
Minimum operating clearance, inches	
horizontal orientation	
No. 1 bearing	0.00124
No. 2 bearing	0.00132

TABLE 21 (Cont'd)

Friction loss per journal, watts	
horizontal orientation	
No. 1 bearing	47.6
No. 2 bearing	45.5
space operation	
No. 1 bearing	42.5
No. 2 bearing	42.5
Radial film stiffness, pounds per inch	
horizontal orientation	
No. 1 bearing	41,000
No. 2 bearing	41,000
Gas film temperature, °F	
No. 1 bearing	300
No. 2 bearing	300
Shaft temperature, °F	
No. 1 bearing	268
No. 2 bearing	275
Bearing temperature, °F	
No. 1 bearing	272
No. 2 bearing	278
Shaft material	AMS 6294 low alloy steel
Bearing material	AMS 5643 type 17-4PH stainless steel
Journal and bearing surfacing material	Chrome oxide

TABLE 21 (Cont'd)

Main Thrust Bearing

Configuration	Dead-ended, inward-pumping spiral-grooved hybrid
Thrust plate diameter, inches	7.000
Spiral groove bearing O.D., inches	6.000
Spiral groove bearing I.D., inches	2.400
Groove depth, inches	0.0057
Number of grooves	15
Orifice diameter, inches	0.031
Number of orifices	36
Design load (aerodynamic), pounds	79
Operating clearance, inches	0.0037
Gas supply pressure, psia	12.0
Gas flow, pounds per second	0.004
Gas supply pressure at startup, psia	16.0
Bearing load at startup, pounds	250
Film clearance at startup, inches	0.0013
Stator support stiffness	
axial, pounds per inch	5,000 - 17,000
radial, pounds per inch	1,500,000
pitch, inch pounds per radian	6,000 - 20,000
Stator temperature at design load, °F	229
Runner temperature at design load, °F	230
Runner material	AMS 6415 low alloy steel
Stator material	AMS 4025 aluminum
Stator and runner surfacing material	Chrome oxide
Friction loss, watts	75

TABLE 21 (Cont'd)

Reverse Thrust Bearing

Configuration	Hydrostatic
Orifice diameter, inches	0.031
Number of orifices	36
Supply gas pressure, psia	16.0
Design load, pounds	100
Clearance at startup, inches	0.0086
Stator material	AMS 5646 type 347 Stainless Steel
Stator and runner surfacing material	Chrome oxide

APPENDIX II

Shaft Fabrication Investigation

Heat shunts are required inside the shaft journals to reduce axial temperature gradients and subsequent coning and crowning distortion in the journal bearings. Plating of the copper was selected over brazing because of the difficulty in assuring adequate braze coverage and to minimize thermal distortion of the shaft. Existing plating experience indicated that copper coatings up to 0.070 inch thick could be attained with adequate bond integrity and thermal cycle integrity. Therefore, Pratt & Whitney Aircraft conducted an investigation of the bond strength of thick (0.125 inch) copper plating inside a steel cylinder.

Before design selection, a test program was conducted to determine the bond integrity of a copper plate 0.125 inch thick on the inside of a sample of the turboalternator shaft. A shaft eight inches long was plated on the inside surface with copper which was machined to a thickness of 0.125 inches. The plating bond was excellent, as determined by sonic inspection. The test piece was subjected to 50 thermal cycles from room temperature to 400°F at a rate of change equivalent to a rapid startup.

Sonic inspection, X-ray inspection, and photomicrographs indicated that no separation between the copper plating and the shaft occurred during thermal cycling. Figure 159 shows the test specimen and Figure 160 shows a photomicrograph of the joint between the copper and the iron after thermal cycling.

The effect of anticipated thermal environment on dimensional stability was also evaluated. The material (AMS 6294) used to fabricate the shaft has properties similar to some rolling contact bearing materials (M-50) which have exhibited dimensional instability when more than 1 percent of austenite is retained in the crystalline structure of the material. The probability of dimensional changes increases with the amount of retained austenite and with the residual stresses entrapped in the material. A section of the shaft specimen was subjected to comprehensive dimensional analysis and X-ray diffraction measurement of the retained austenite level and residual surface stresses. Four six-hour thermal cycles were conducted; two cycles were made to 350°F, one to 500°F, and the last to 600°F. No visible deterioration of the copper-plate bond was evident.

The retained austenite was one percent in both the sample and in the actual turboalternator shafts. This level did not change throughout the test sequence. No significant dimensional or residual stress level change was observed until the 600°F temperature cycle was conducted. An increase of approximately 0.0002

inches occurred in out-of-roundness and the residual stress dropped by approximately 50 percent. The turboalternator shaft should not encounter temperatures higher than 500°F and thus should remain dimensionally stable.

APPENDIX III

Journal Bearing Mount Thermal and Deflection Tests

Proper journal bearing temperatures in the turboalternator are maintained by the flow of liquid coolant in heat exchangers. The two journal bearing support assemblies are similar in construction, consisting of a bearing support ring supported by a thin-walled cylinder from the main outer locating flange. A cylindrical heat exchanger is similarly supported from each side of the bearing support ring (Figure 161).

Each heat exchanger is a brazed double wall cylinder surrounding the shaft with a radial gap of 0.005". Fins between the two cylinders direct the flow of liquid coolant axially through ten segments. An orifice hole at the discharge end of each segment meters the uniform flow required to maintain proper journal bearing temperature level and distribution (Figure 162).

Coolant is fed independently to the two heat exchangers through tubes which lead from fittings on the outer flange. The bearing support ring also has coolant provisions. Thin cylindrical supports join the heat exchangers to the bearing support ring and also join the bearing support ring to the outer flange. These cylindrical supports uncouple the thermal growth of the heat exchangers from the bearing support ring and from the outer flange. The heat exchangers and bearing support ring are of type 347 stainless steel, and their rigid construction minimizes distortions due to restraint from the thin support cylinders so that each can accommodate a different temperature. The bearing support rings were designed to operate at temperature differentials up to 150°F from the remainder of the support structure, so that bearing clearance may be adjusted by thermal manipulation of the bearing support ring.

Pratt & Whitney Aircraft conducted tests on the turboalternator journal bearing mounts to determine if there were any blockage of coolant flow and if temperature differentials resulted in excessive distortion of the heat exchangers or the bearing support ring.

Braze material during fabrication could cause blockage of the heat-exchanger segments; therefore, the heat exchangers were tested. A thermocouple was placed at the axial center of each flow segment inside the heat exchanger bore (Figure 163). The heat exchanger was then submerged in an ice bath (Figure 164) to exaggerate any temperature differences, and hot and cold water were alternately flowed through the exchanger. The test setup is shown in Figure 165. Thermocouple transients were recorded on a strip chart recorder, and Figure 166 shows the temperature transient for a heat exchanger with no blockage. Another heat exchanger produced a transient with four of the

thermocouples responding very slowly and blockage was suspected. Overall pressure-drop data taken for this bearing support (Figure 167) indicated blockage in the rear heat exchanger. The pressure drop includes both the heat exchanger and the test equipment and is thus valid only for comparison with similar data, as in Figures 168, 169 and 170, where the thermal response of the heat exchangers indicated no blockage. The No. 1 bearing mount with the defective heat exchanger was repaired, and retest showed no remaining flow blockage (Figure 167). When the temperature transient was measured with the heat exchanger out of the ice bath, in air, which is similar to the environment in the turboalternator, the temperature maldistribution was much less. This is attributed to circumferential heat conduction which was designed into the heat exchangers to compensate for possible small flow maldistribution.

To determine the effect of temperature differential on the bearing support assembly distortion, a front journal bearing mount was set up for test (Figure 171) with thermocouples and dial-indicators at each end of the front heat exchanger, at the bearing support-ring, and at the outer flange. Hot water was supplied to the heat exchanger and cold water was supplied to the support-ring. A temperature differential of approximately 60°F produced coning of 0.0001" over the 3" length of the heat exchanger. The radial clearance between the heat exchanger and the shaft is 0.005", and thermal deflections up to 0.0003" are acceptable.

APPENDIX IV

Preparation for Shipment

Three methods of packaging the turboalternators for shipment were investigated:

- Ship the units completely assembled.
- Disassemble the unit completely after the acceptance test and support the rotor and bearings in separate containers.
- Install shipping fixtures to minimize disassembly of the bearings and turboalternators.

Shipping the units completely assembled involved risk of damage to the bearings under the anticipated shock and vibration loads. Disassembly of the units would delay the test program at Lewis Research Center. Consequently, a relatively simple fixture system was devised, which provides a rigid support for the rotor assembly independent of the gas bearings. Installation and removal of the special shipping fixtures does not require adjustment of the gas bearings or disassembly of critical elements of the turboalternator.

The rotor was centered by a fixture at the turbine inlet (Figure 172) and by radial bolts at the thrust runner rim (Figure 173). The ground-to-shaft capacitance probes were used to monitor rotor position. The rotor was lowered gently against the bottom journal pads and the upper journal pads were gently pushed against their journals by spring-loaded fixtures (Figure 174). Radial shock loads are thus transmitted through the fixtures rather than through the journal bearing flexures and the pads are restrained from rattling against the shaft. To prevent thrust-bearing damage. the rotor was positioned midway between the two bearing faces by the front fixture (Figure 175), and by a rod from the rear cover to the center of the thrust runner (Figures 176 and 177).

Each turboalternator was bolted to a special shock mounted base, enclosed in a plastic bag containing dessicant, and covered with the shipping container as shown in Figure 178.

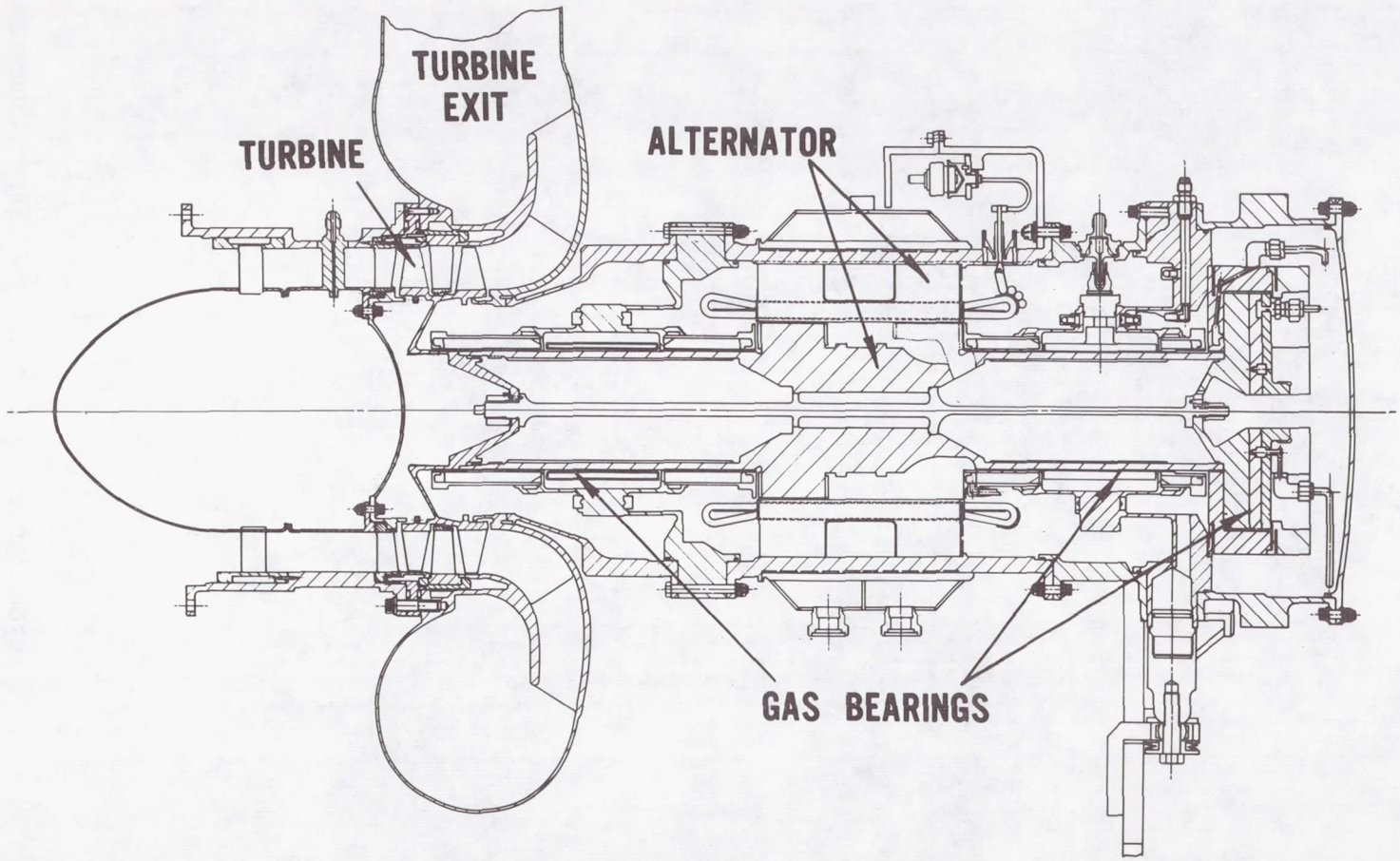

Figure 2 Turboalternator

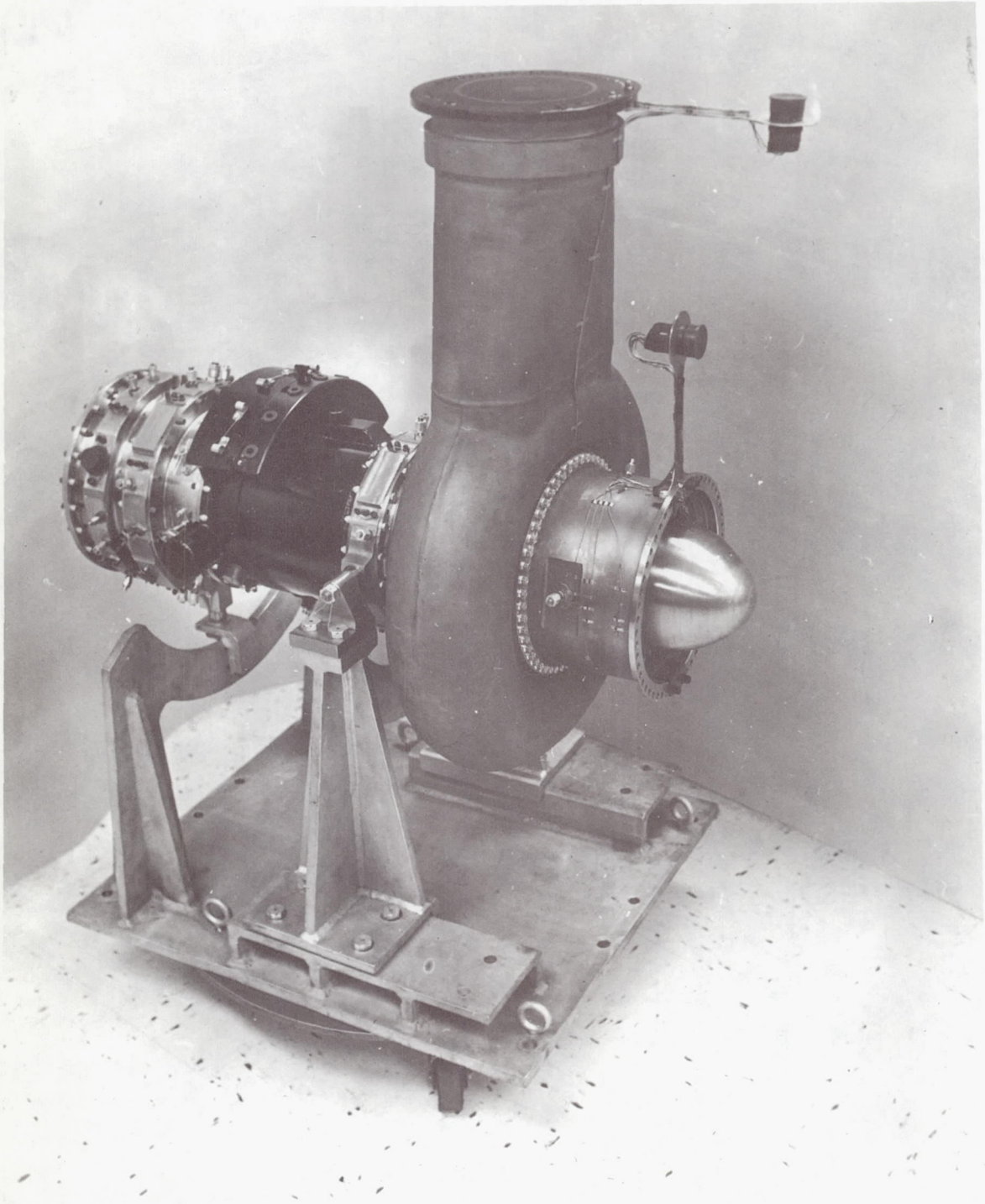

Figure 3 Turboalternator Package, Front Three-Quarter View (CN-9989)

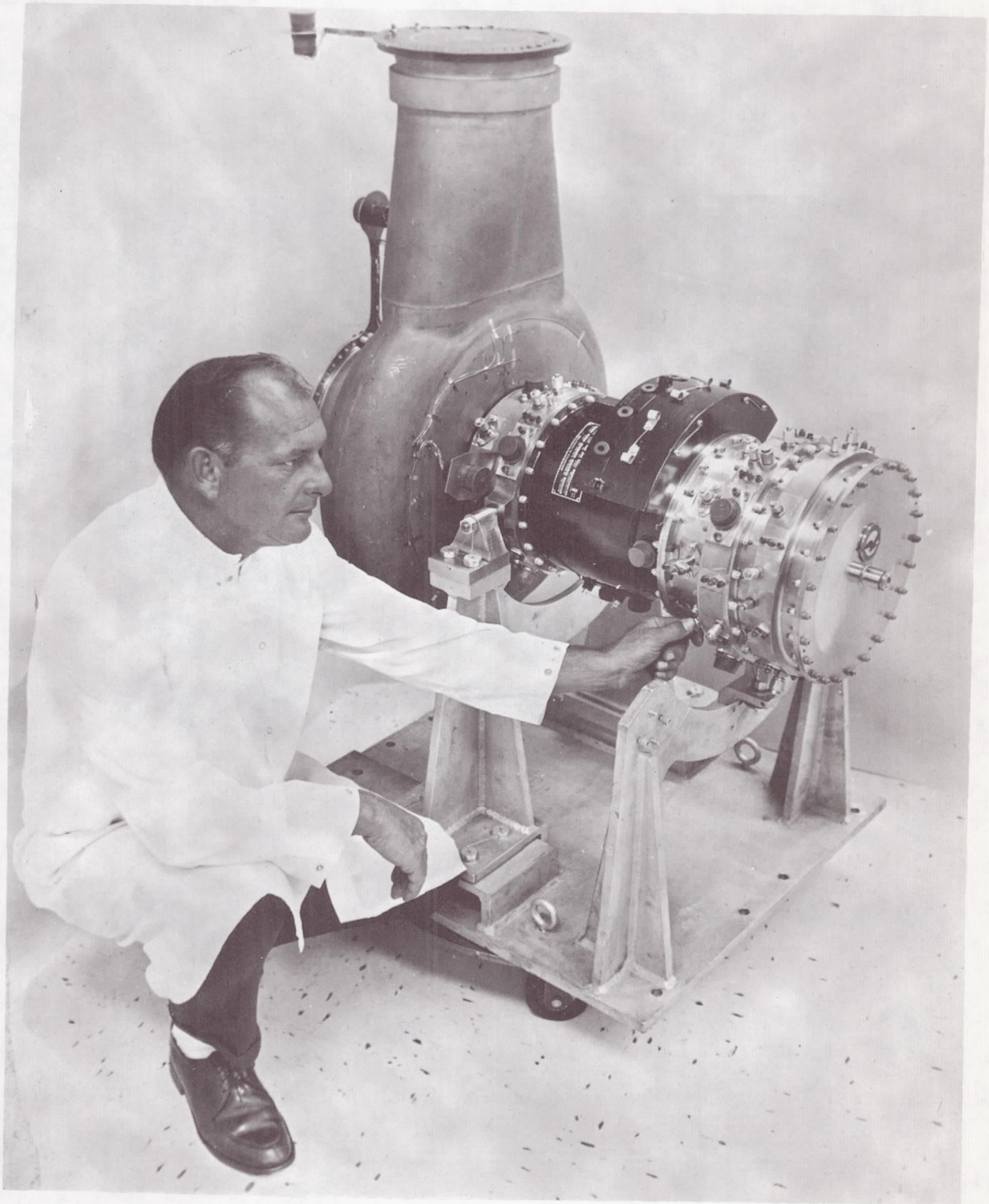

Figure 4 Turboalternator Package, Rear Three-Quarter View (CN-9995)

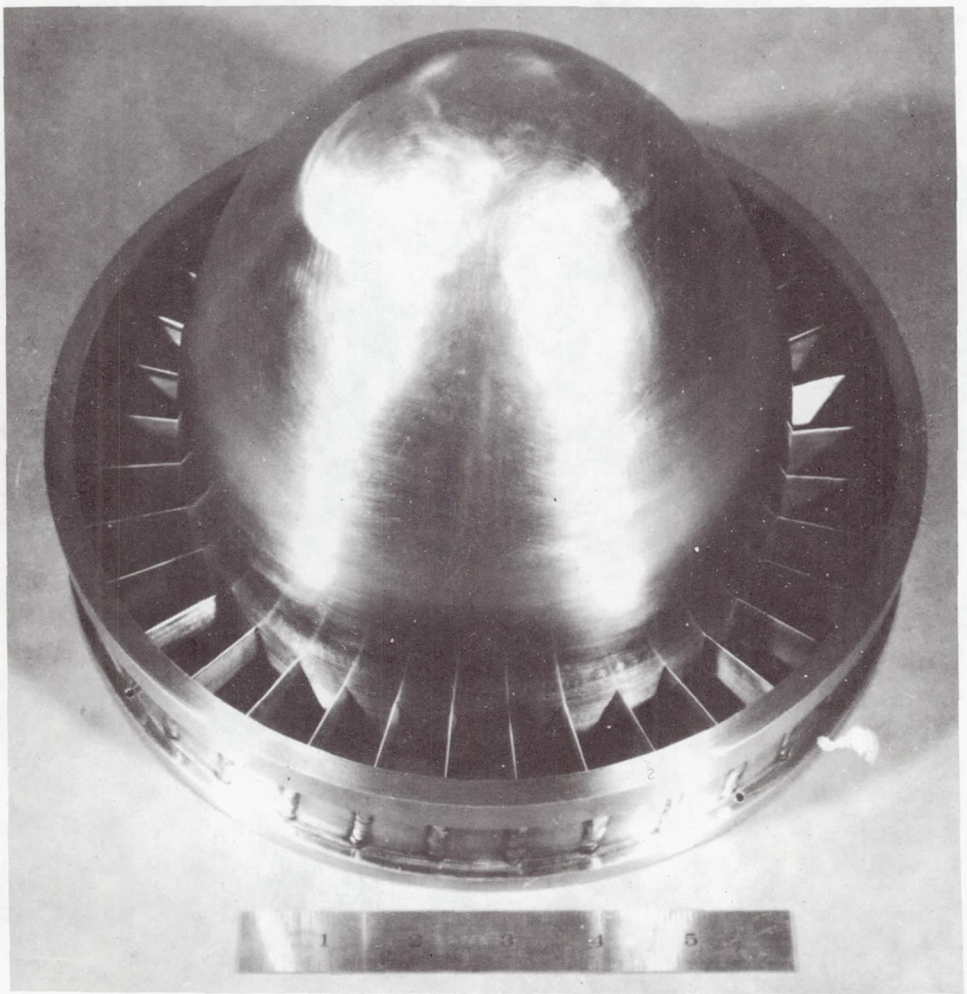

Figure 5 Inlet Nose Cone and Pre-Rotation Vane Assembly (M-44247)

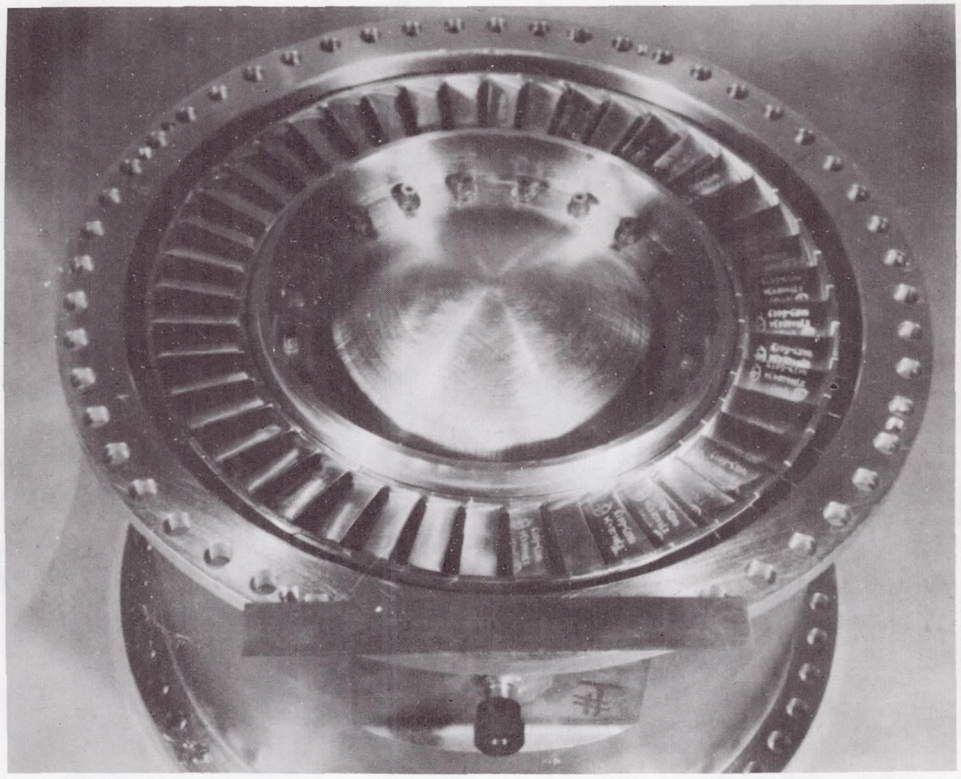

Figure 6 First-Stage Nozzle Vanes Assembled in Turbine Inlet Case (M-44255)

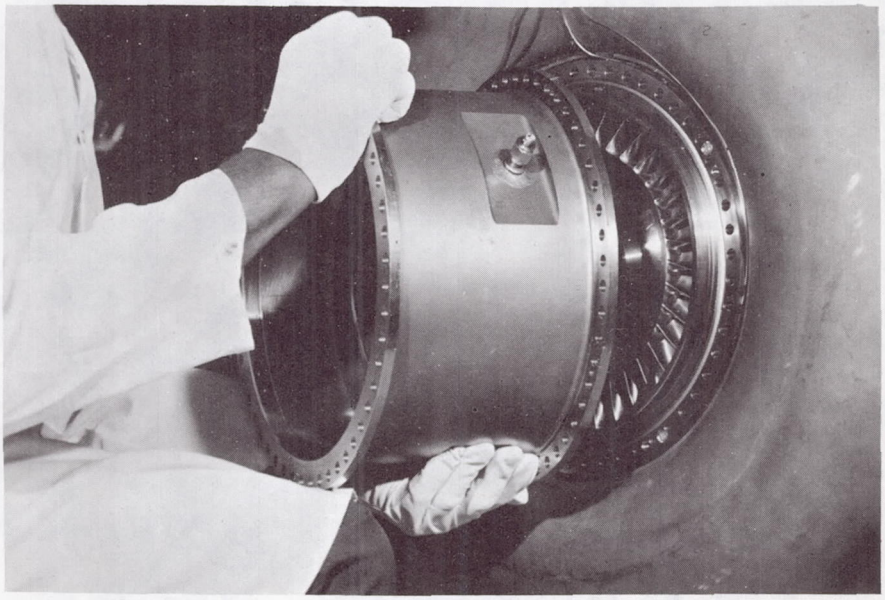

Figure 7 Inlet Duct Assembly Installation (CN-9543)

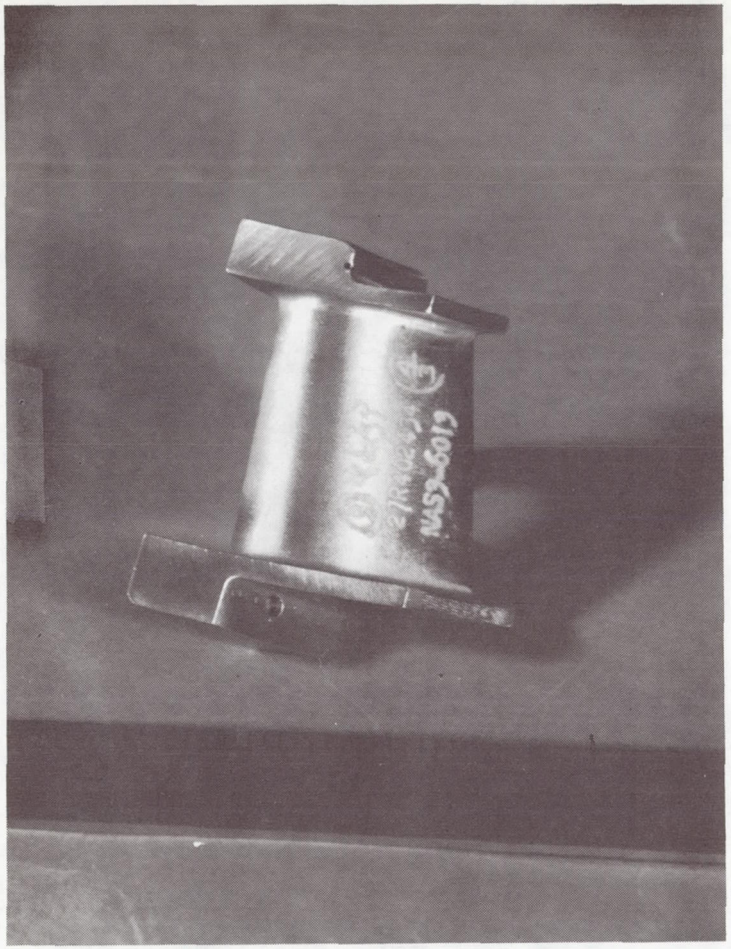

Suction Side

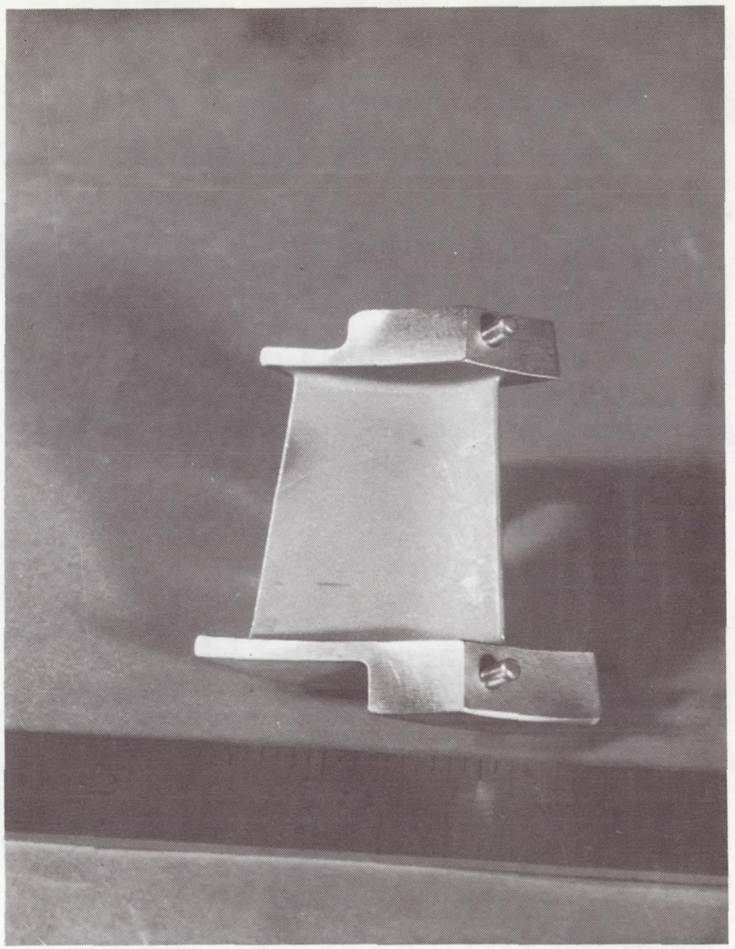

Pressure Side

Figure 8 First-Stage Turbine Nozzle Vane (M-44252)

Front View

Rear View

Figure 9 Front Inner Cover (M-42018)

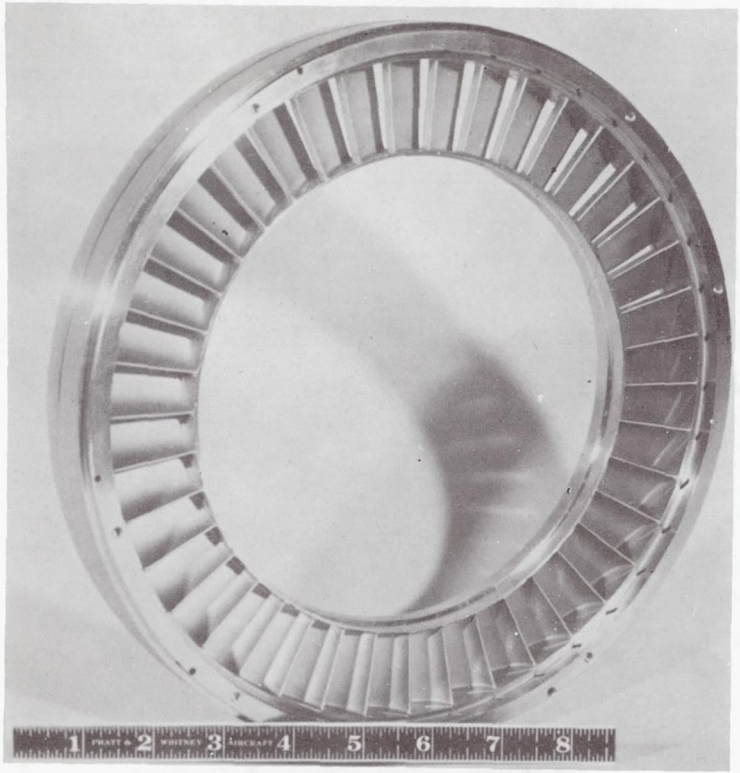

Leading Edge View

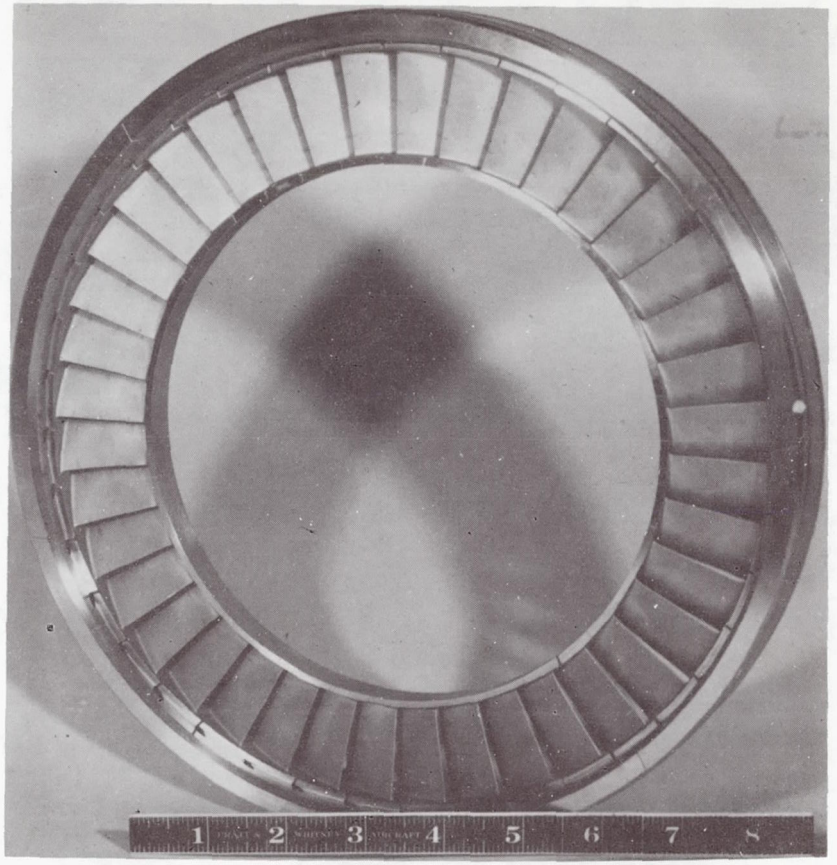

Trailing Edge View

Figure 10 Turbine Second Nozzle Assembly (M-44256)

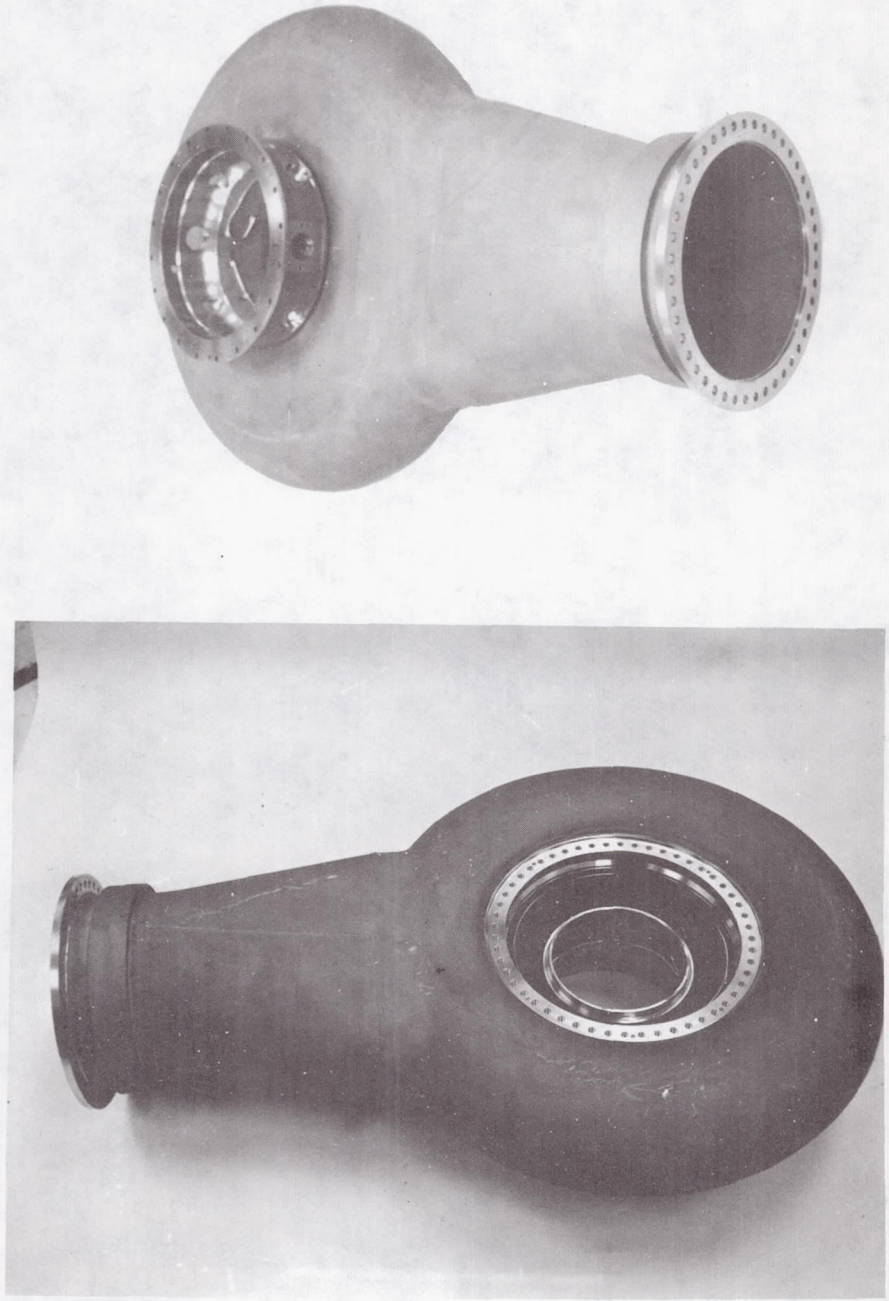

Figure 11 Turbine Scroll (CN-10284 & CN-10285)

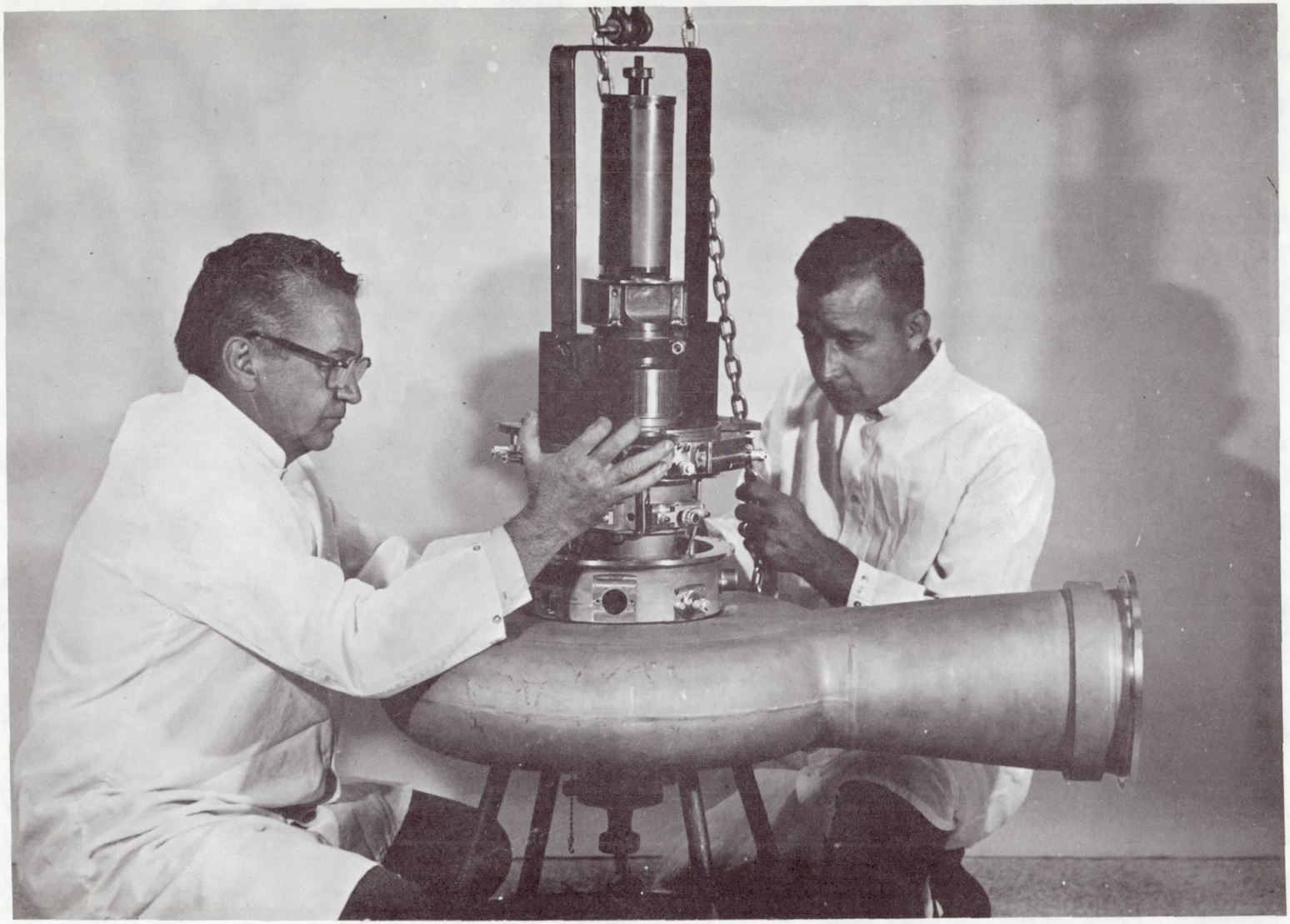

Figure 12 Installing Front Bearing Assembly into Turbine Scroll (CN-9352)

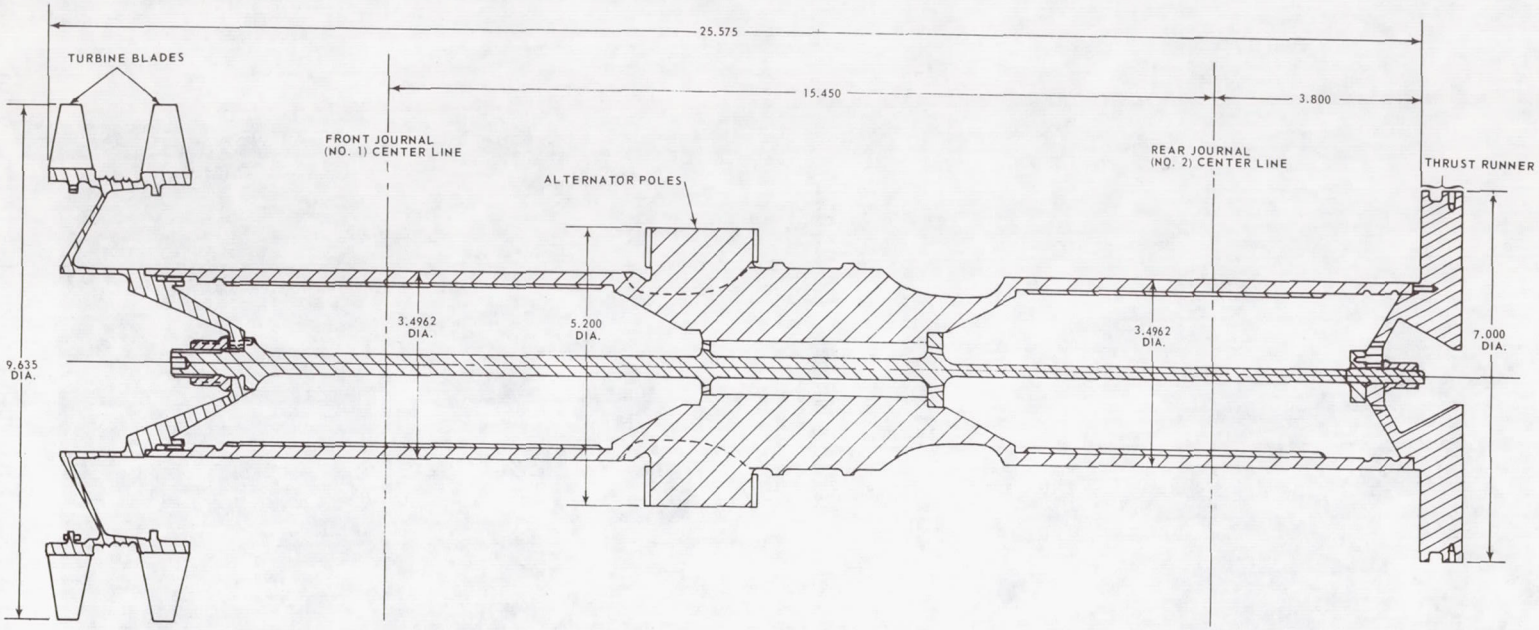

Figure 13 Rotor Assembly Design

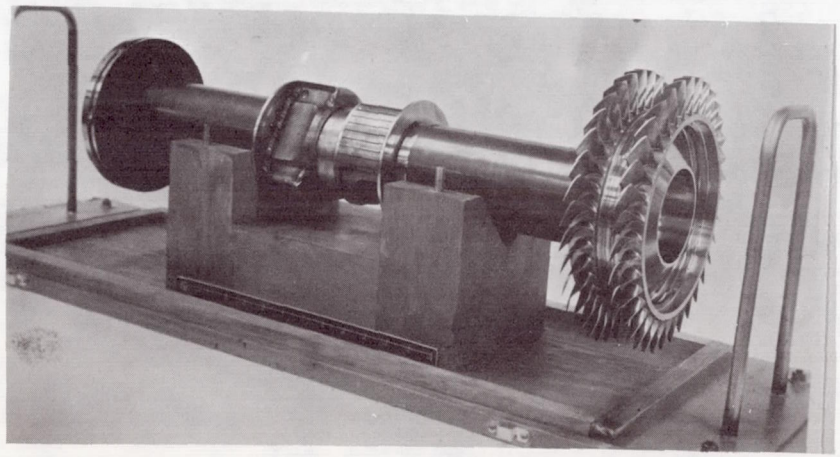

Figure 14 Rotor Assembly Photo
(CN-8940)

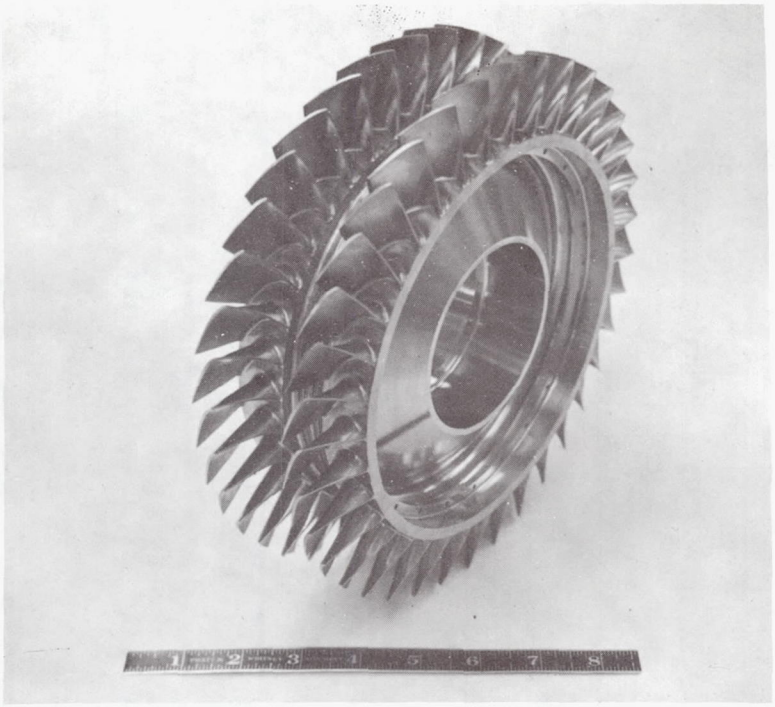

Figure 15 Turbine Wheel, Leading Edge (X-25092)

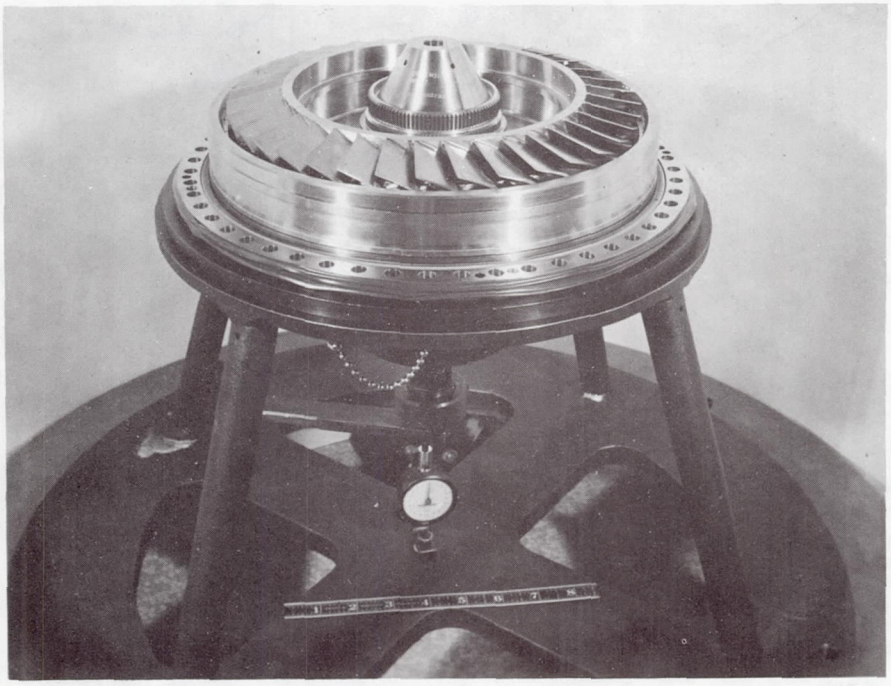

Figure 16 Turbine Wheel at Assembly, Trailing Edge (CN-9289)

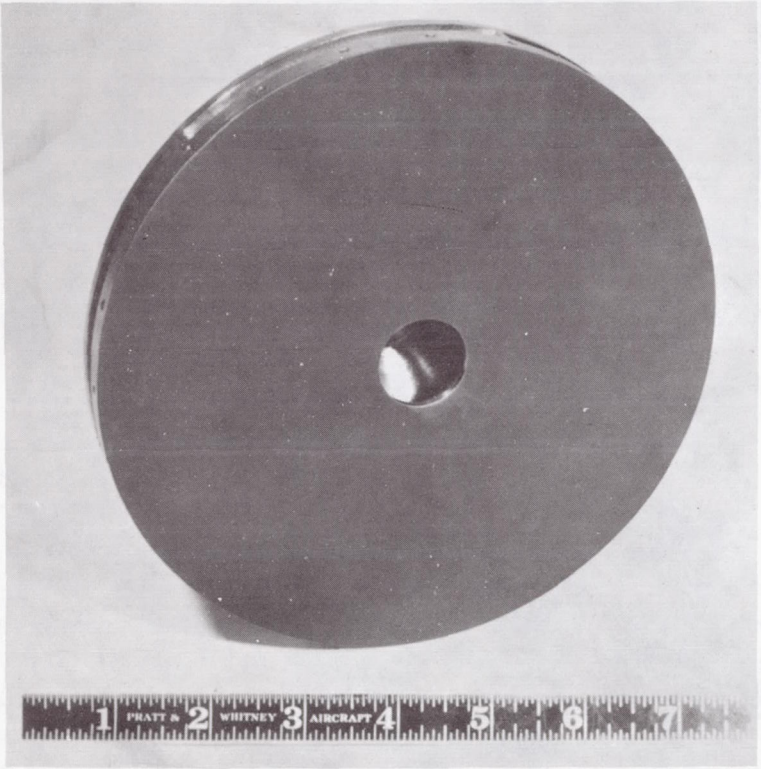

Main Thrust Face

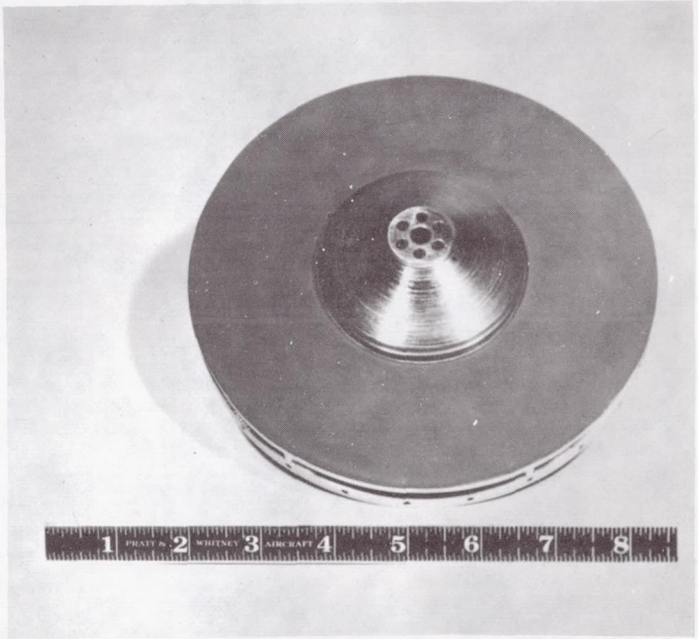

Reverse Thrust Face

Figure 17 Thrust Runner (M-45053)

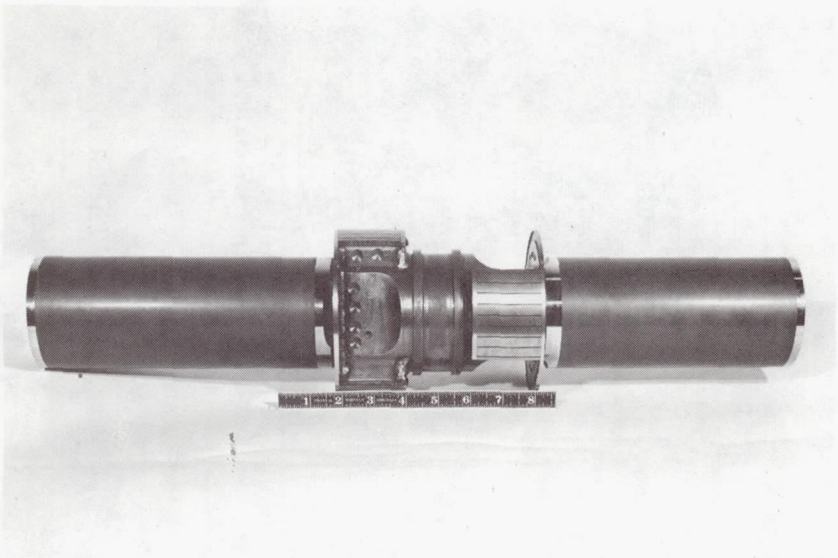

Figure 18 Alternator Shaft (M-44260)

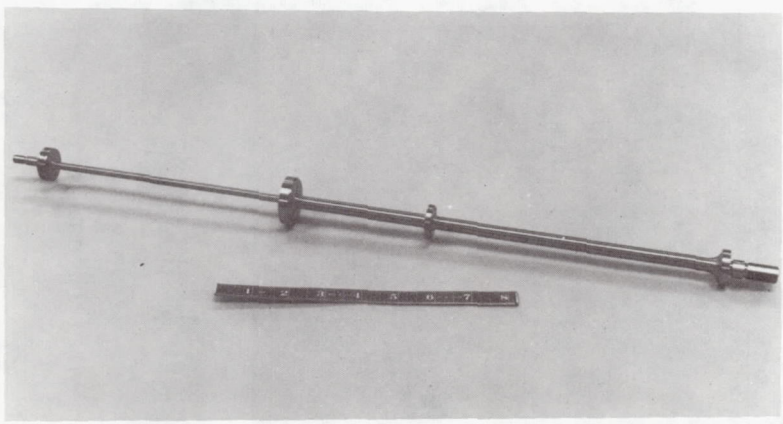

Figure 19 Rotor Tiebolt (M-42015)

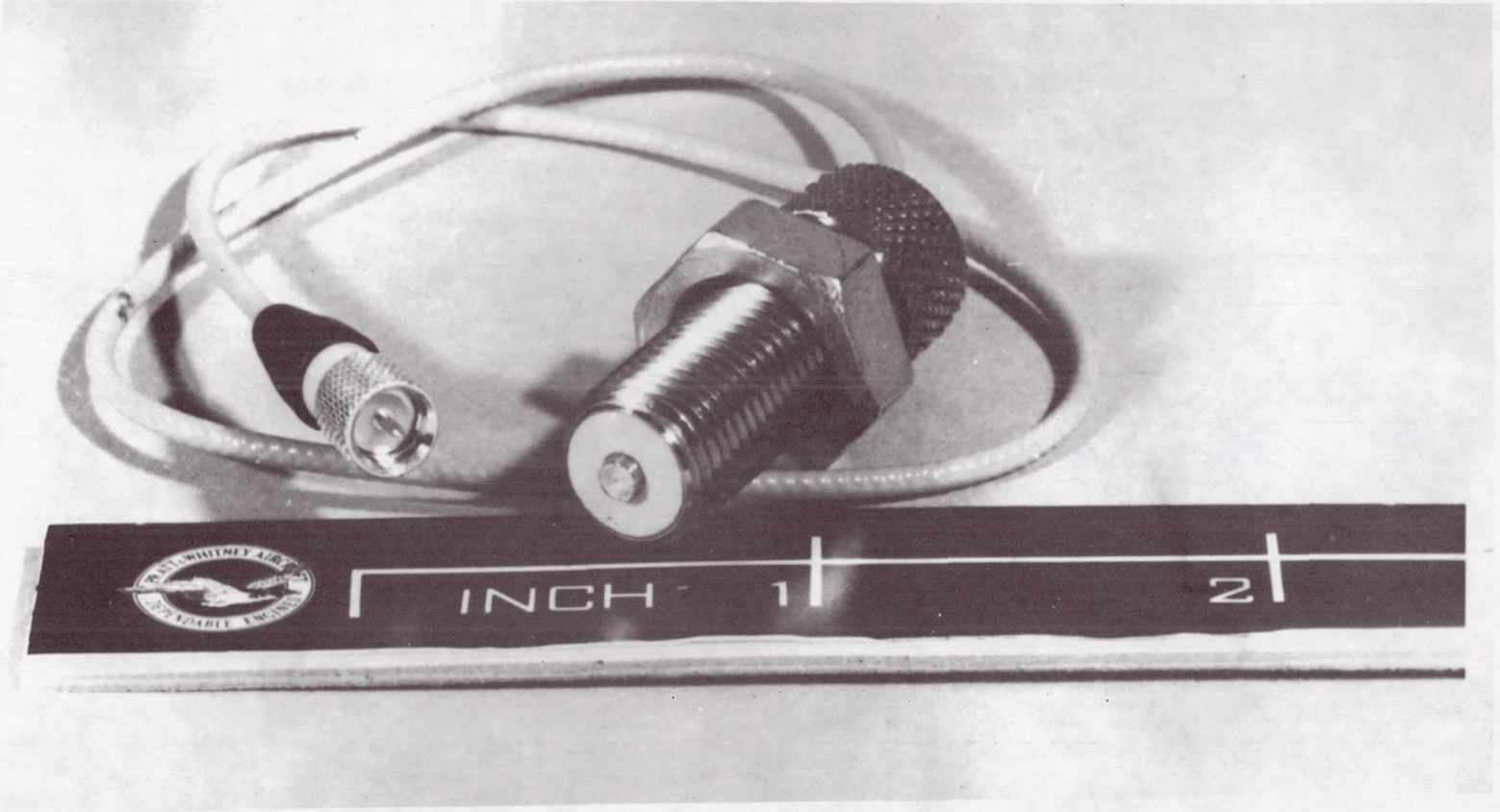

Figure 20 Magnetic Speed Pickup (M-42016)

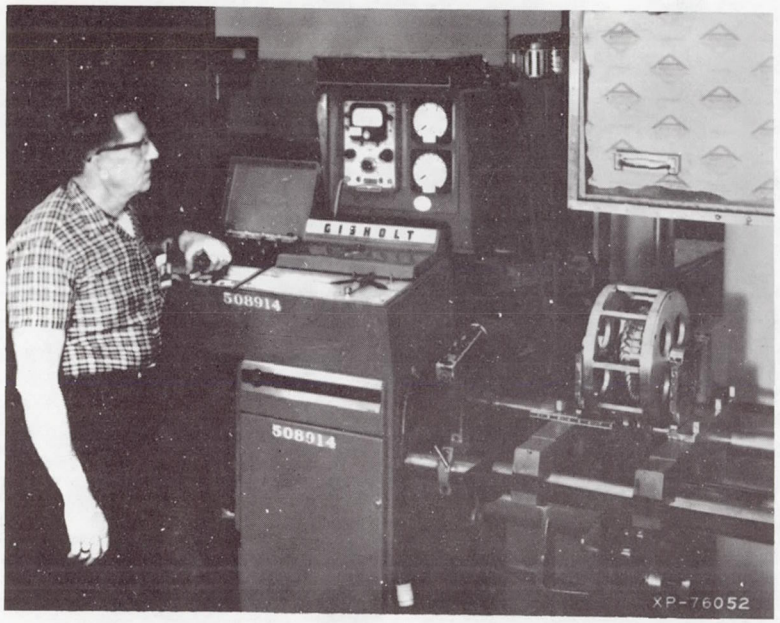

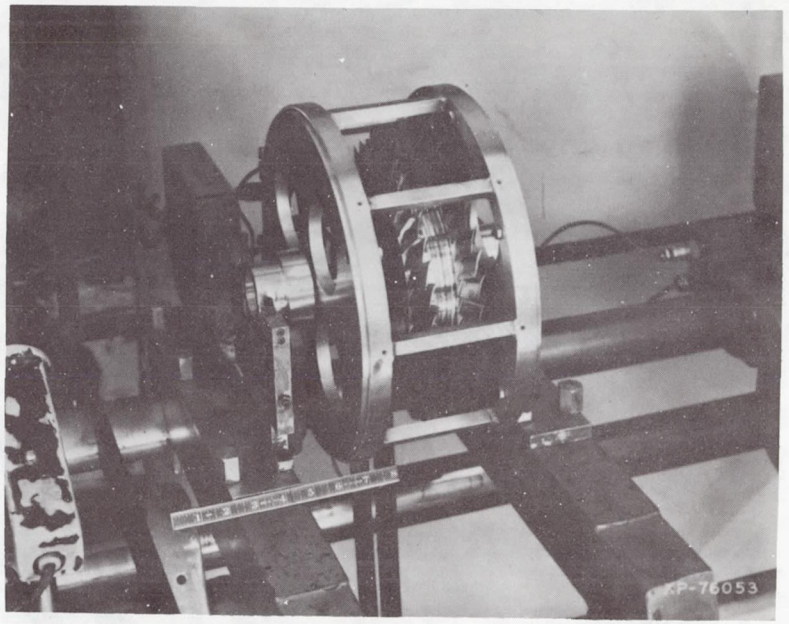

Figure 21 Turbine Wheel Balancing (M-45056)

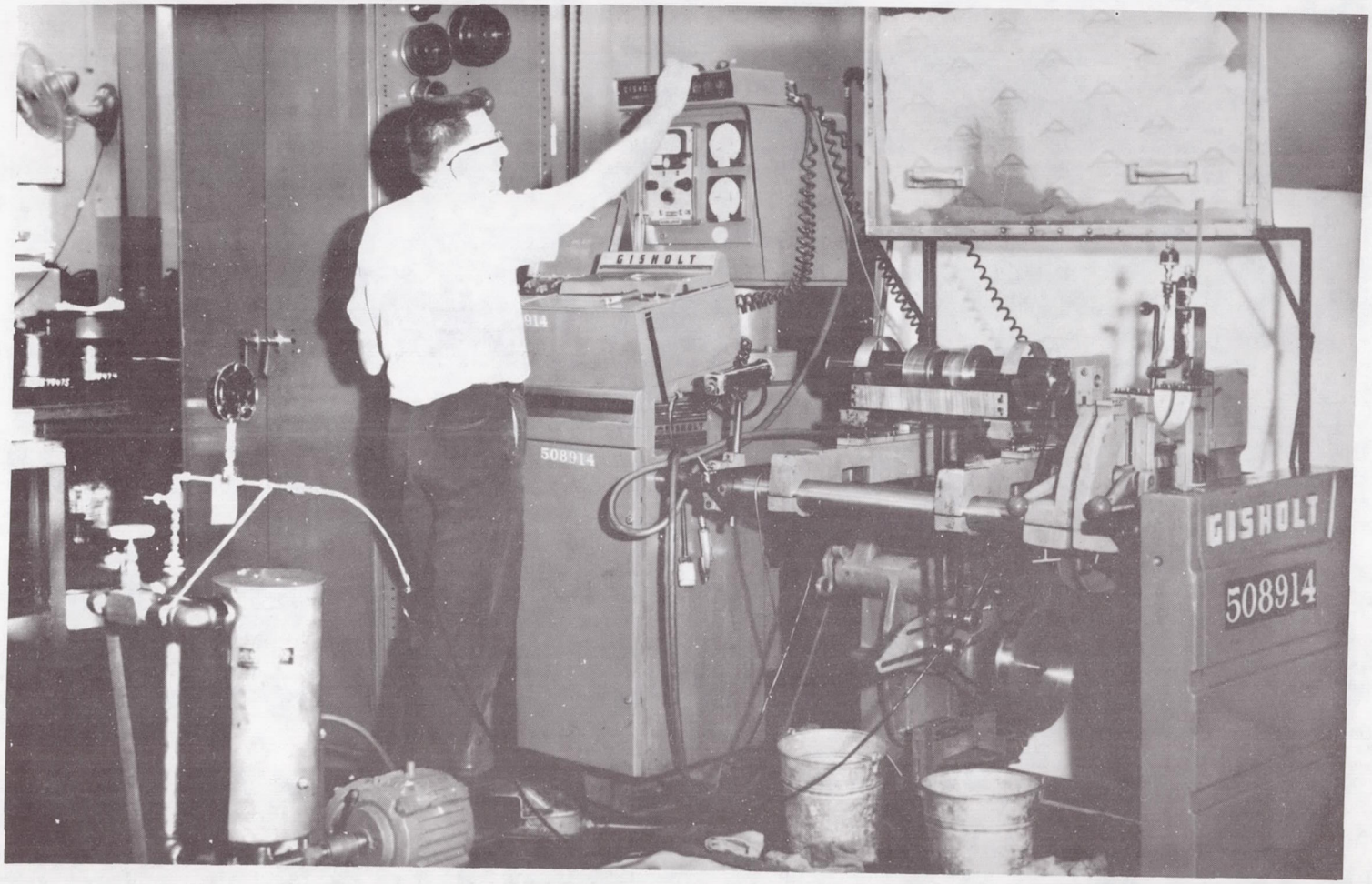

Figure 22 Shaft Being Balanced (XP-77758)

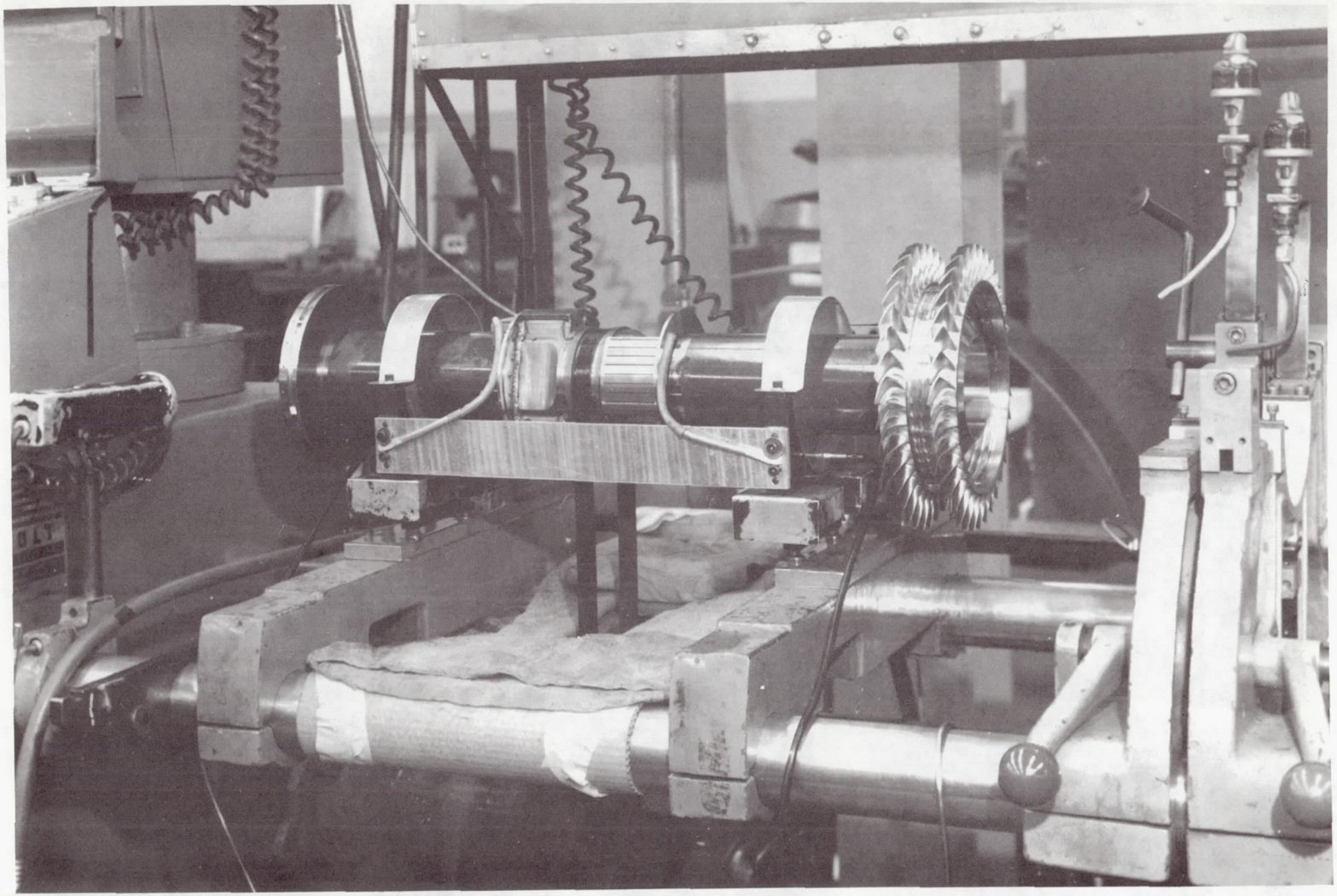

Figure 23 Rotor Assembly at Balance (XP-77758)

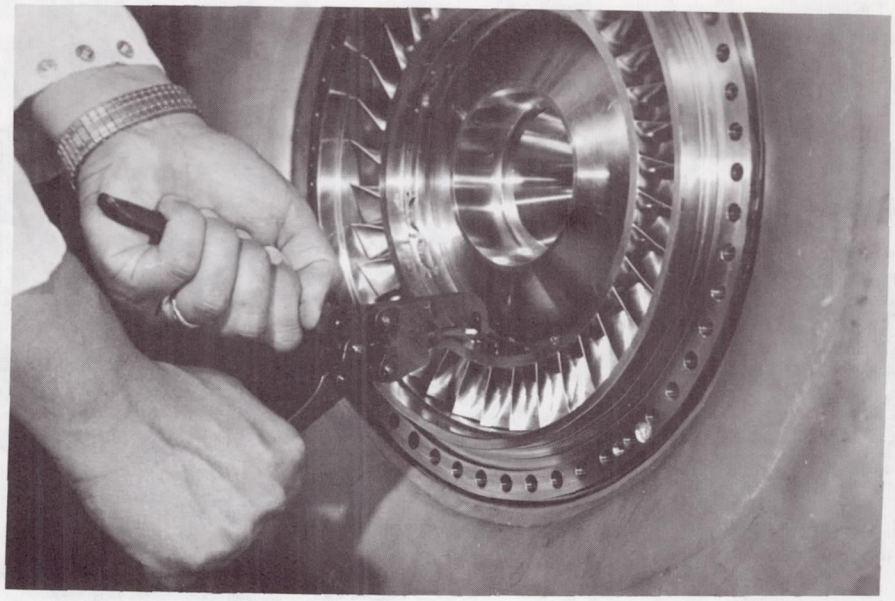

Figure 24 Installing Balance Rivets in Turbine Wheel (CN-9539)

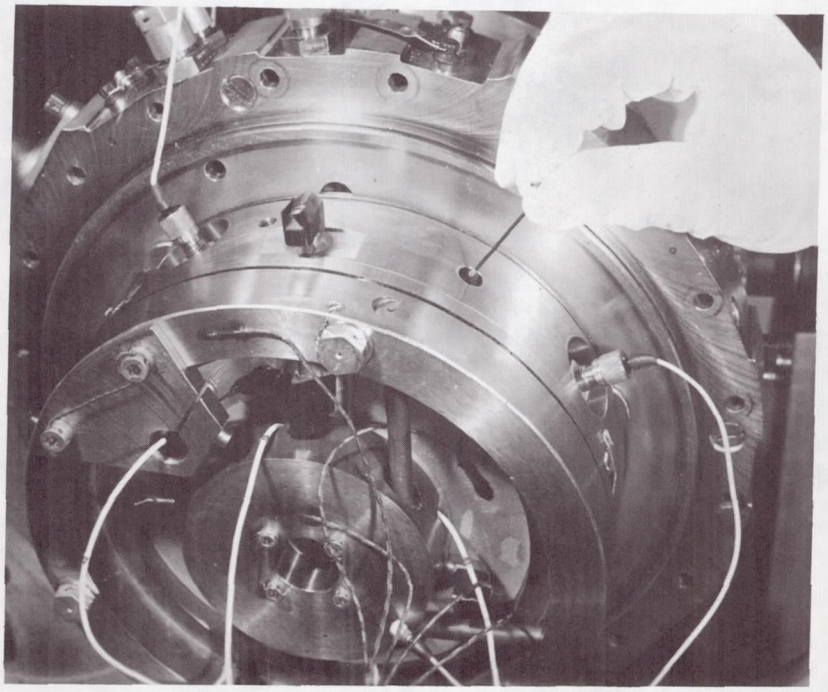

Figure 25 Installing Balance Screws Through Reverse Thrust Stator into Thrust Runner Rim (CN-9572)

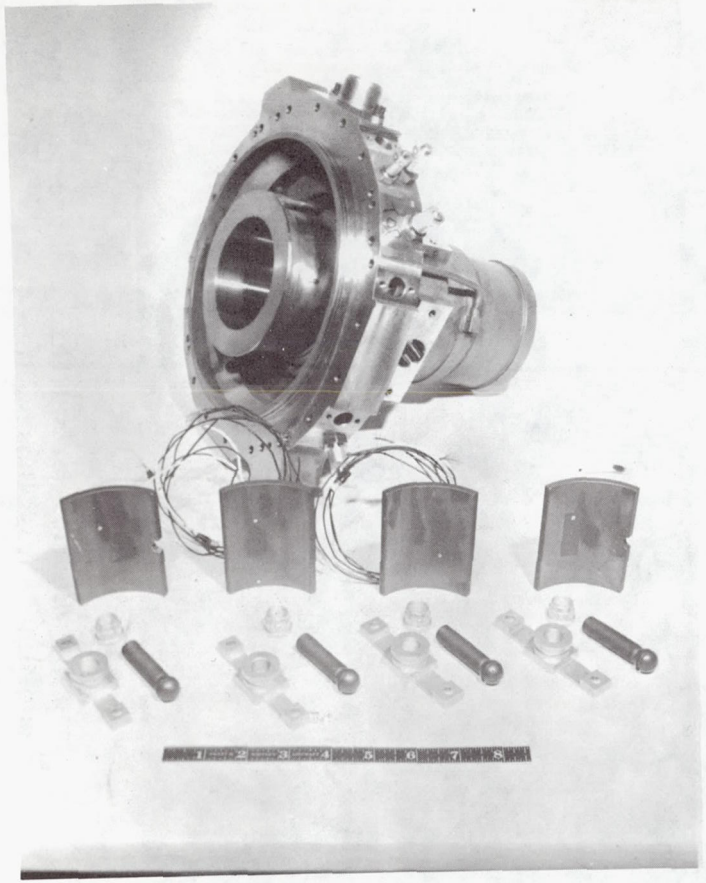

Figure 26 Parts Layout for Front Journal Bearing Assembly (CN-9321)

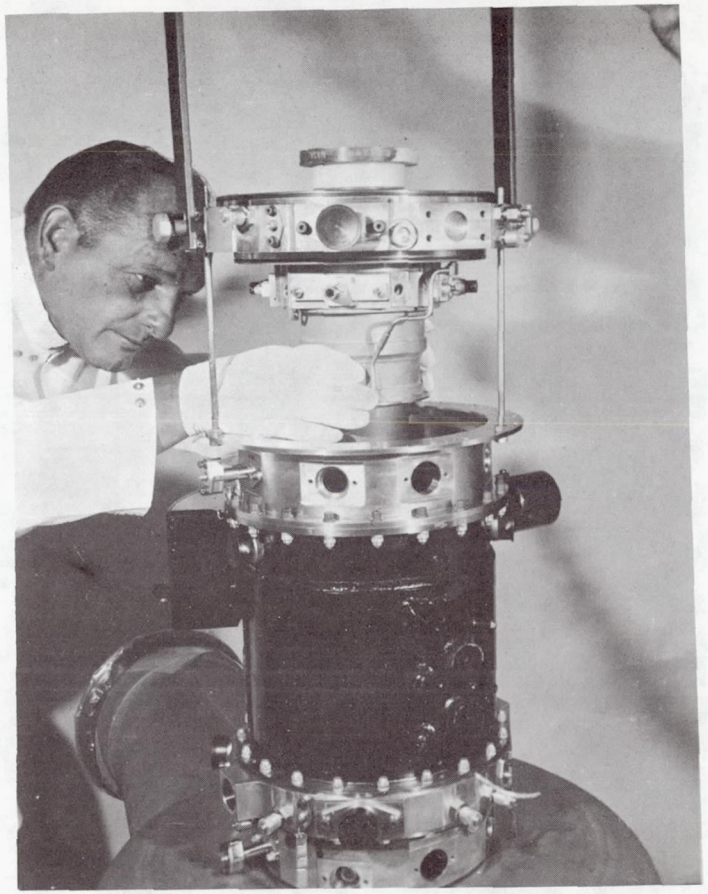

Figure 27 Installing Rear Journal Bearing Assembly (CN-9451)

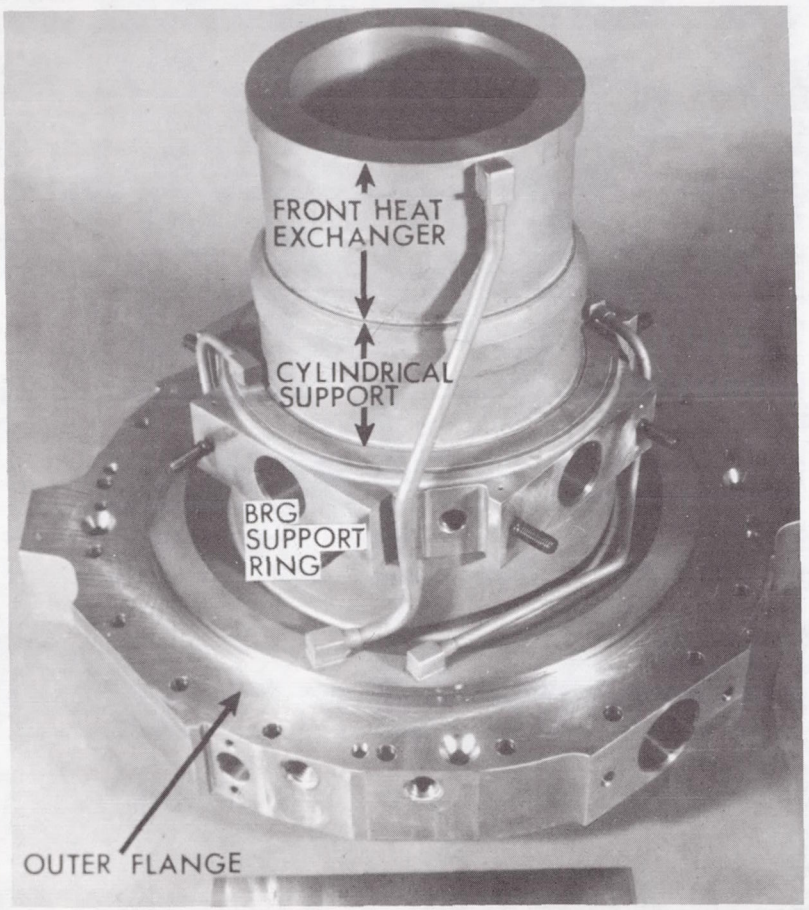

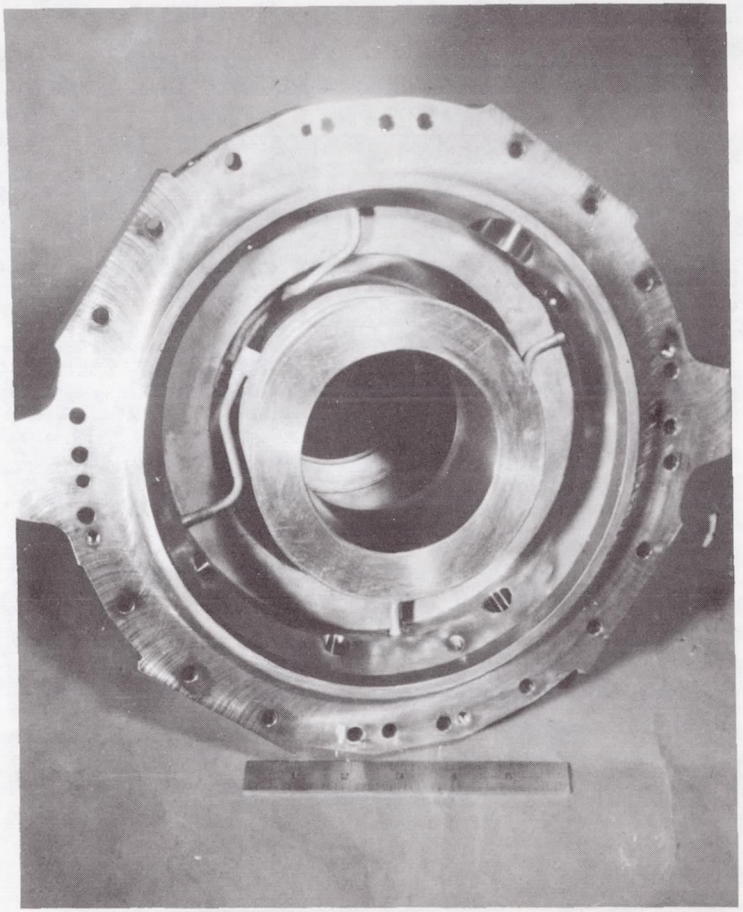

Figure 28 Front Journal Bearing Mount and Heat Exchanger Assembly (M-44253)

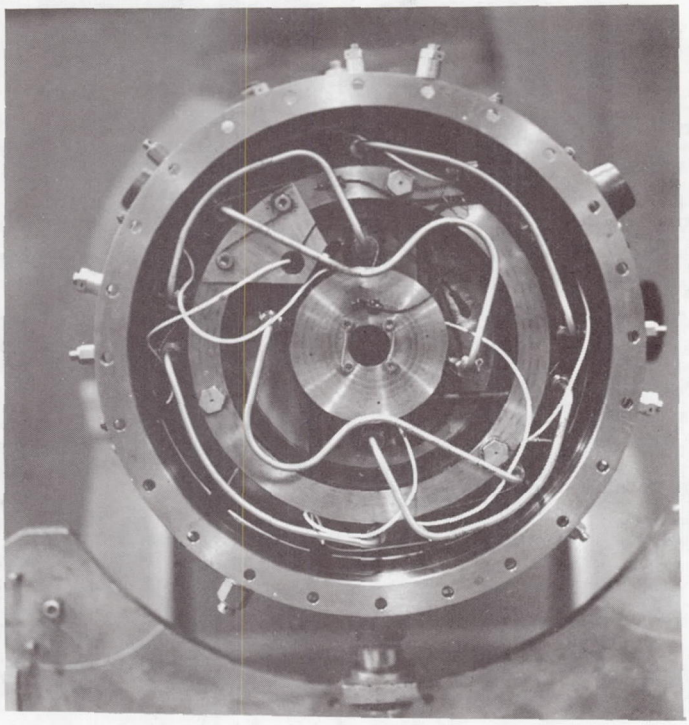

Figure 29 Thrust Bearing Compartment (CN-9990)

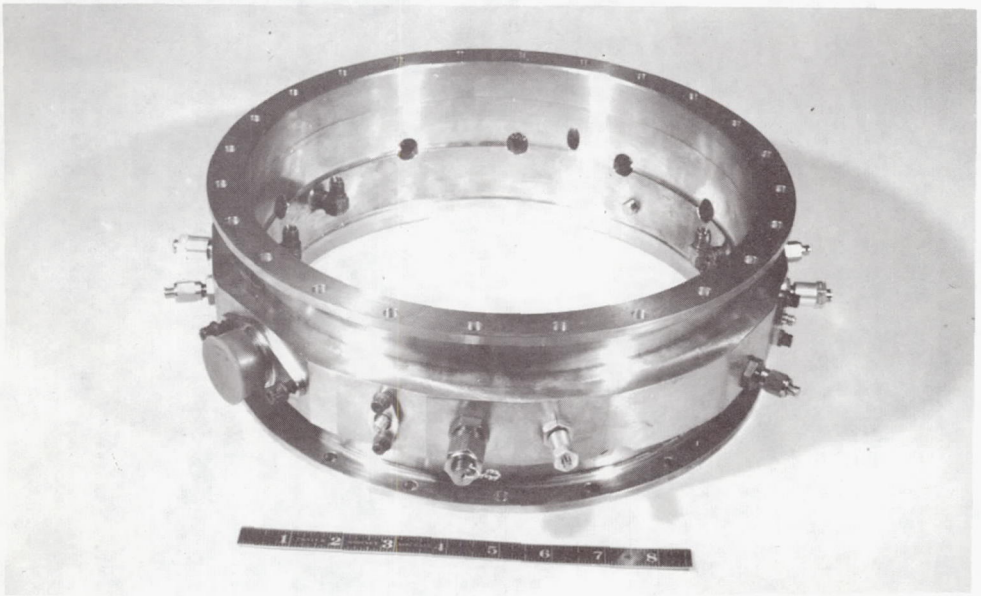

Figure 30 Rear Outer Case (X-25644)

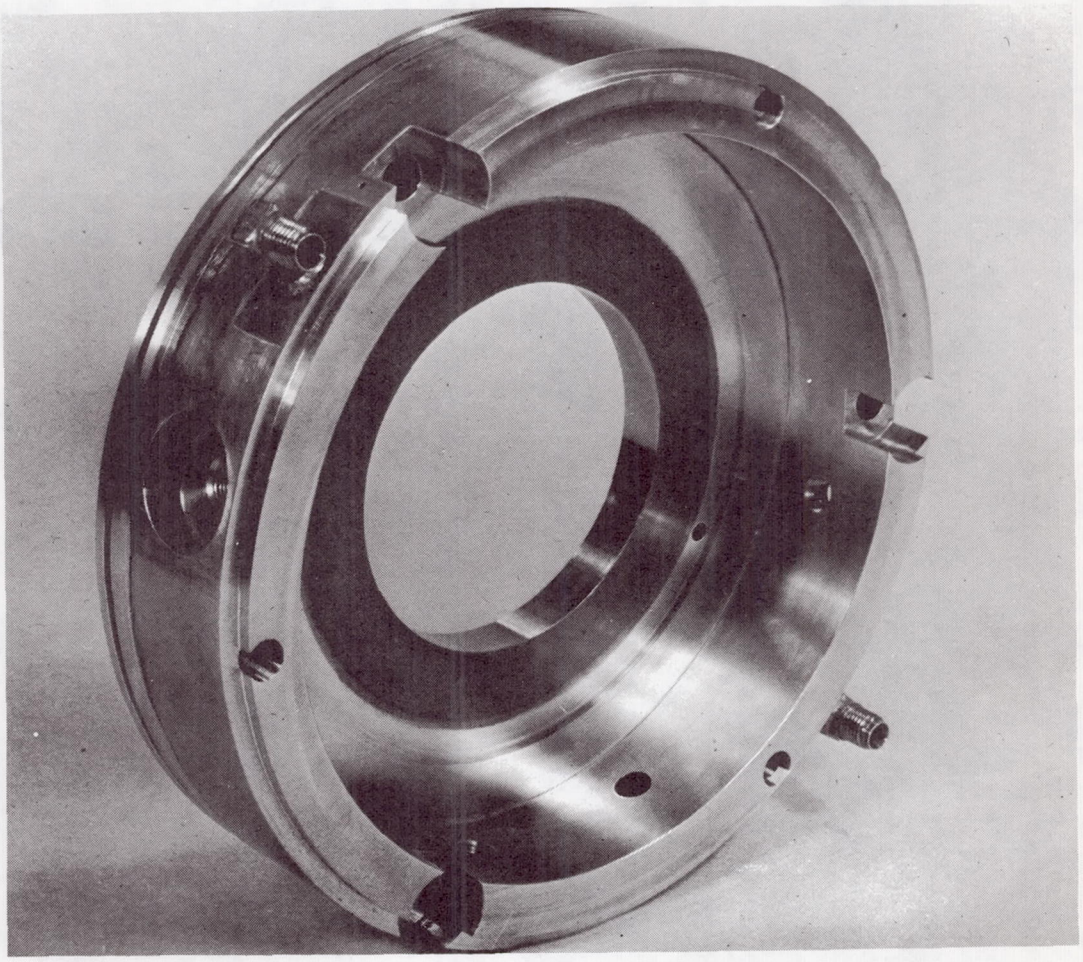

Figure 31 Reverse Thrust Stator (M-42651)

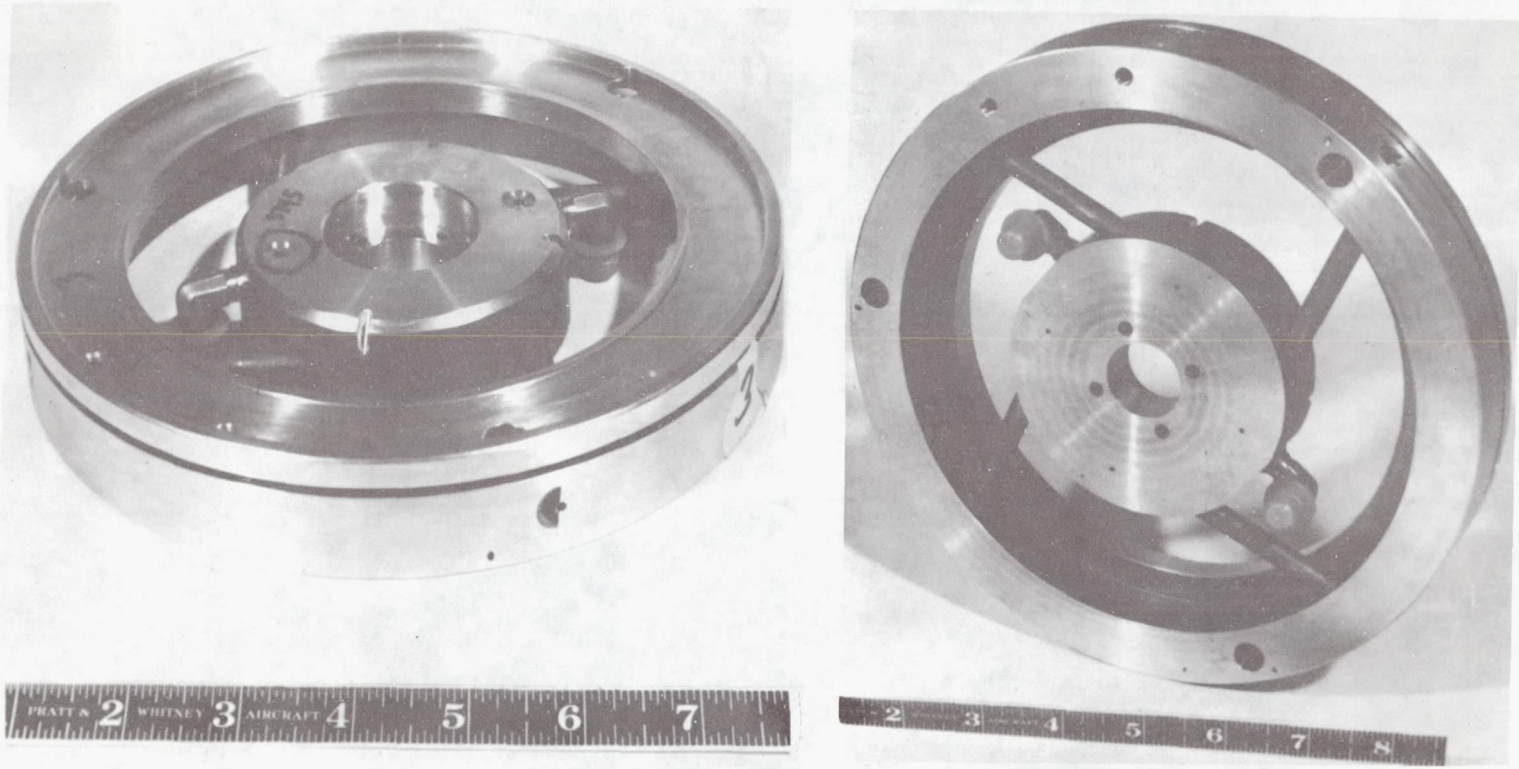

Figure 32 Main Thrust Plate Support (M-44261)

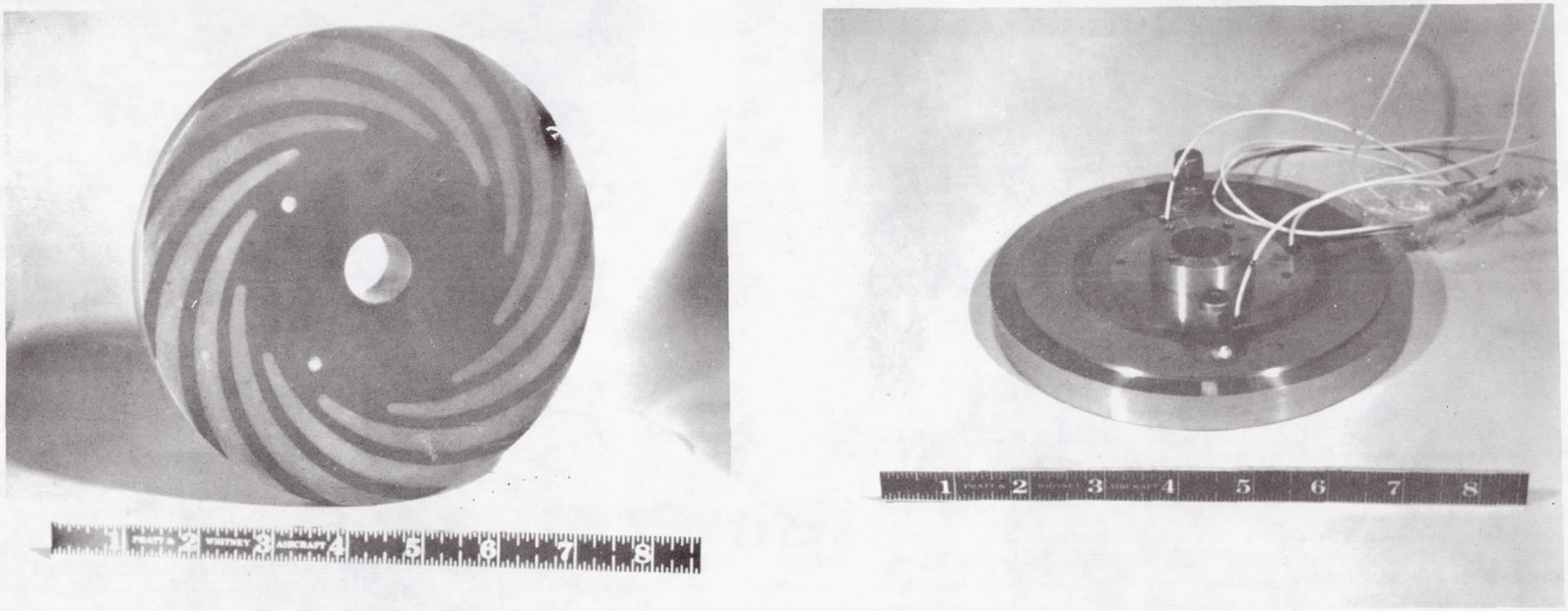

Figure 33 Main Thrust Plate (M-45055)

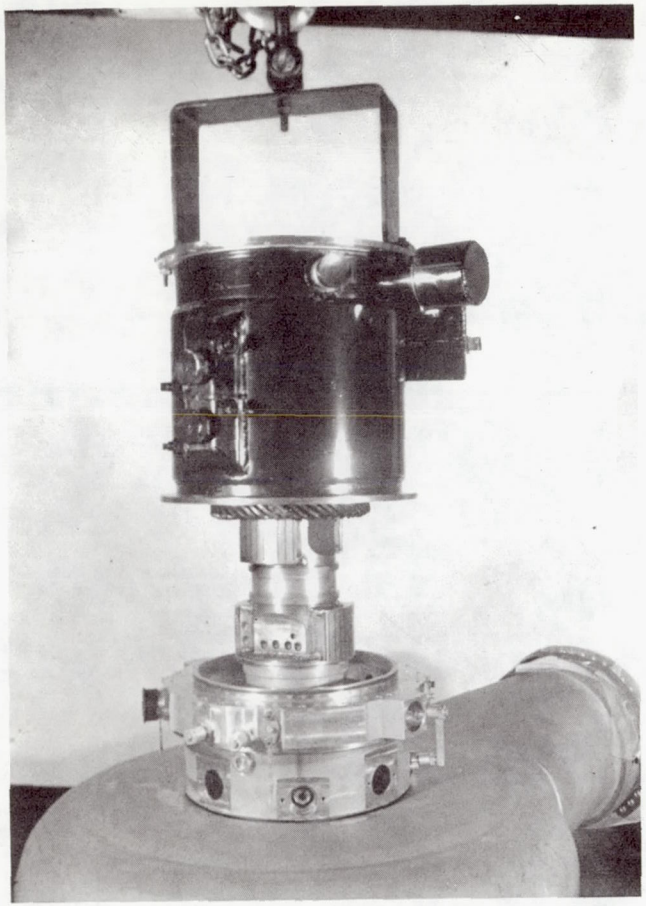

Figure 34 Installing Alternator Stator (CN-9452)

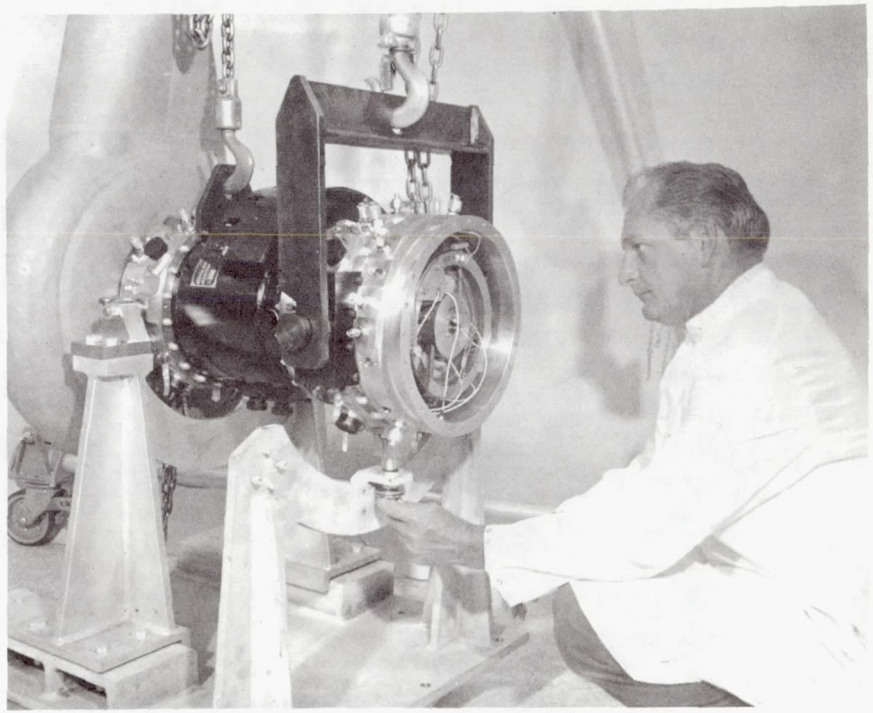

Figure 35 Installation of Mounts (CN-9570)

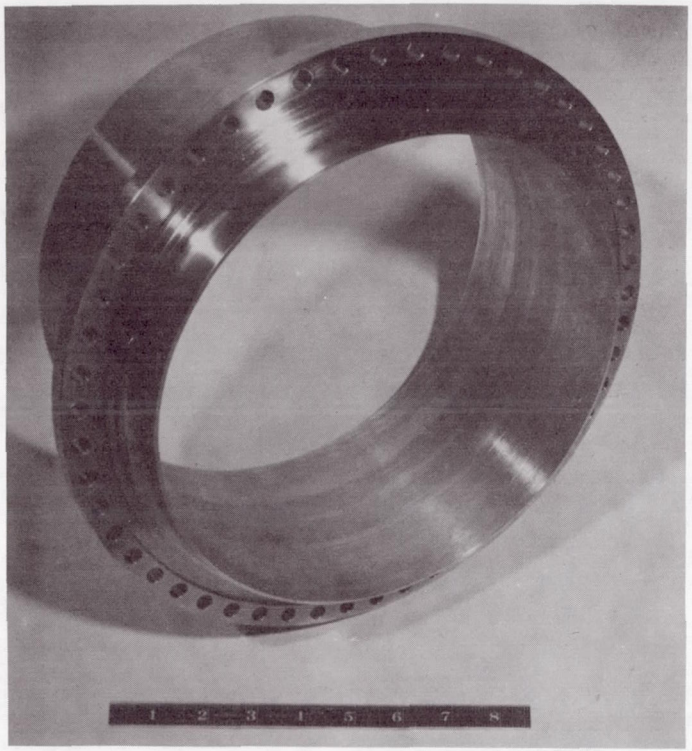

Figure 36 Turbine Inlet Flange

(XP-75878)

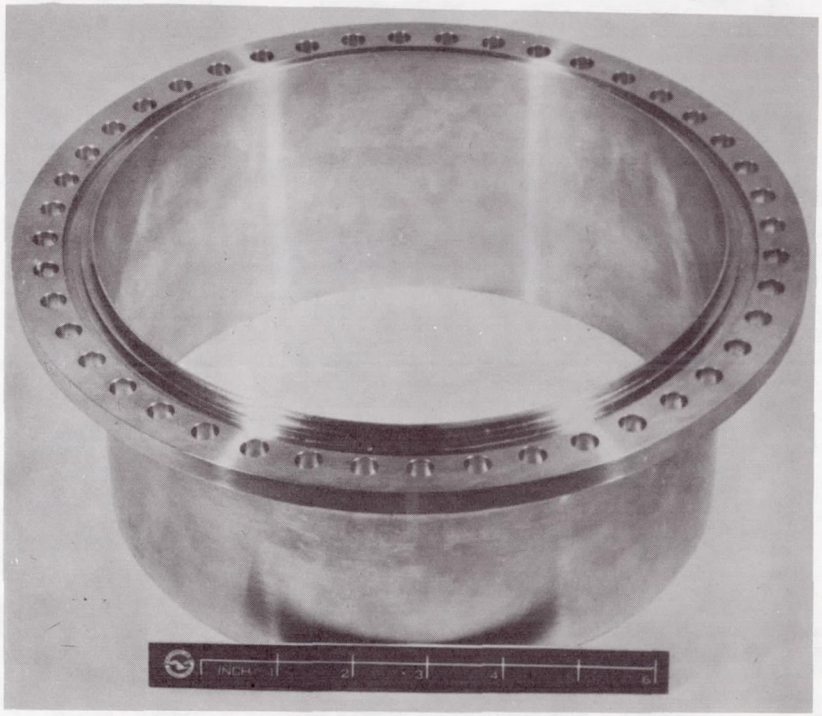

Figure 37 Turbine Exhaust Flange

(M-42022)

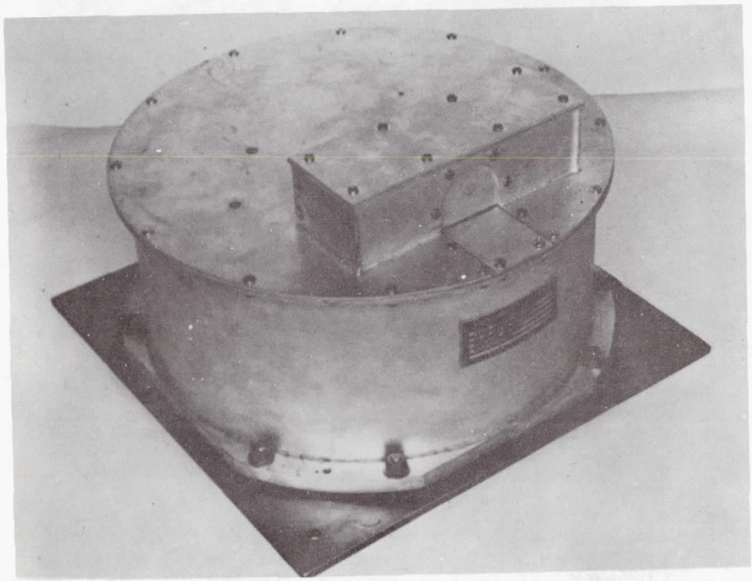

Figure 38 Voltage Regulator (M-39476)

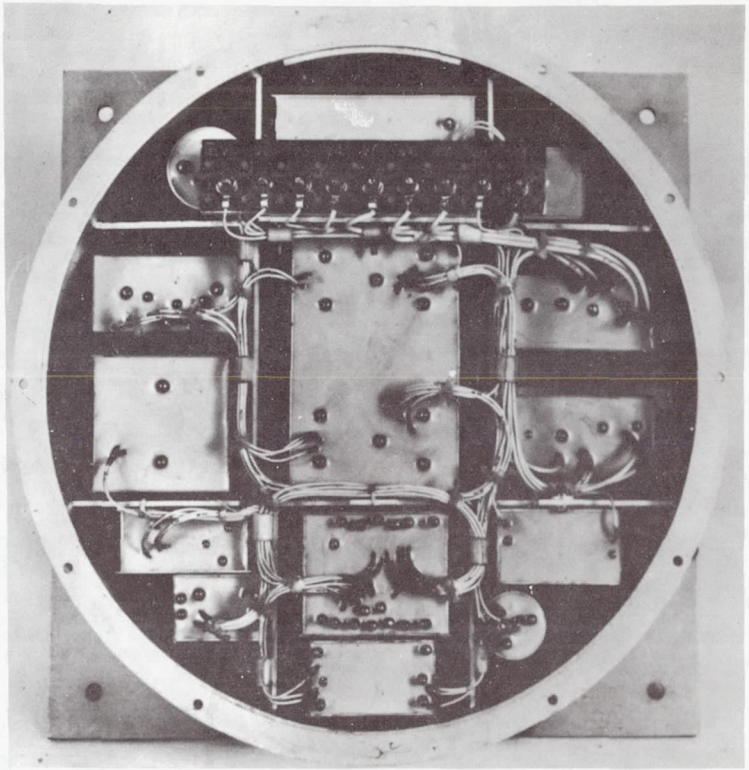

Figure 39 Voltage Regulator, Cover Removed (M-39474)

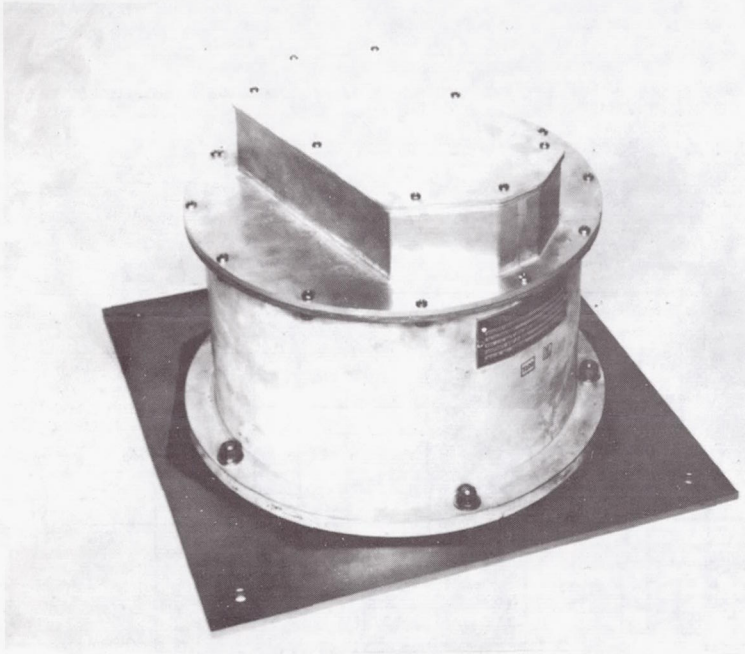

Figure 40 Exciter (M-39467)

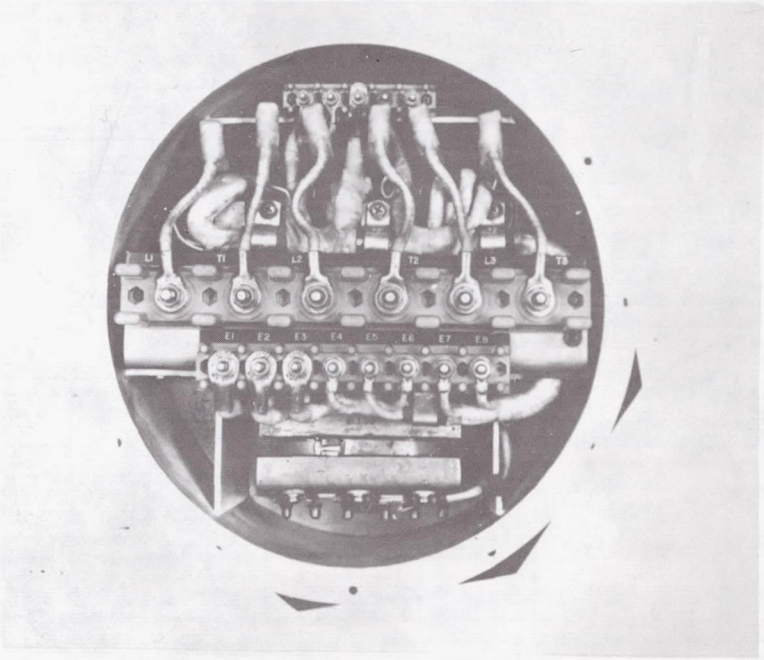

Figure 41 Exciter, Cover Removed (M-39468)

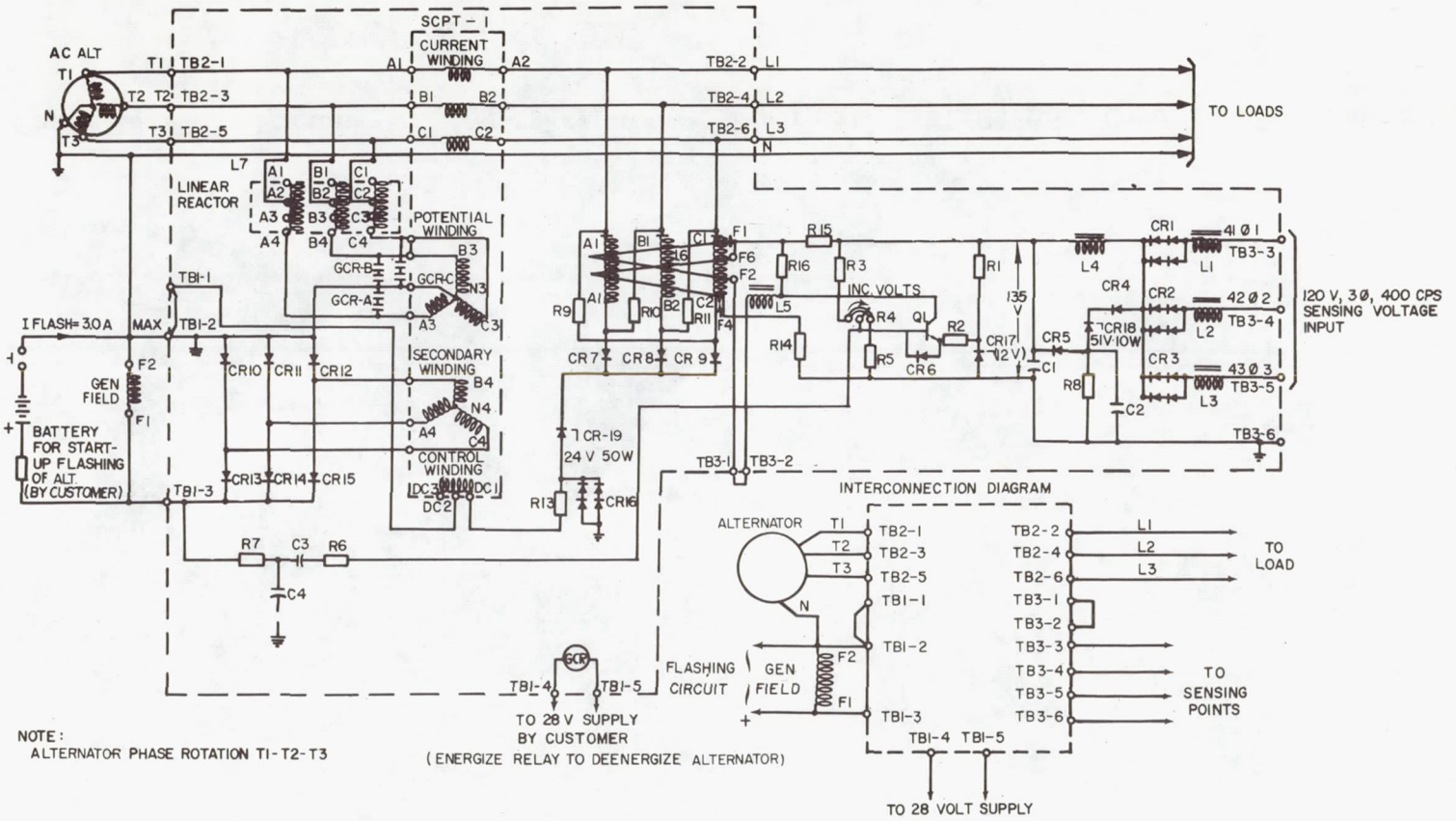

Figure 42 Circuit Diagram, Voltage Regulator-Exciter

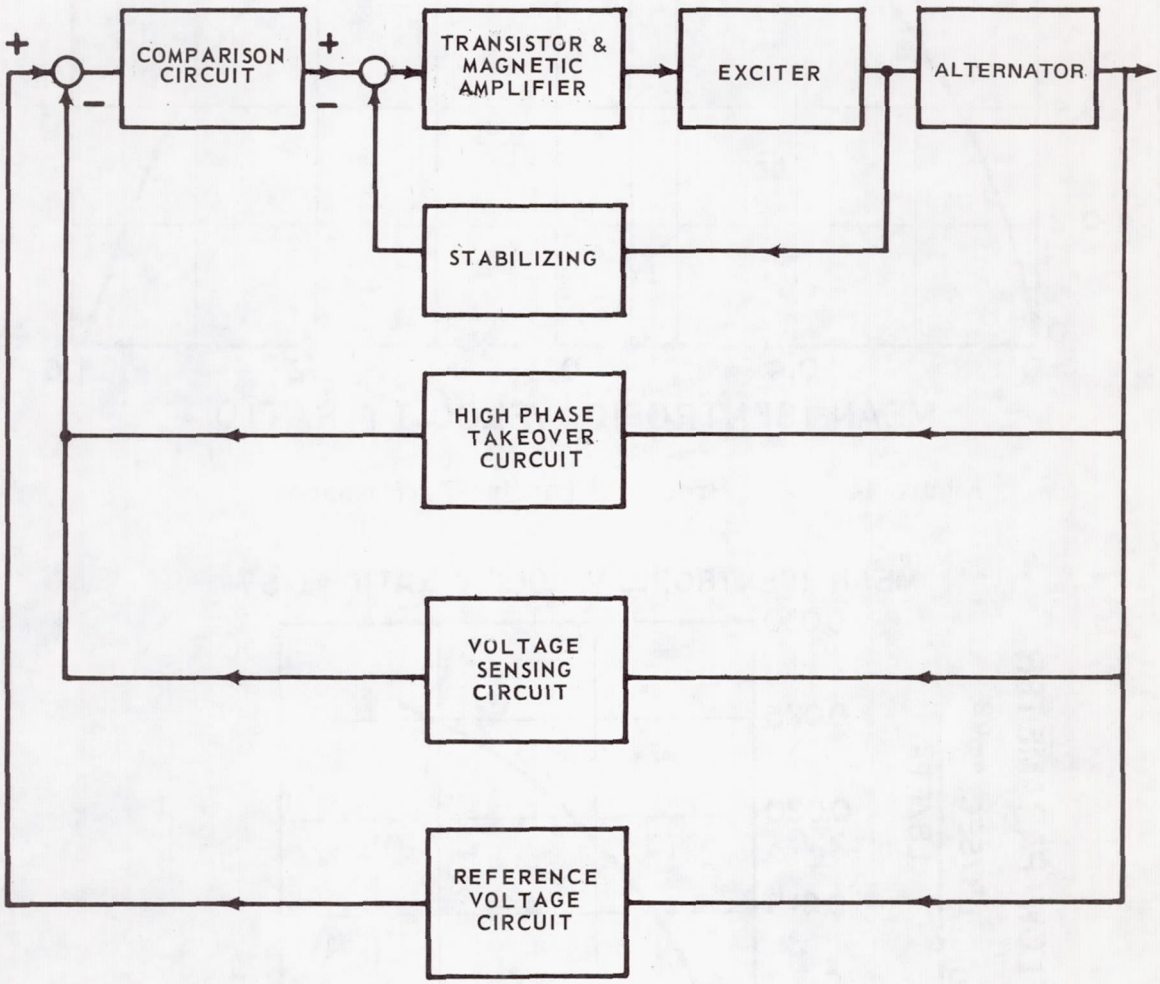

Figure 43 Block Diagram of Exciter-Regulator

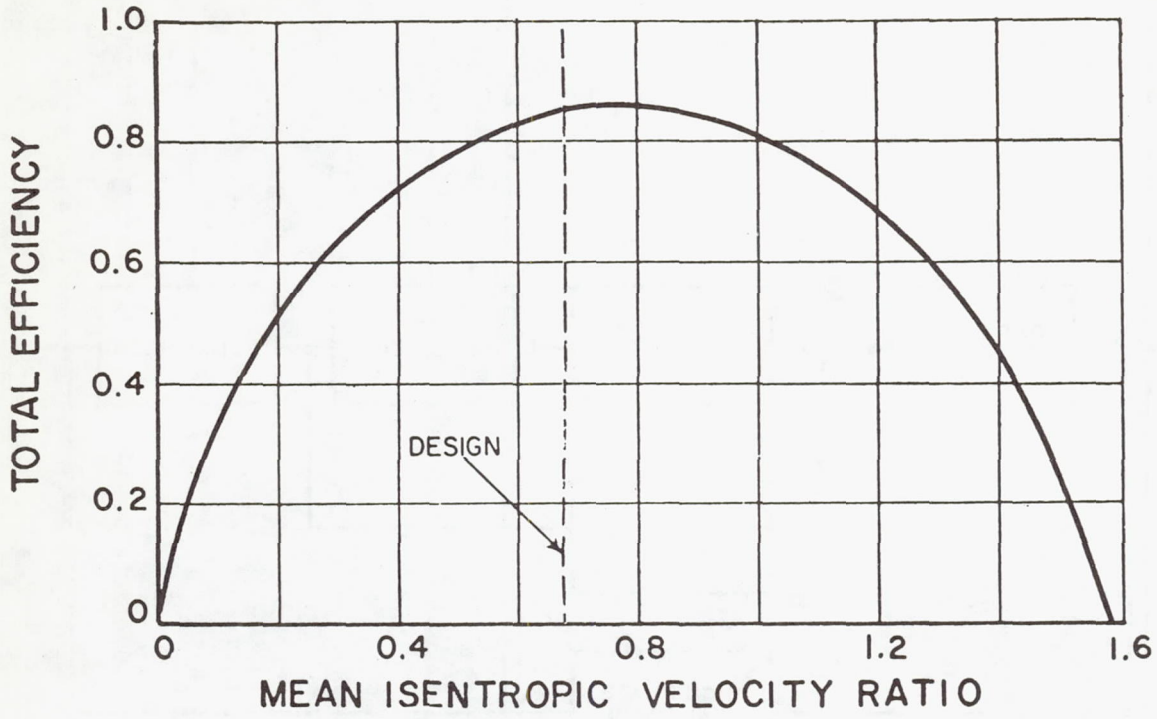

Figure 44 Predicted Turbine Performance

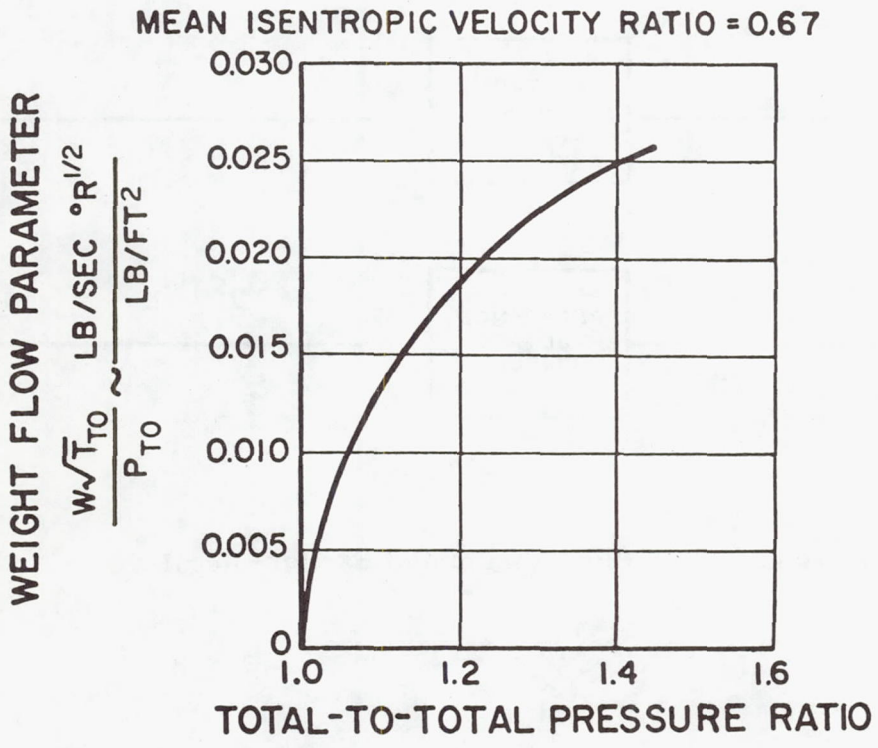

Figure 45 Predicted Weight-Flow Parameter for Turbine

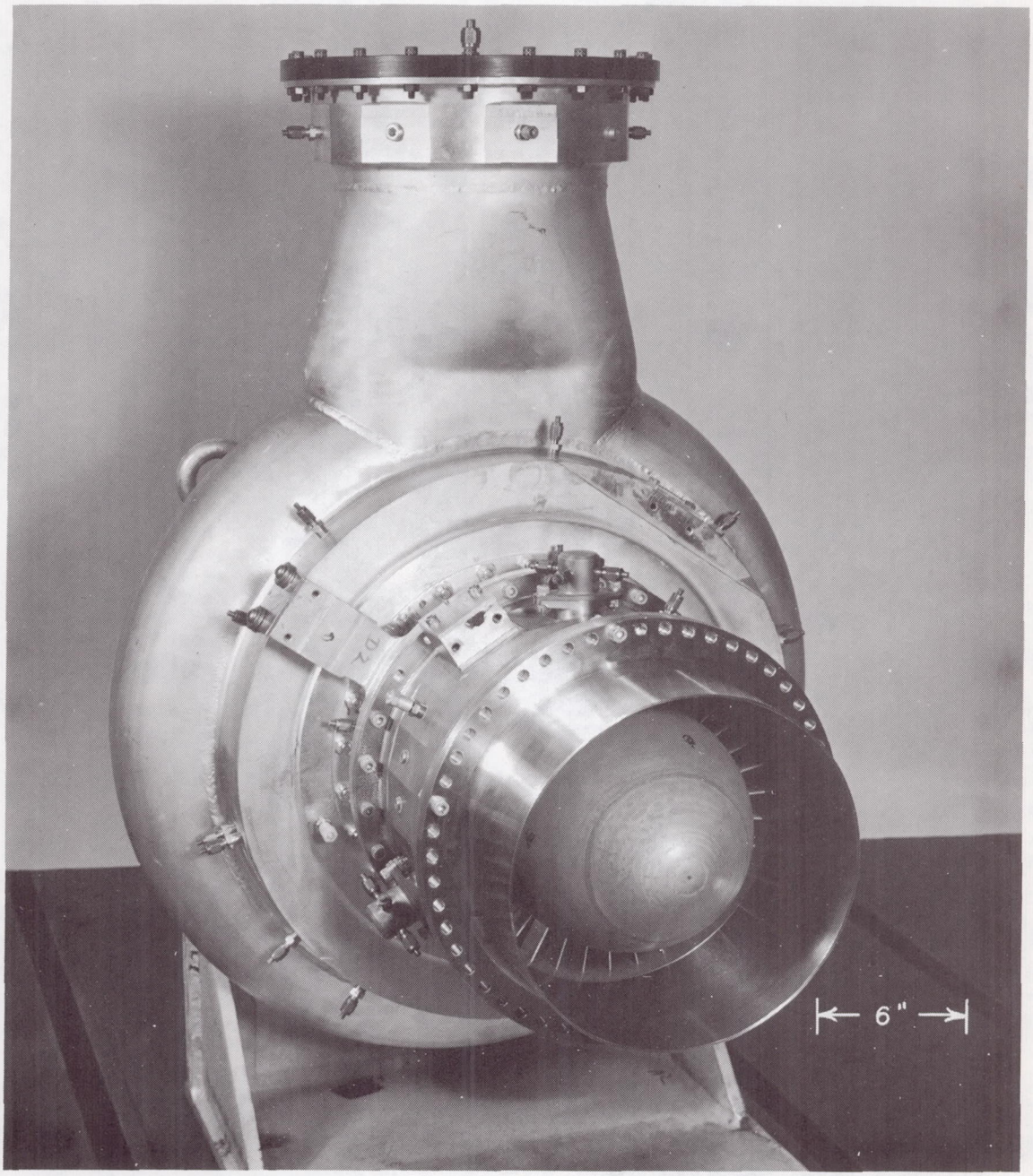

Figure 46 Turbine Research Package (XP-59999)

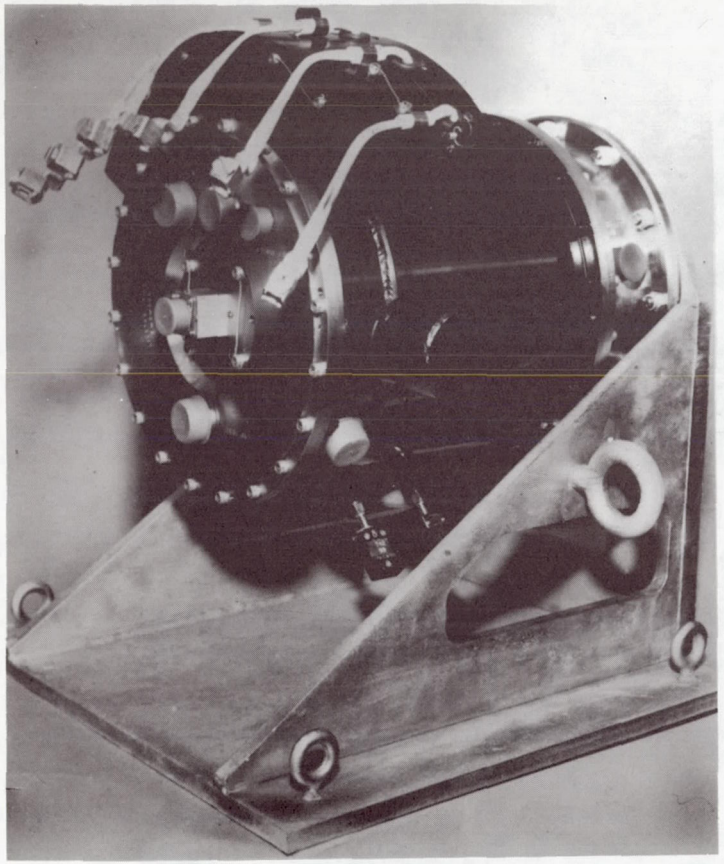

Figure 47 Alternator Research Package Photo
(M-37533)

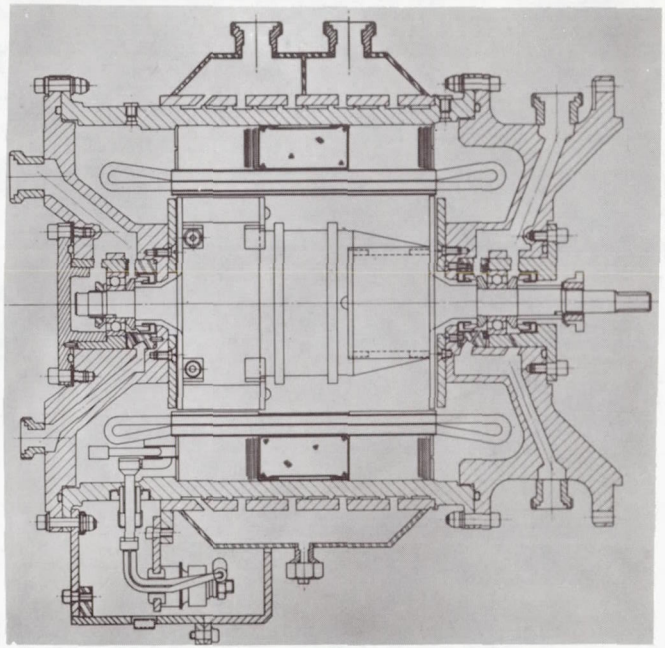

Figure 48 Alternator Research Package Design (M-32768)

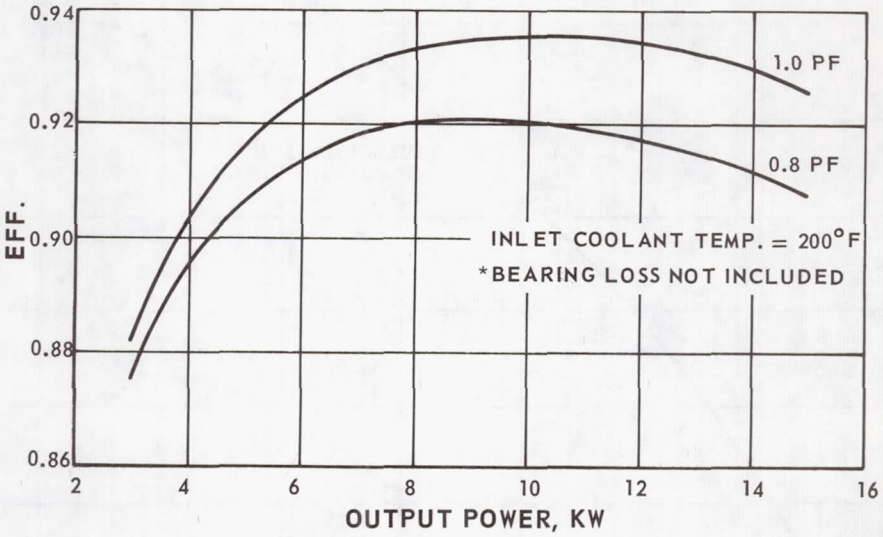

Figure 49 Measured Alternator Efficiency

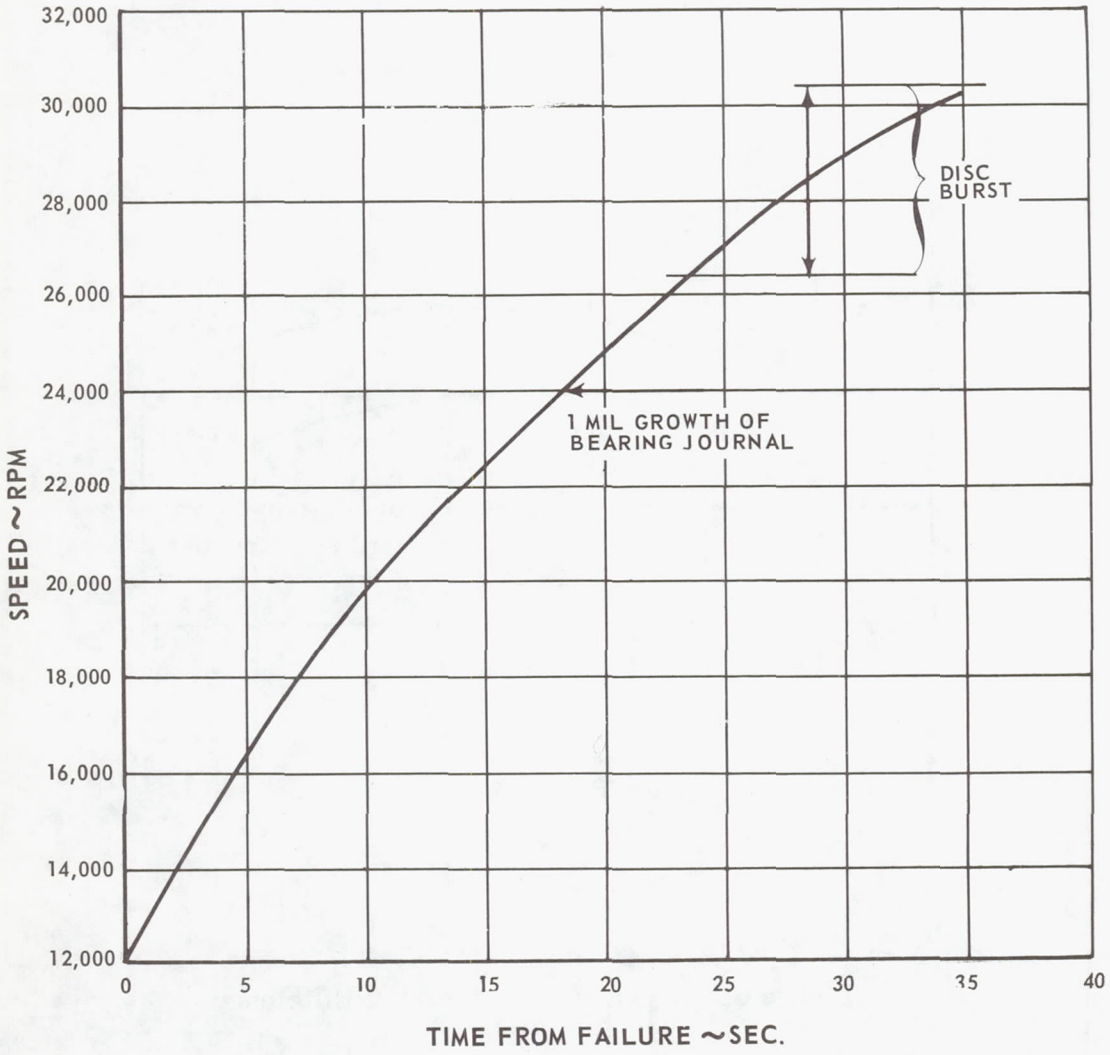

Figure 50 Estimated Rotor Runaway Speed for Complete Electrical Load Failure

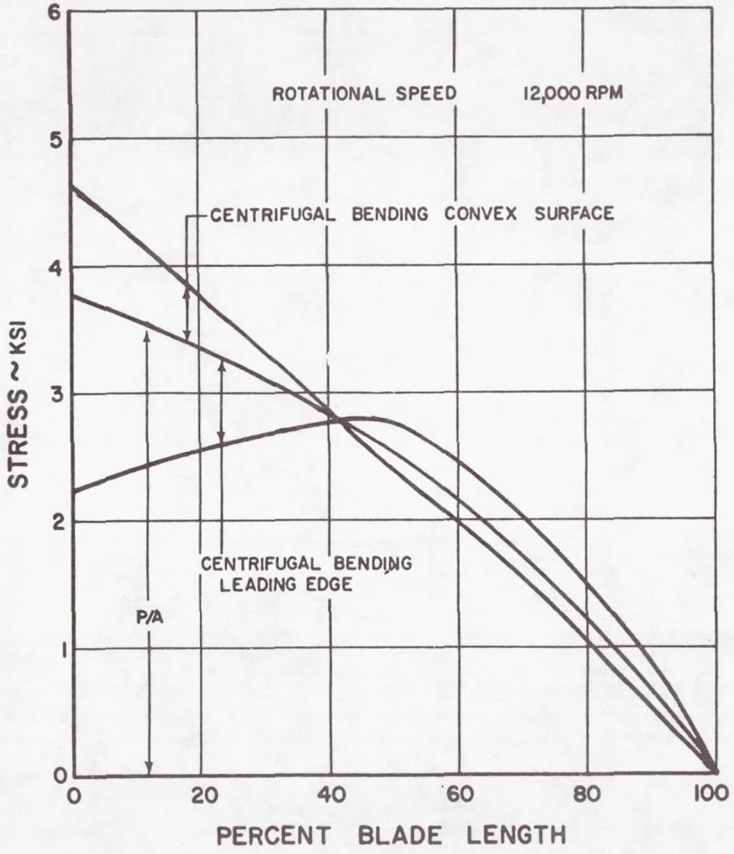

Figure 51 Stress Distribution in First Stage Blade

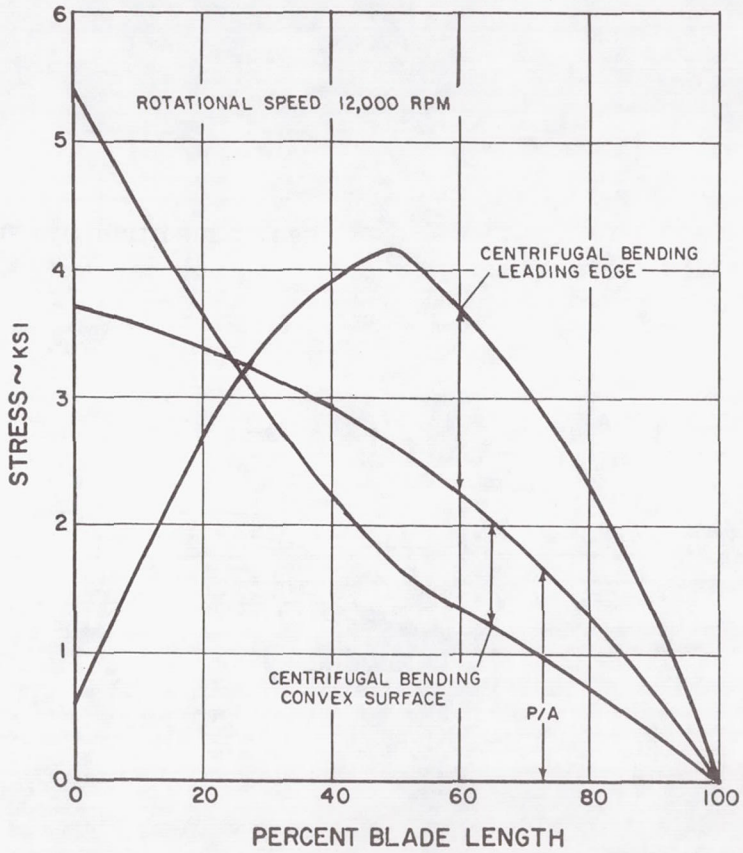

Figure 52 Stress Distribution in Second Stage Blade

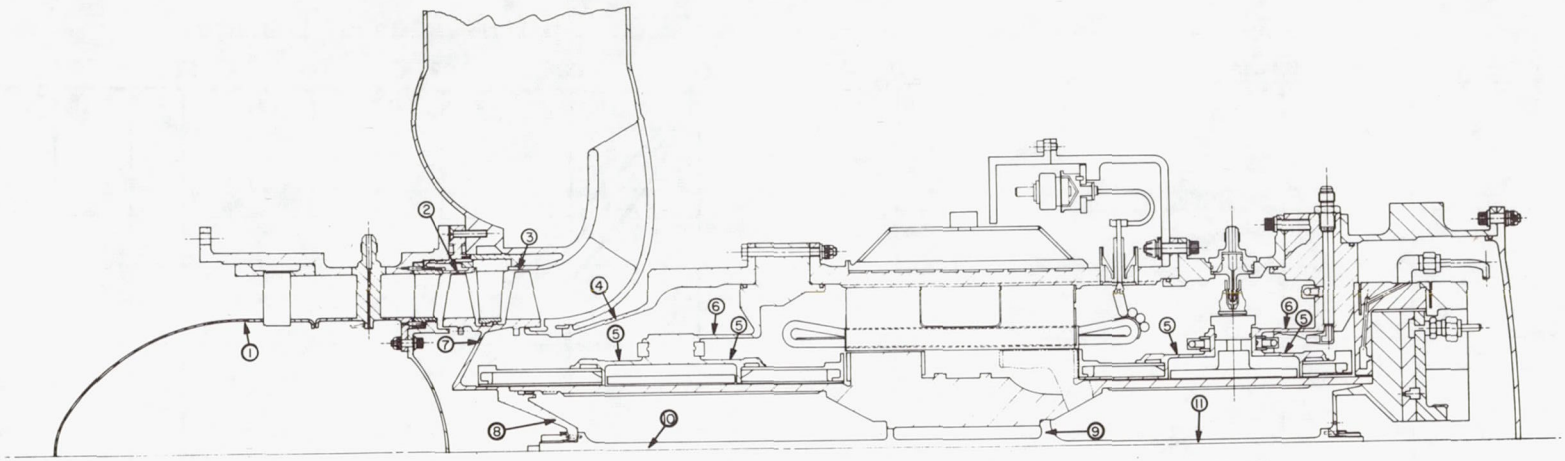

Figure 53 Locations of Significant Stress

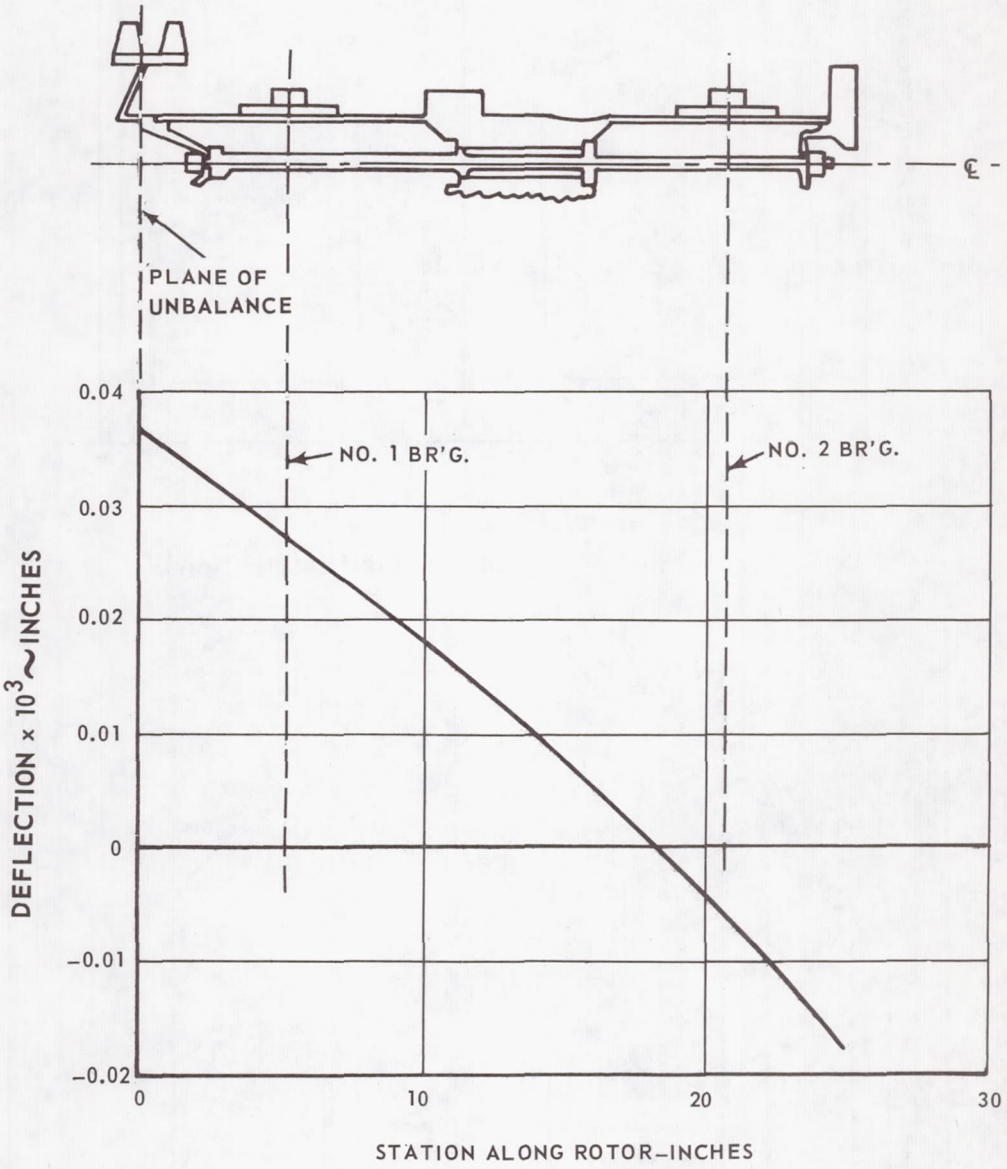

Figure 54 Rotor Deflection

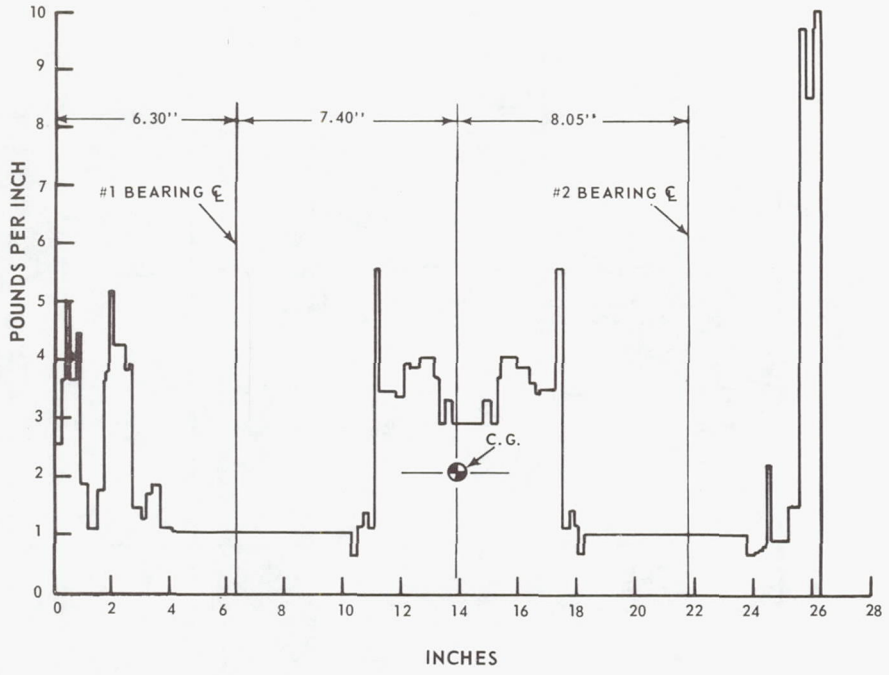

Figure 55 Rotor Mass Distribution

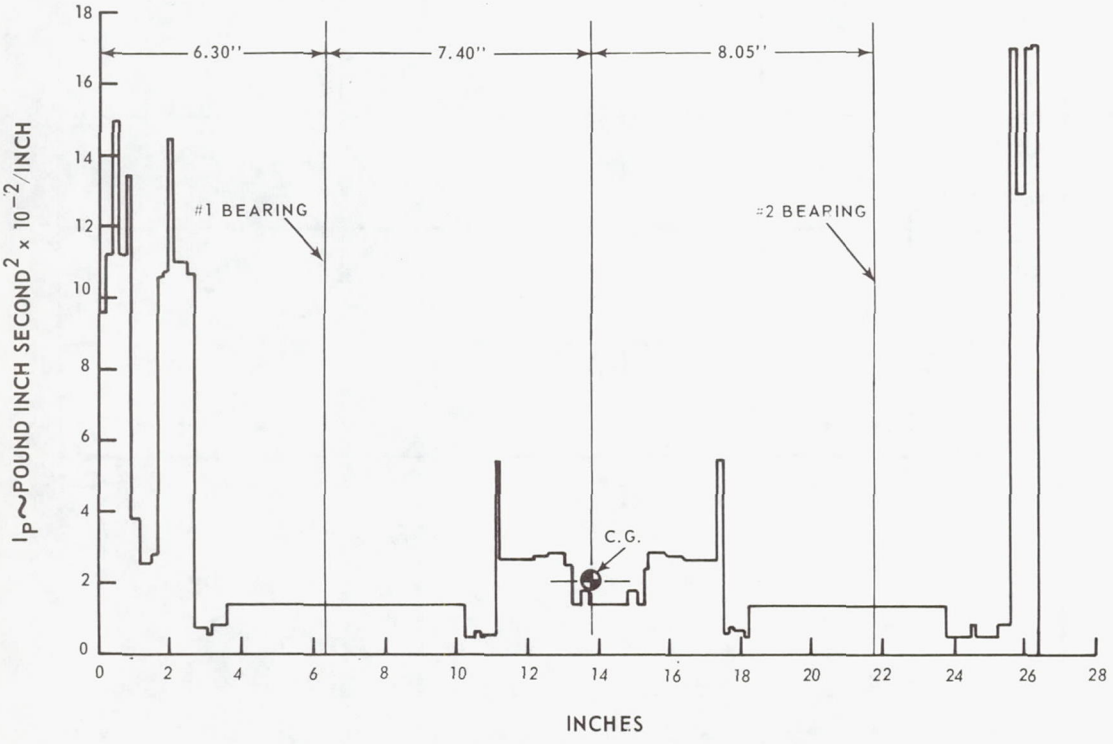

Figure 56 Rotor I_p Distribution

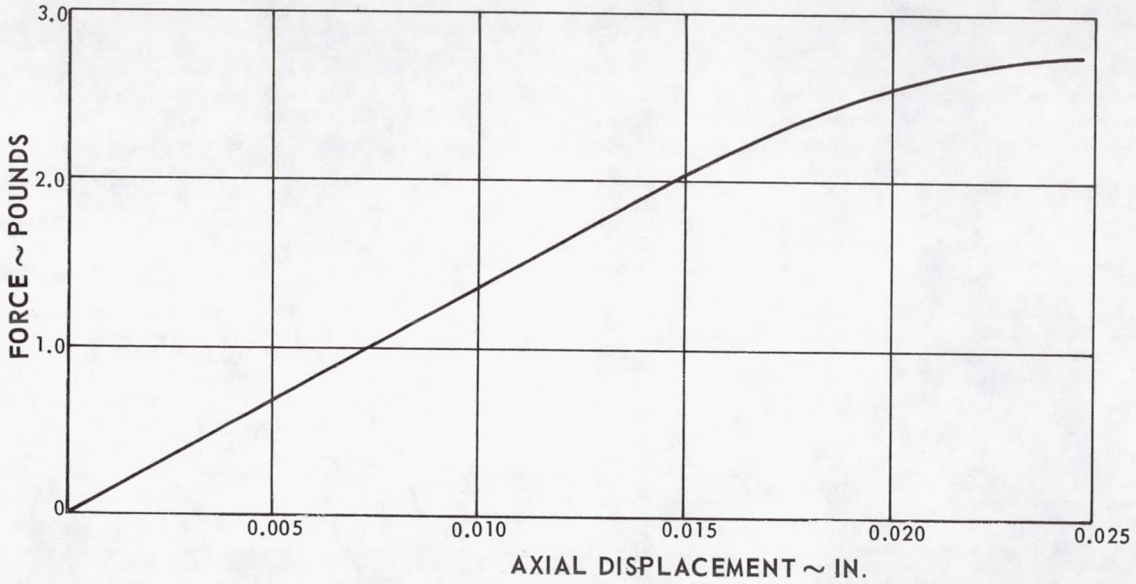

Figure 57 Alternator Axial Force on Rotor vs Axial Misalignment

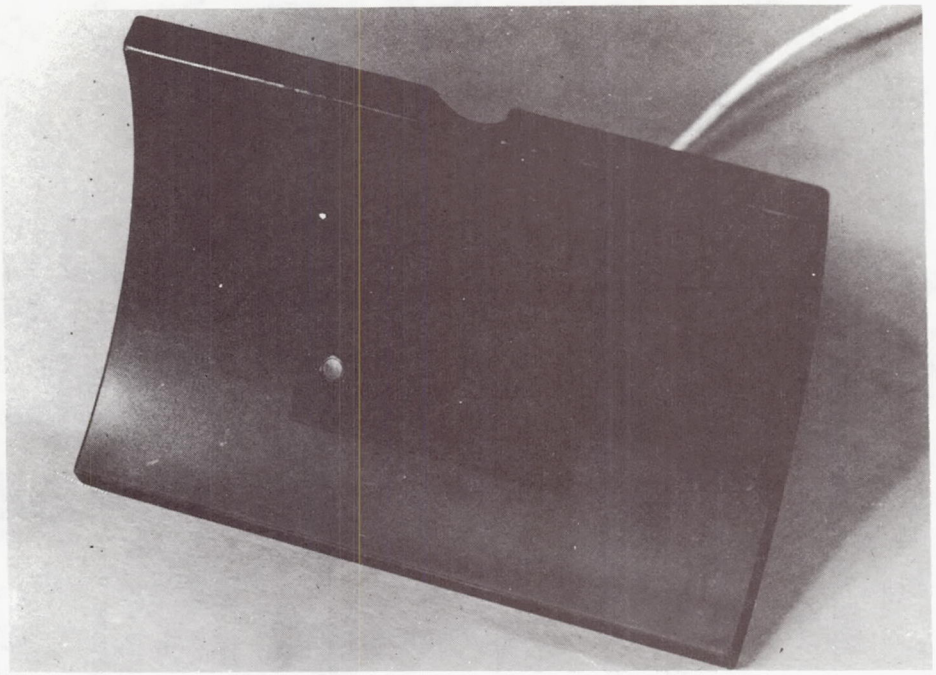

Figure 58 Journal Bearing Pad with Hydrostatic Jacking Gas Orifice and Pad-To-Shaft Probe (M-42649)

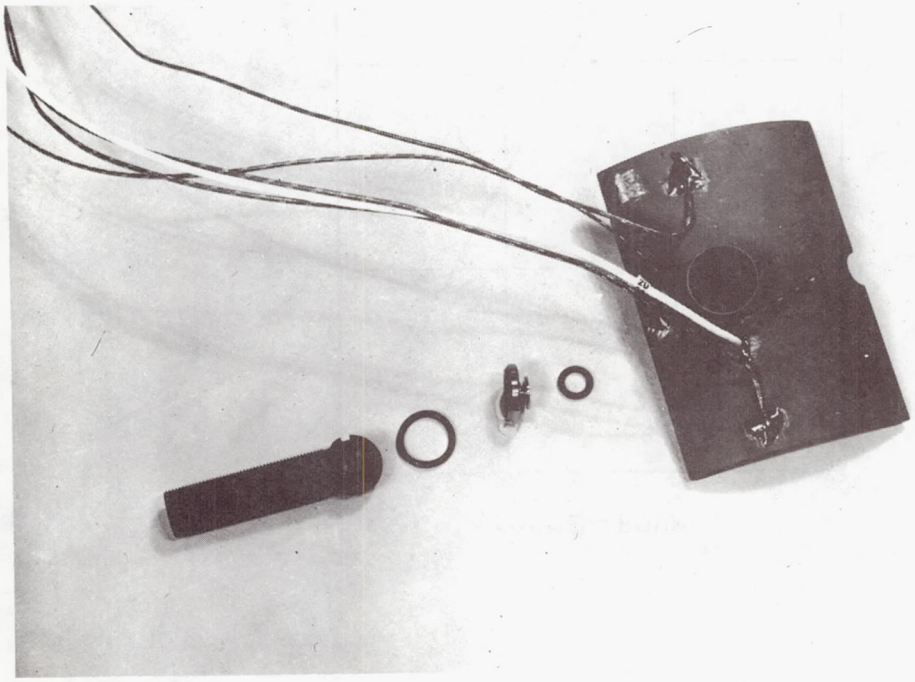

Figure 59 Journal Bearing Pad, Pivot, and Seals (M-42647)

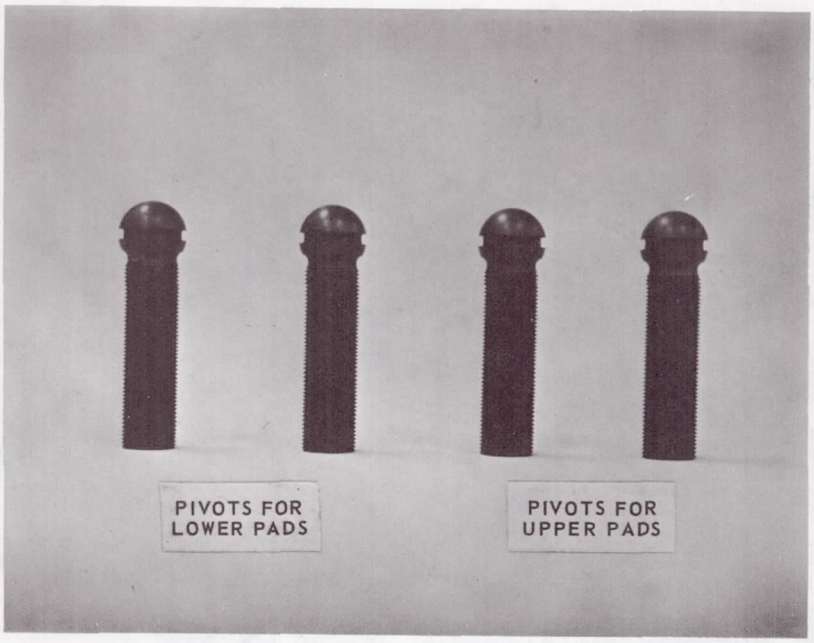

Figure 60 Journal Bearing Pivot (CN-9038)

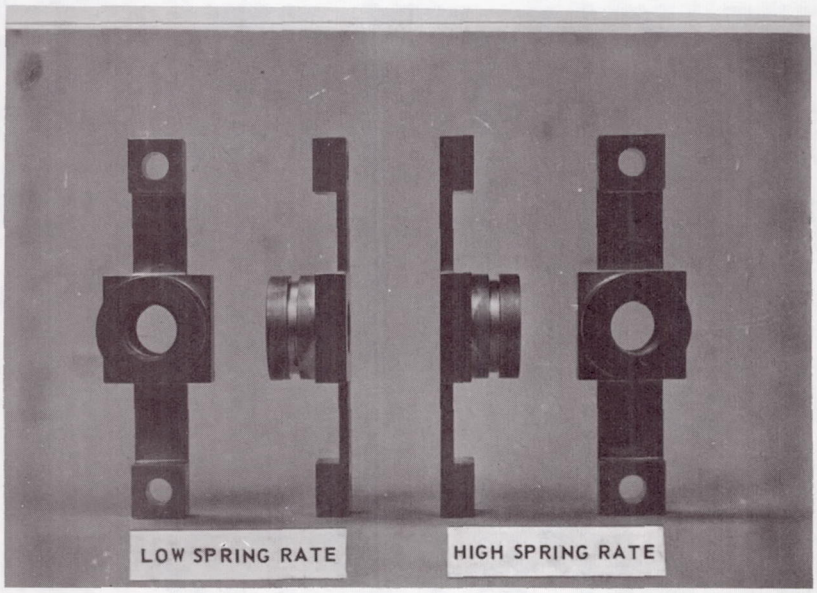

Figure 61 Journal Bearing Flexures (CN-9039)

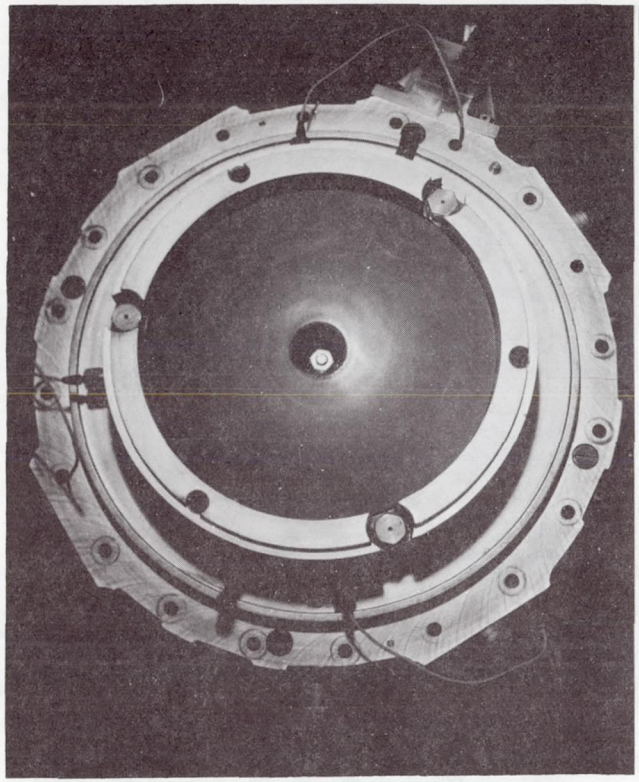

Figure 62 Thrust Runner Installed in Reverse Thrust Stator (CN-9492)

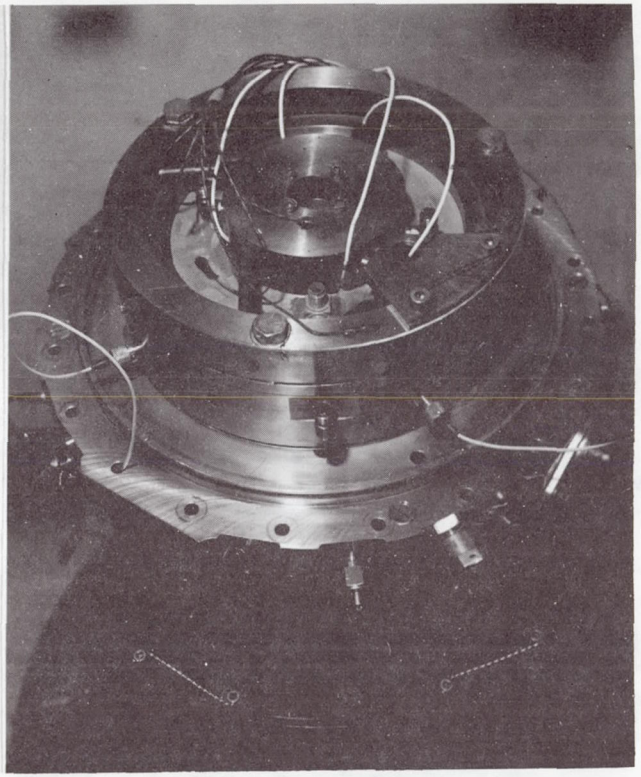

Figure 63 Main Thrust Stator and Flexible Support (CN-9491)

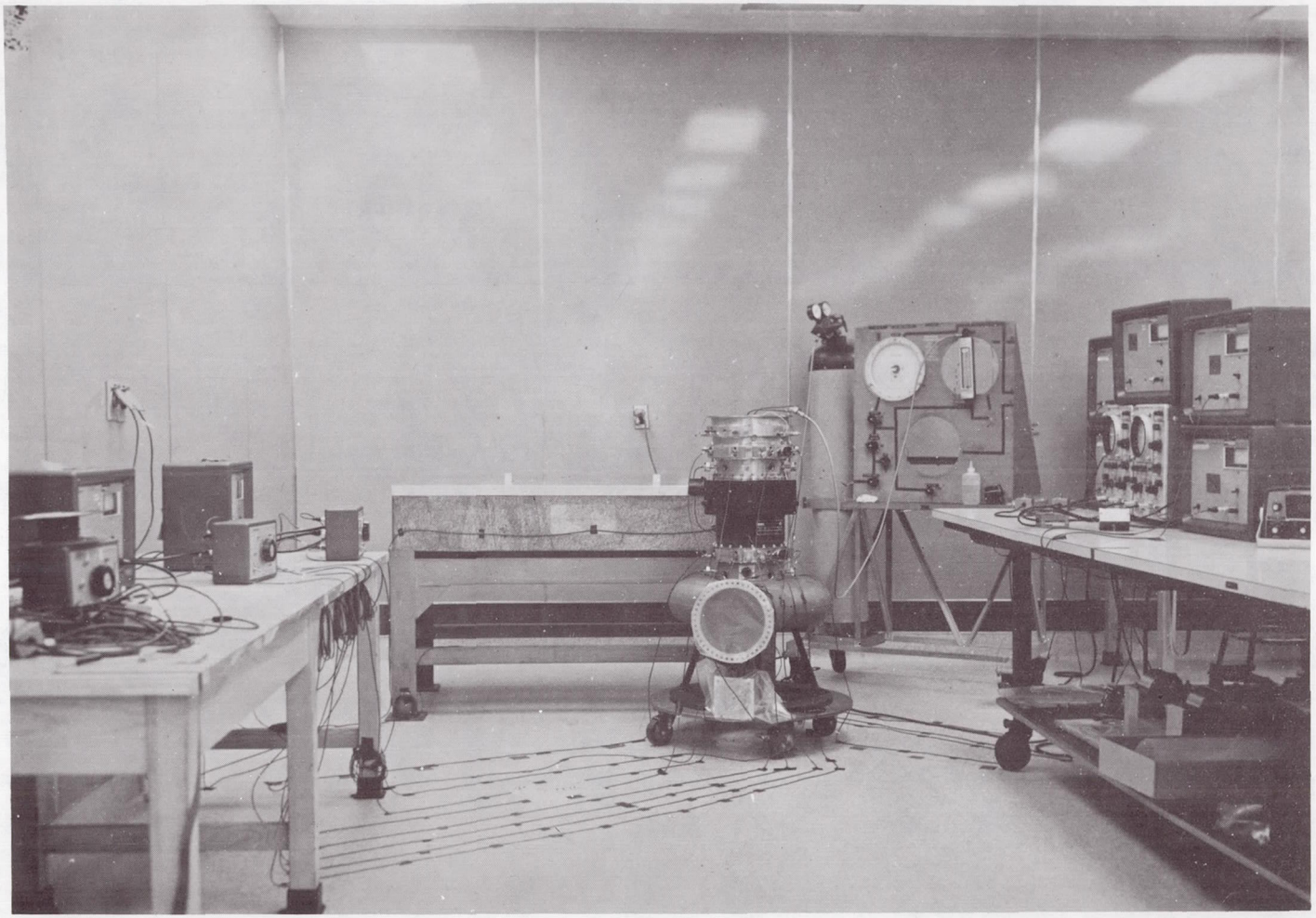

Figure 64 Capacitance Probe Readout Equipment for Gas Bearing Set-Up (CN-9416)

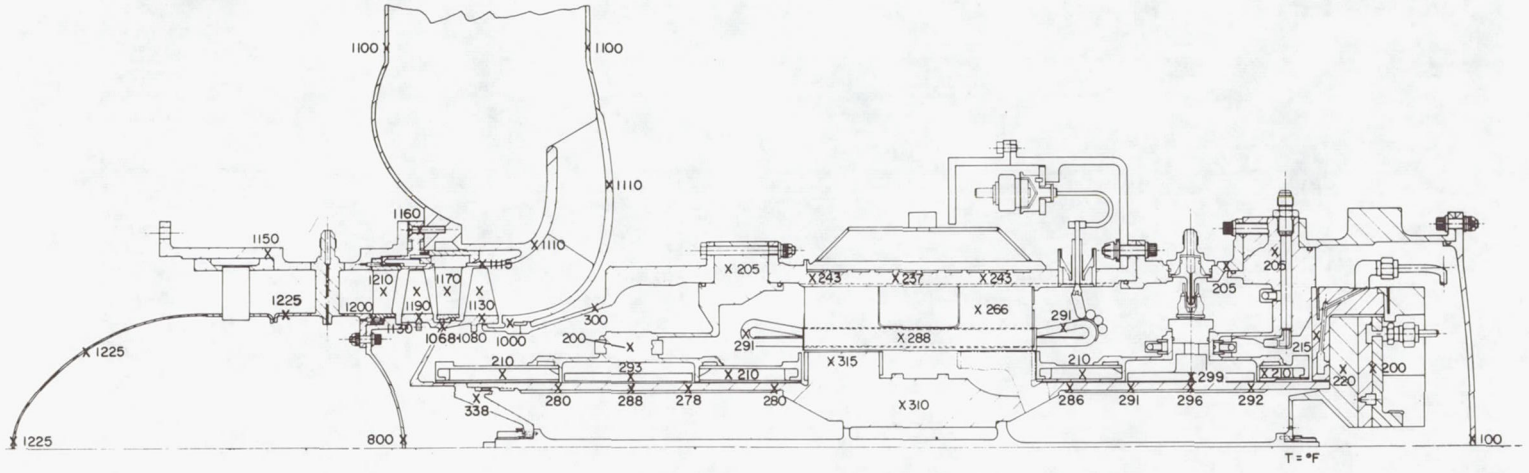

Figure 65 Over-All Thermal Map

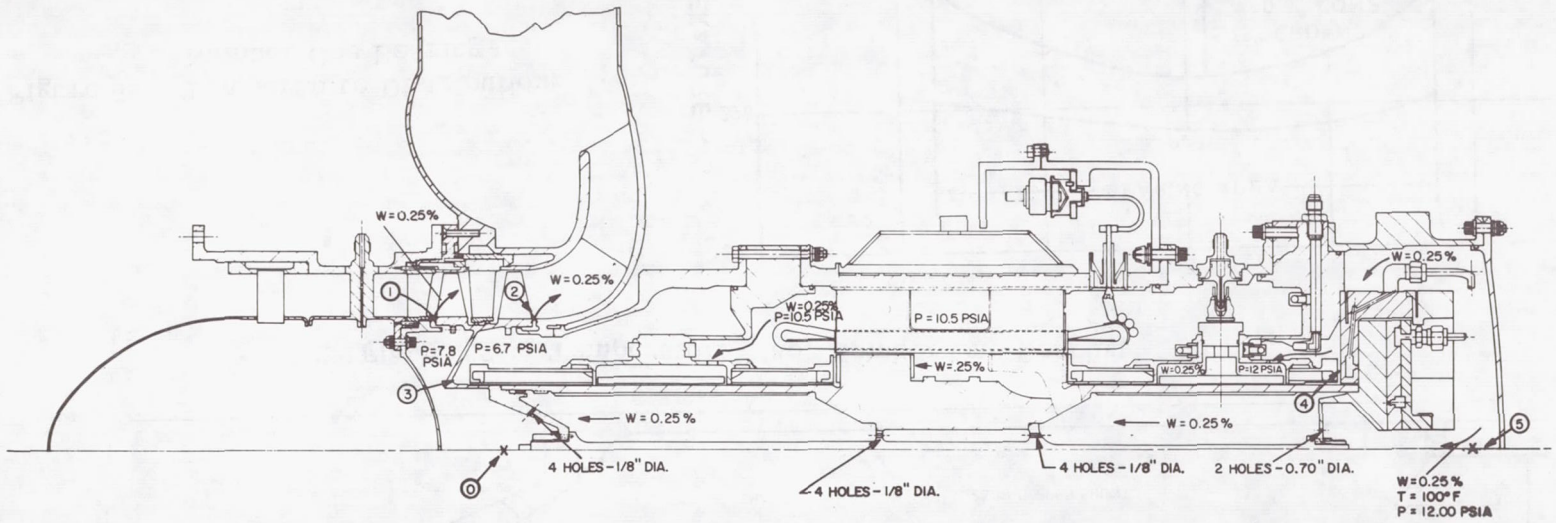

Figure 66 Gas Flow and Pressure in Turboalternator

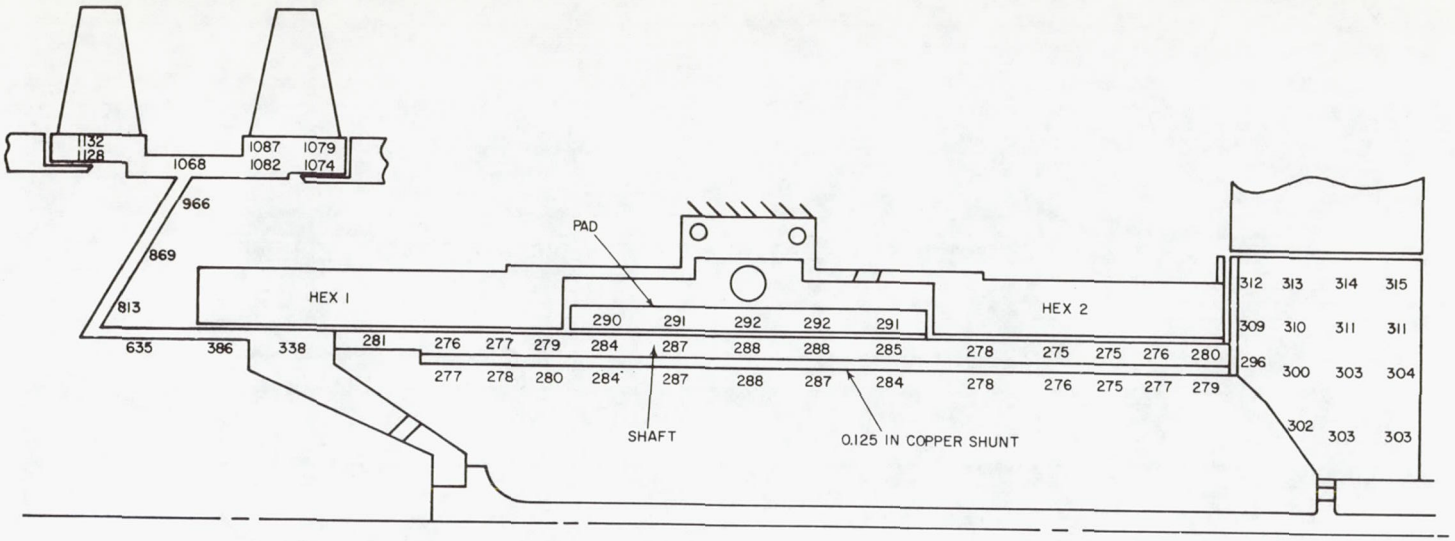

Figure 67 Temperature Map, Number One Bearing

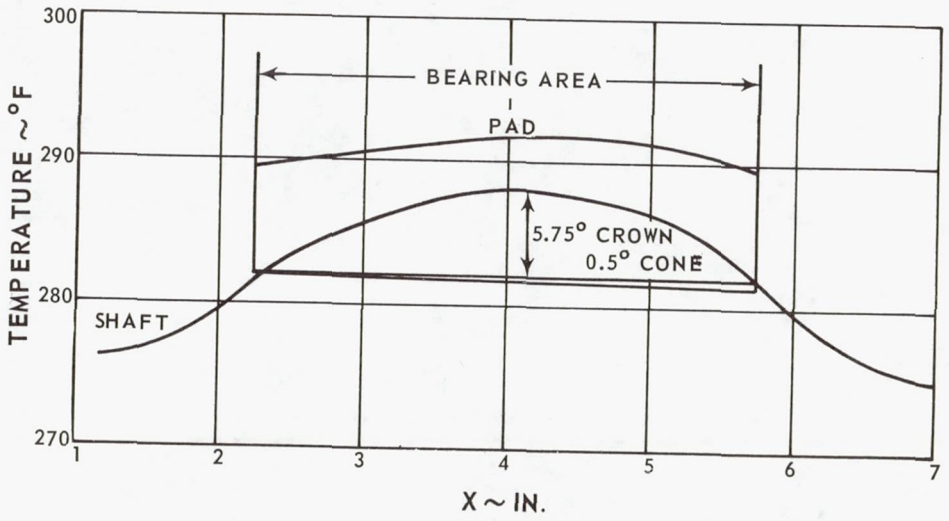

Figure 68 Temperature Distribution, Number One Bearing

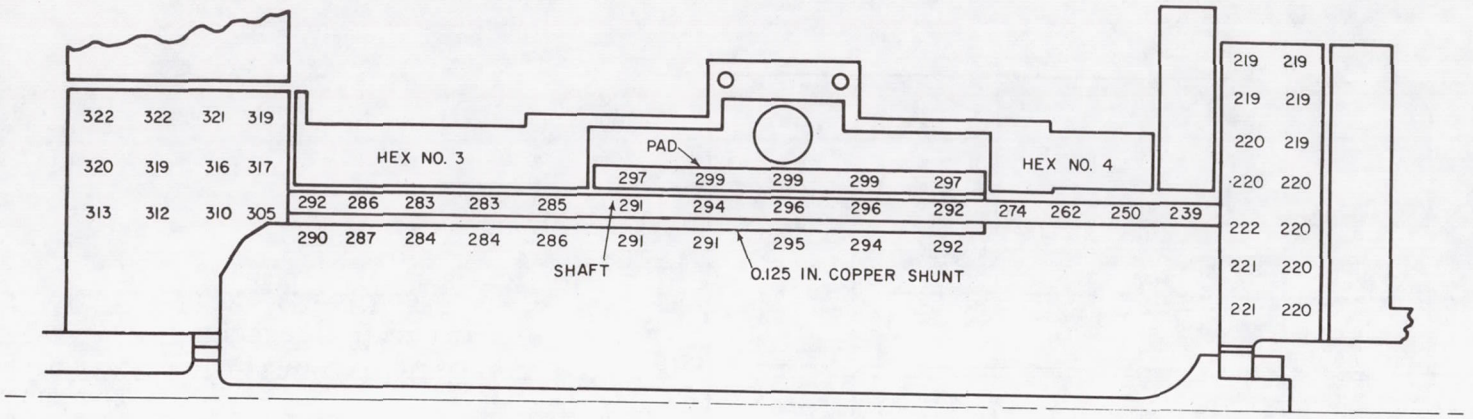

Figure 69 Temperature Map, Number Two Bearing

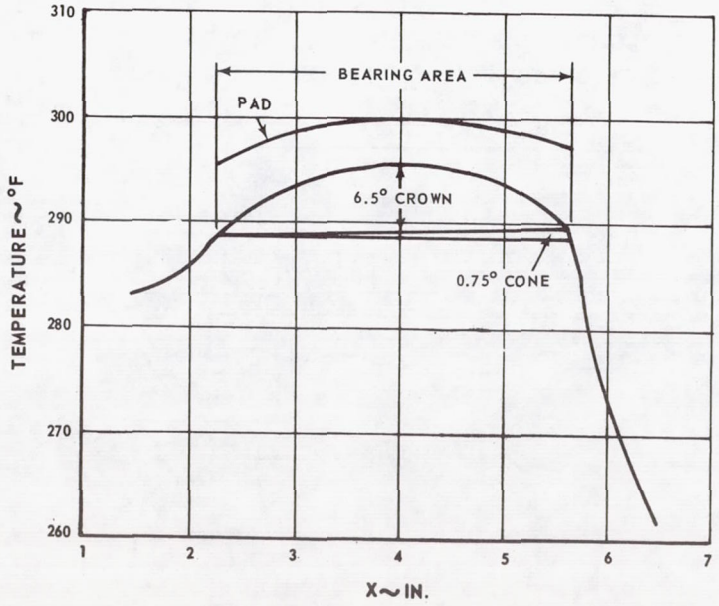

Figure 70 Temperature Distribution, Number Two Bearing

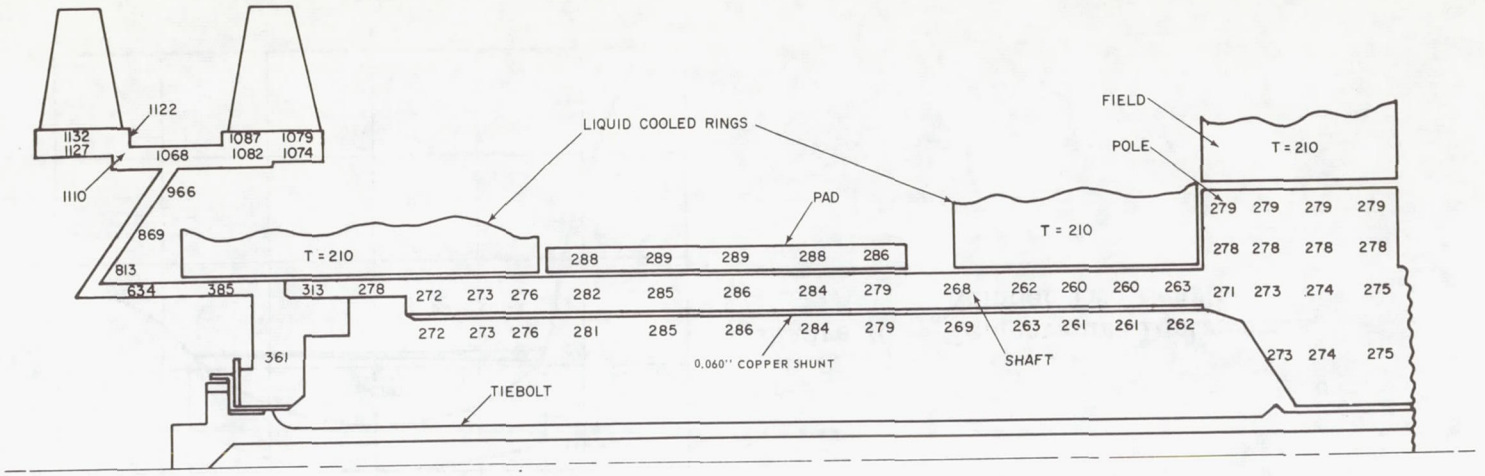

Figure 71 Temperature Map, Number One Bearing, with No Electrical Losses

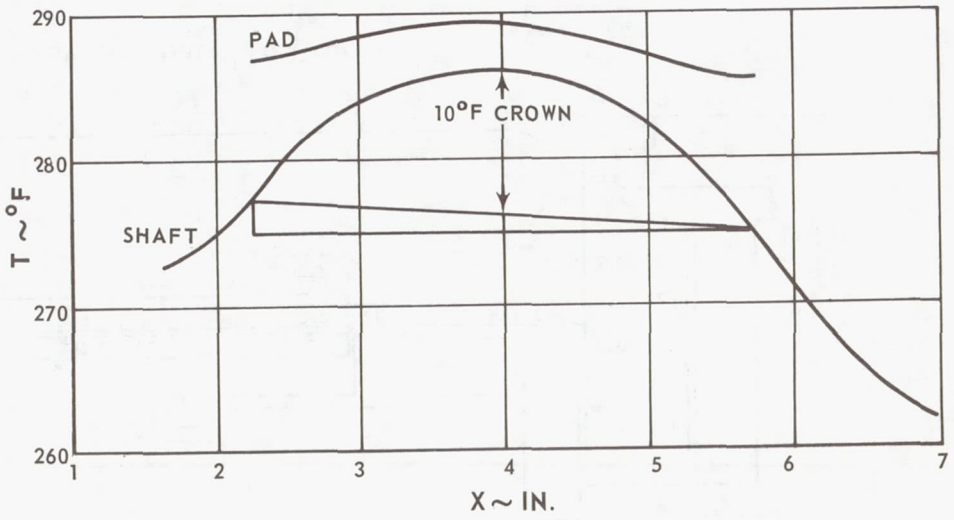

Figure 72 Temperature Distribution, Number One Bearing, with No Electrical Losses

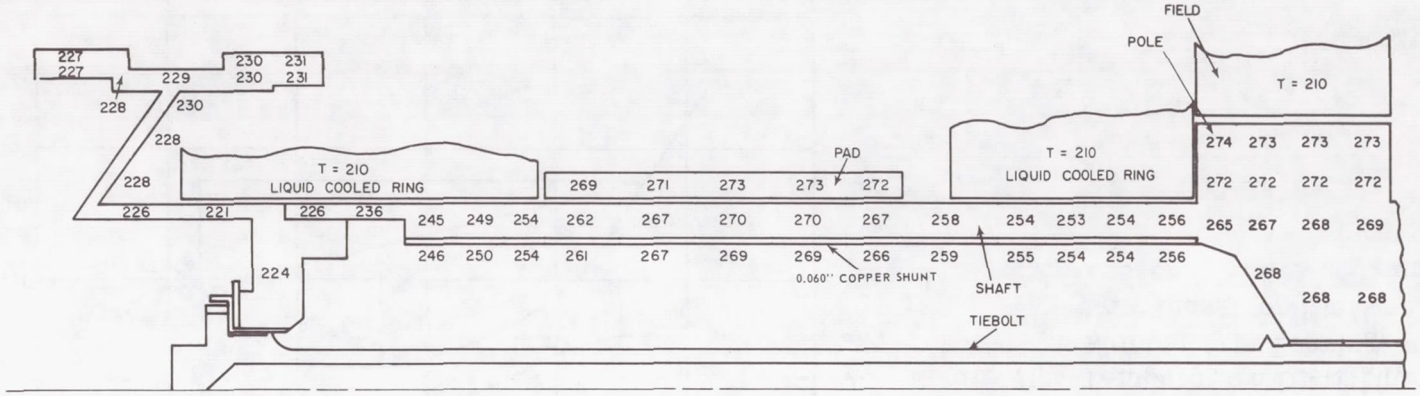

Figure 73 Temperature Map, Number One Bearing, with No Electrical Losses, No Turbine Heat Input

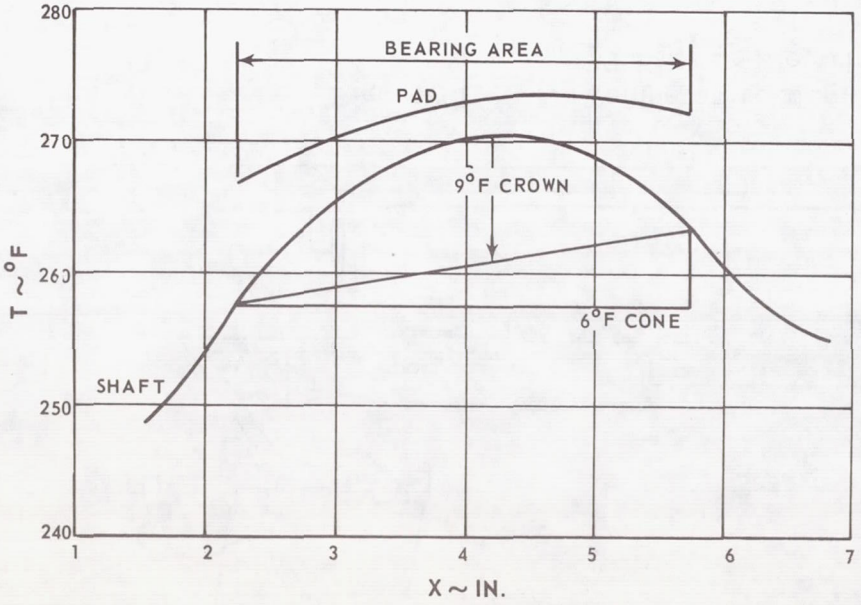

Figure 74 Temperature Distribution, Number One Bearing. with No Electrical Losses, No Turbine Heat Input

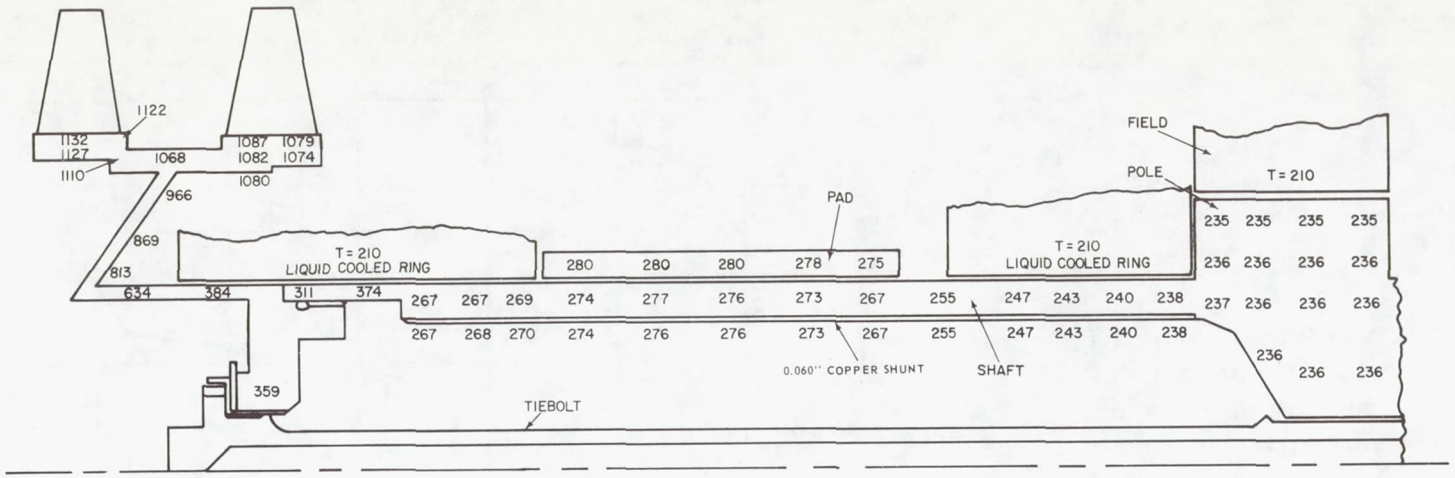

Figure 75 Temperature Map, Number One Bearing, with No Windage or Electrical Losses

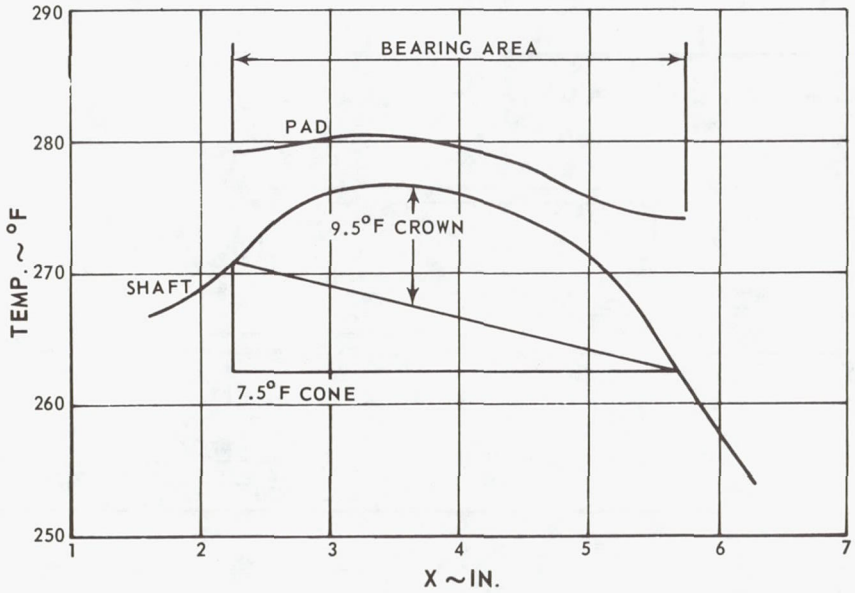

Figure 76 Temperature Distribution, Number One Bearing, with No Windage or Electrical Losses

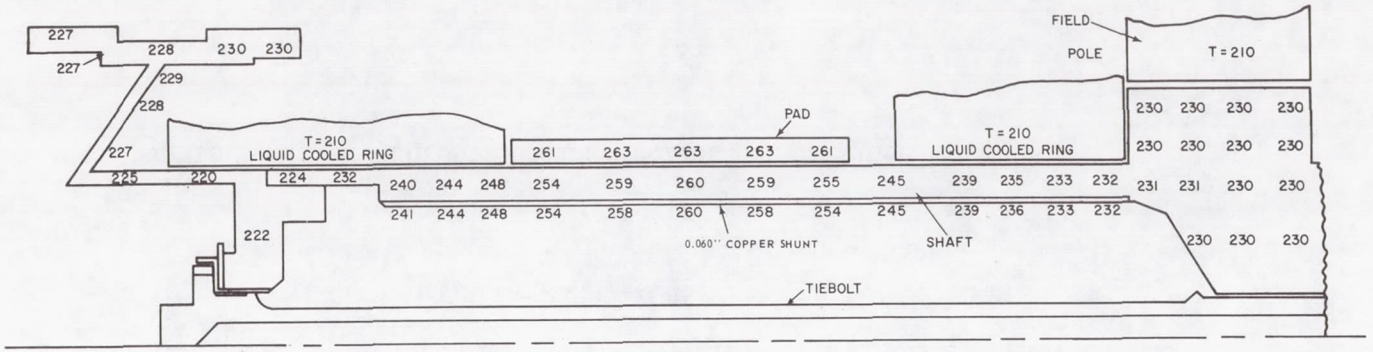

Figure 77 Temperature Map, Number One Bearing, with No Windage or Electrical Losses and No Turbine Heat Input

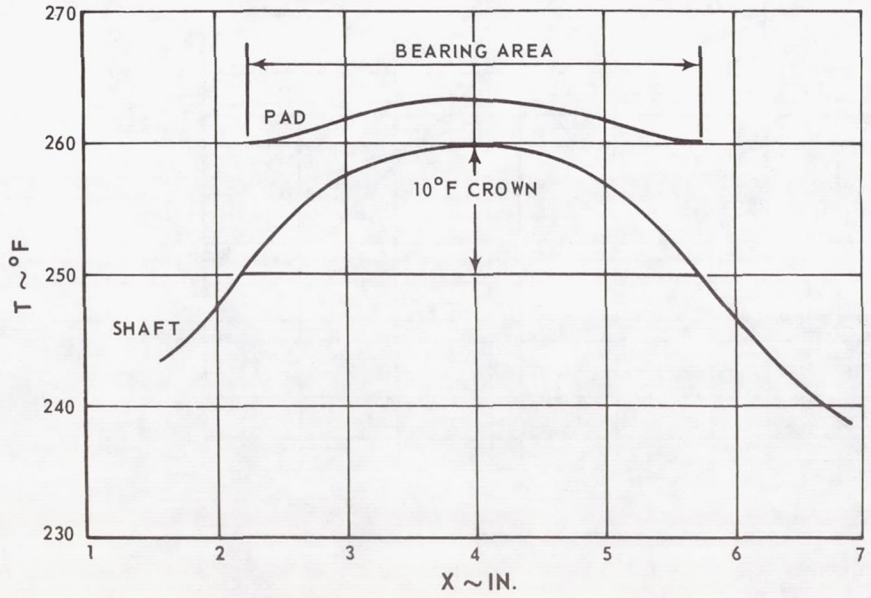

Figure 78 Temperature Distribution, Number One Bearing, with No Windage or Electrical Losses and No Turbine Heat Input

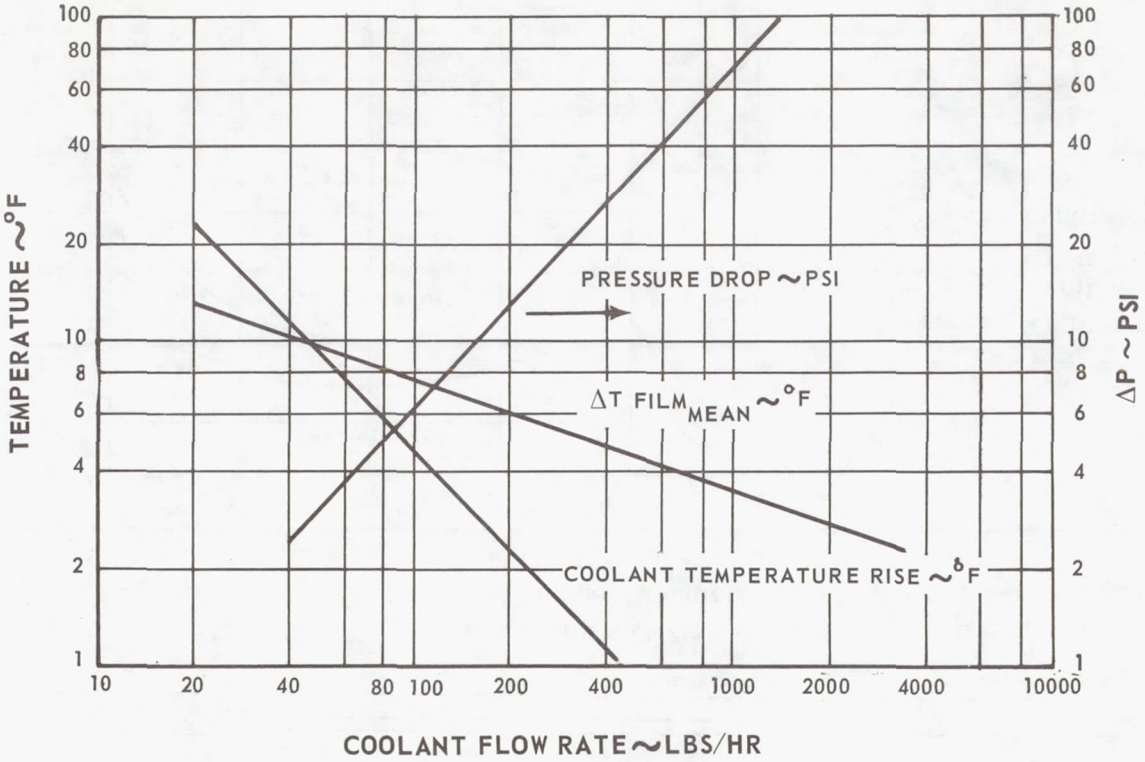

Figure 79 Thrust Bearing Coolant Performance

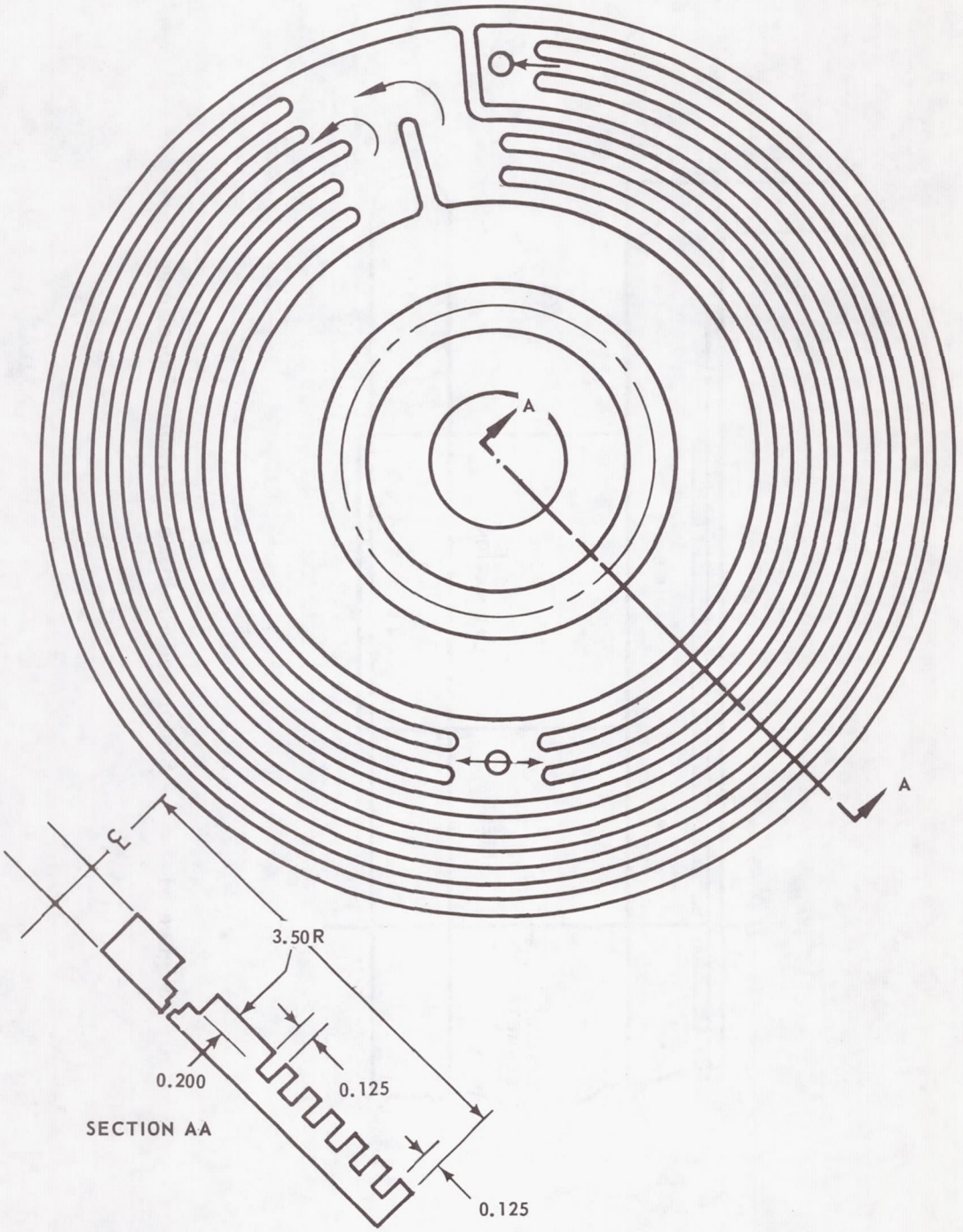

Figure 80 Thrust Plate Coolant Channel Pattern

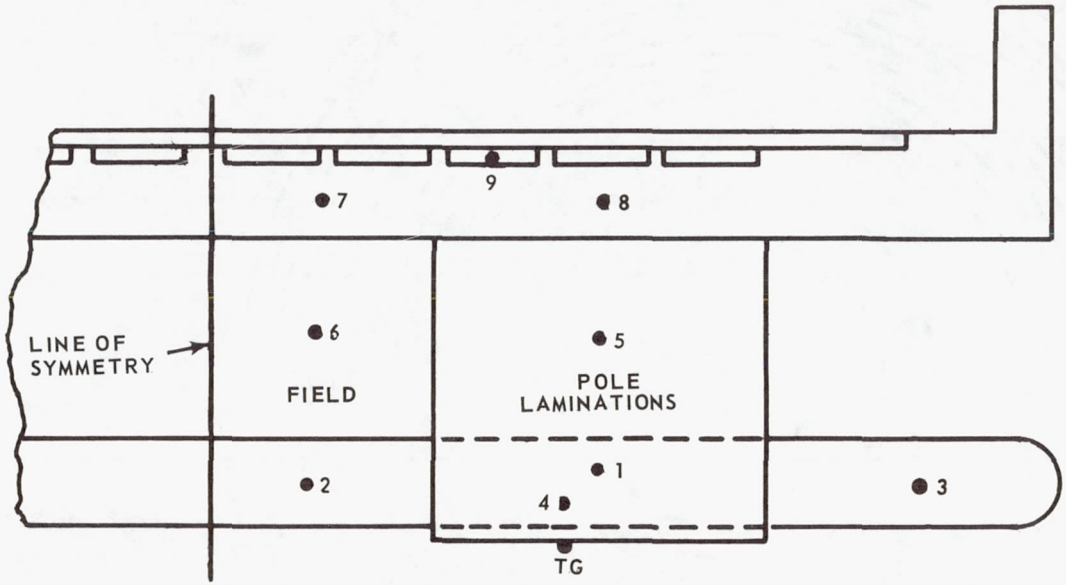

Figure 81 Stator and Field Temperature Locations

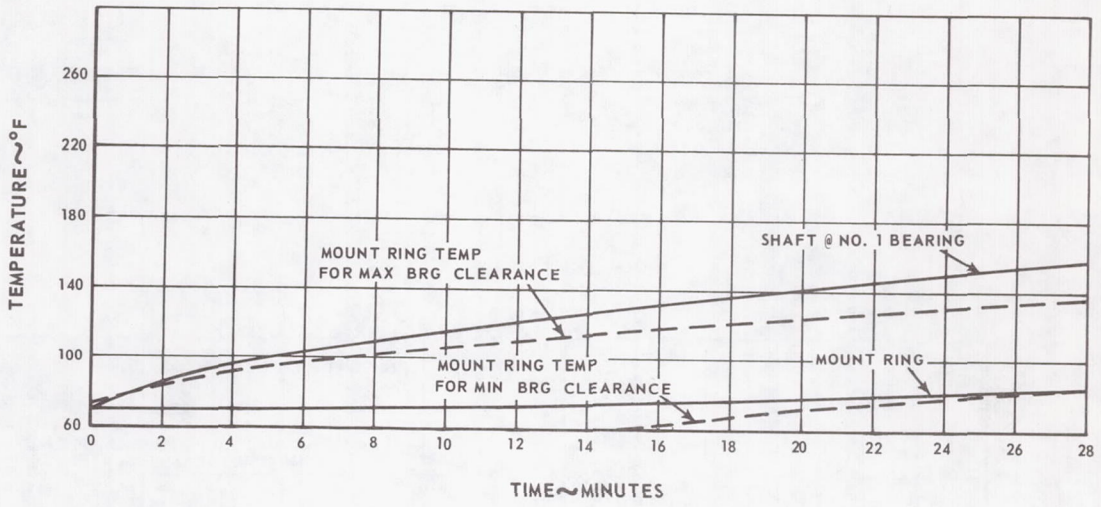

Figure 82 Temperature vs Time for Transient Heat-Up of Number One Bearing, No Coolant Flow

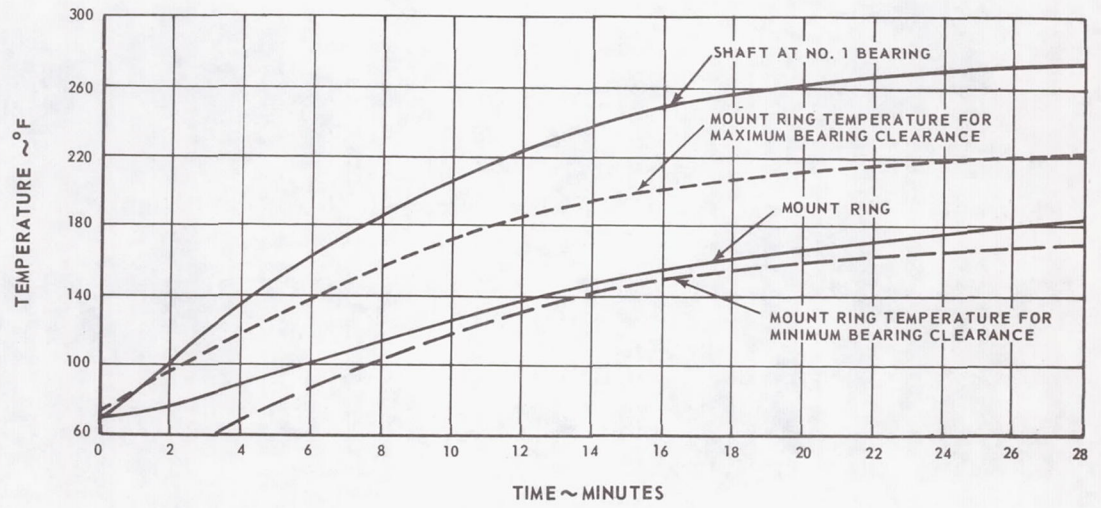

Figure 83 Temperature vs Time for Transient Heat-Up of Number One Bearing, Coolant at 200°F

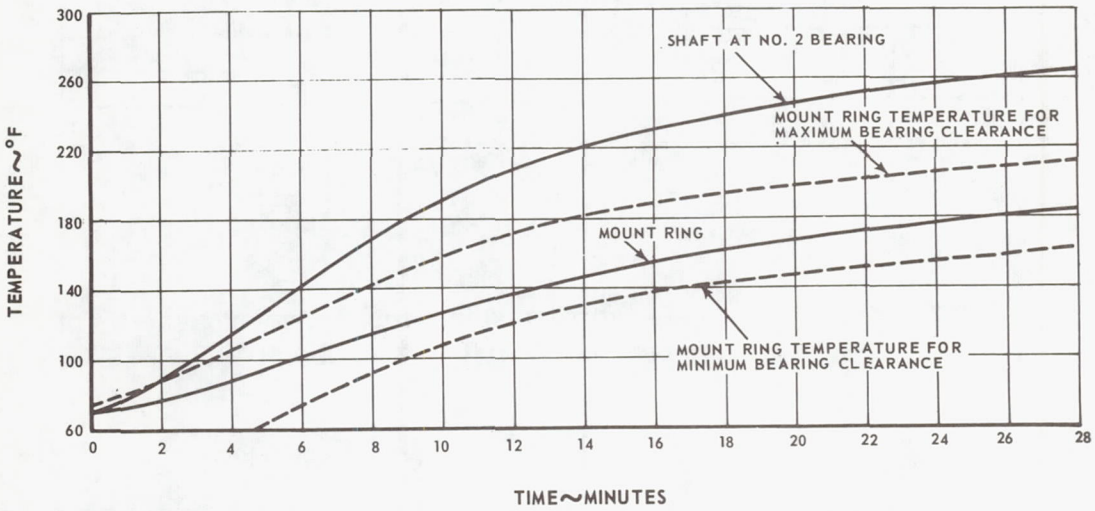

Figure 84 Temperature vs Time for Transient Heat-Up of Number Two Bearing, Coolant at 200° F

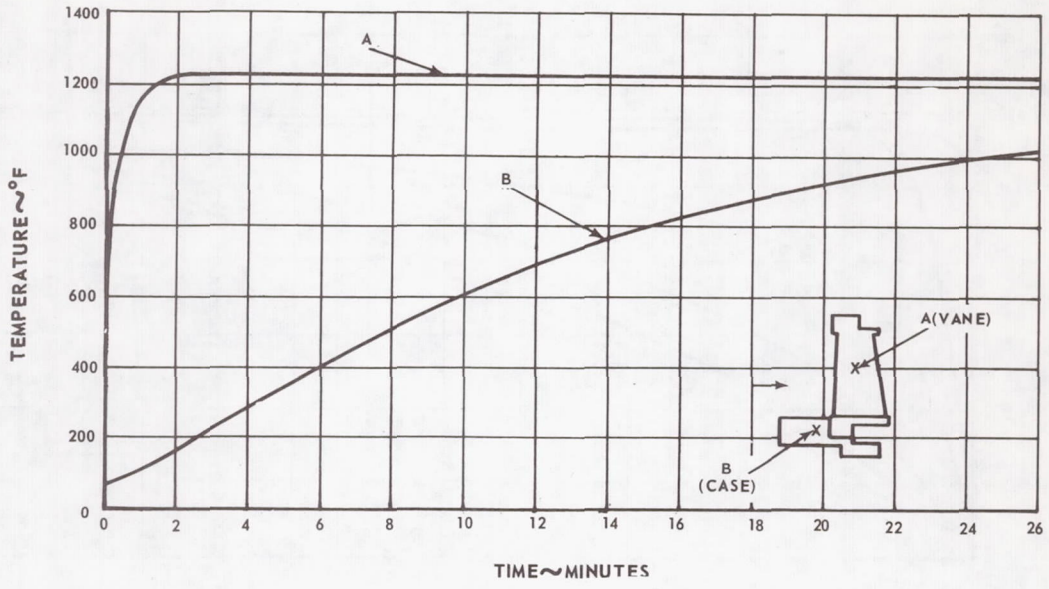

Figure 85 Temperature vs Time, First Stage Turbine Vane Area

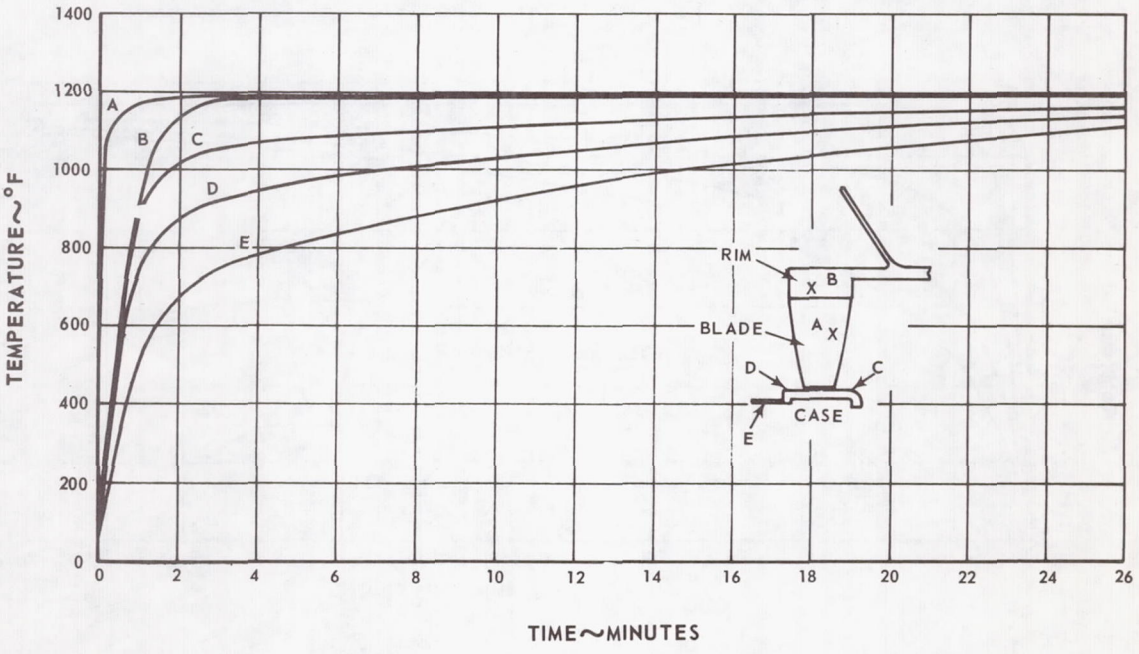

Figure 86 Temperature vs Time, First Stage Turbine Blade Area

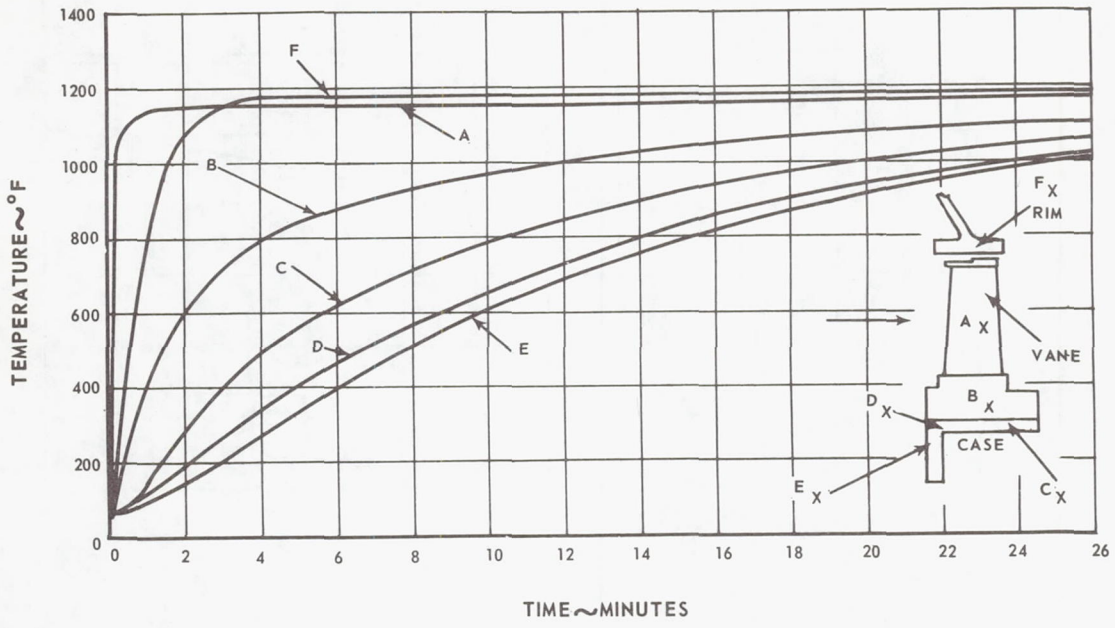

Figure 87 Temperature vs Time, Second Stage Turbine Vane Area

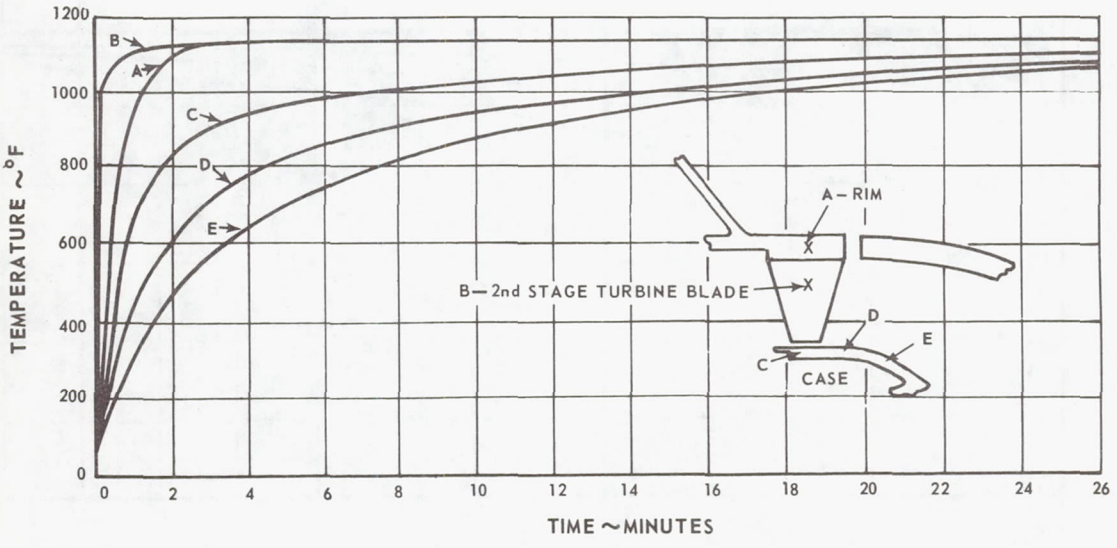

Figure 88 Temperature vs Time, Second Stage Turbine Blade Area

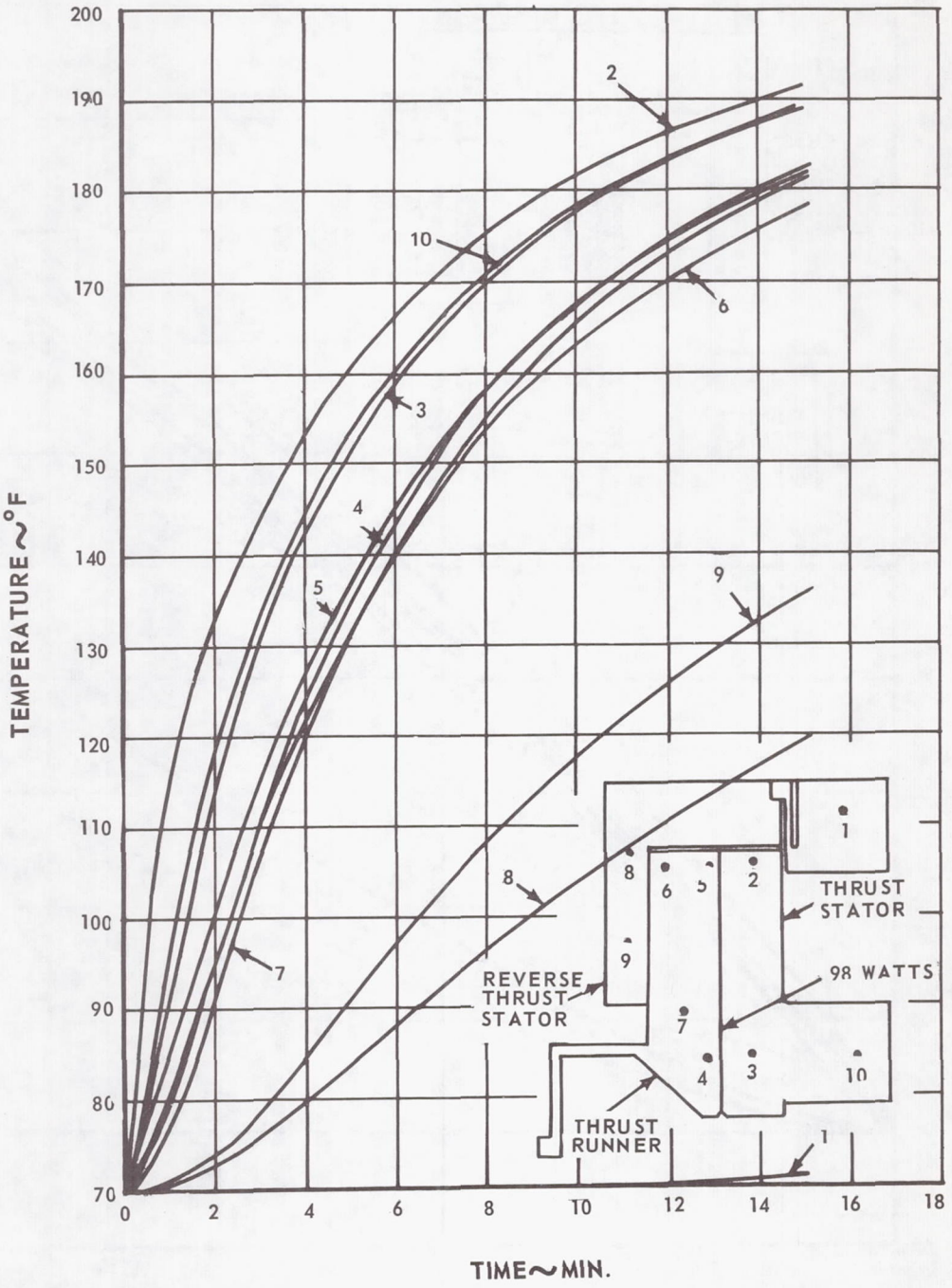

Figure 89 Transient Temperature Response, Thrust Bearing, Coolant at 200° F

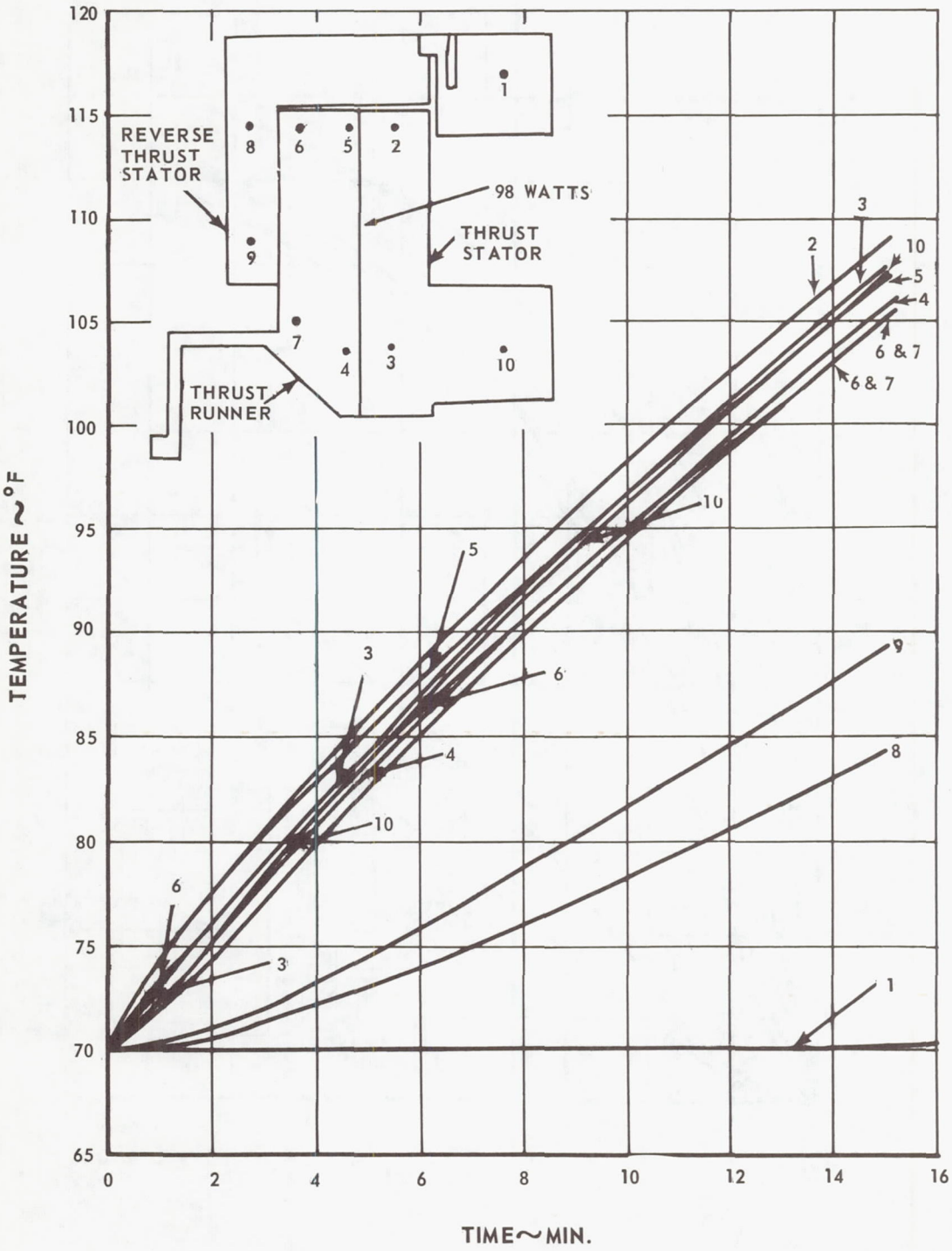

Figure 90 Transient Temperature Response, Thrust Bearing , No Cooling

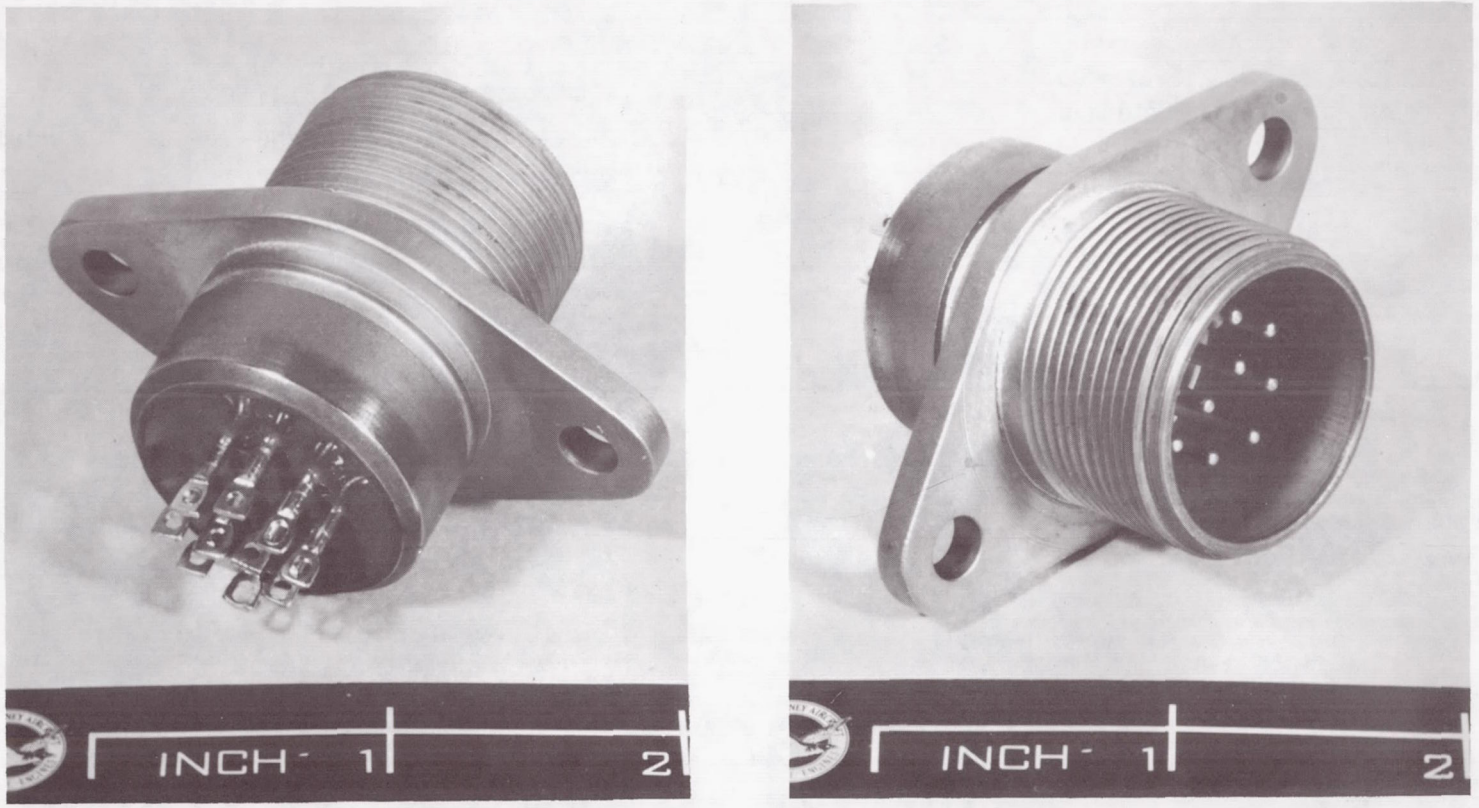

Figure 91 Hermetic Thermocouple Connector (M-42023)

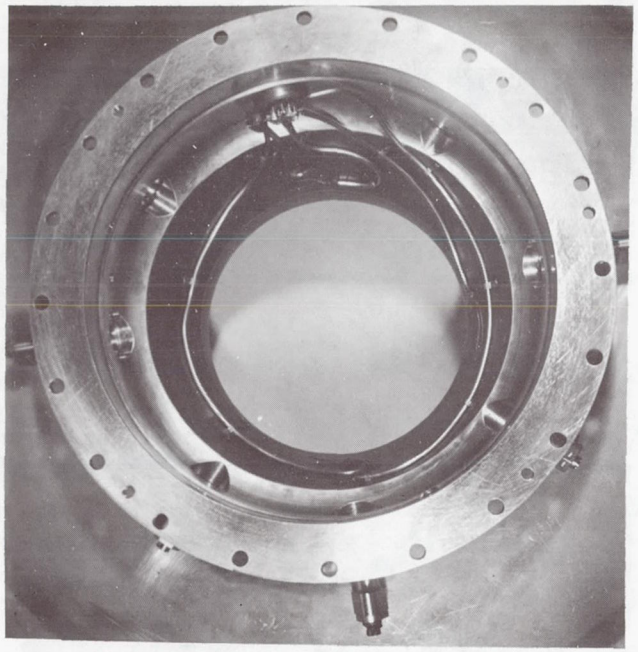

Figure 92 Thermocouples Inside Turbine Scroll Case (CN-9361)

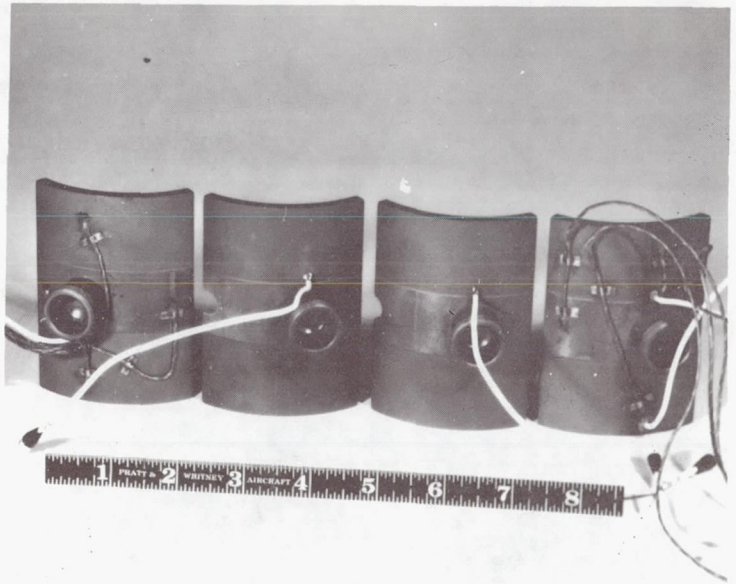

Figure 93 Instrumentation on Journal Pads (X-25650)

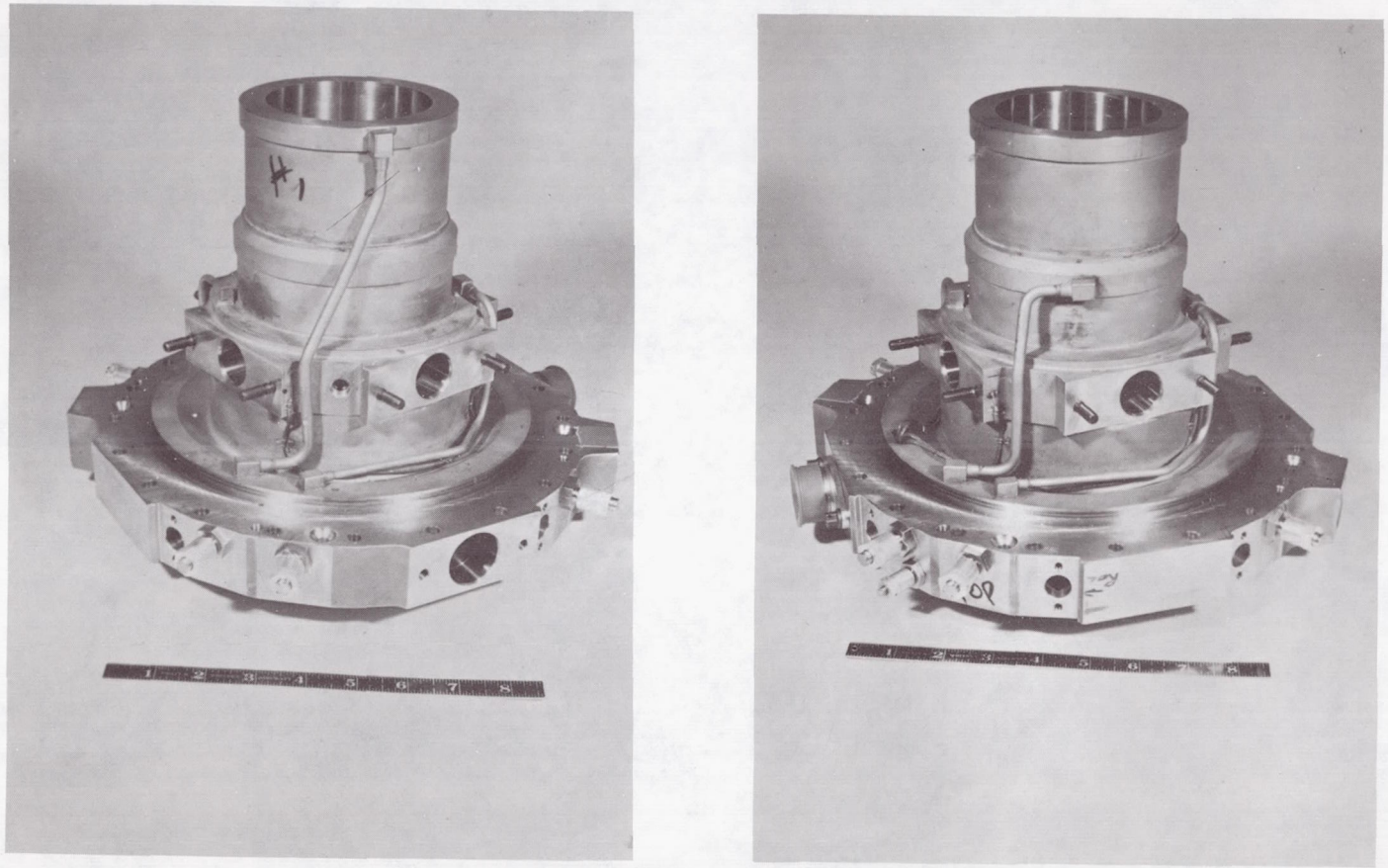

Figure 94 Thermocouples on Number One Bearing Mount Ring (X-25653 & X-25654)

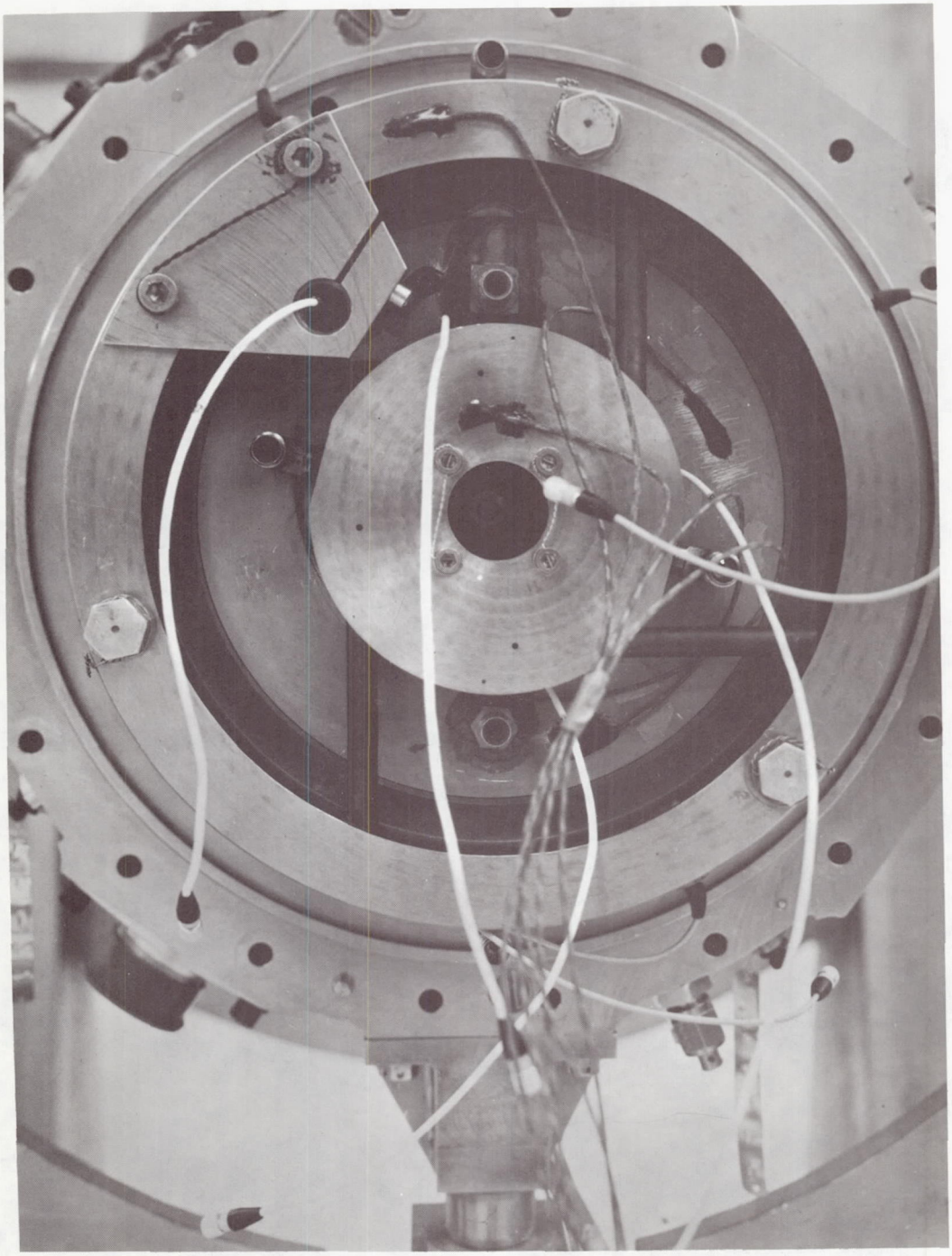

Figure 95 Thermocouples on Main Thrust Stator and Support (X-25912)

1. FRAME INNER DIAMETER
2. STATOR CORE OUTER DIAMETER
3. STATOR TOOTH
4. D.E. END TURN
5. D.E. END TURN (180° FROM (4) ABOVE)
6. FRAME INNER DIAMETER
7. 180° BUS ON END CONNECTIONS
8. 180° BUS ON END CONNECTIONS (OPPOSITE (7) ABOVE)
9. STATOR TOOTH
10. A.D.E. END TURNS

Figure 96 Stator Thermocouple Locations

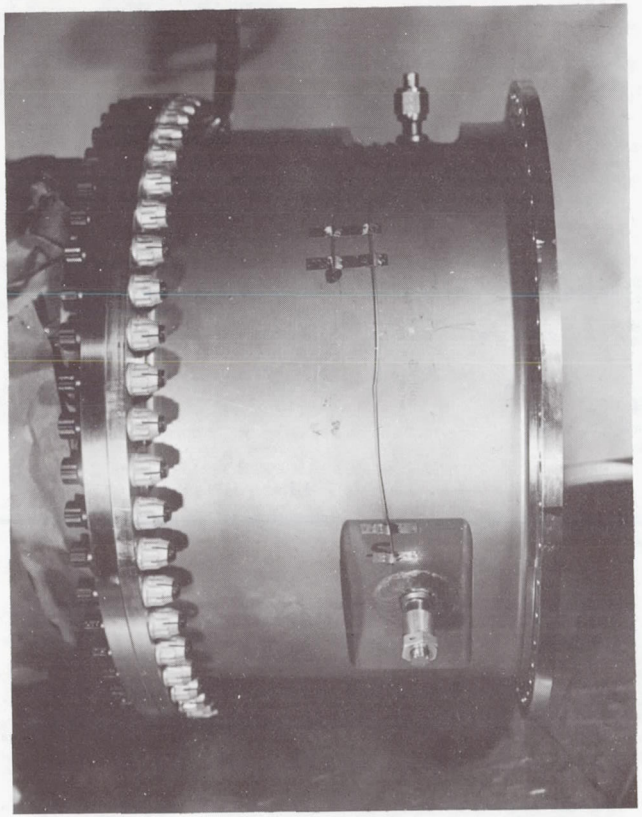

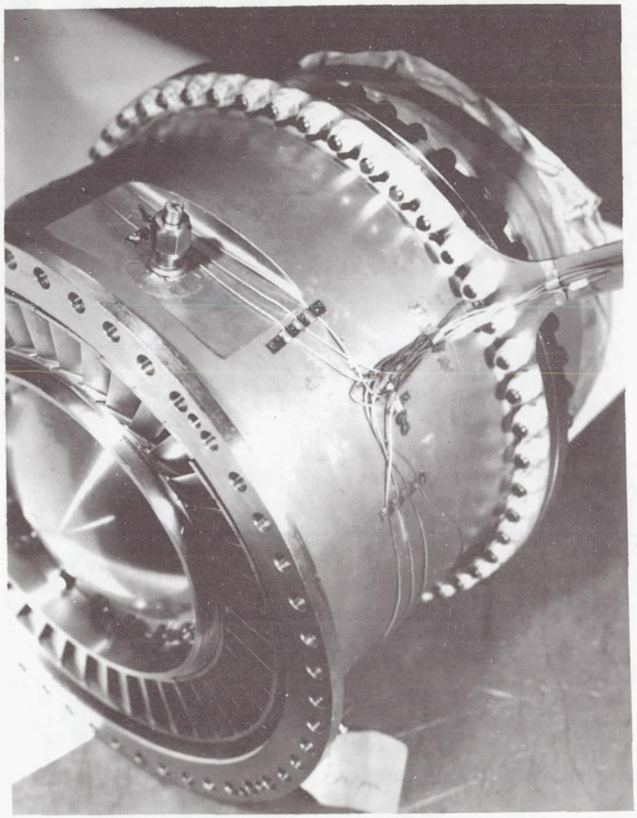

Figure 97 Thermocouples on Turbine Inlet Case (CN-9915 & CN-9916)

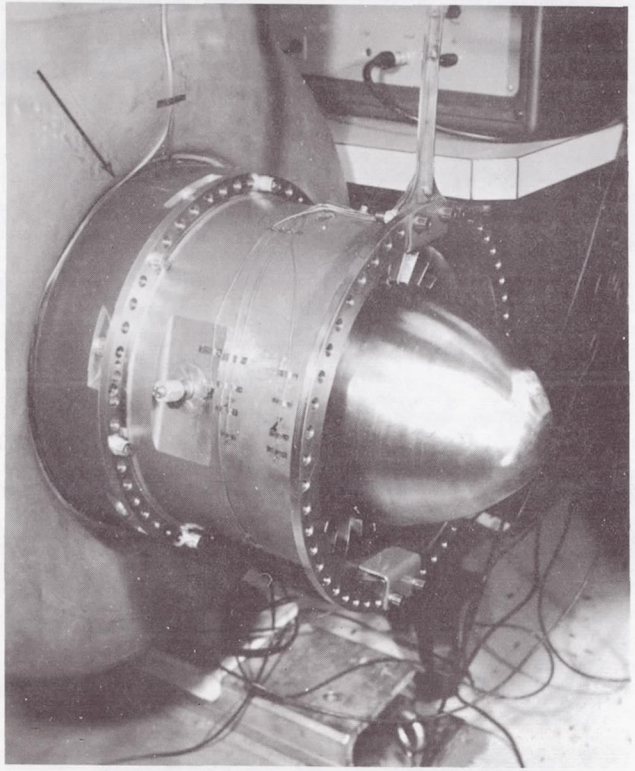

Figure 98 Thermocouples on First Stage Rotor Shroud (CN-10123)

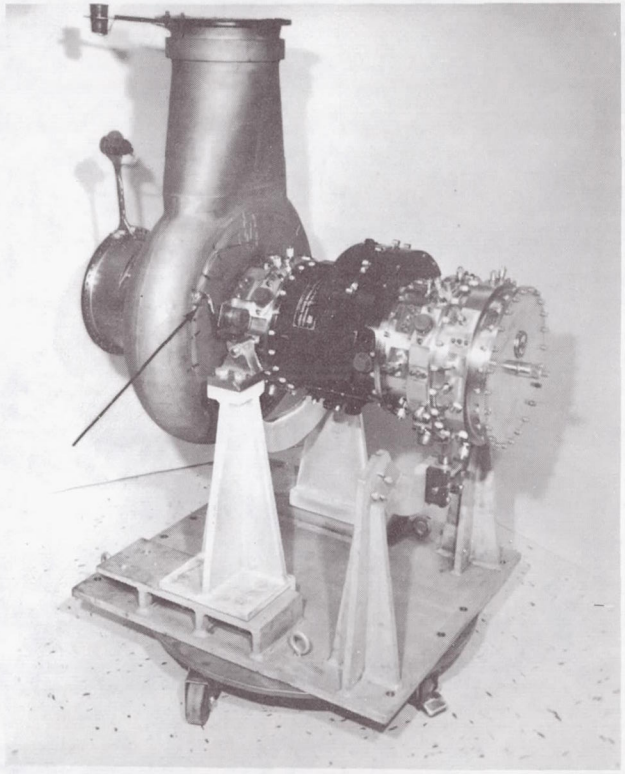

Figure 99 Thermocouples on Turbine Scroll Rear Wall (CN-10125)

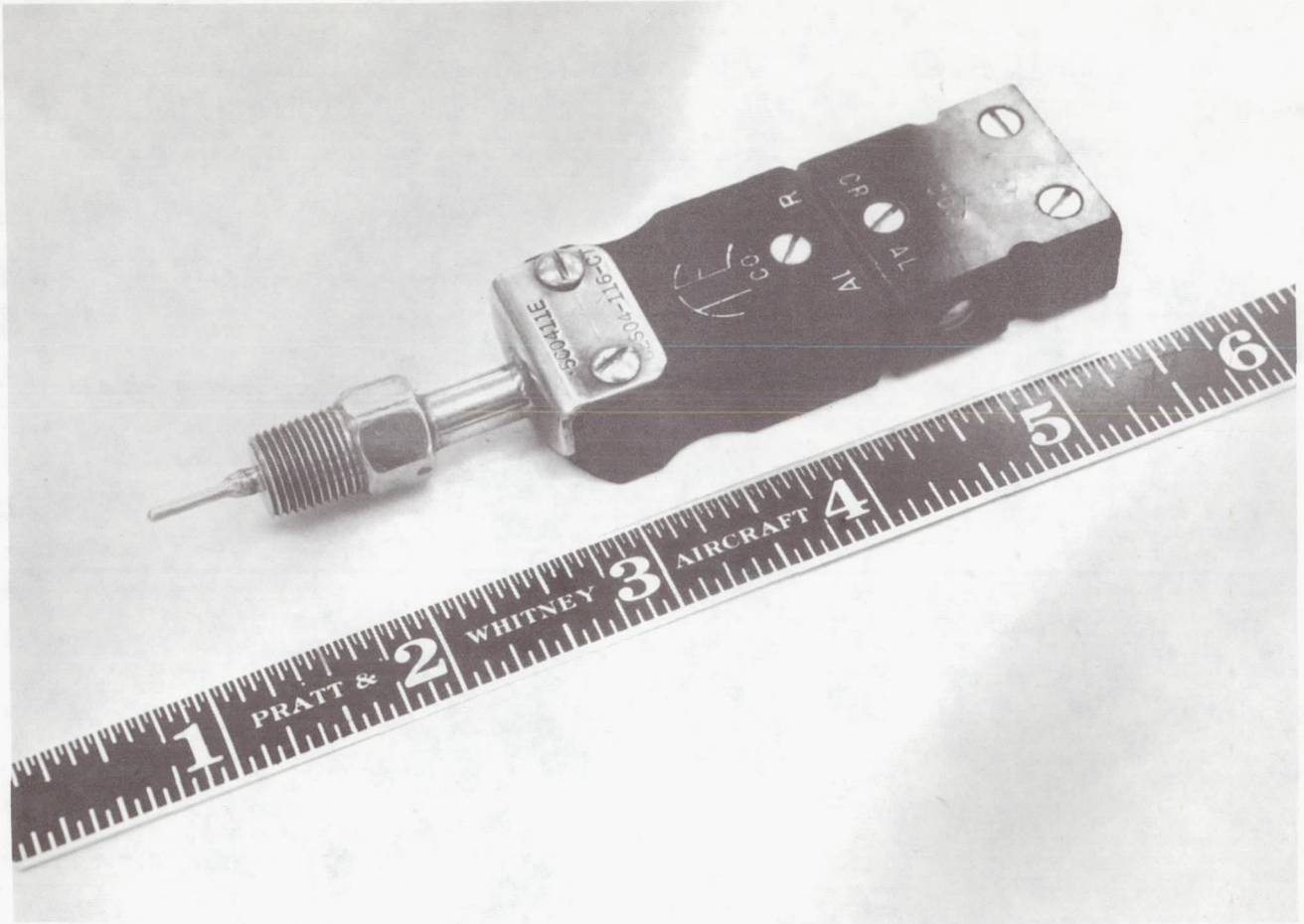

Figure 100 Stator Coolant Thermocouple (X-25906)

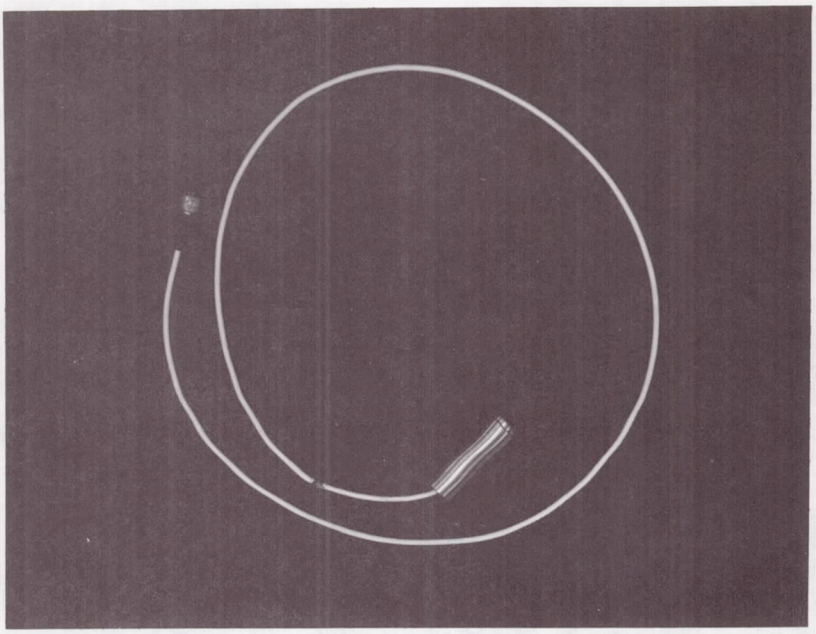

Figure 101 Ground-to-Main-Thrust-Plate Capacitance Probe (CN-10282)

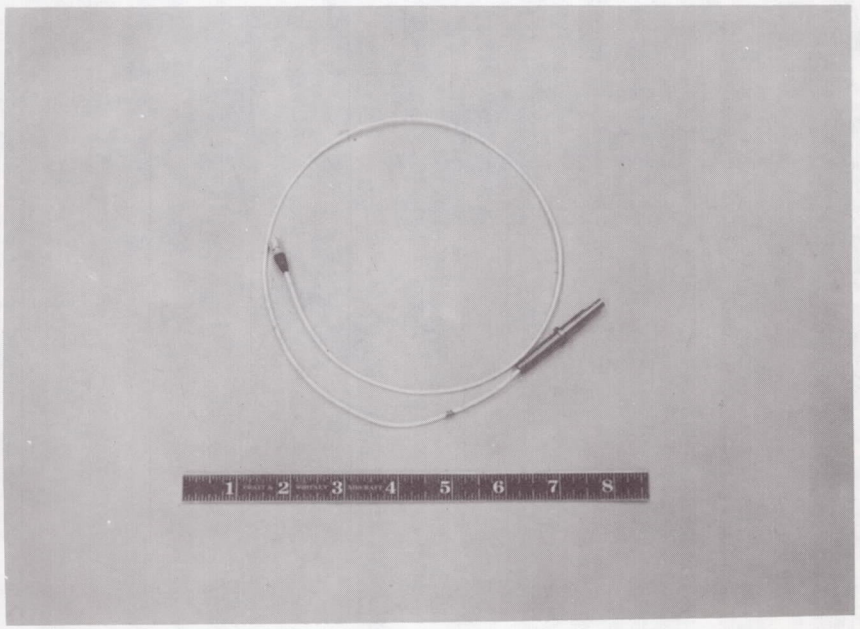

Figure 102 Ground-to-Shaft Capacitance Probe (X-25911)

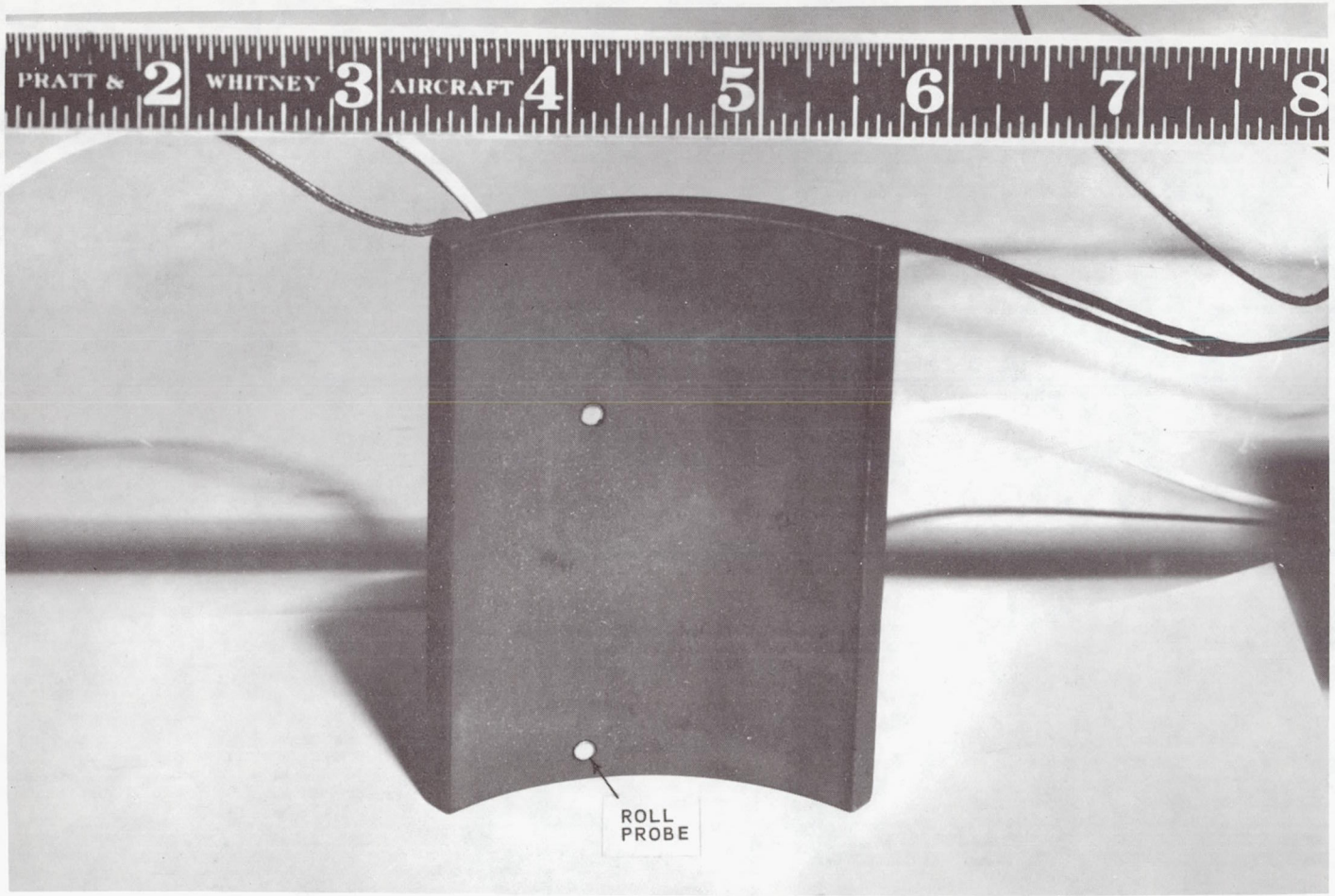

Figure 103 Journal Pad, Showing Roll Probe (X-25643)

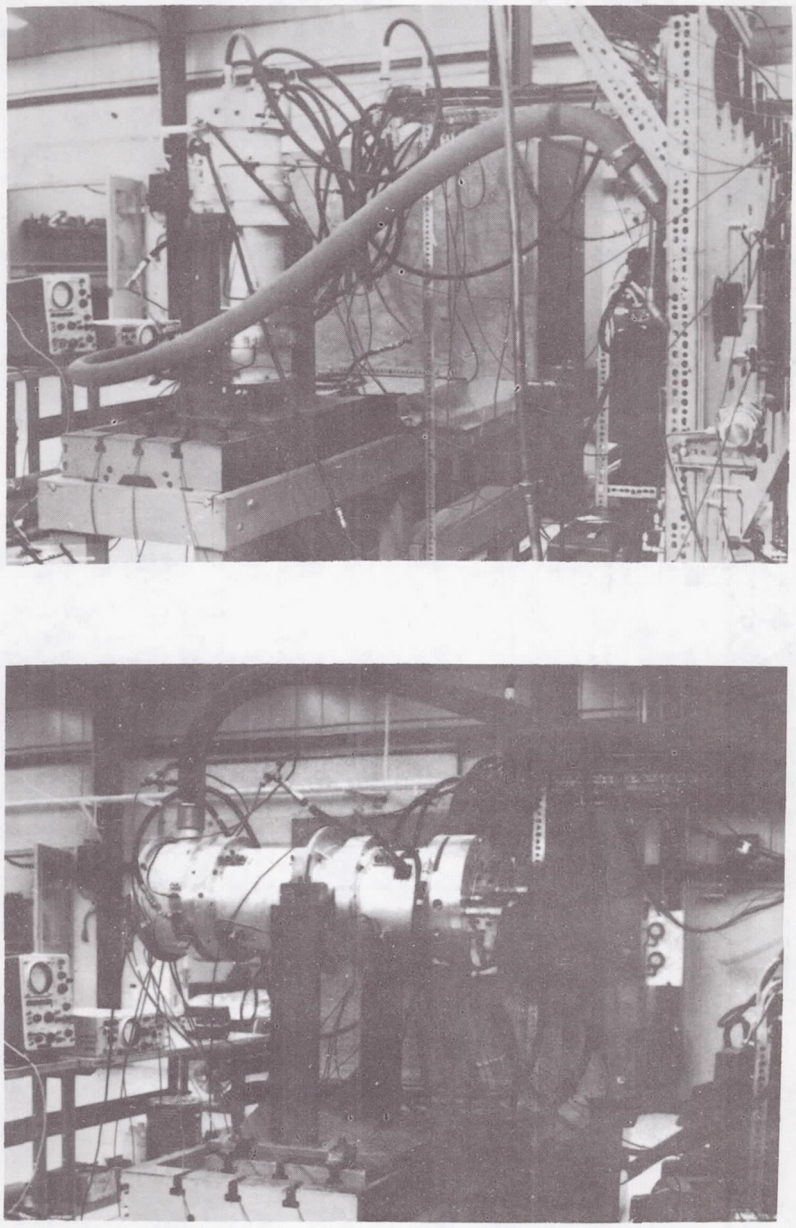

Figure 104 Gas Bearing Dynamic Simulator (M-36203)

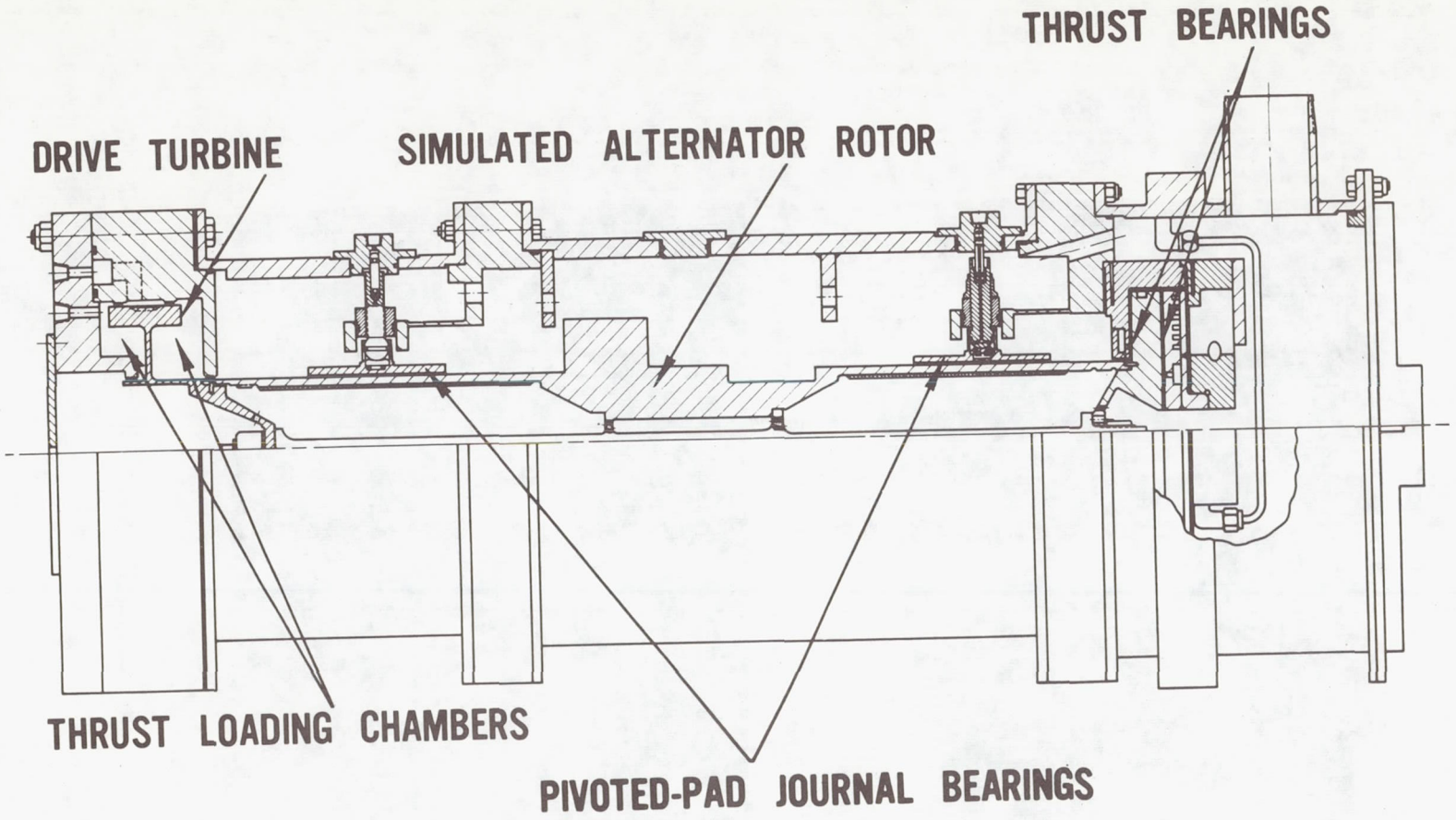

Figure 105 Gas Bearing Rotor Dynamic Simulator (Initial) (M-36920)

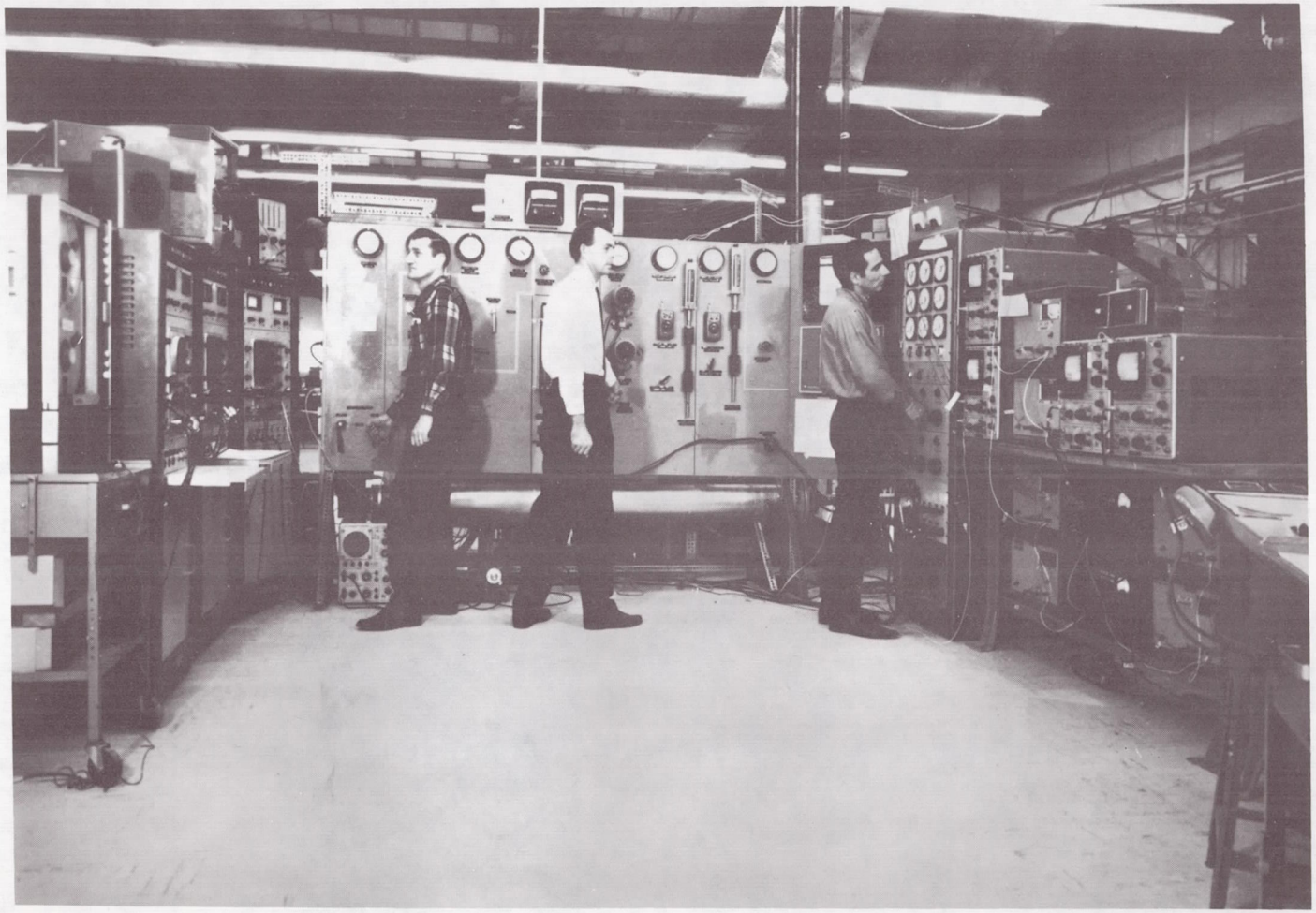

Figure 106 Simulator Test Facility at MTI

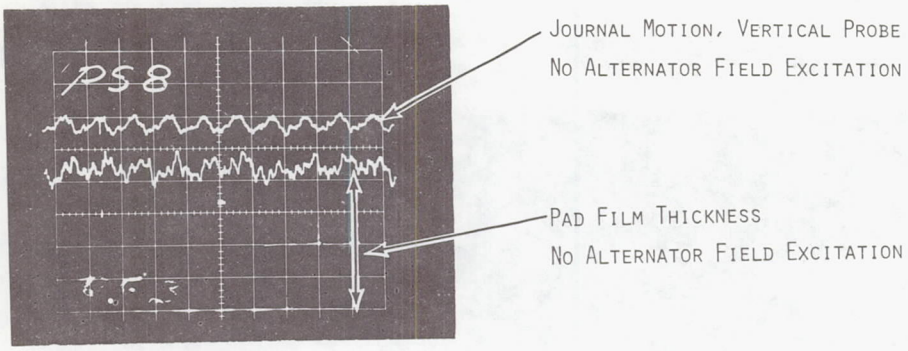

(A)

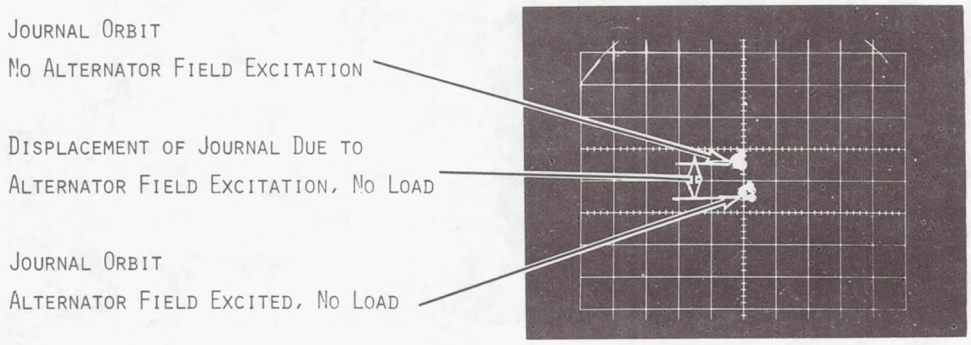

(B)

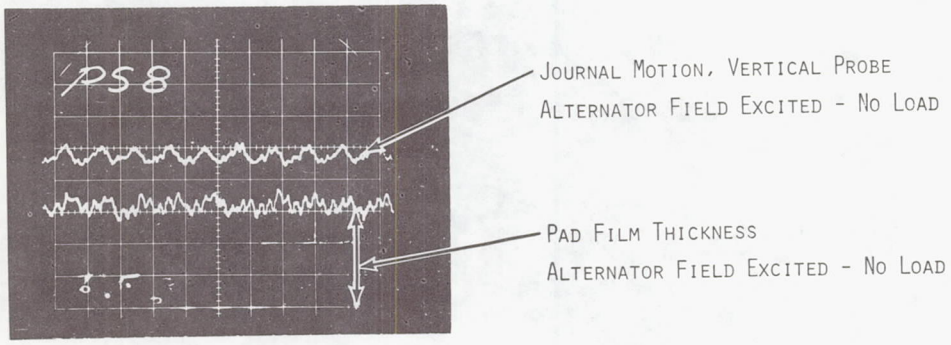

(C)

SENSITIVITY - JOURNAL TRACES AND ORBITS 0.32×10^{-3} INCHES/MAJOR DIVISION
SENSITIVITY - PAD TRACES 0.153×10^{-3} INCHES/MAJOR DIVISION
TIME BASE - ALL TRACES 5×10^{-3} SECS/MAJOR DIVISION

Figure 107 Simulator Turbine End Journal Bearing Performance at 12,000 rpm and 7.2 psia Ambient Pressure Rotor Horizontal and Eccentric by 0.003 - 0.004 Inches

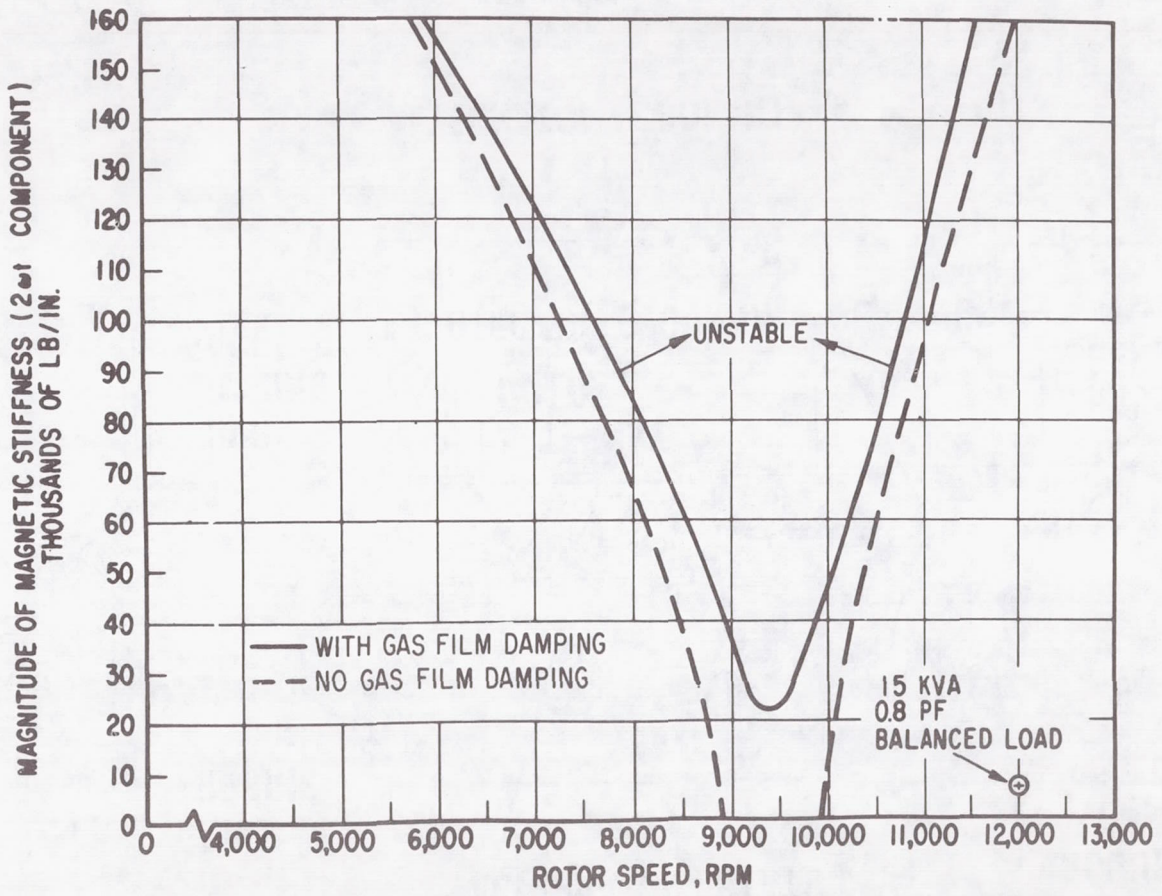

Figure 108 Calculated Stability Map for the Rotor-Bearing System

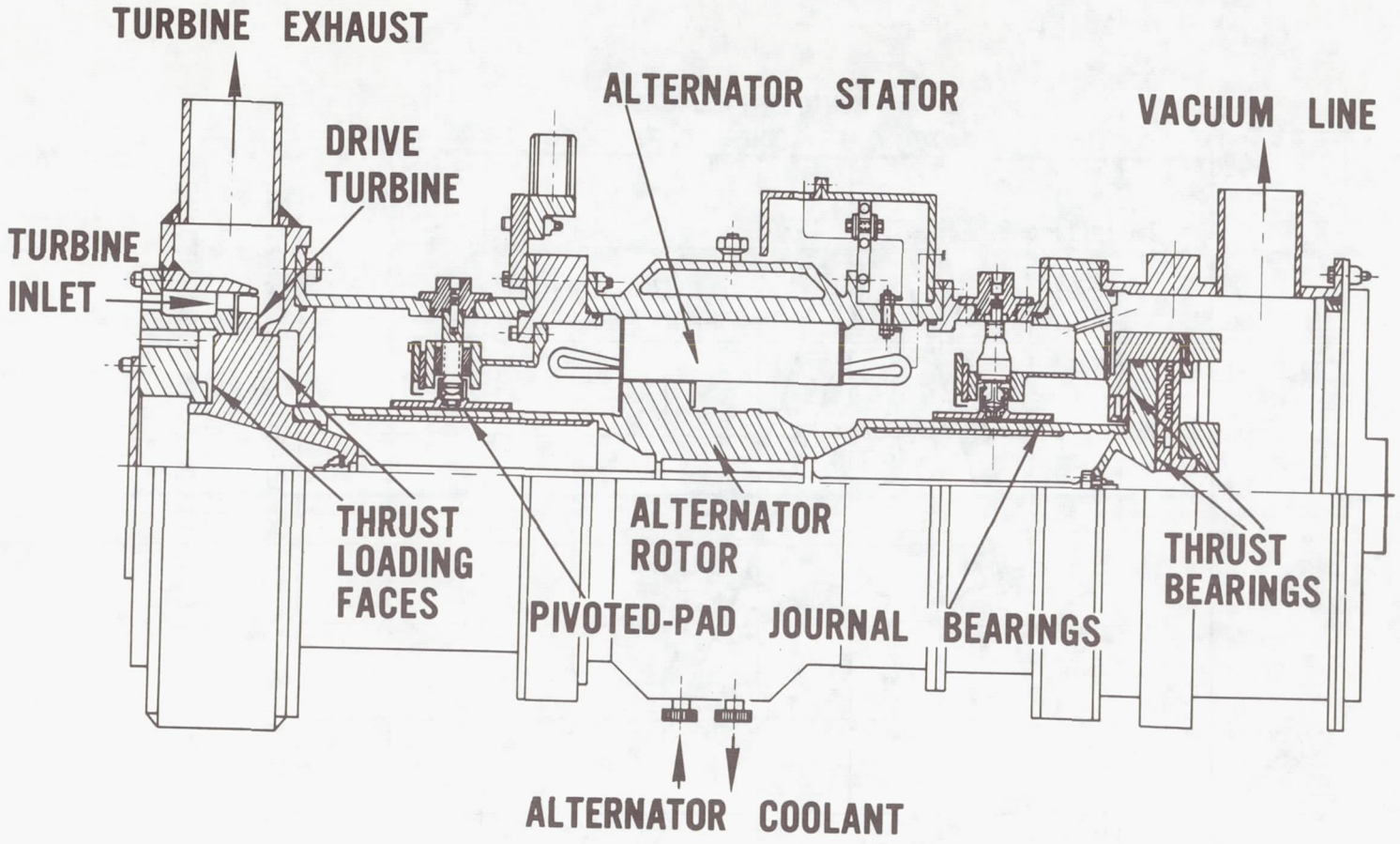

Figure 109 Gas Bearing Rotor Dynamic Simulator with Alternator (Final Configuration) (M-44248)

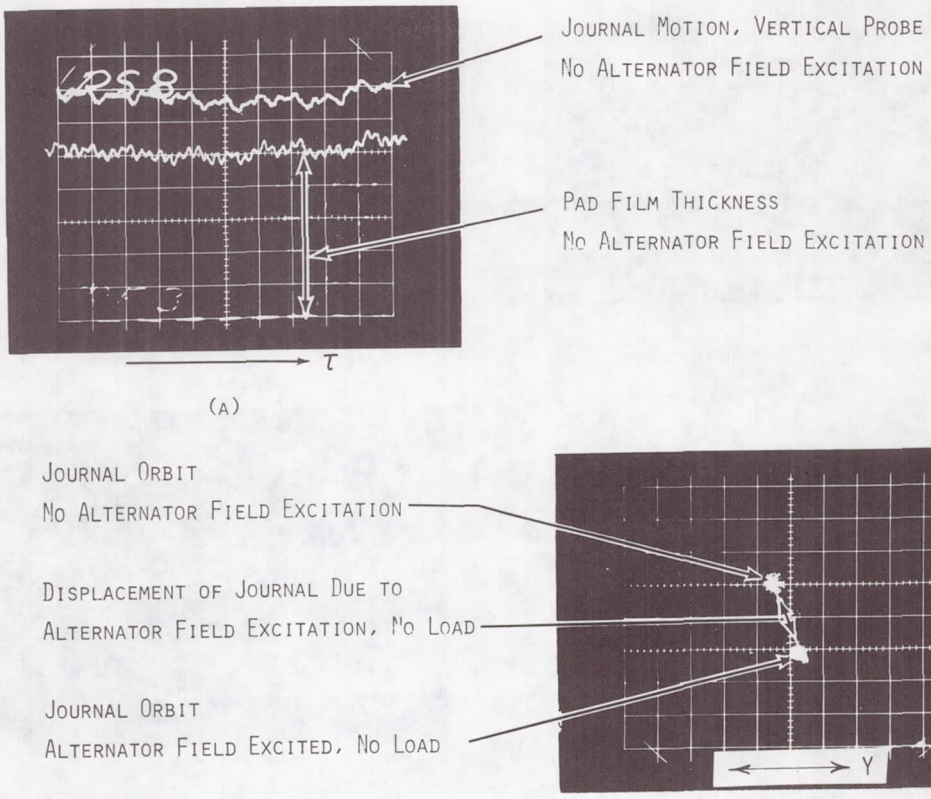

Figure 110 Simulator Turbine End Journal Bearing Performance at 12,000 rpm and 7.2 psia Ambient Pressure, Rotor Vertical and Eccentric by 0.002 - 0.003 Inches

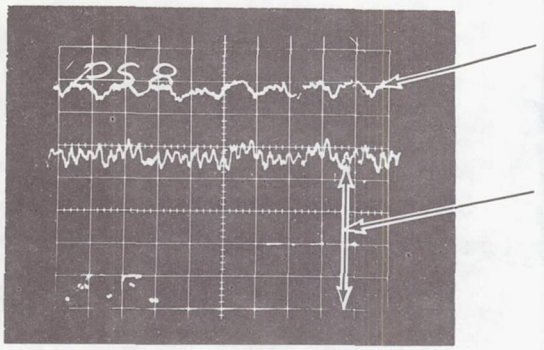

JOURNAL MOTION, VERTICAL PROBE
12 KW - 3 PHASE - 0.8 PF

PAD FILM THICKNESS
12 KW - 3 PHASE - 0.8 PF

(A)

JOURNAL MOTION, VERTICAL PROBE
DURING A SINGLE PHASE SHORT CIRCUIT

PAD FILM THICKNESS
DURING A SINGLE PHASE SHORT CIRCUIT

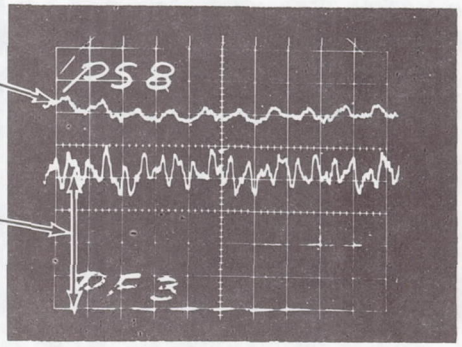

(B)

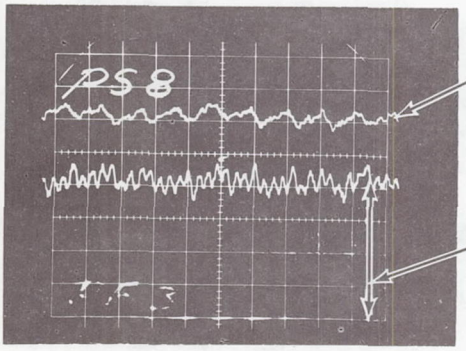

JOURNAL MOTION, VERTICAL PROBE
DURING A THREE PHASE SHORT CIRCUIT

PAD FILM THICKNESS
DURING A THREE PHASE SHORT CIRCUIT

(C)

SENSITIVITY - JOURNAL TRACES AND ORBITS 0.28×10^{-3} INCHES/MAJOR DIVISION
SENSITIVITY - PAD TRACES 0.153×10^{-3} INCHES/MAJOR DIVISION
TIME BASE - ALL TRACES 5×10^{-3} SECS/MAJOR DIVISION

Figure 111 **Simulator Turbine End Journal Bearing Performance at 12,000 rpm and 7.2 psia Ambient Pressure, Rotor Vertical and Eccentric by 0.002 - 0.003 Inches**

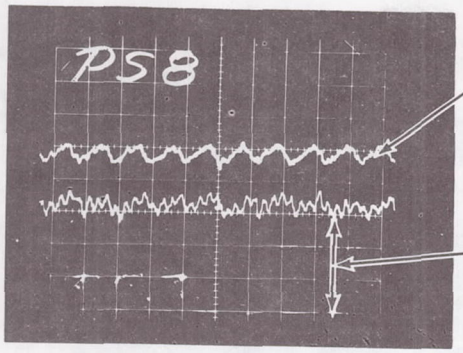

JOURNAL MOTION, VERTICAL PROBE
12 KW - 3 PHASE - 0.8 PF

PAD FILM THICKNESS
12 KW - 3 PHASE - 0.8 PF

(A)

JOURNAL ORBIT
12 KW - 3 PHASE - 0.8 PF

JOURNAL ORBIT DURING SINGLE
PHASE SHORT CIRCUIT

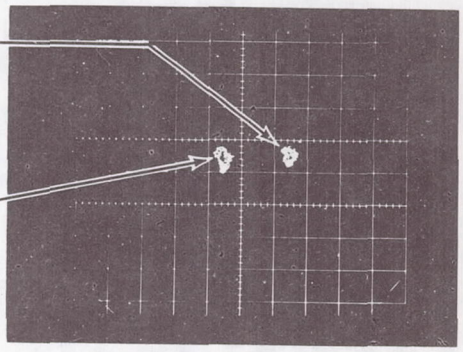

(B)

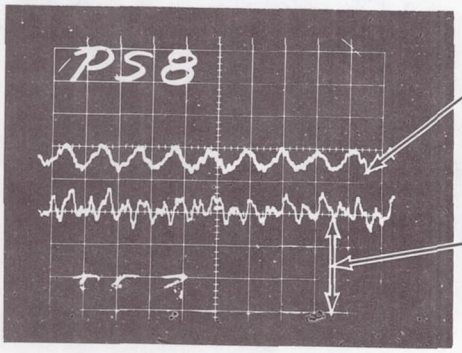

JOURNAL MOTION, VERTICAL PROBE
DURING SINGLE PHASE SHORT CIRCUIT

PAD FILM THICKNESS DURING SINGLE
PHASE SHORT CIRCUIT

(C)

SENSITIVITY - JOURNAL TRACES AND ORBITS 0.32×10^{-3} INCHES/MAJOR DIVISION
SENSITIVITY - PAD TRACES 0.153×10^{-3} INCHES/MAJOR DIVISION
TIME BASE - ALL TRACES 5×10^{-3} SECS/MAJOR DIVISION

Figure 112 Simulator Turbine End Journal Bearing Performance at 12,000 rpm and 7.2 psia Ambient Pressure, Rotor Horizontal and Eccentric by 0.003 - 0.004 Inches

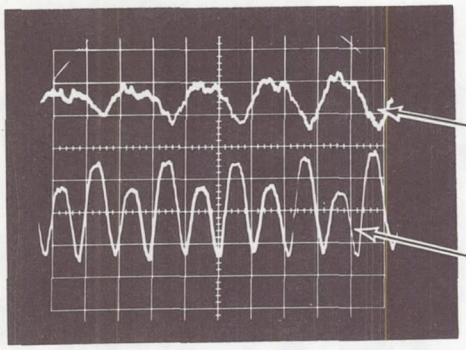

JOURNAL MOTION DURING LABYRINTH RUB AND 3 PHASE SHORT CIRCUIT

HORIZONTAL PROBE

VERTICAL PROBE

(A)

JOURNAL ORBIT BEFORE LABYRINTH RUB
12 KW - 3 PHASE - 0.8 PF

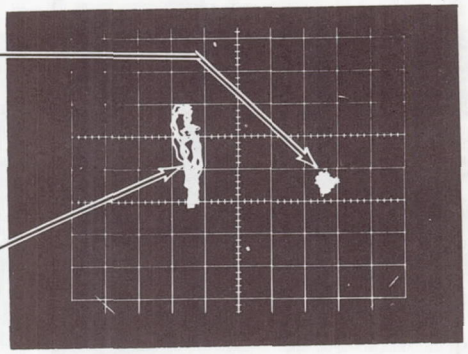

JOURNAL ORBIT DURING LABYRINTH RUB AND 3 PHASE SHORT CIRCUIT

(B)

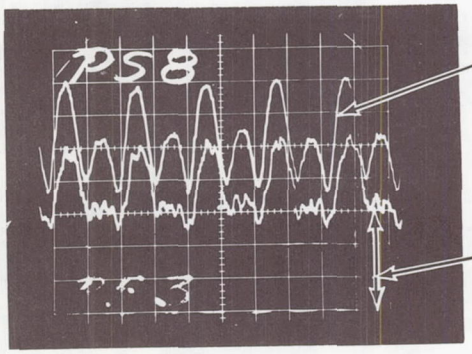

JOURNAL MOTION DURING LABYRINTH RUB AND 3 PHASE SHORT CIRCUIT

VERTICAL PROBE

PAD FILM THICKNESS DURING LABYRINTH RUB AND 3 PHASE SHORT CIRCUIT

(C)

SENSITIVITY - JOURNAL TRACES AND ORBITS - 0.32×10^{-3} INCHES/MAJOR DIVISION
SENSITIVITY - PAD TRACES 0.153×10^{-3} INCHES/MAJOR DIVISION
TIME BASE - ALL TRACES 5×10^{-3} SECS/MAJOR DIVISION

Figure 113 Simulator Turbine End Journal Bearing Performance at 12,000 rpm and 7.2 psia Ambient Pressure, Rotor Horizontal and Eccentric by 0.003 - 0.004 Inches

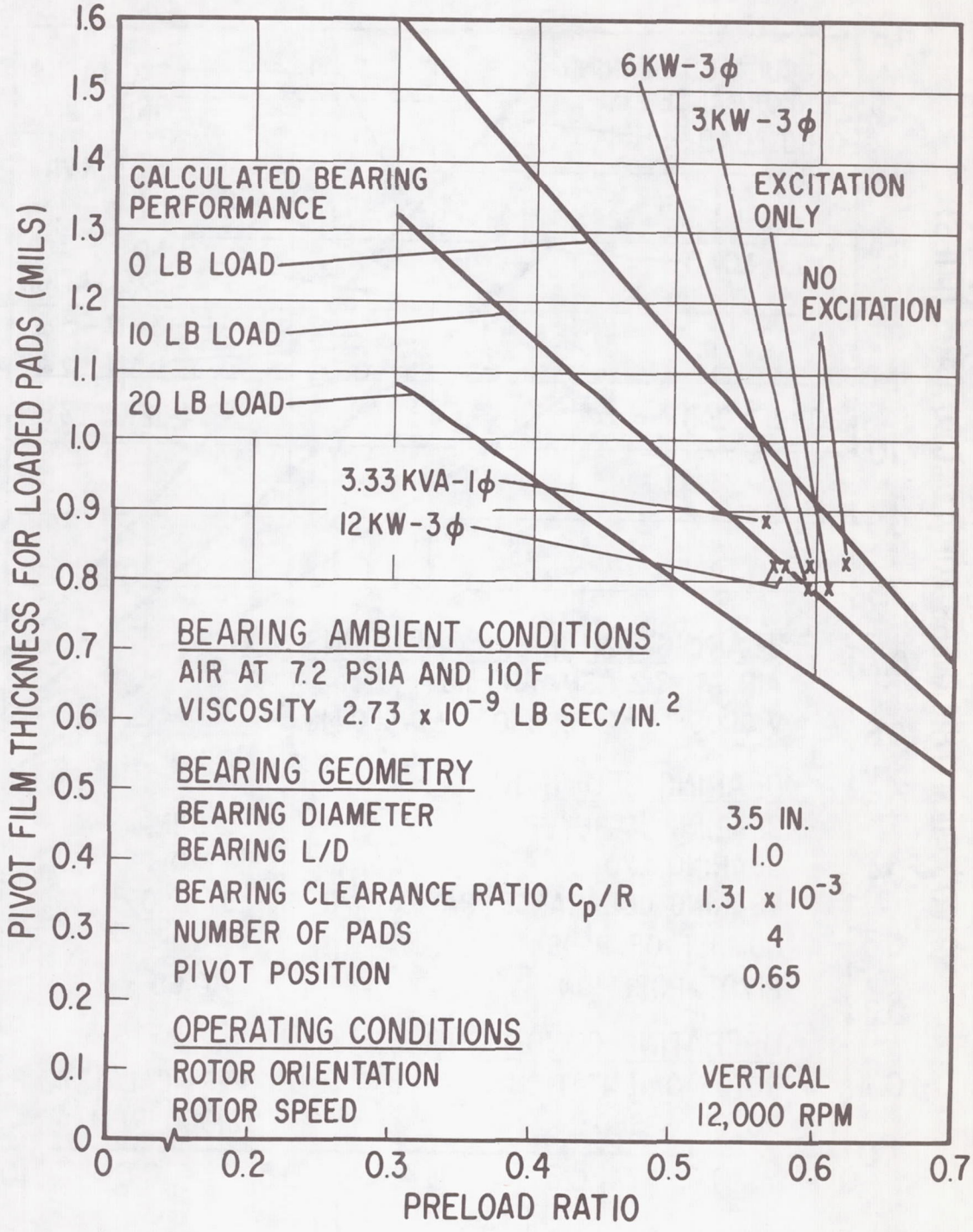

Figure 114 Calculated and Experimental Performance of the Journal Bearing Adjacent to the Thrust Bearing at High Preloads, Rotor Vertical

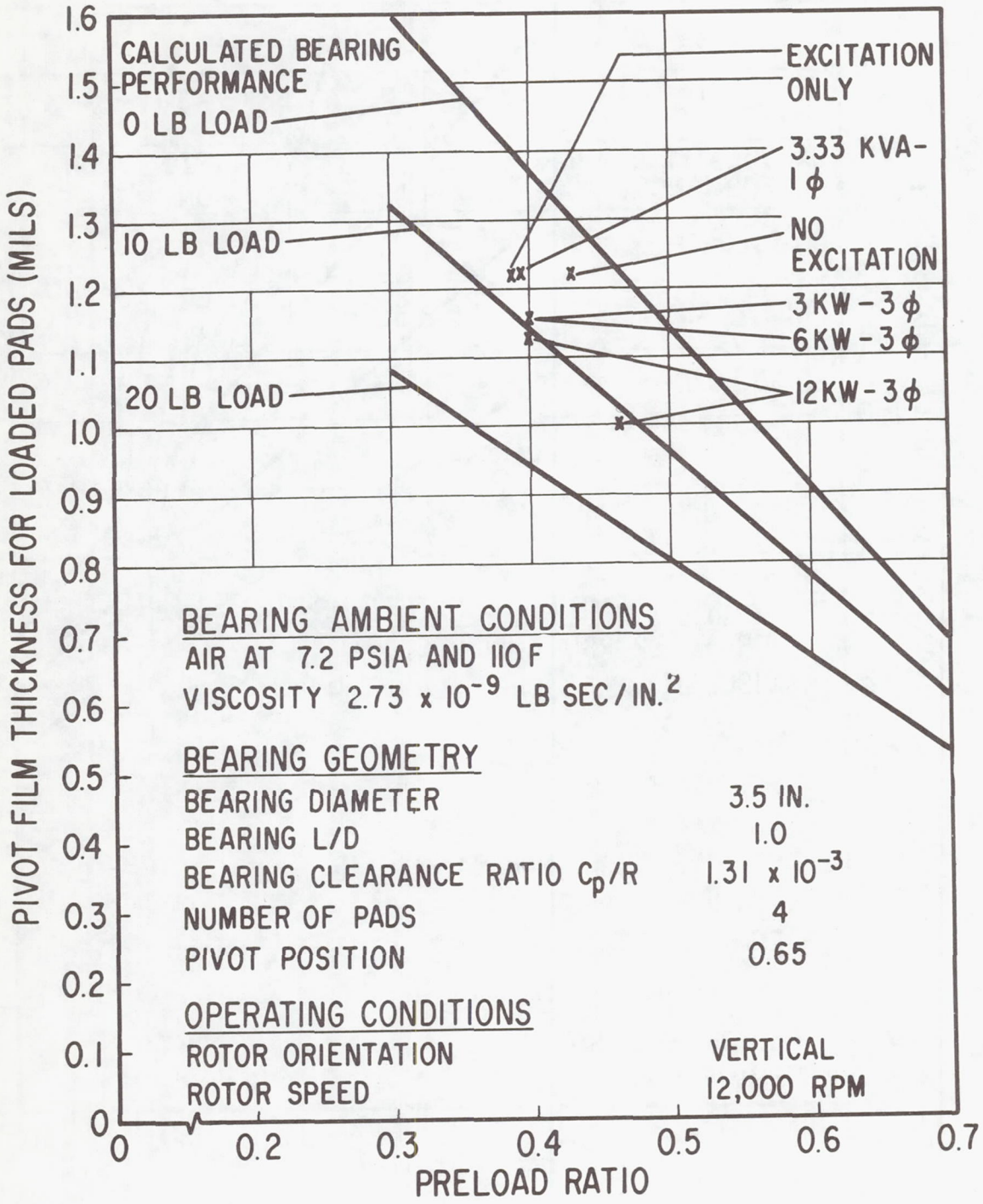

Figure 115 Calculated and Experimental Performance of the Journal Bearing Adjacent to the Thrust Bearing at Low Preloads, Rotor Vertical

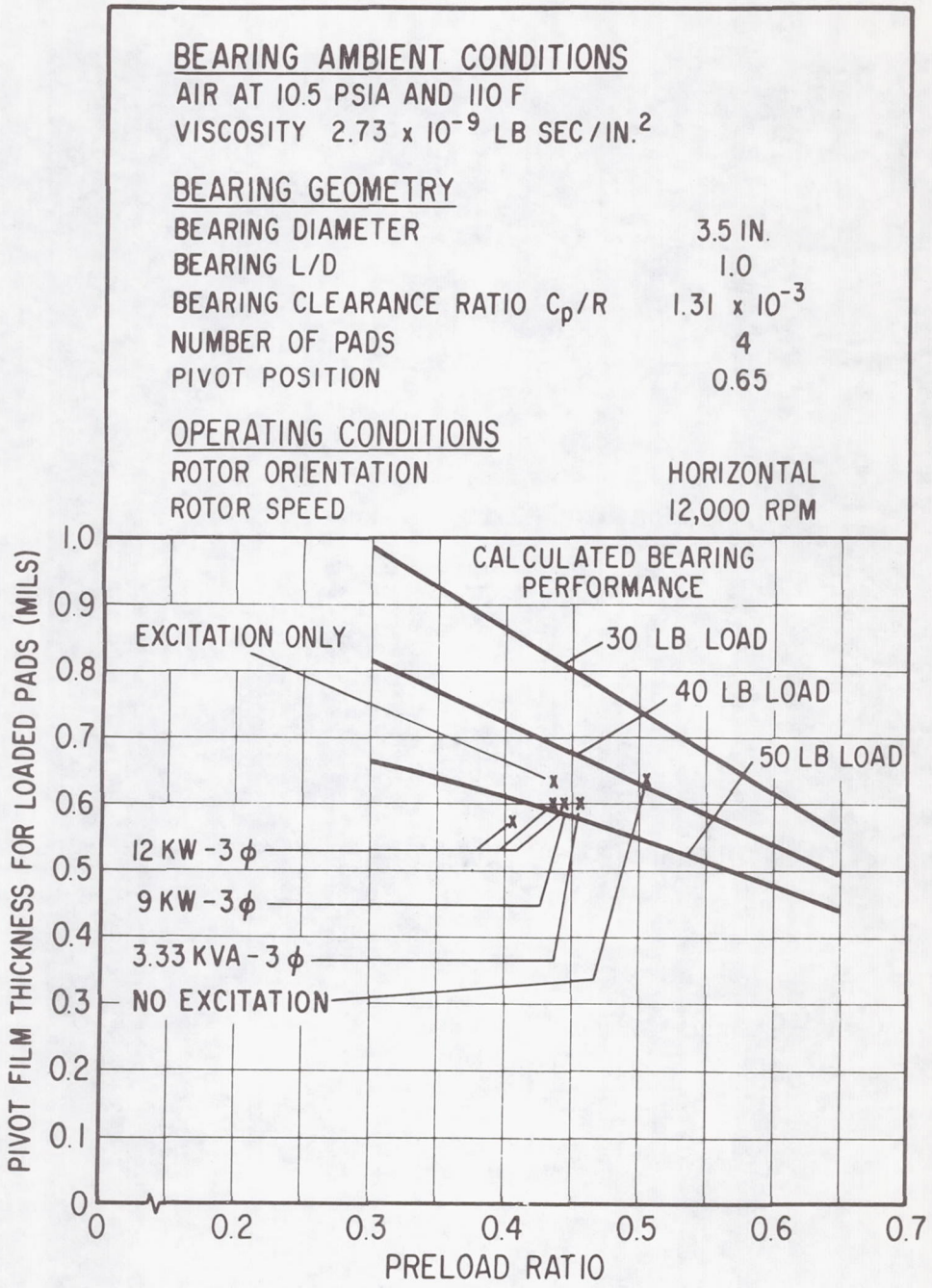

Figure 116 Calculated and Experimental Performance of the Journal Bearing Adjacent to the Thrust Bearing at Low Preloads, Rotor Horizontal

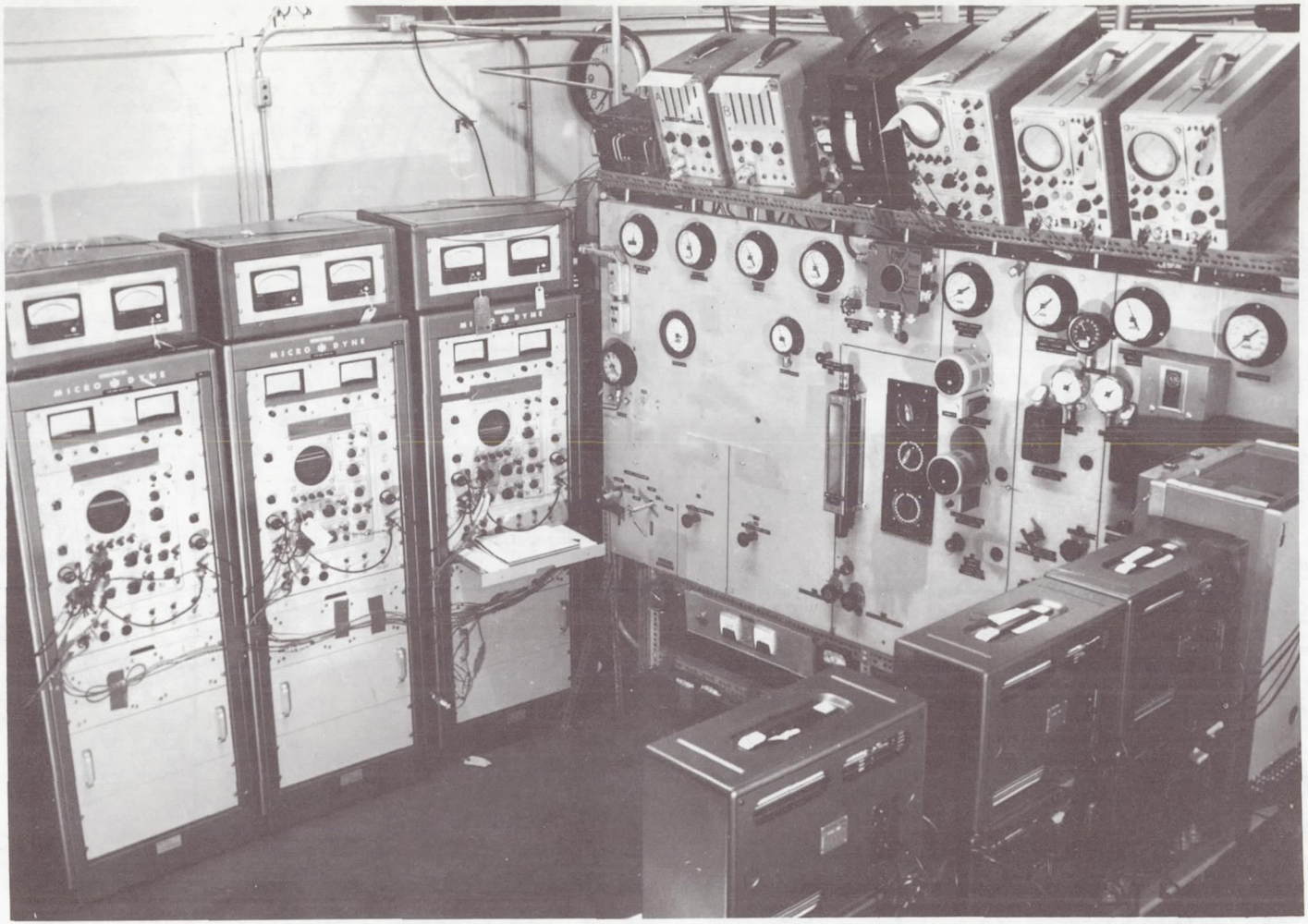

Figure 117 Turboalternator Test Facility Control Panel and Instrumentation Readout Equipment (CN-9854)

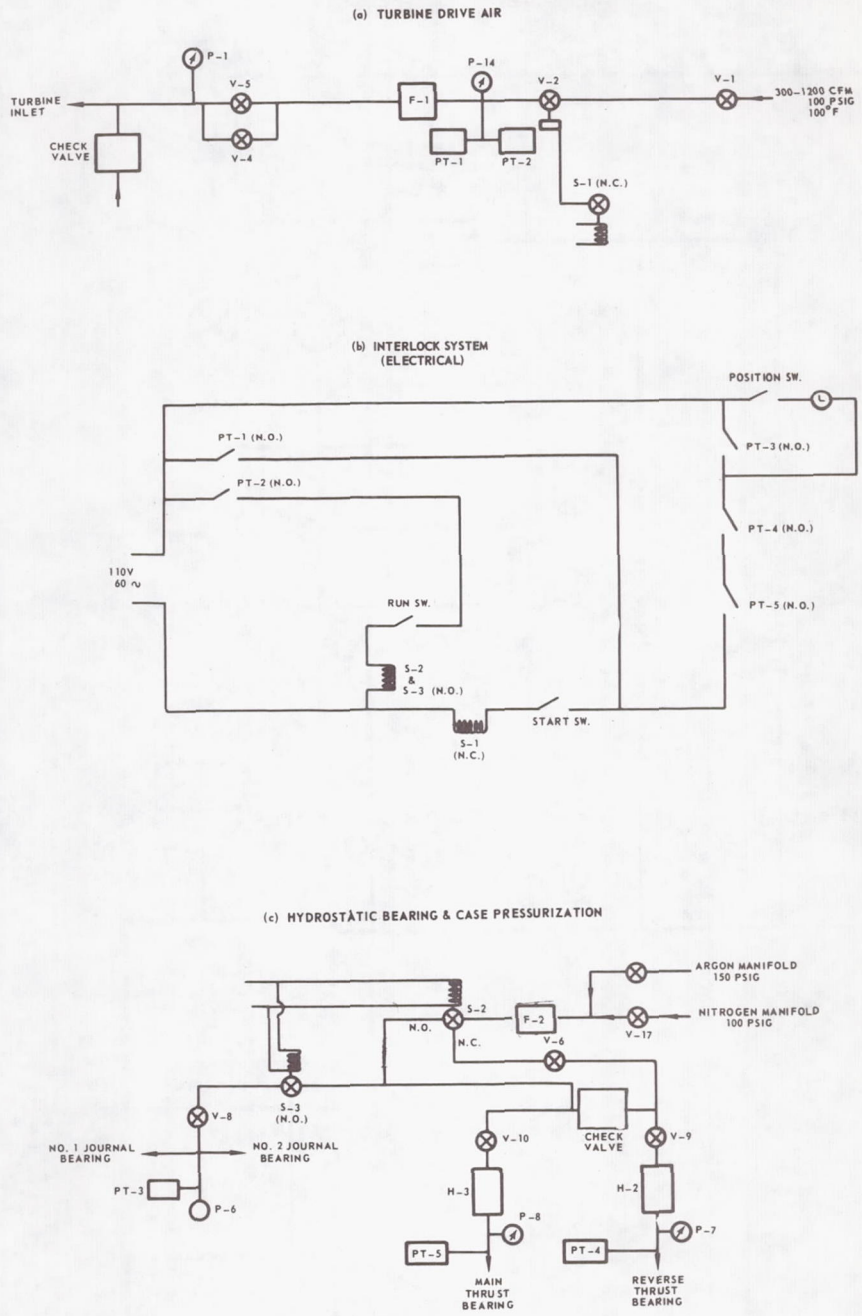

Figure 118 Turbine Gas Supply, Hydrostatic Gas Supply, and Interlock Systems

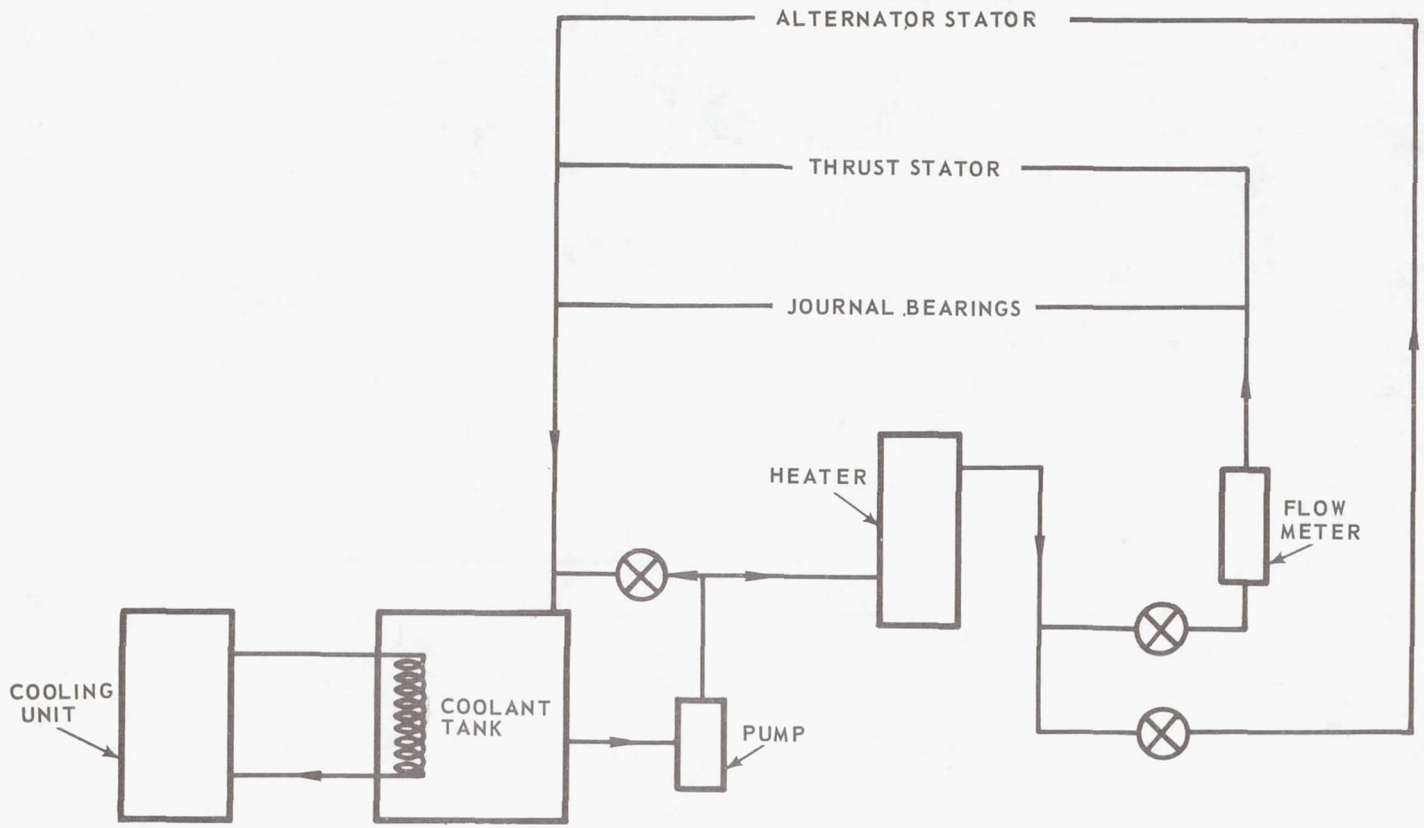

Figure 119 Water Recirculating System

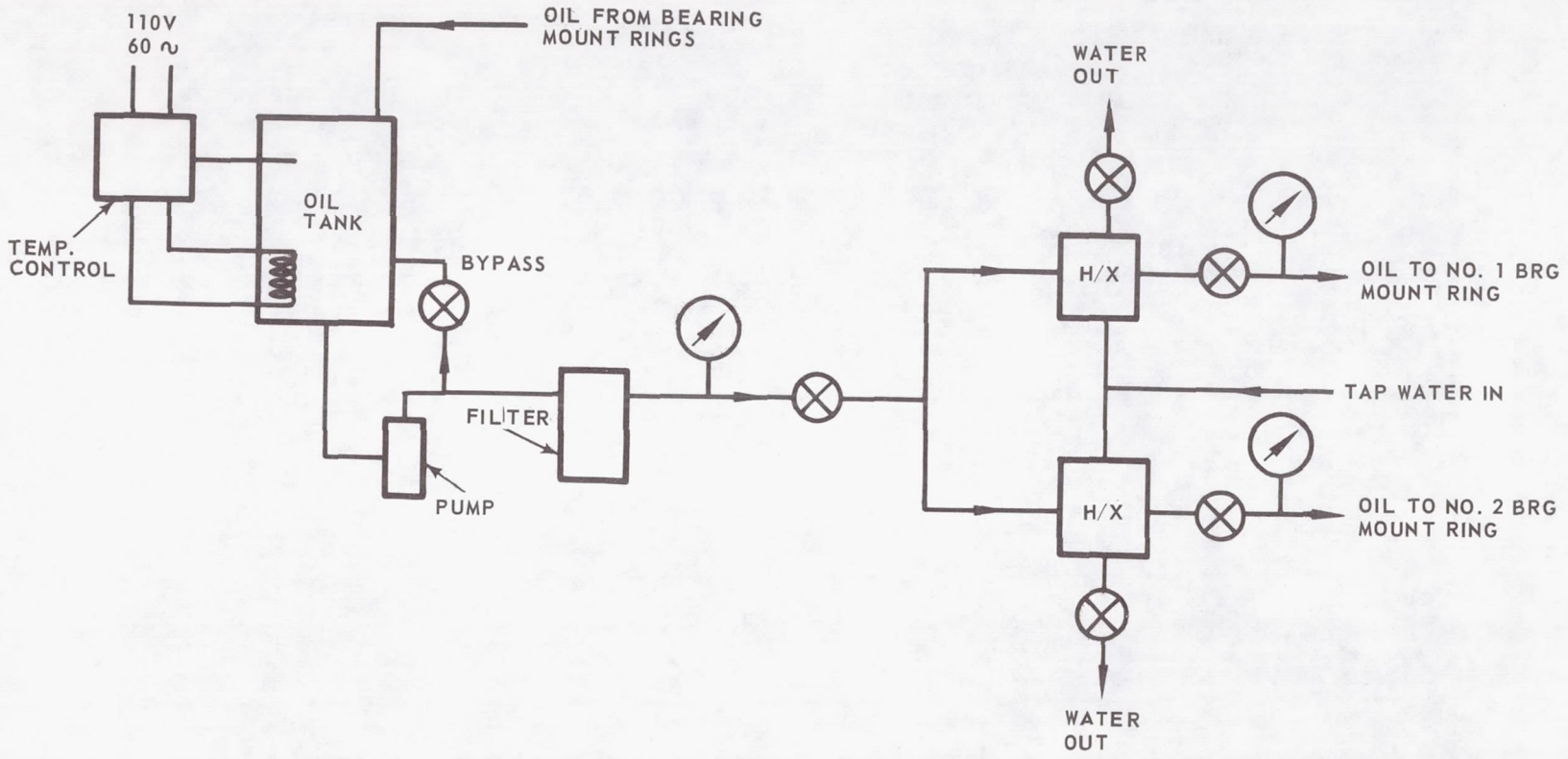

Figure 120 Oil Circulating System

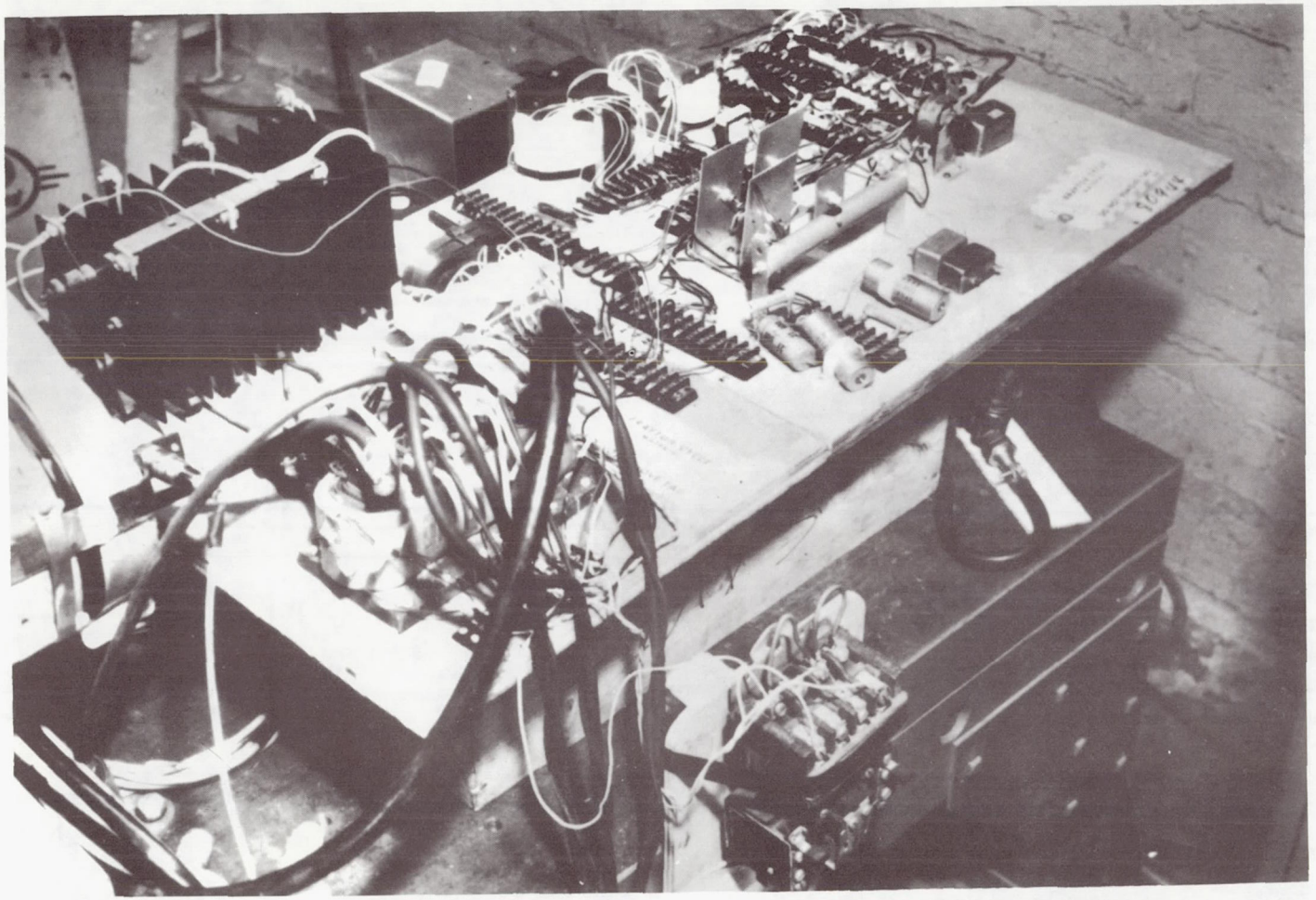

Figure 121 Engineering Breadboard Voltage Regulator - Exciter (M-41529)

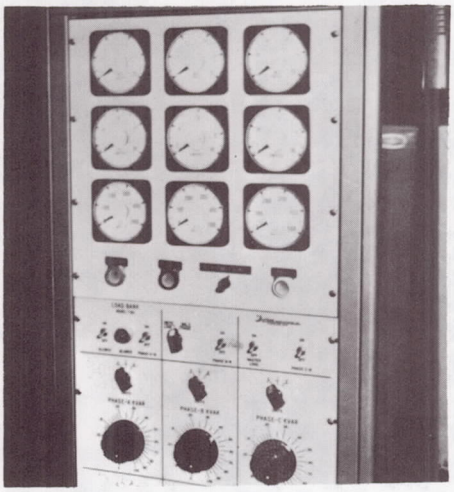

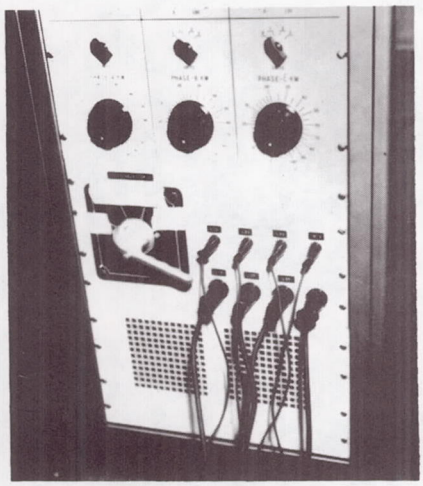

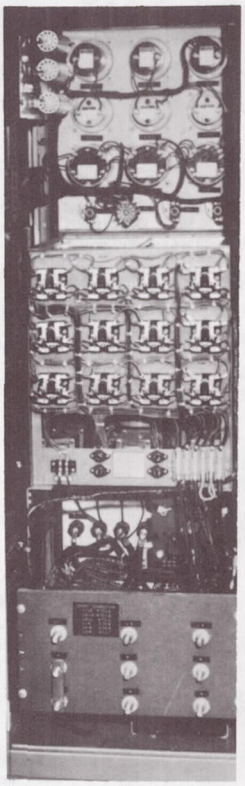

Figure 122 Load Bank (M-41528)

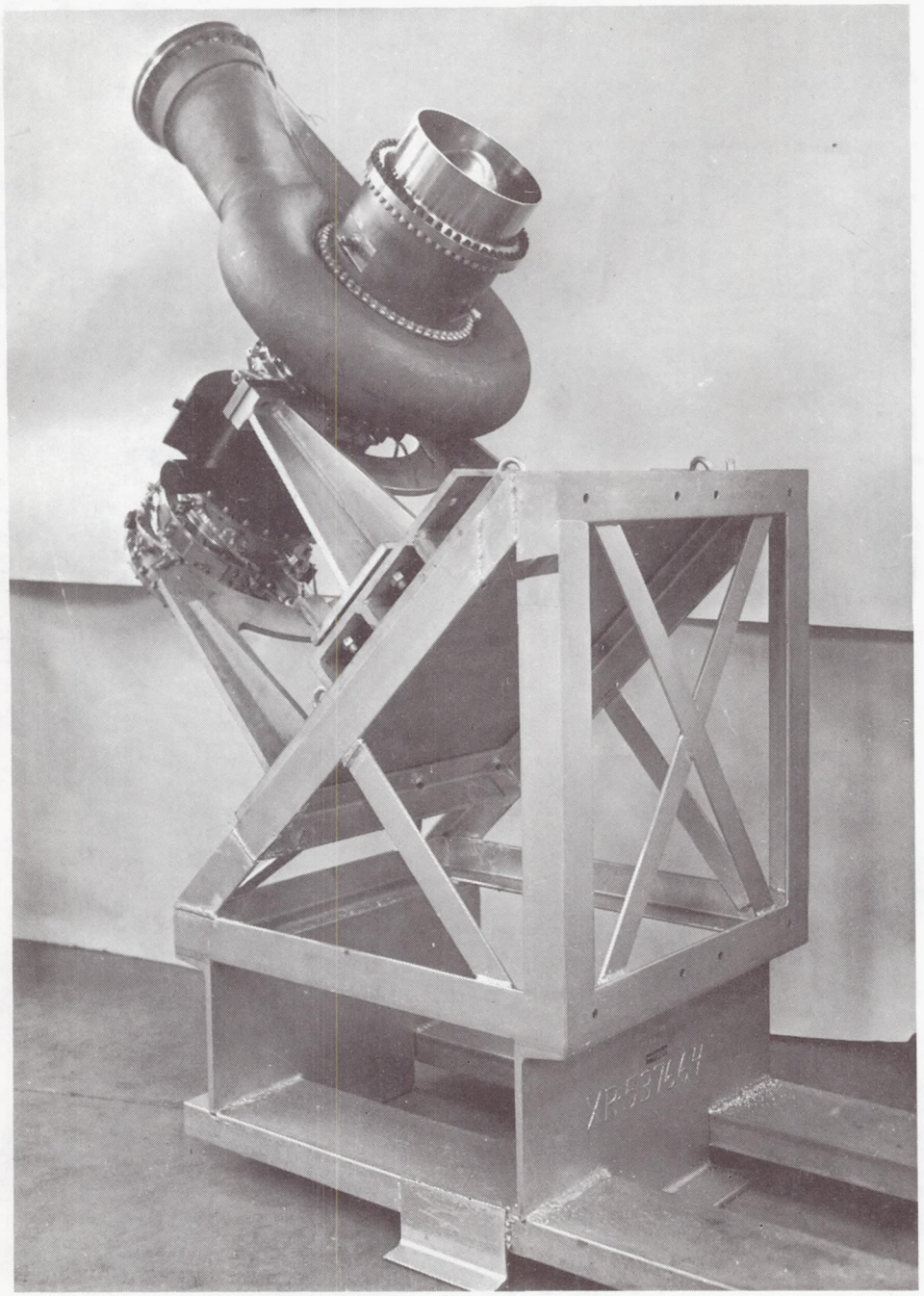

Figure 123 Turboalternator Mounted at 45° Angle (CN-9563)

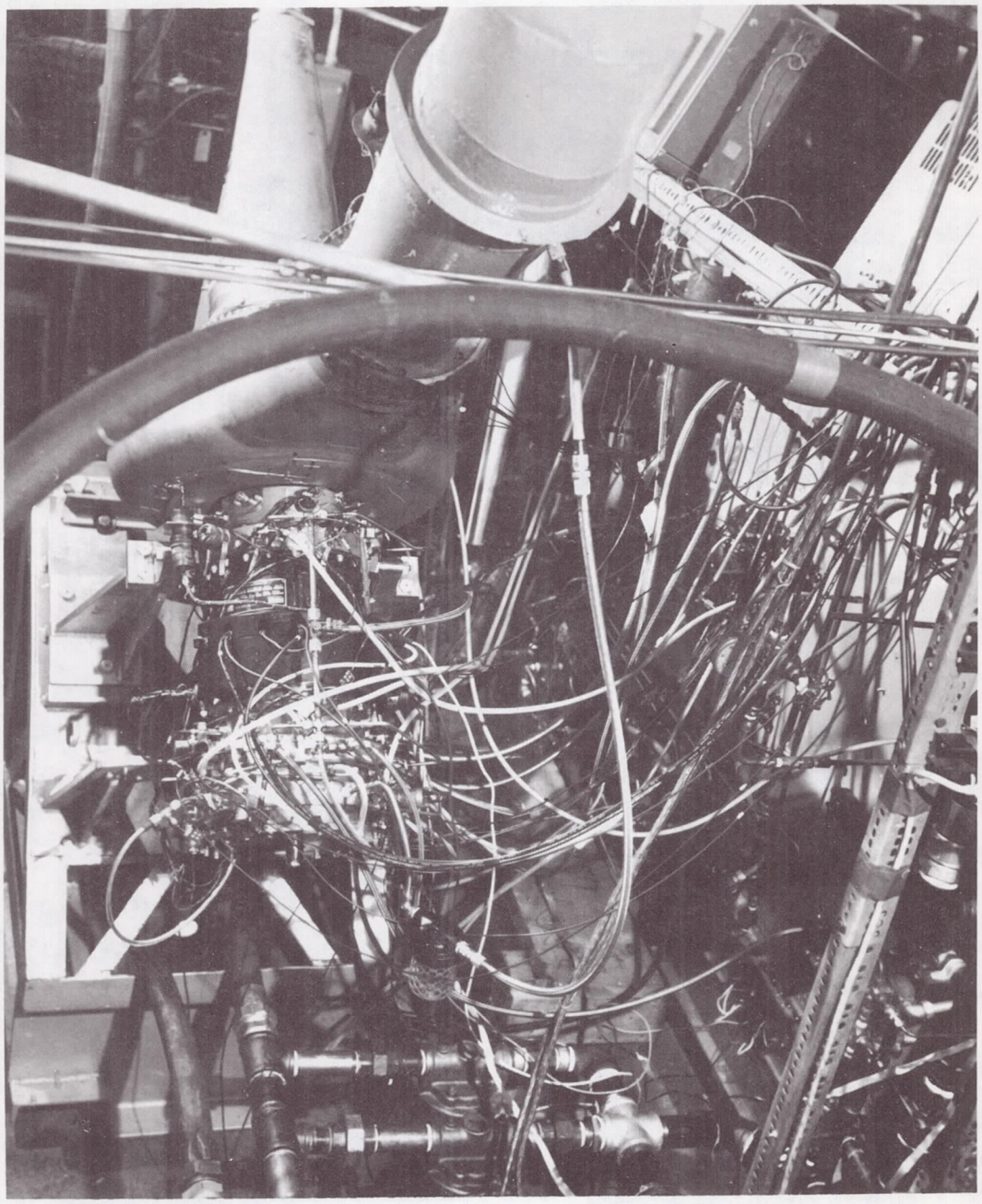

Figure 124 Turboalternator Mounted at Test Facility (CN-9853)

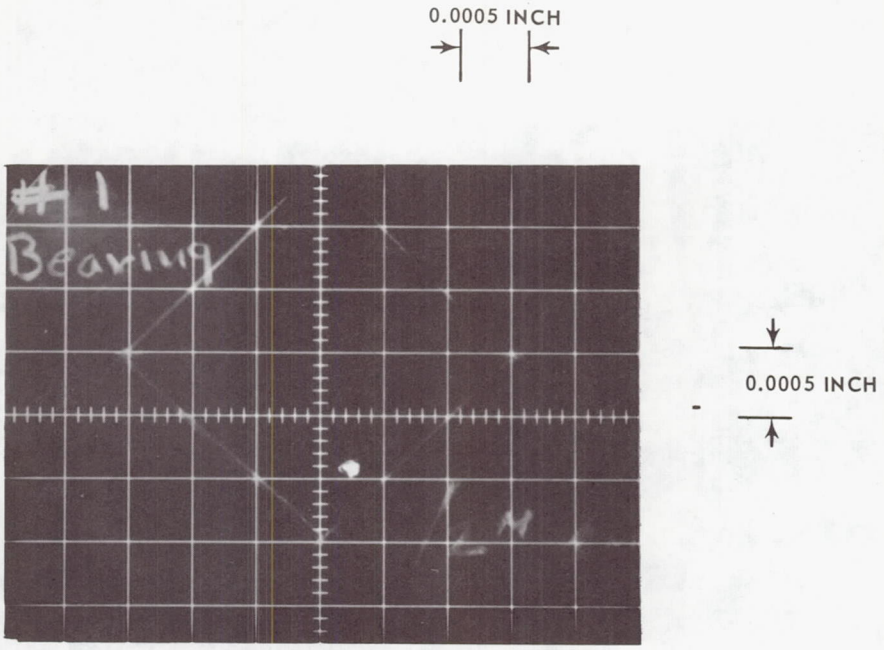

NUMBER ONE (FRONT) JOURNAL BEARING

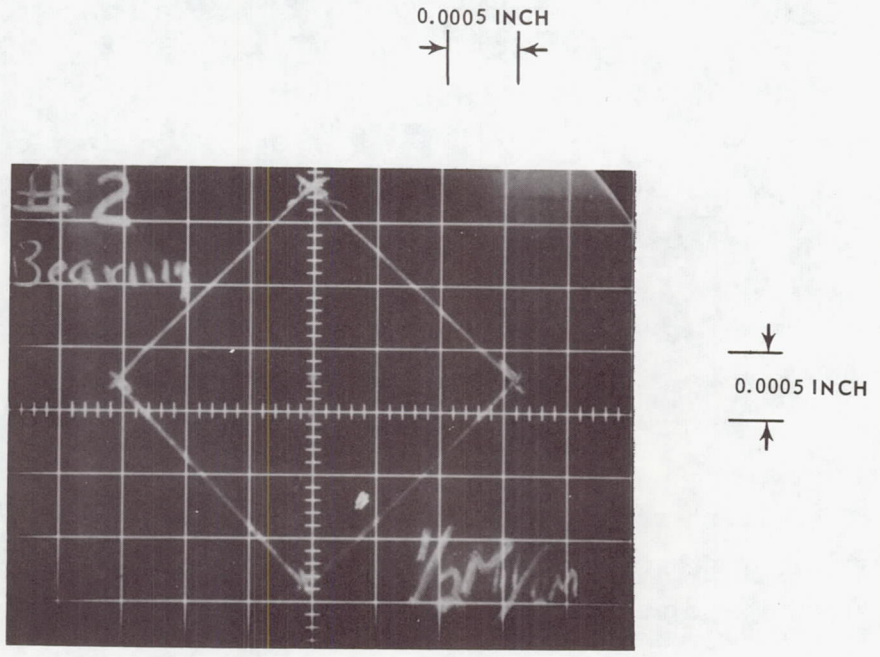

NUMBER TWO (REAR) JOURNAL BEARING

Figure 125 Journal Bearing Orbits at 14,400 rpm (Alternator Field Excited) XP-81604

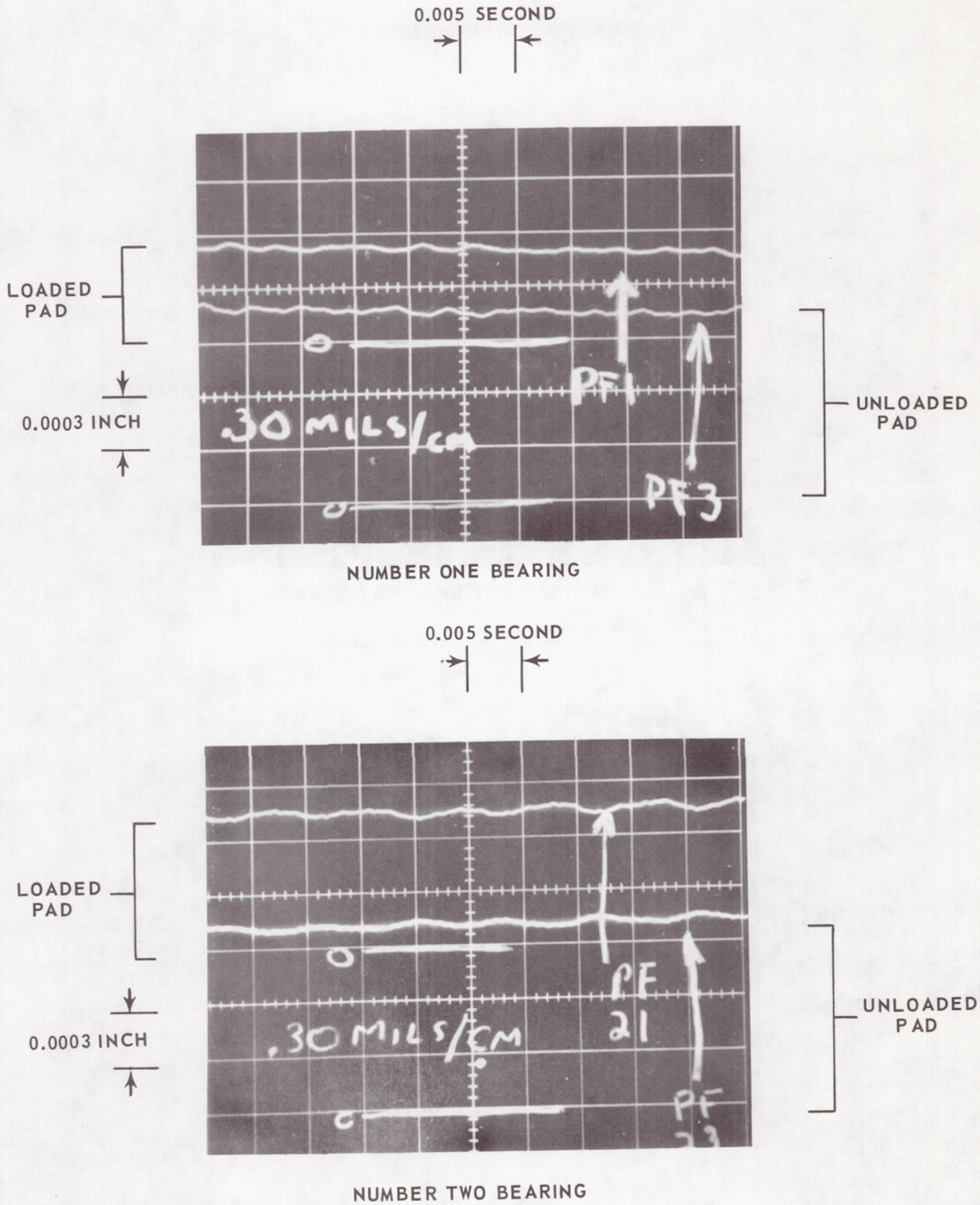

Figure 126 Journal Bearing Film Thicknesses at 14,400 rpm (Alternator Field Excited) XP-81602 XP-81603

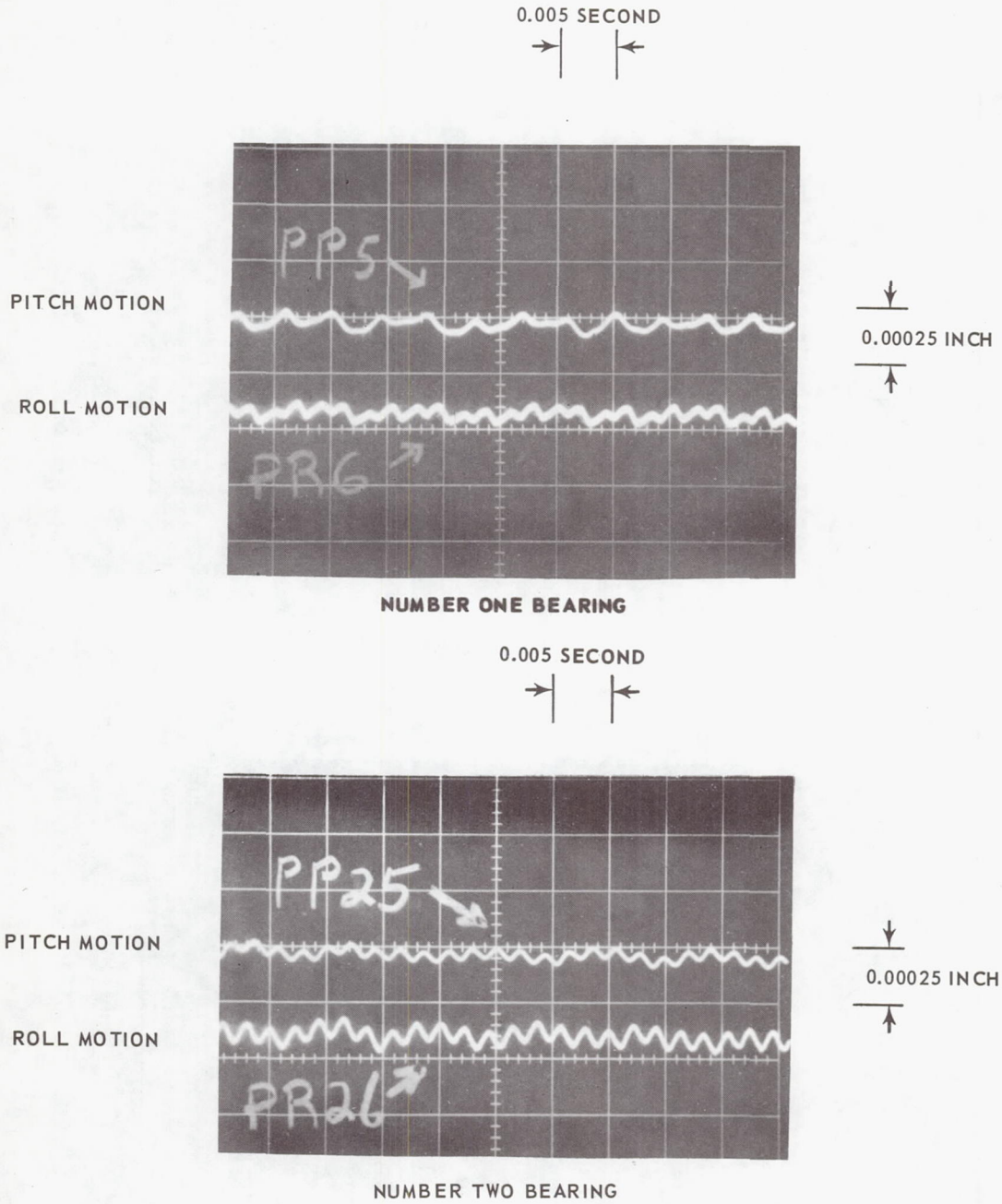

Figure 127 Journal Bearing Dynamic Motion at 14,400 rpm (Alternator Field Excited)

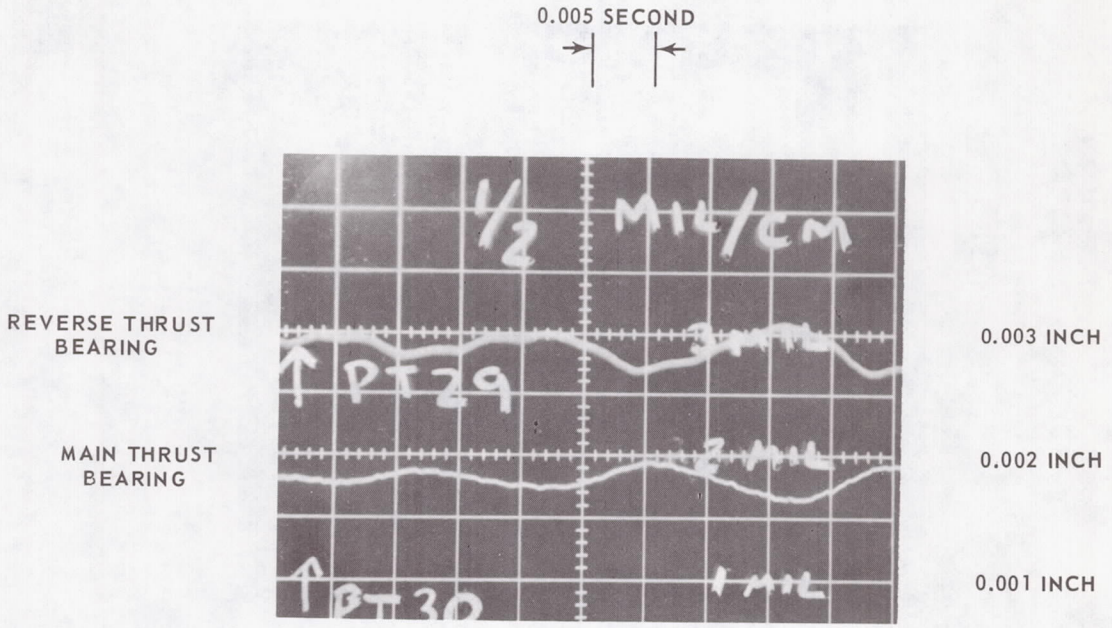

Figure 128 Thrust Bearing Film Thicknesses at 14,400 rpm XP-81601

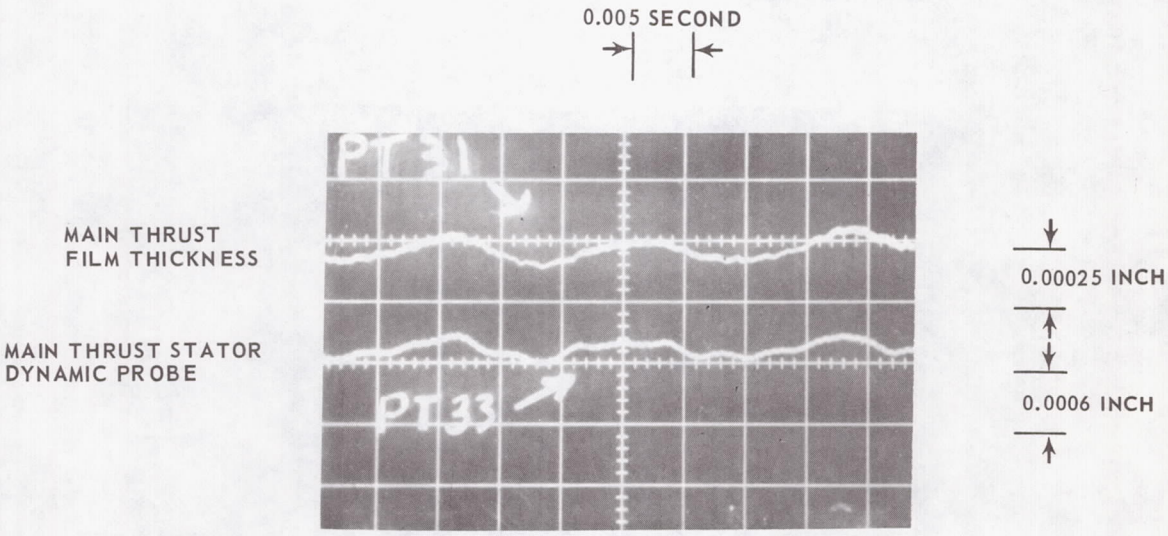

Figure 129 Main Thrust Stator Motion at 14,400 rpm XP-81601

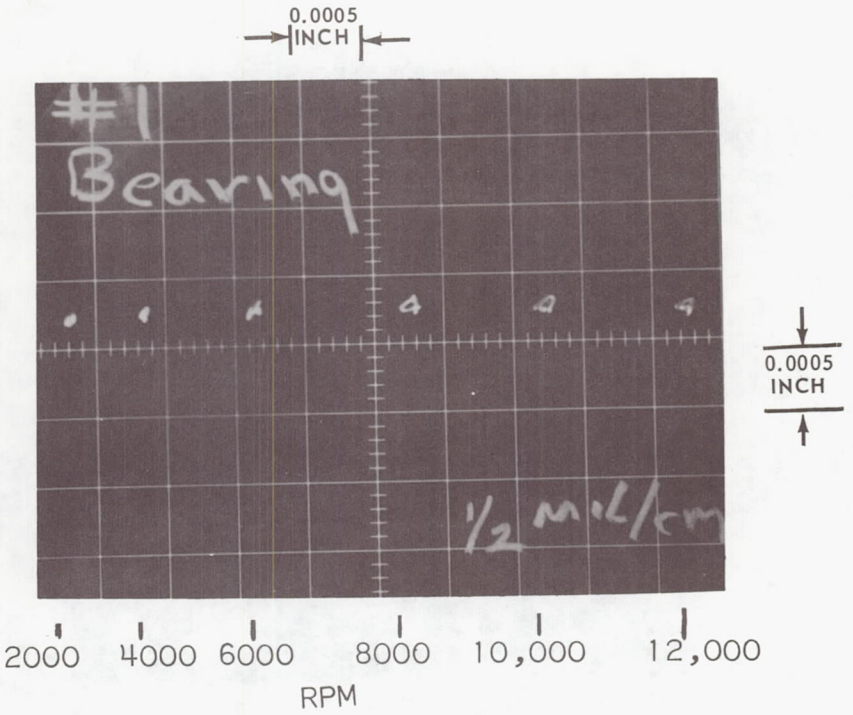

Figure 130 Number One Journal Orbit in 2,000-12,000 rpm Speed Range, Hydrostatic, No Electrical Load, Field Excited above 7,000 rpm

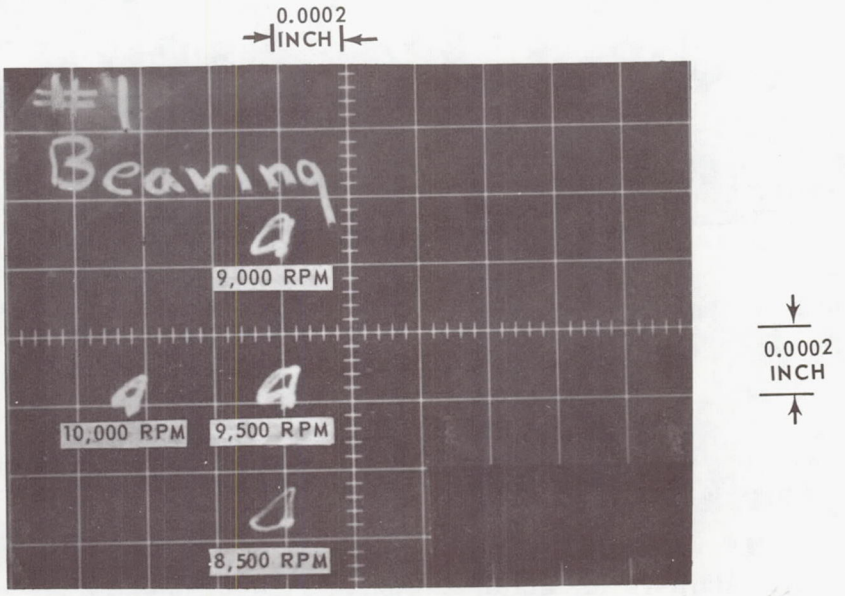

Figure 131 Enlargement of Number One Journal Orbit in Critical Speed Range During Coasting Deceleration XP-81600

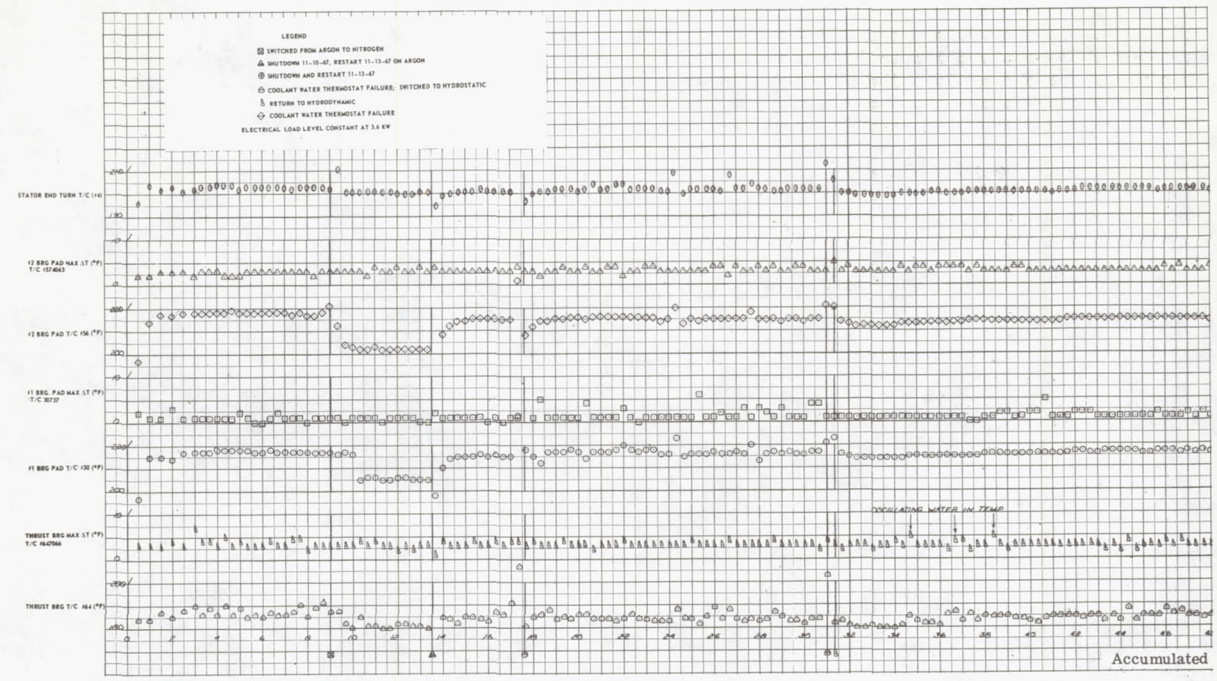

Figure 132 100-Hour

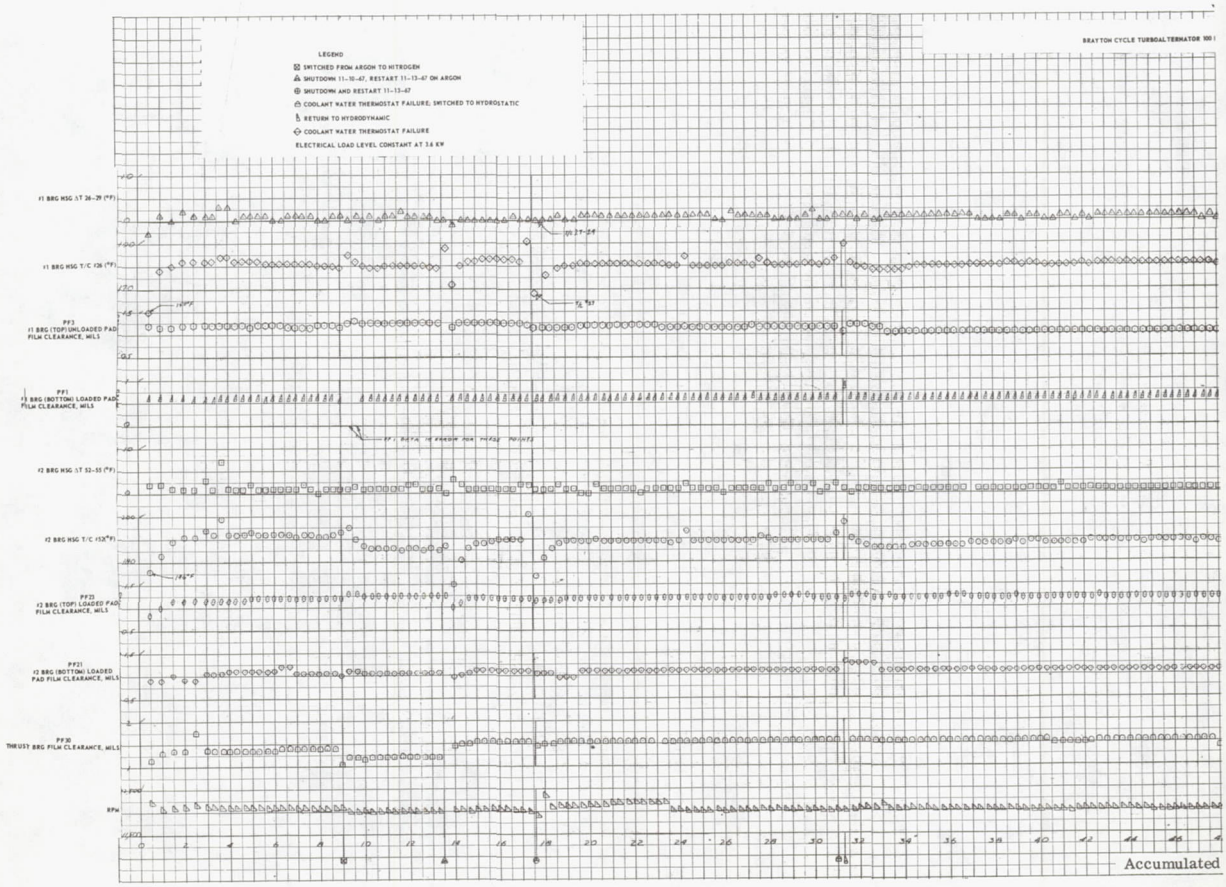

Figure 133 100-Hour

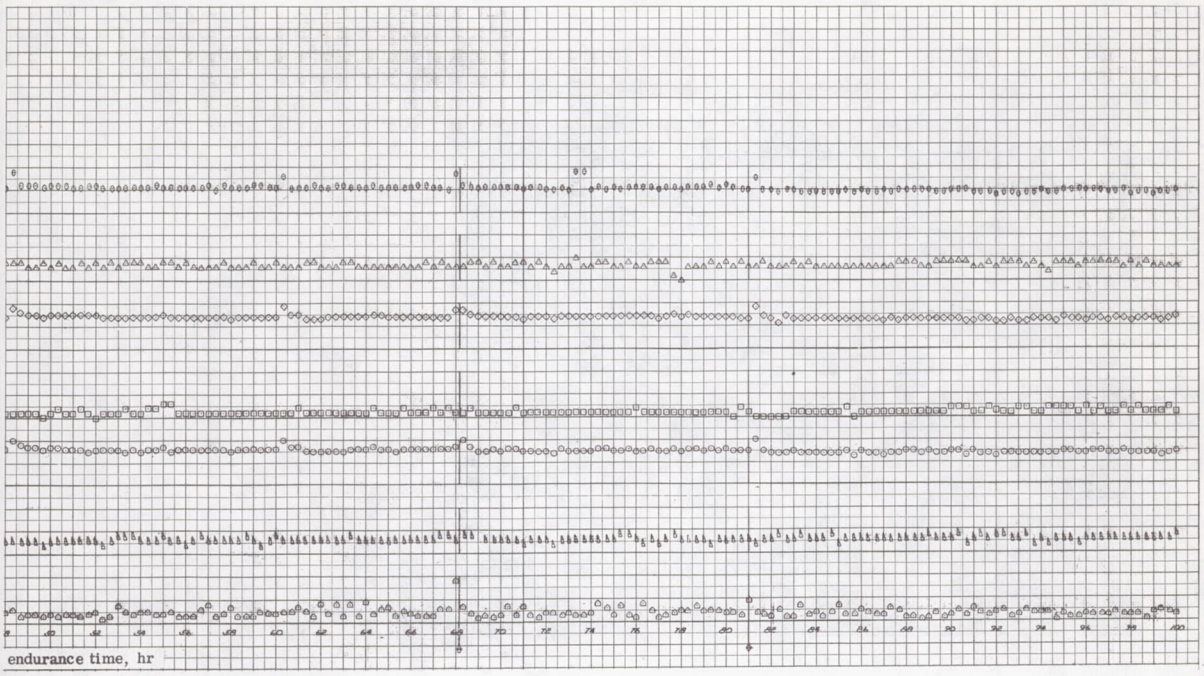

Endurance Test Log (Sheet 1)

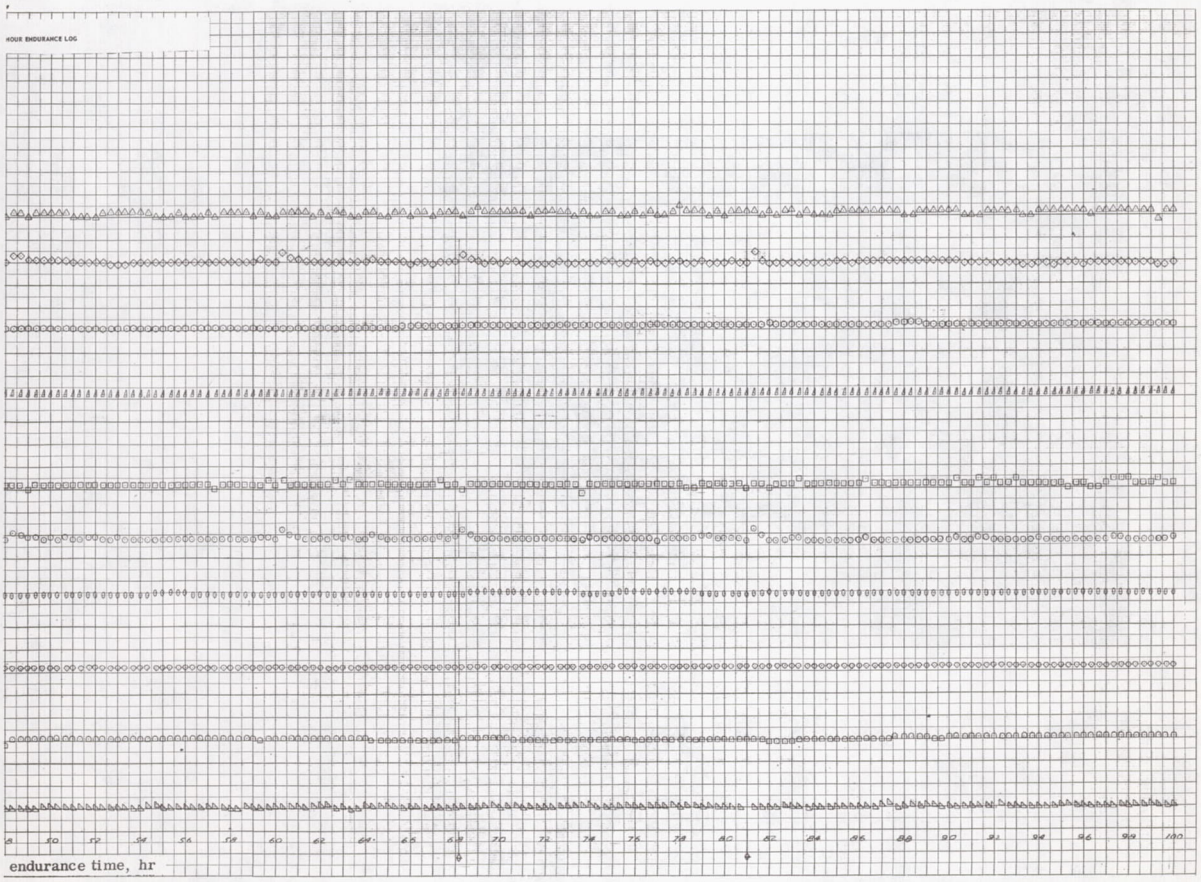

Endurance Test Log (Sheet 2)

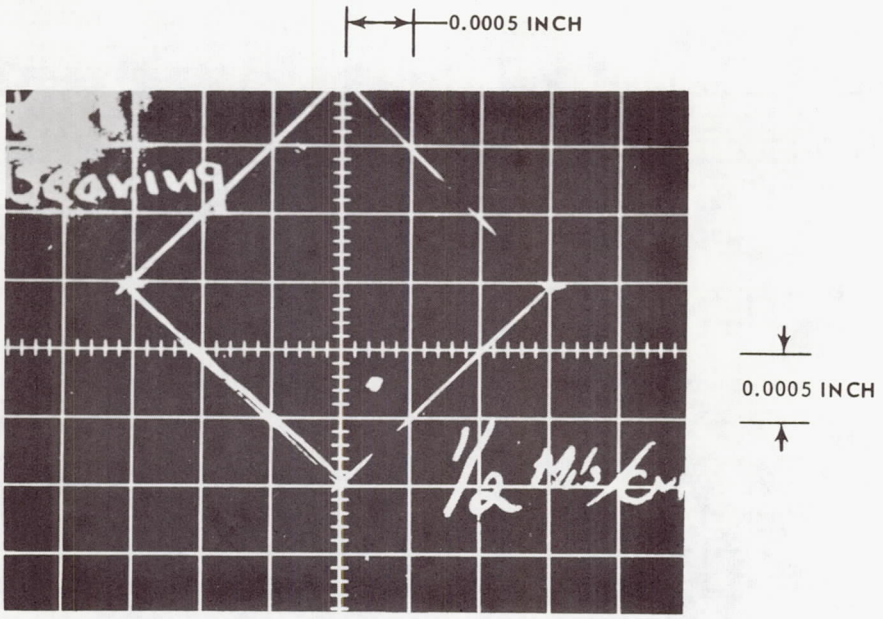

Number One Bearing (XP-80175)

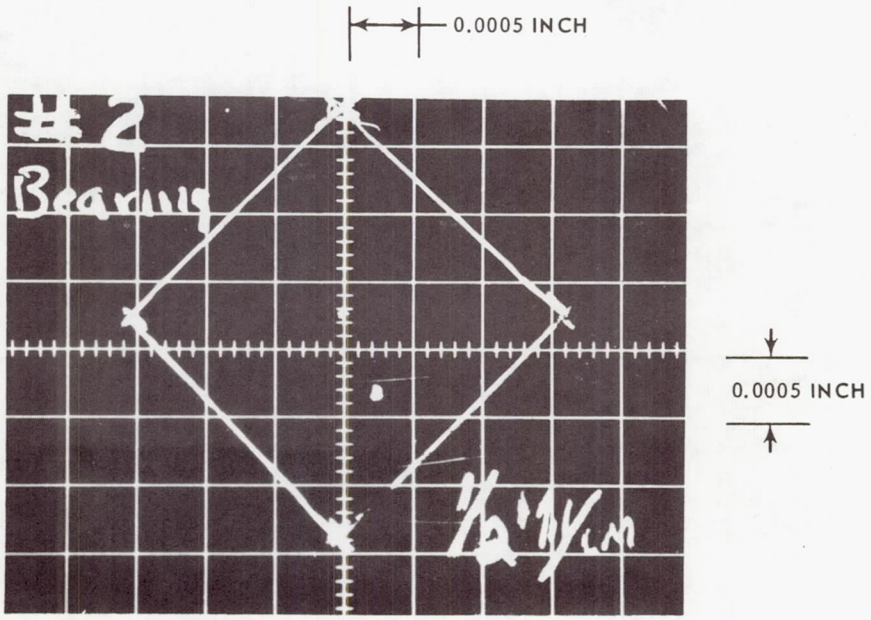

Number Two Bearing (XP-80176)

Figure 134 Journal Bearing Orbits, Acceptance Test of #1 Turboalternator (Alternator Field Excited)

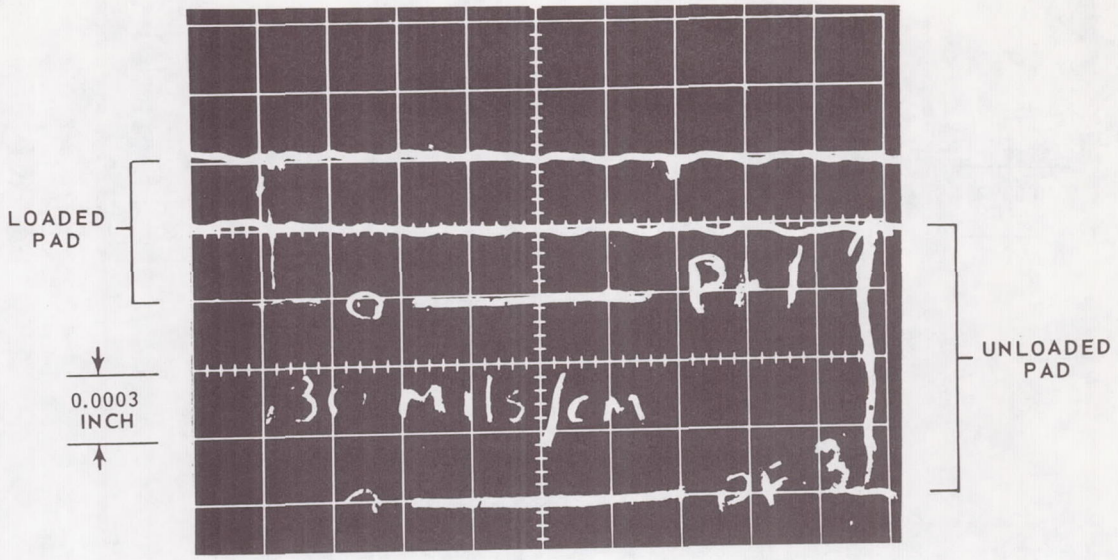

Number One Bearing (XP-80178)

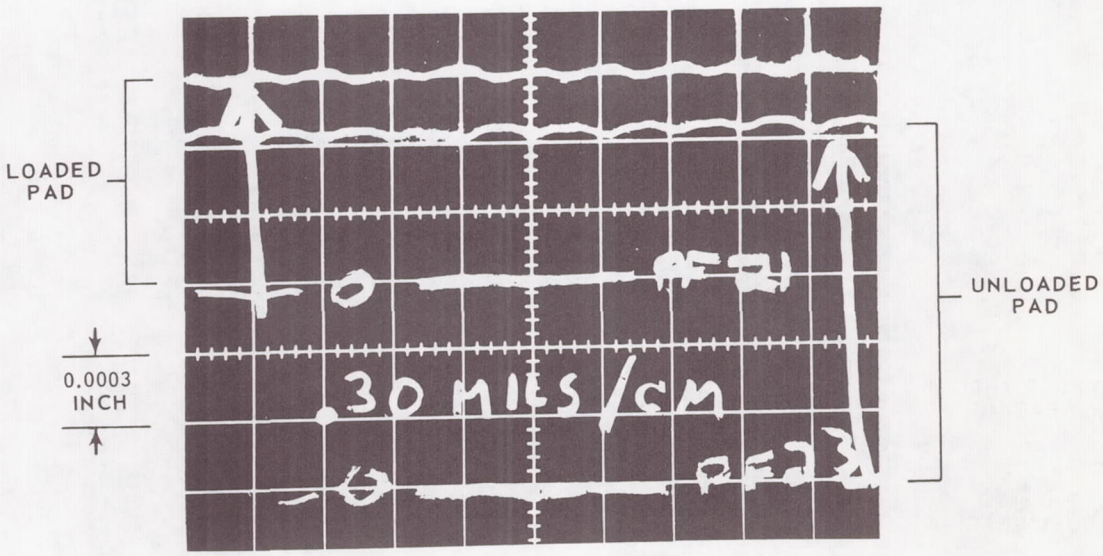

Number Two Bearing (XP-80177)

Figure 135 Journal Bearing Film Thicknesses, Acceptance Test of #1 Turboalternator (Alternator Field Excited)

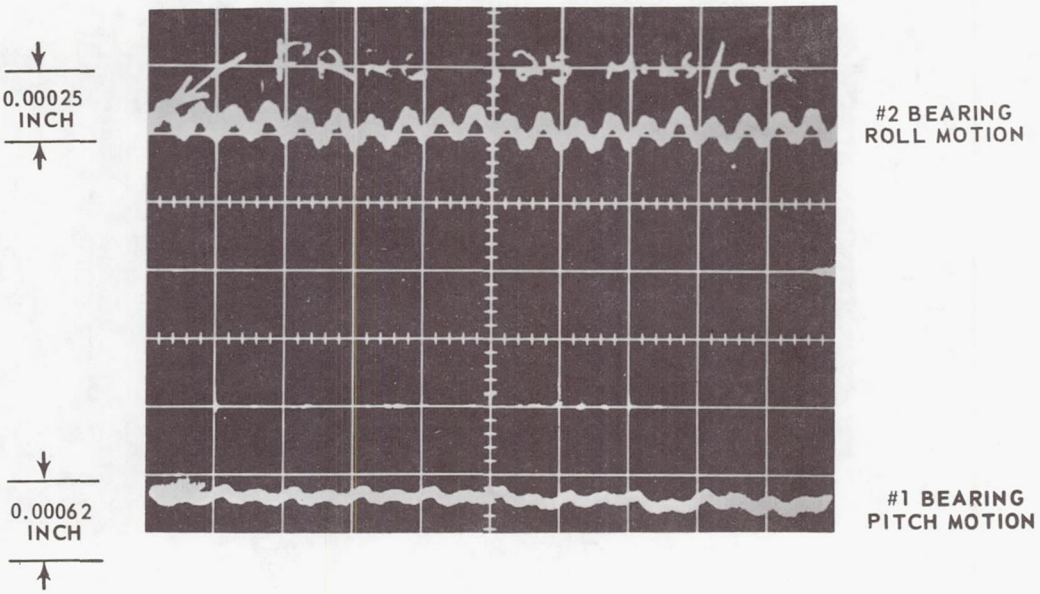

Figure 136 Journal Bearing Pad Dynamic Motion, Acceptance Test of #1 Turboalternator (Alternator Field Excited) (XP-80179)

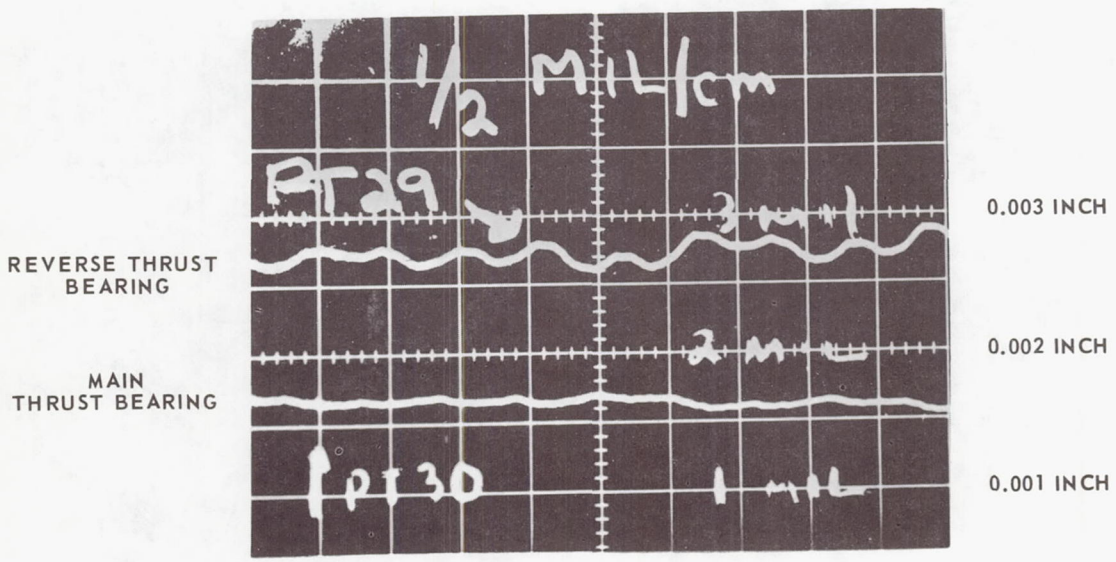

Figure 137 Thrust Bearing Film Thicknesses, Acceptance Test of #1 Turboalternator (XP-80180)

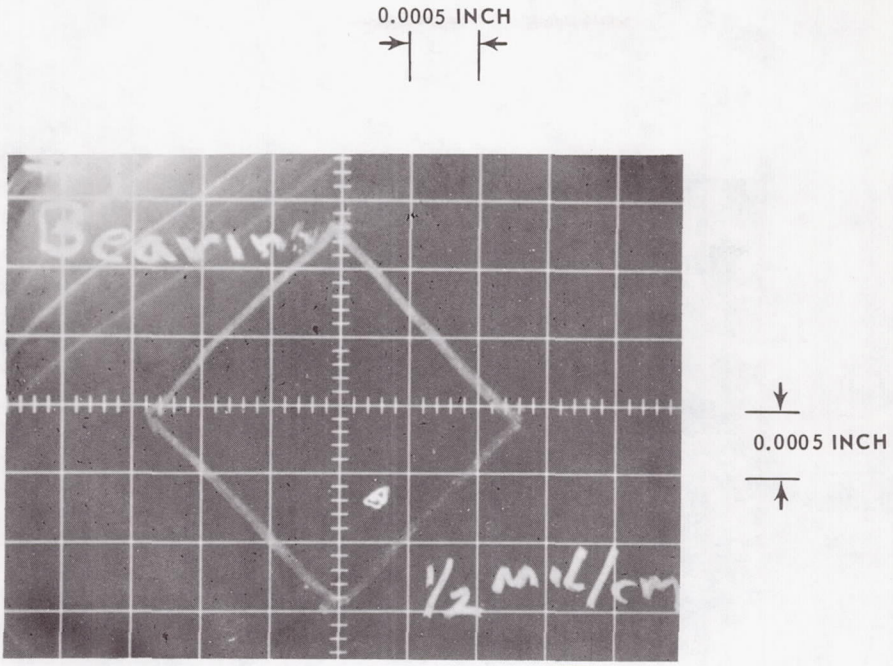

NUMBER ONE BEARING

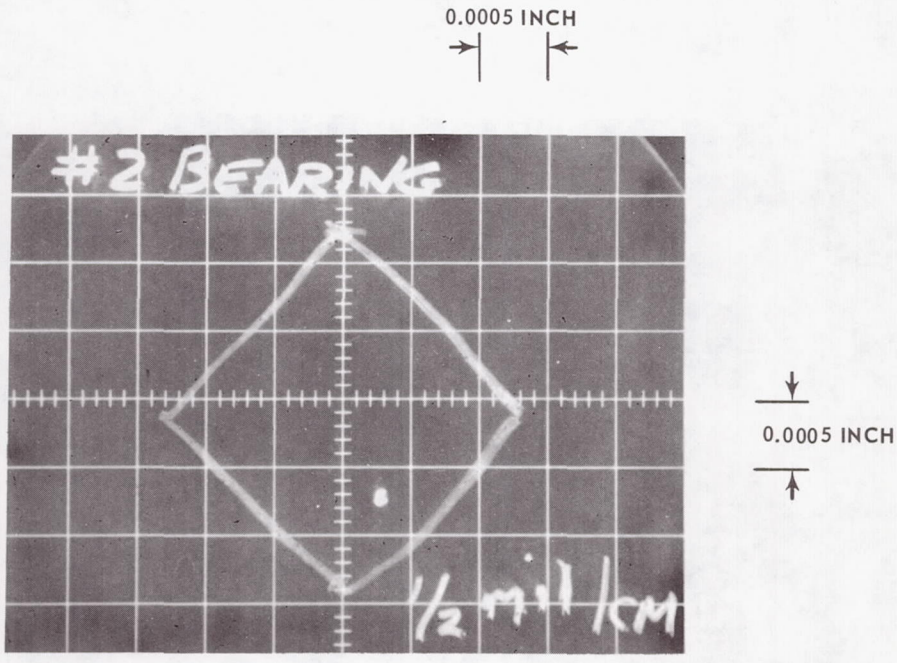

NUMBER TWO BEARING

Figure 138 Journal Bearing Orbits, Acceptance Test of No. 2 Turboalternator (3.6 Kw) XP-81605

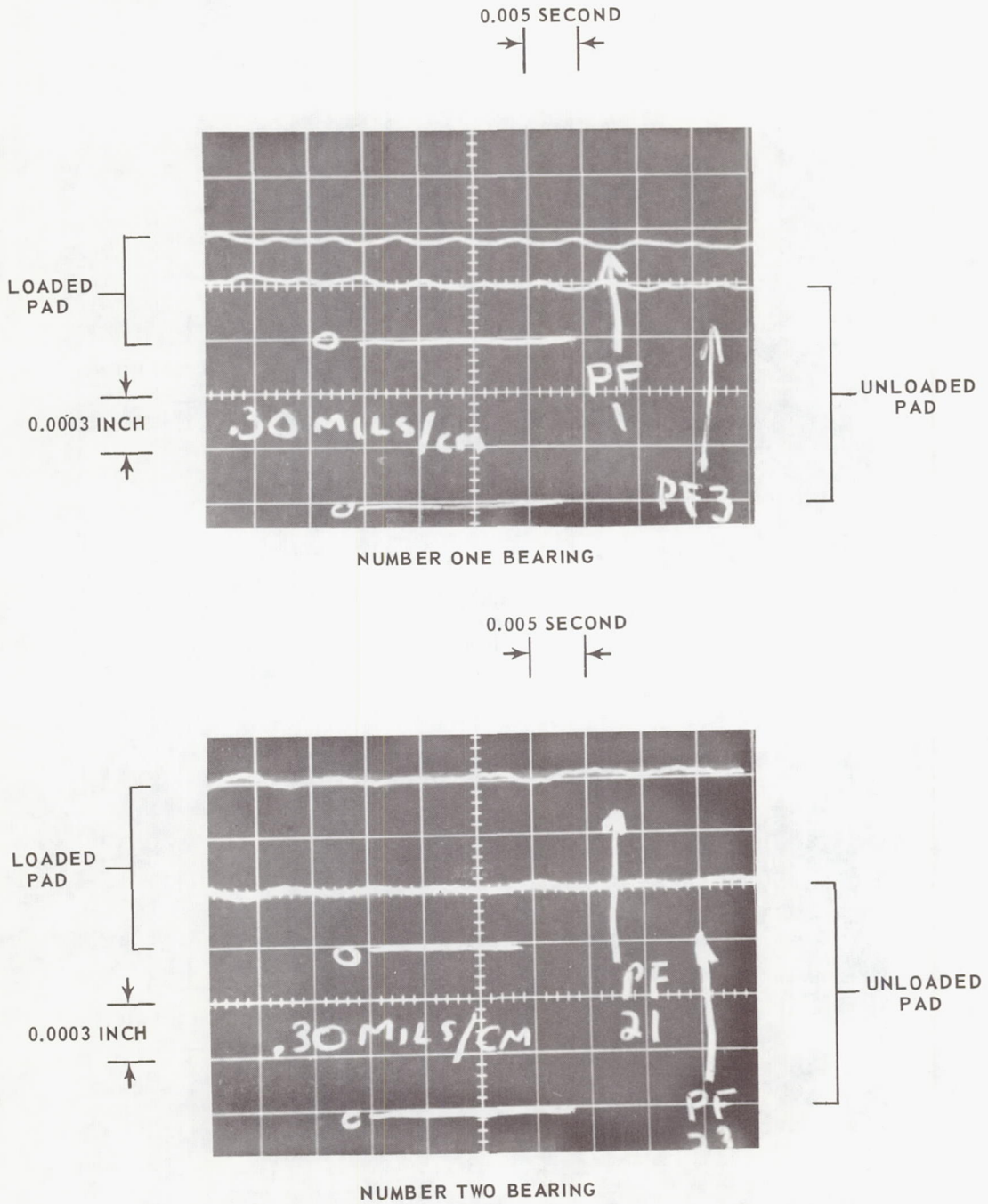

Figure 139 Journal Bearing Film Thicknesses, Acceptance Test of No. 2 Turboalternator (3.6 Kw) XP-81599

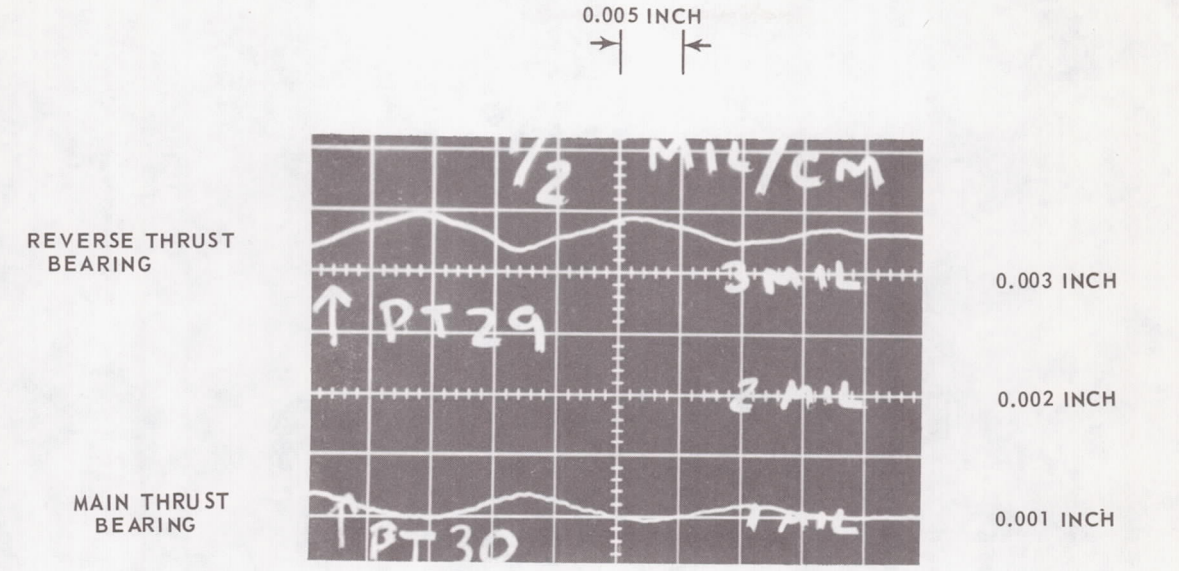

Figure 140 Thrust Bearing Film Thicknesses, Acceptance Test of No. 2 Turboalternator (3.6 Kw)

XP-81599

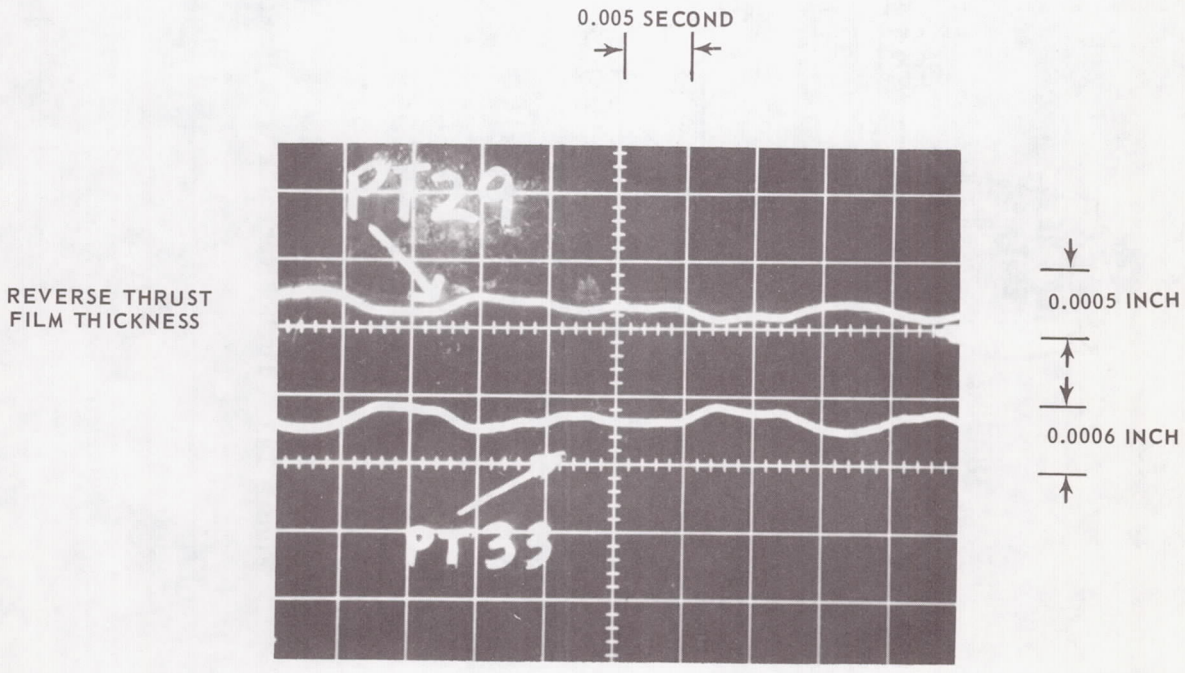

Figure 141 Main Thrust Stator Motion, Acceptance Test of No. 2 Turboalternator (3.6 Kw)

XP-81606

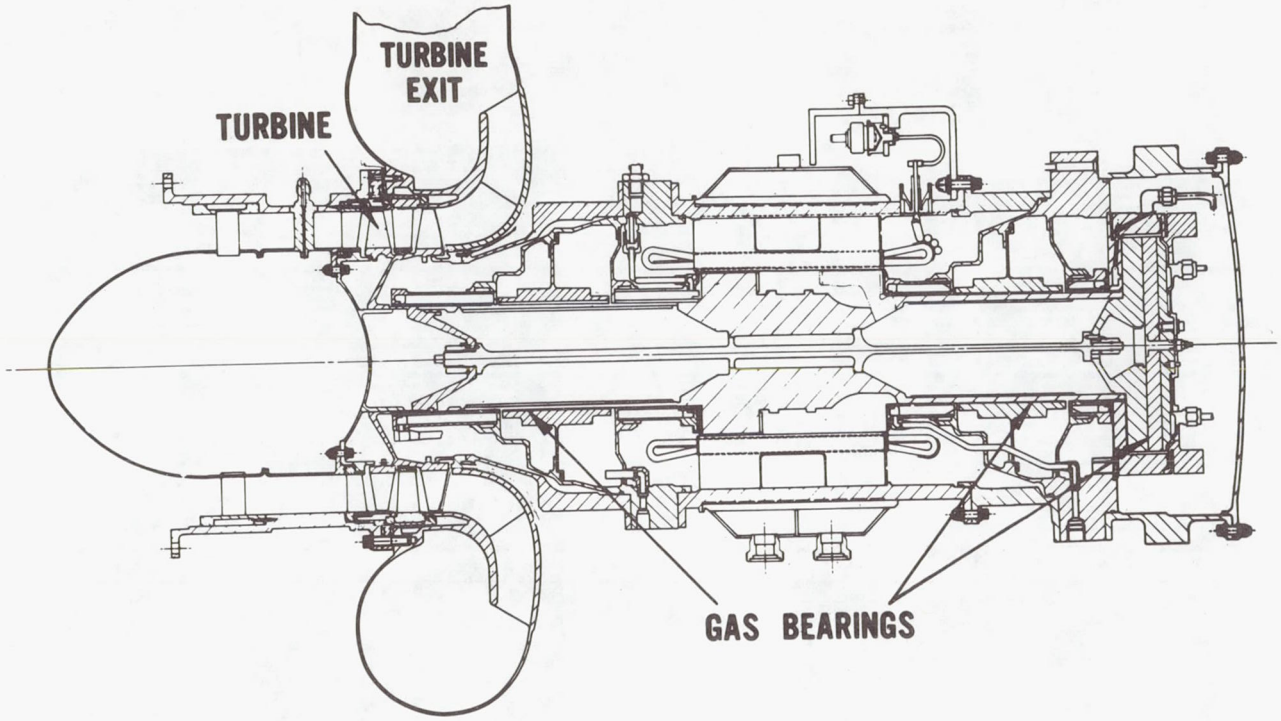

Figure 142 Turboalternator with Back-up Bearings (M-36878)

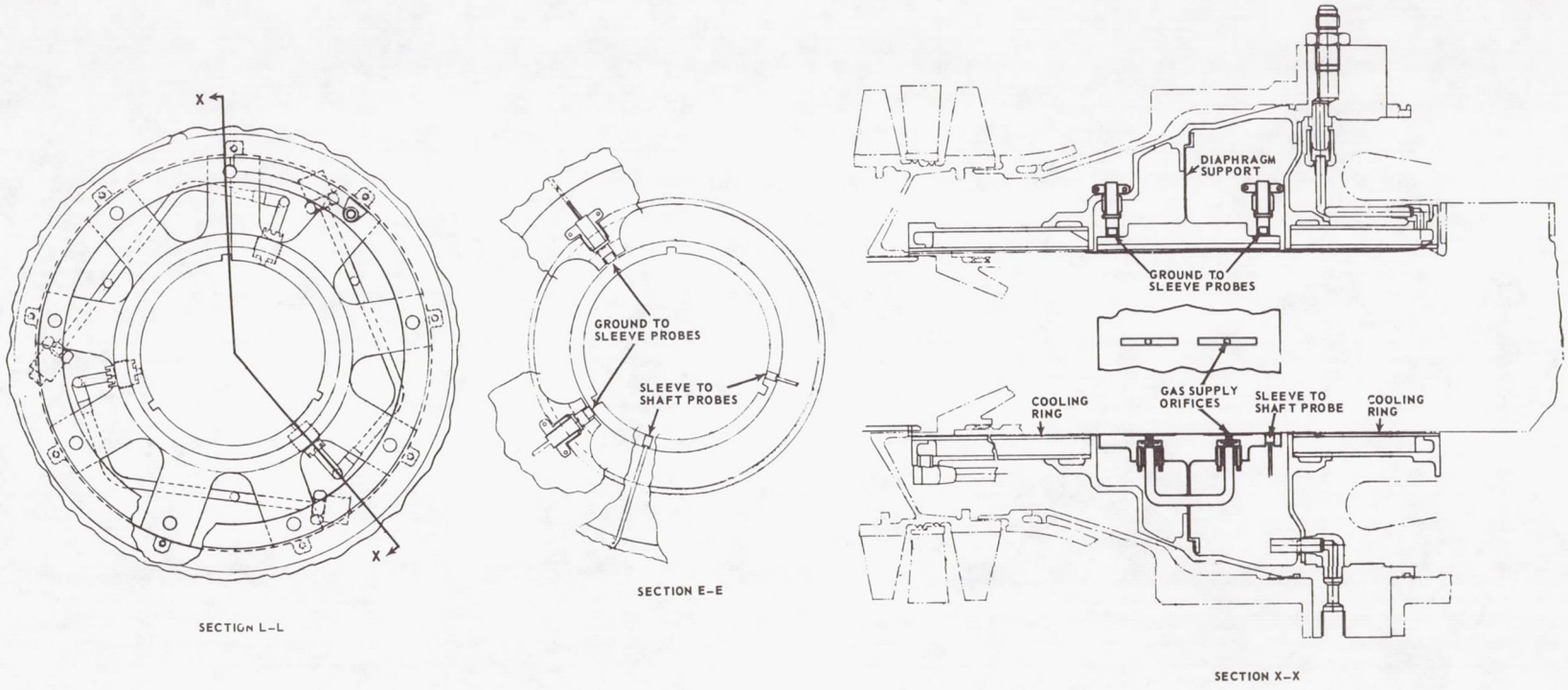

Figure 143 Front Journal Bearing (Back-up Design)

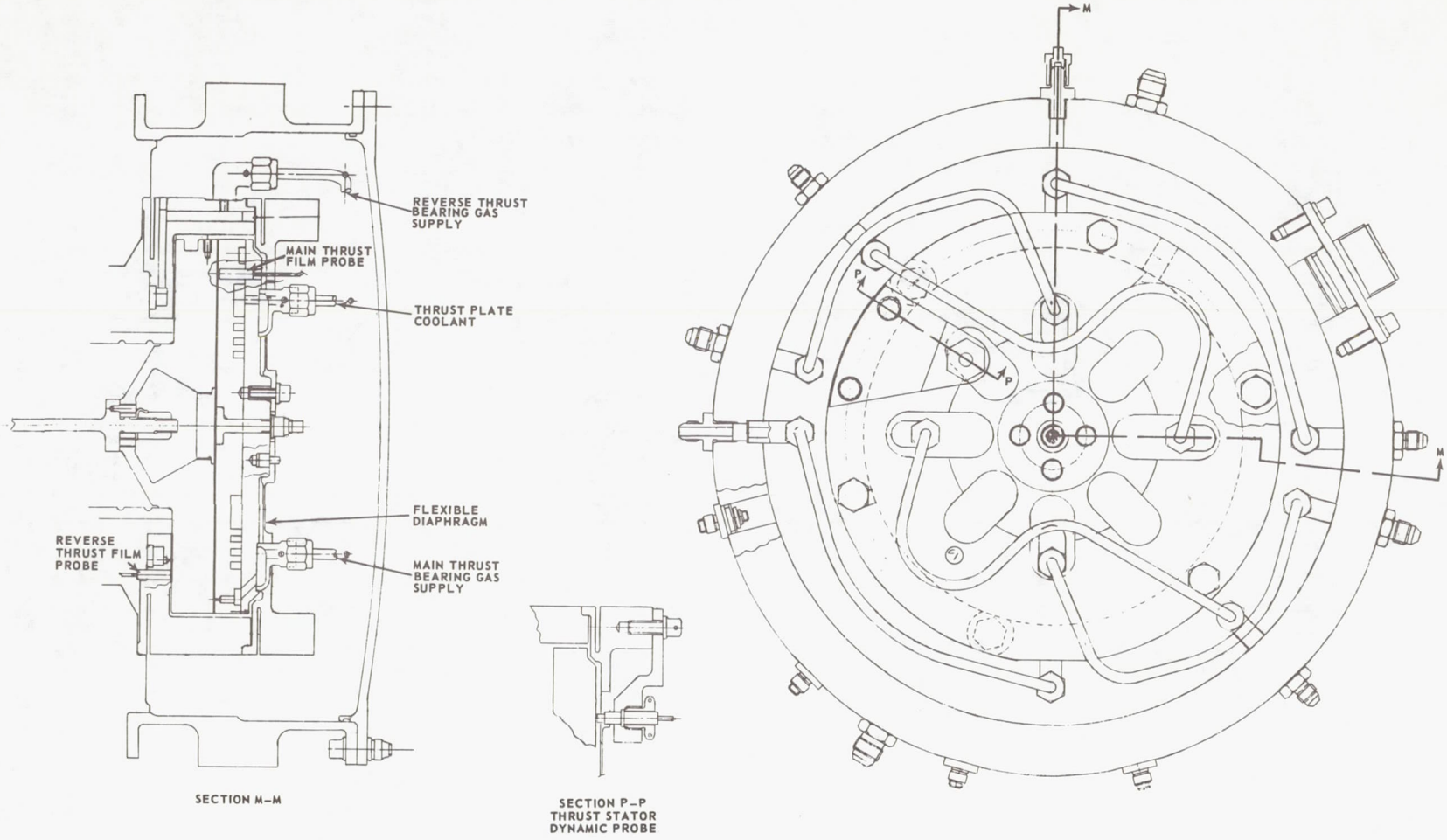

Figure 144 Thrust Bearing (Back-up Design)

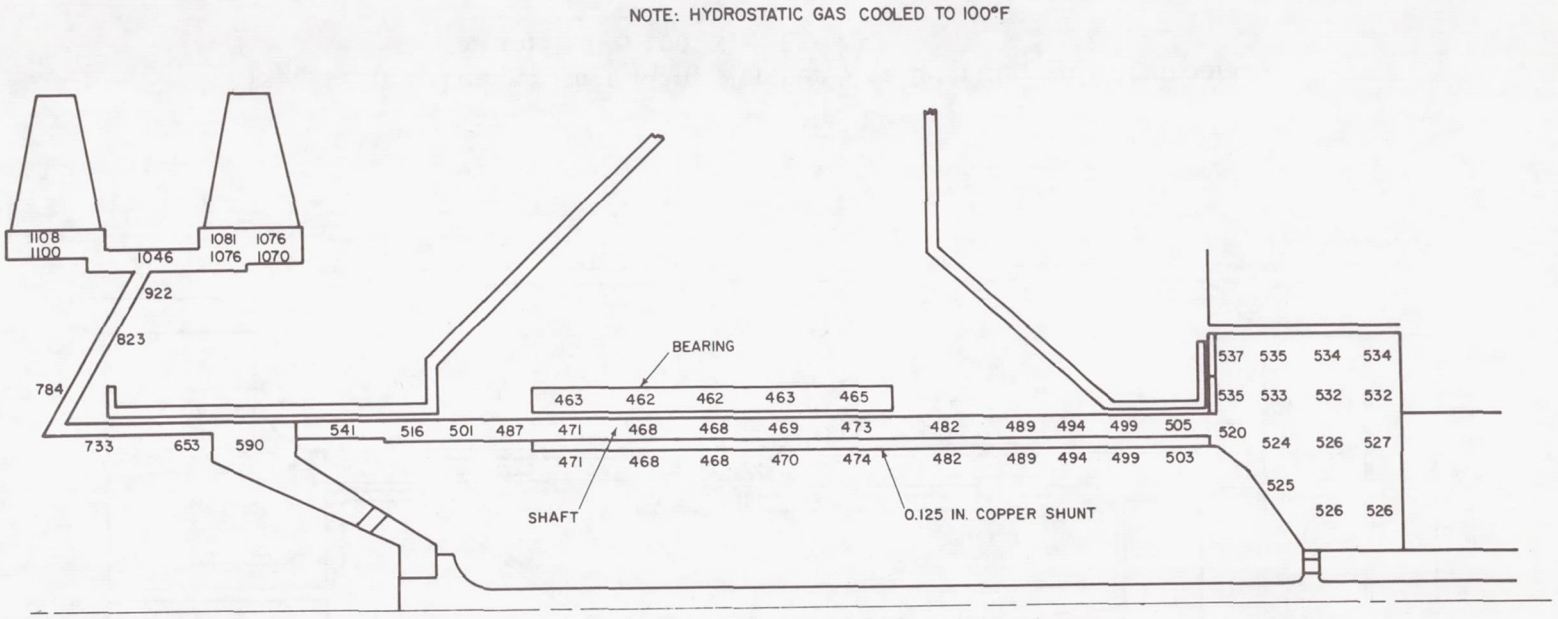

Figure 145 Temperature Map, Number One Bearing, with Hydrostatic Gas Cooled to 100° F

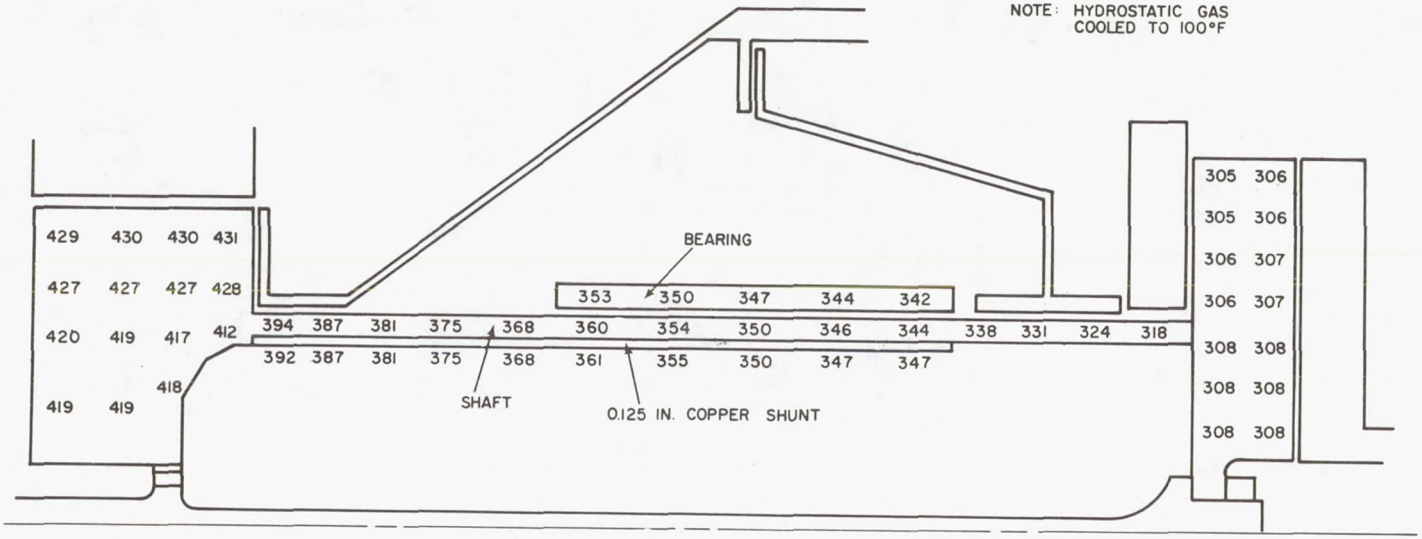

Figure 146 Temperature Map, Number Two Bearing, with Hydrostatic Gas Cooled to 100° F

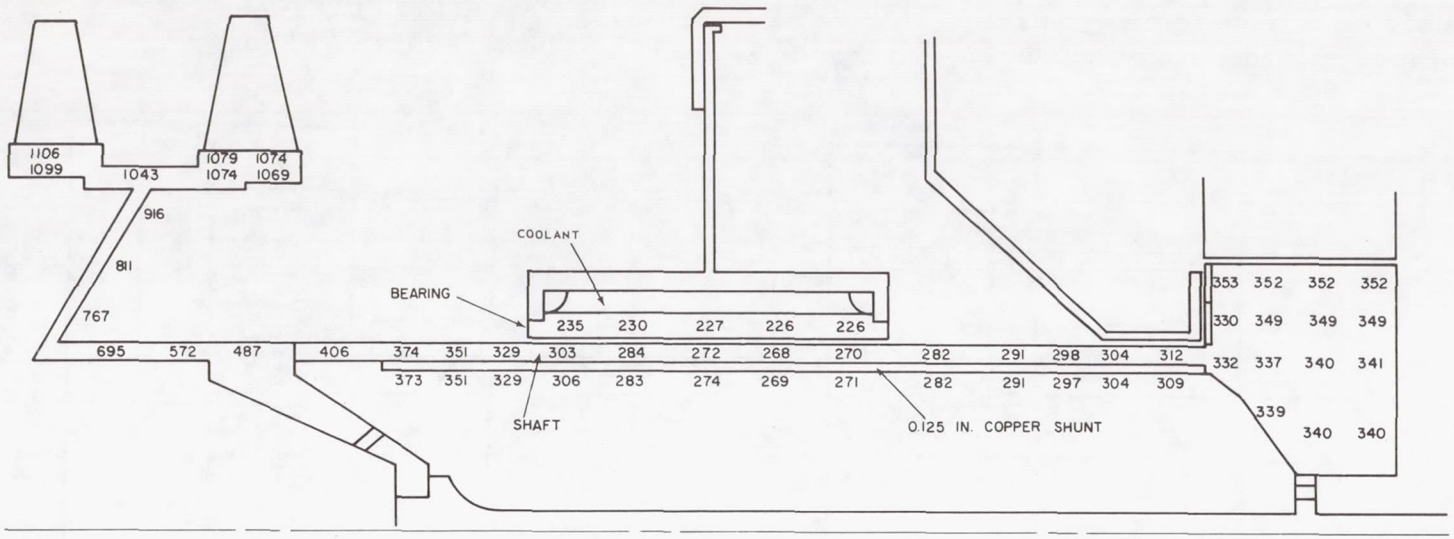

Figure 147 Temperature Map, Number One Bearing with Liquid Cooling

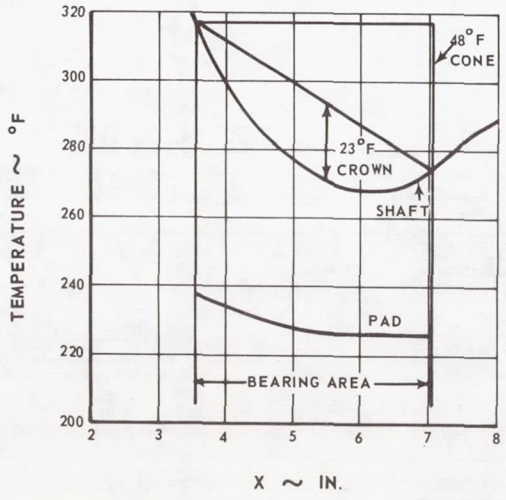

Figure 148 Temperature Distribution, Number One Bearing, with Liquid Coolant at 200° F

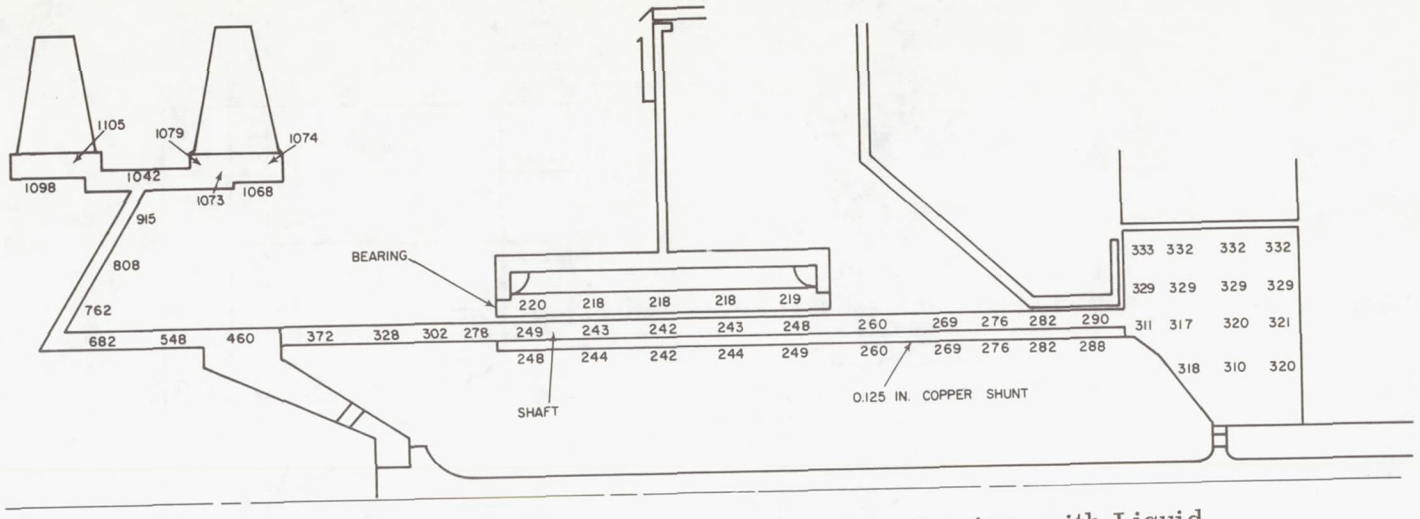

Figure 149 Temperature Map, Number One Bearing, with Liquid Coolant at 200° F and Reduced Shunt Length

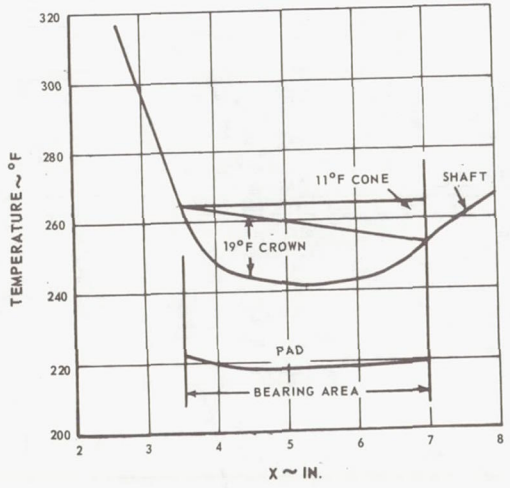

Figure 150 Temperature Distribution, Number One Bearing, with Liquid Coolant at 200°F and Reduced Shunt Length

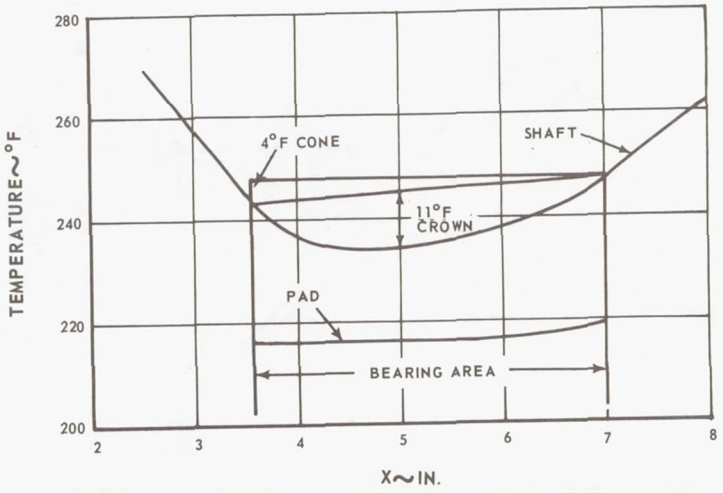

Figure 151 Temperature Distribution, Number One Bearing, with Liquid Cooling and Reduced Heat Exchanger Length

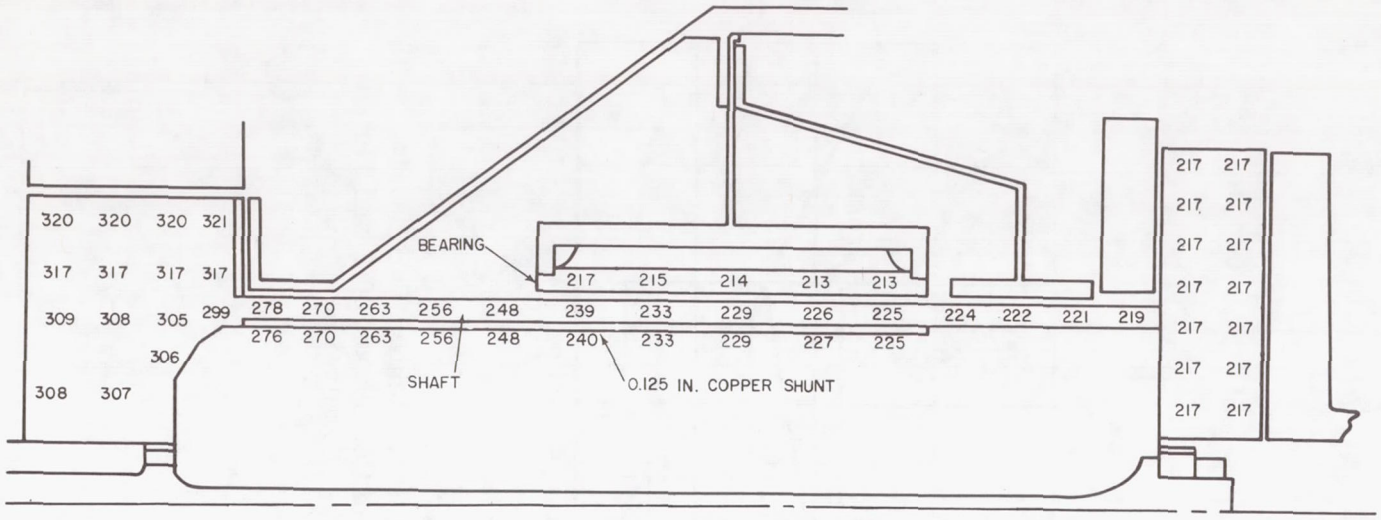

Figure 152 Temperature Map, Number Two Bearing, with Liquid Coolant at 200° F

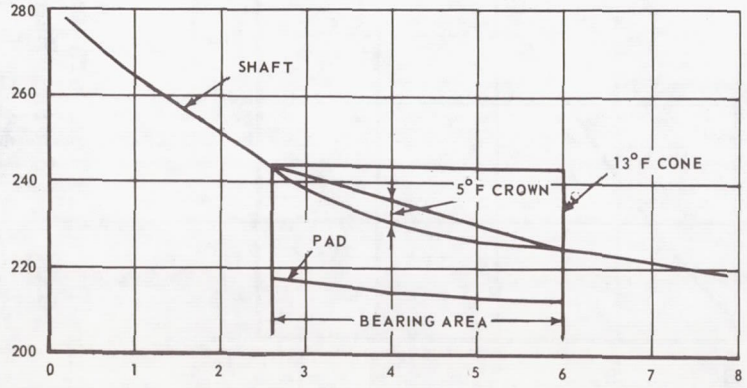

Figure 153 Temperature Distribution, Number Two Bearing, with Liquid Coolant in Journal and Thrust Bearings at 200°F

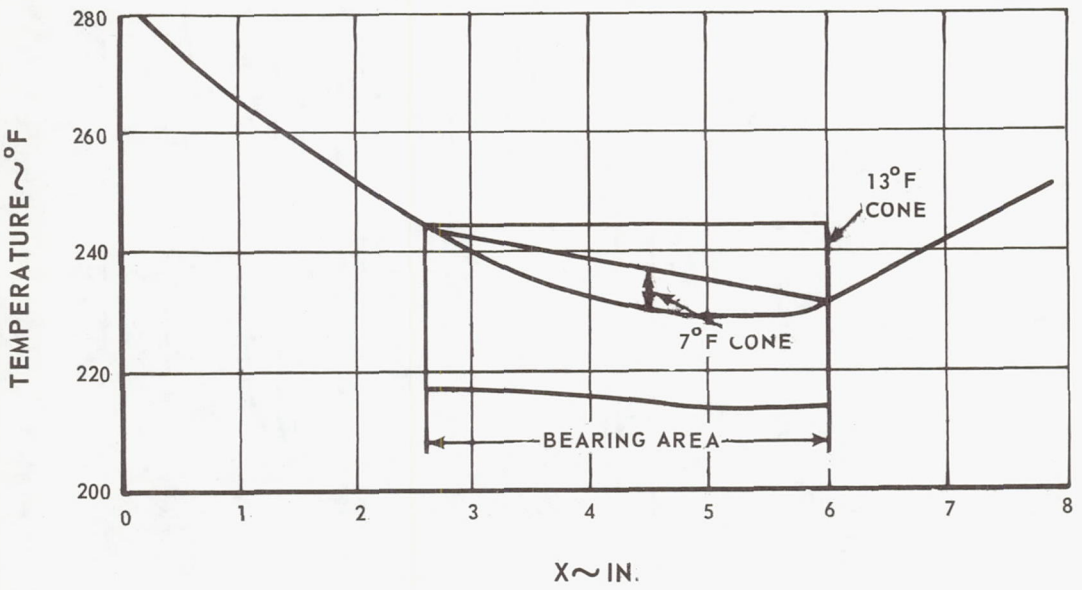

Figure 154 Temperature Distribution, Number Two Bearing, with Journal Bearing Liquid Coolant at 200°F and Thrust Bearing Liquid Coolant at 240°F

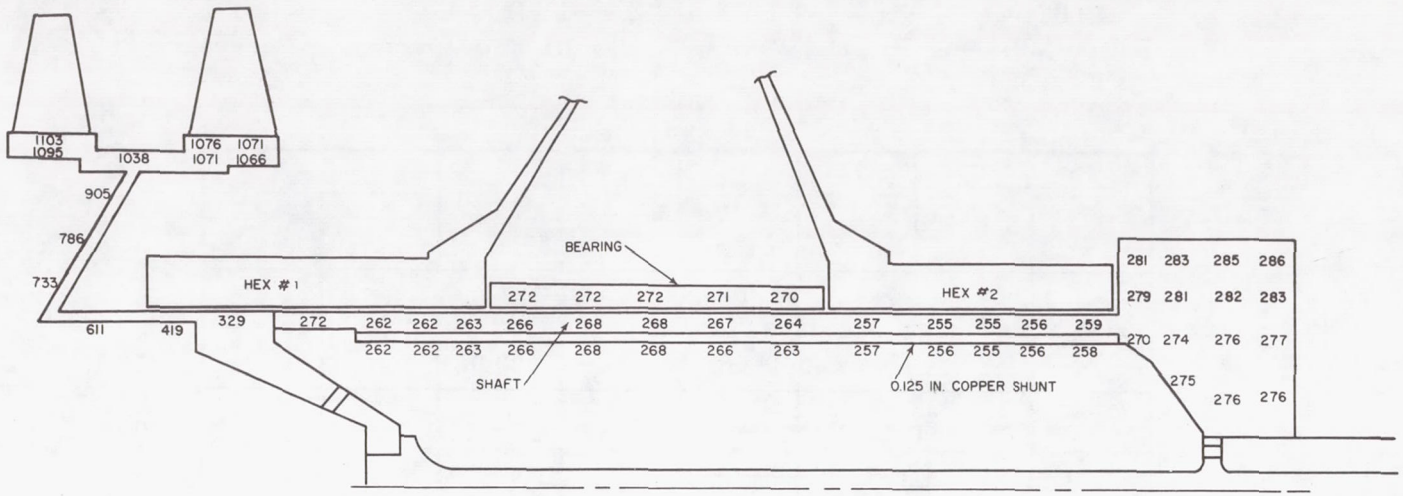

Figure 155 Temperature Map, Number One Bearing, with Liquid Coolant in Cooling Rings at 200°F

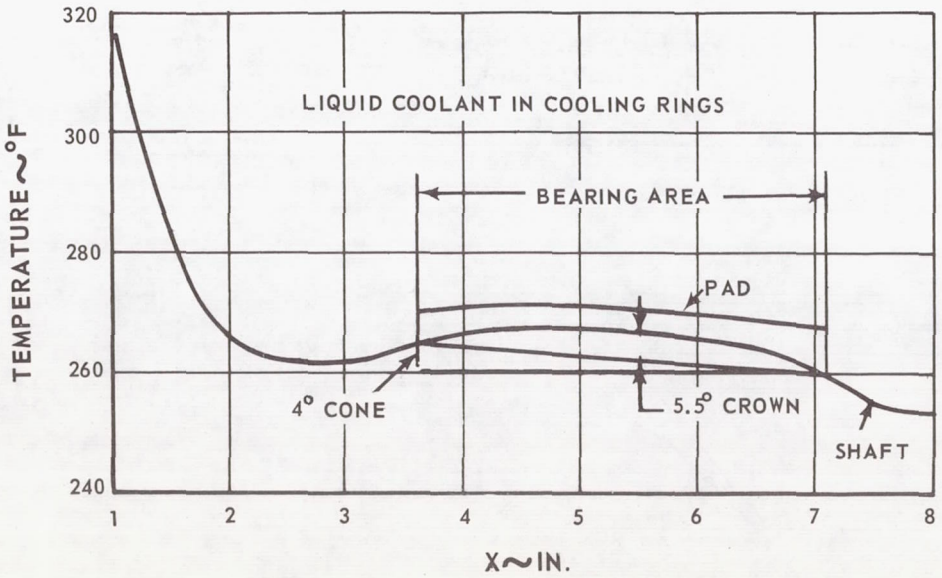

Figure 156 Temperature Distribution, Number One Bearing, with Liquid Coolant in Cooling Rings at 200°F

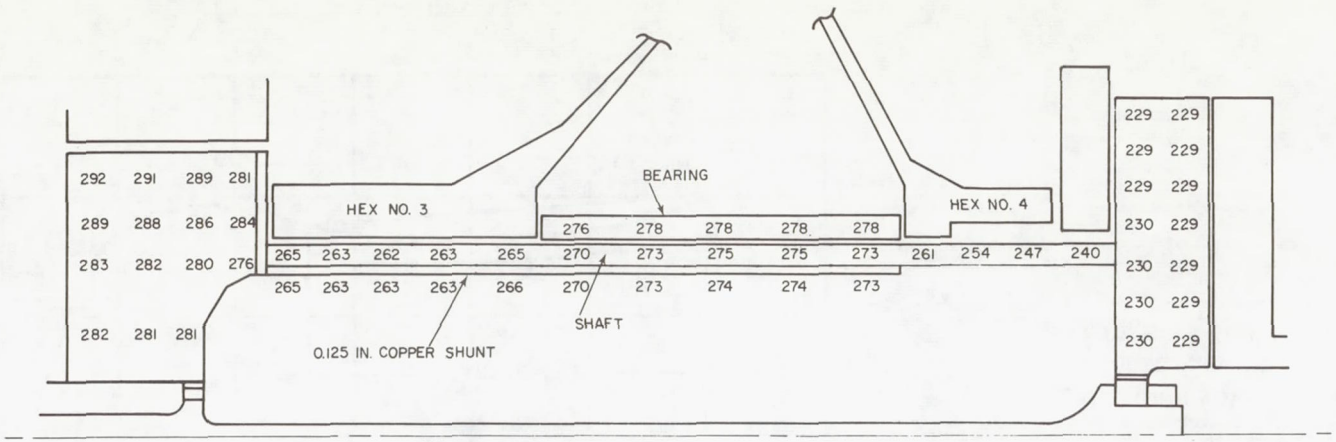

Figure 157 Temperature Map, Number Two Bearing, with Liquid Coolant in Cooling Rings and Thrust Bearing at 200°F

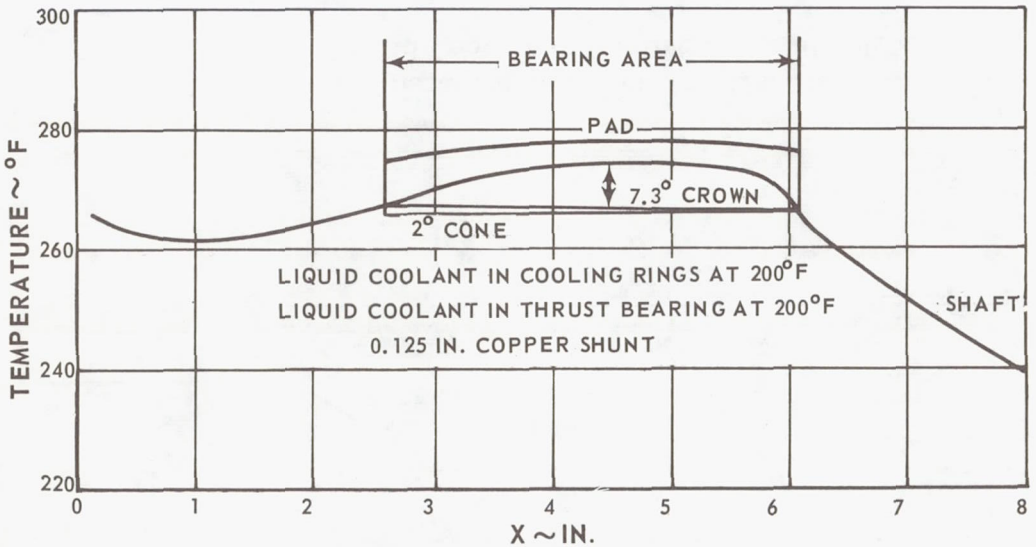

Figure 158 Temperature Distribution, Number Two Bearing, with Liquid Coolant in Cooling Rings and Thrust Bearing at 200°F

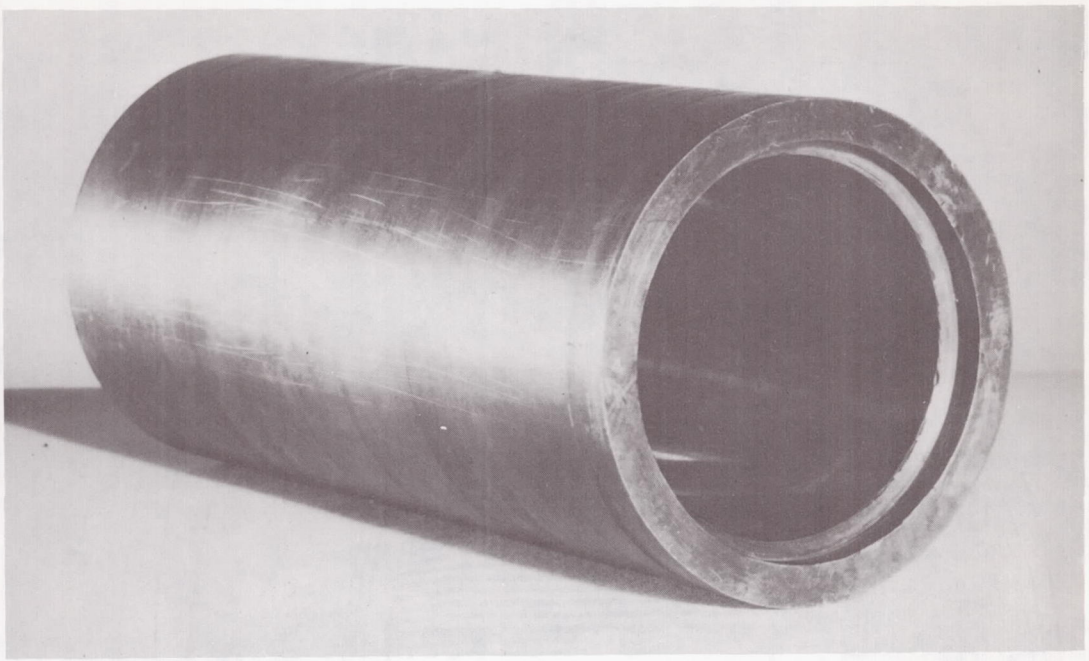

Figure 159 Copper Heat Shunt Test Specimen (M-33431)

Mag: 100X

Figure 160 Photomicrograph of Bond Area Between Copper Heat Shunt and Shaft (X-24307)

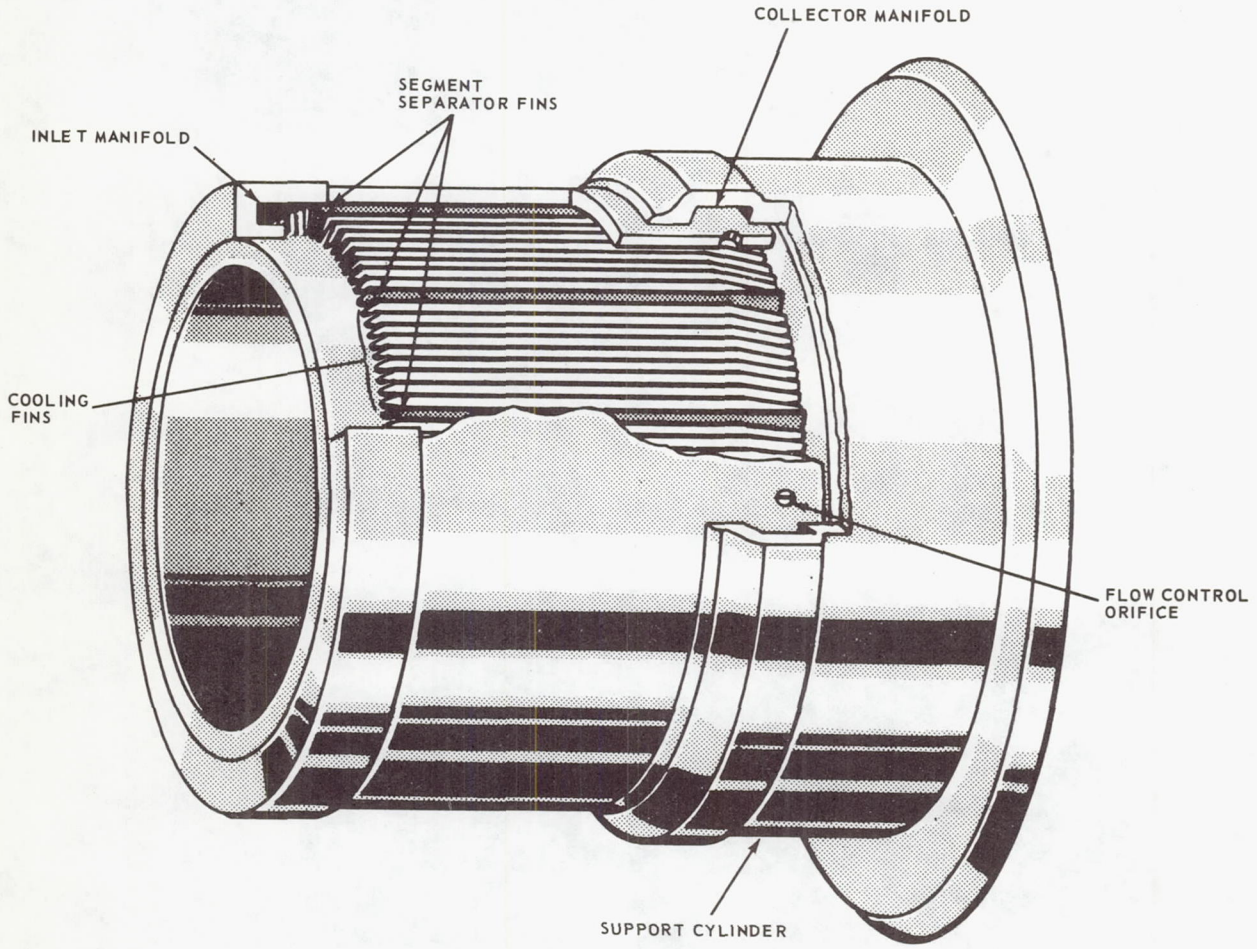

Figure 161 Cutaway of Typical Journal Bearing Heat Exchanger

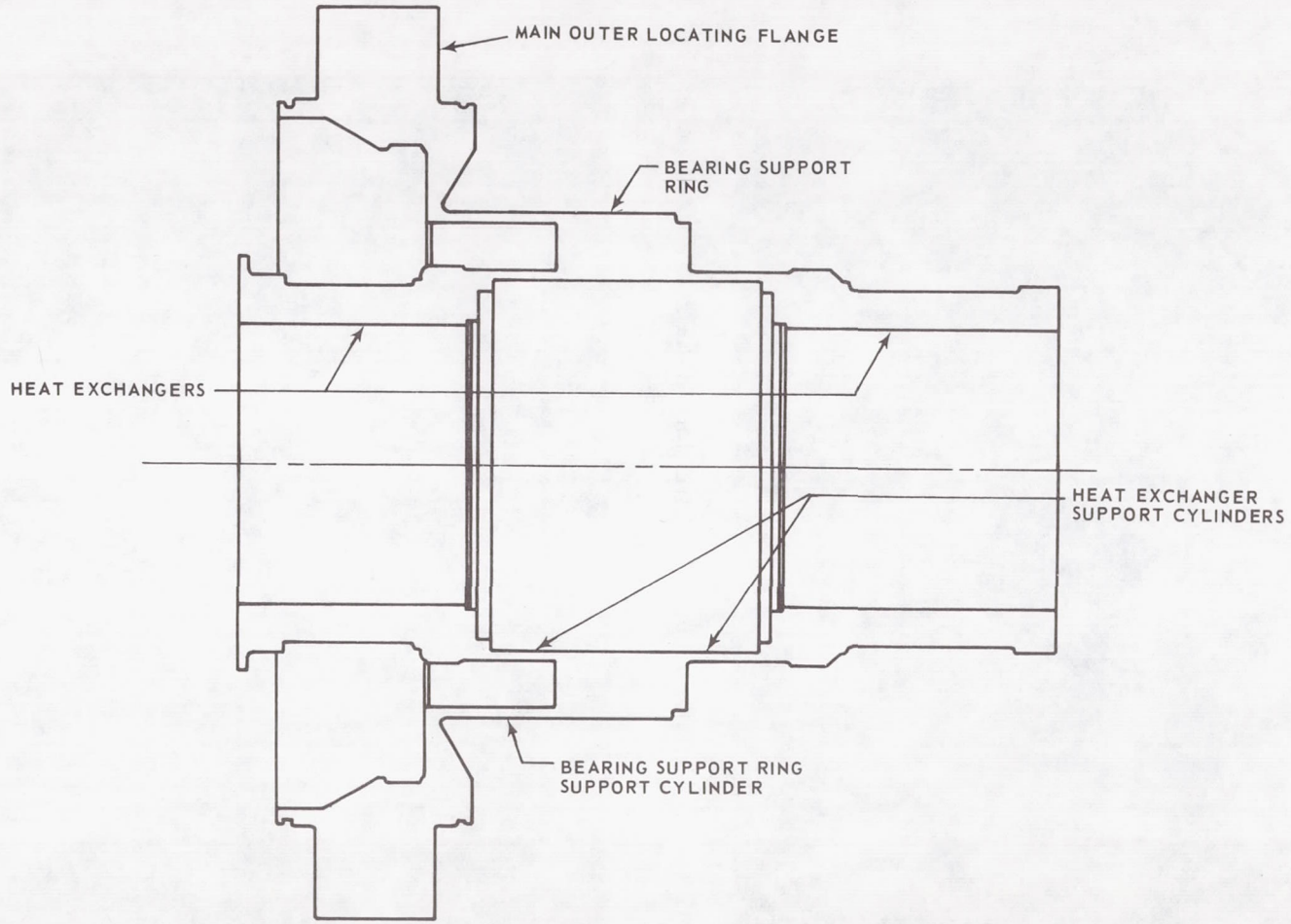

Figure 162 Cross-Section of Bearing Support Assembly

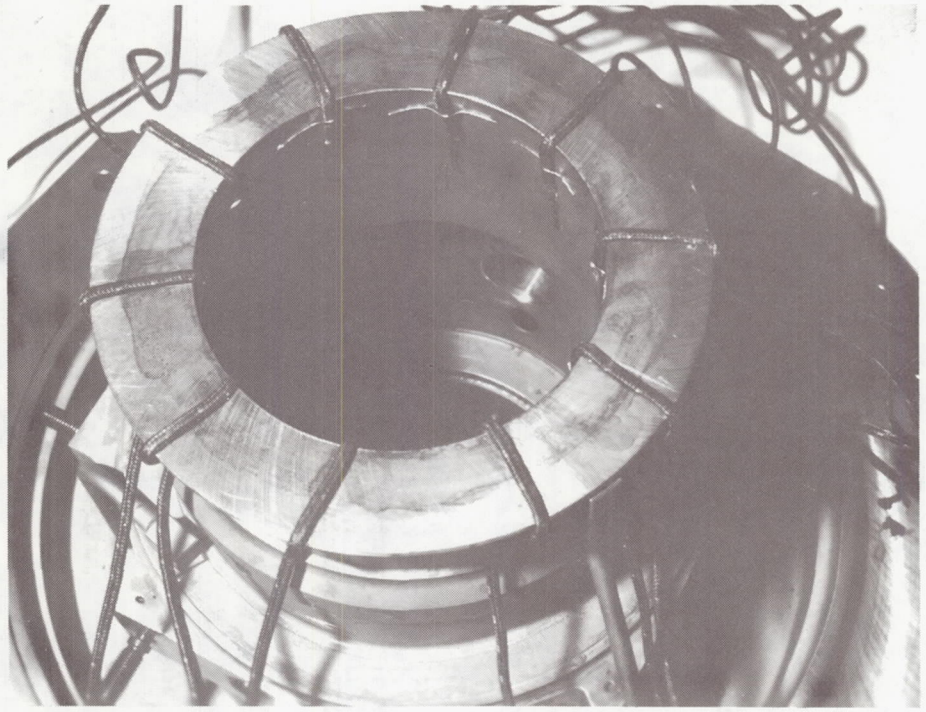

Figure 163 Thermocouple Installation in Journal Heat Exchanger (X-24304)

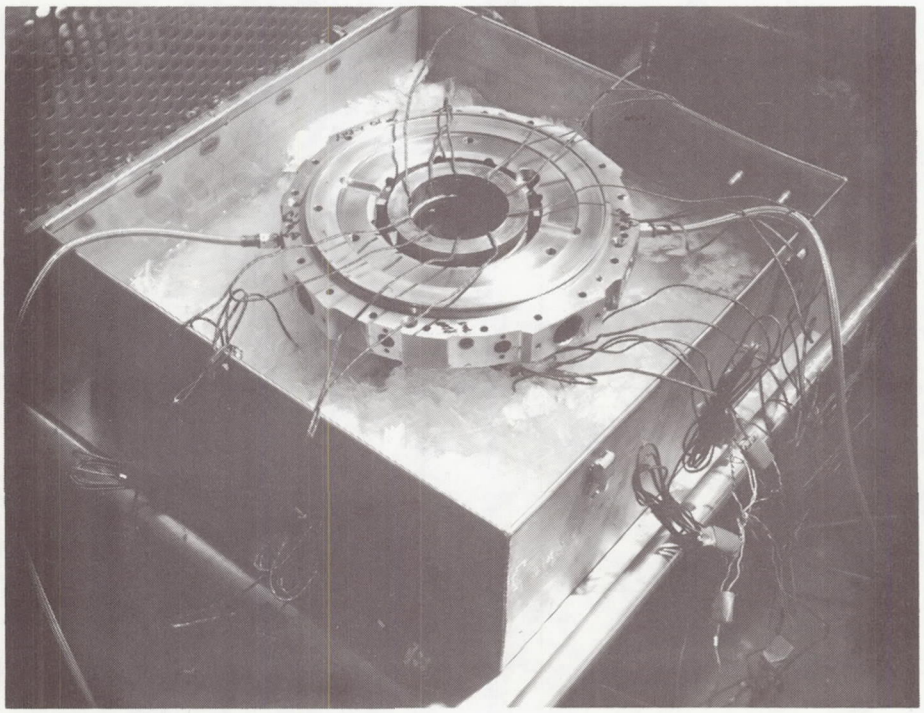

Figure 164 Journal Bearing Mount in Ice Bath (X-24303)

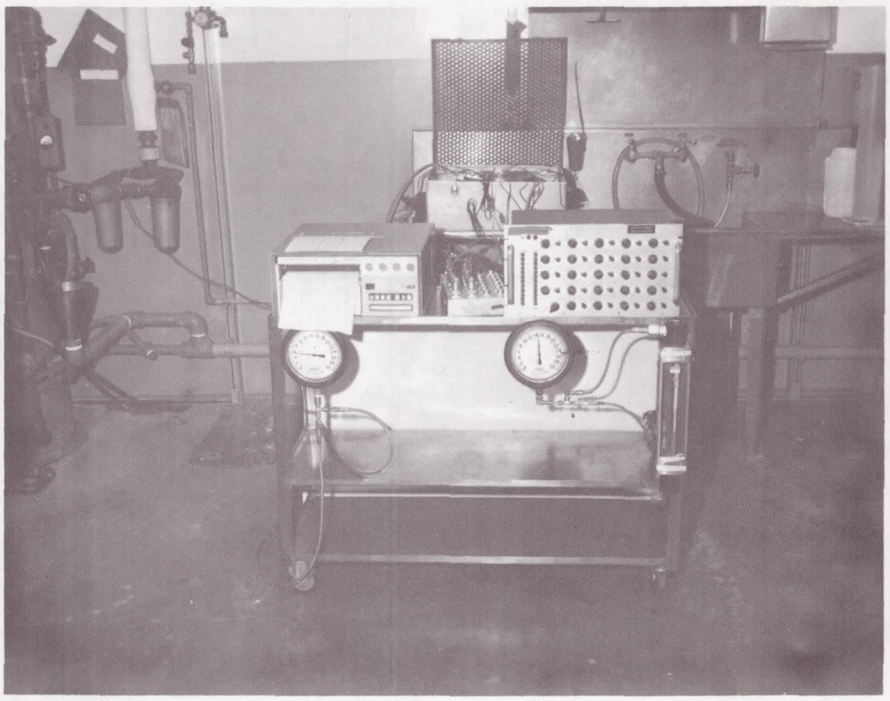

Figure 165 Test Facility for Journal Bearing Heat Exchanger Flow Check

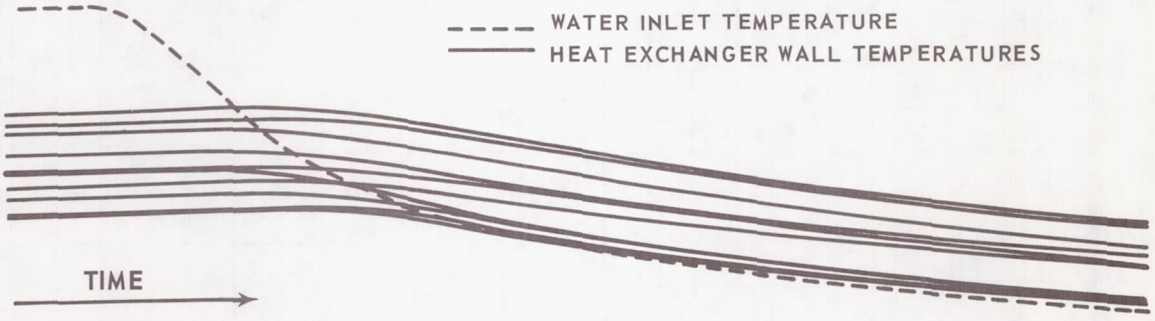

Figure 166 Temperature Transient for Heat Exchanger with No Blockage

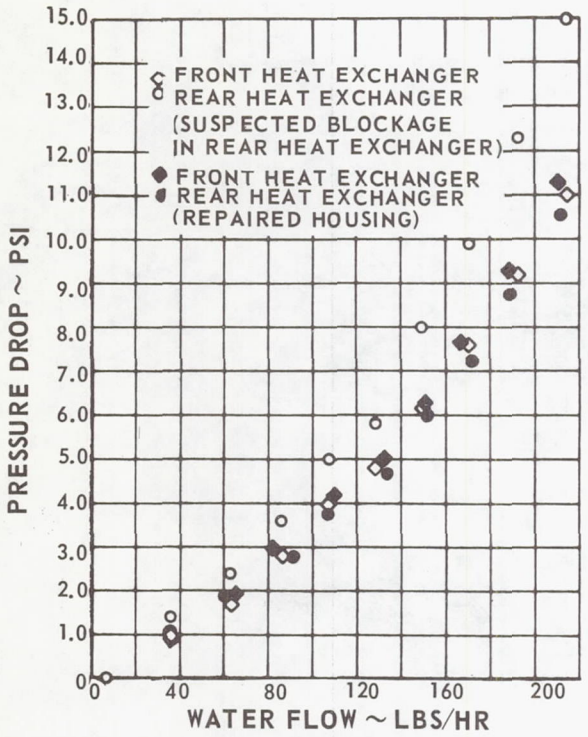

Figure 167 Number One Bearing Housing Pressure Drop

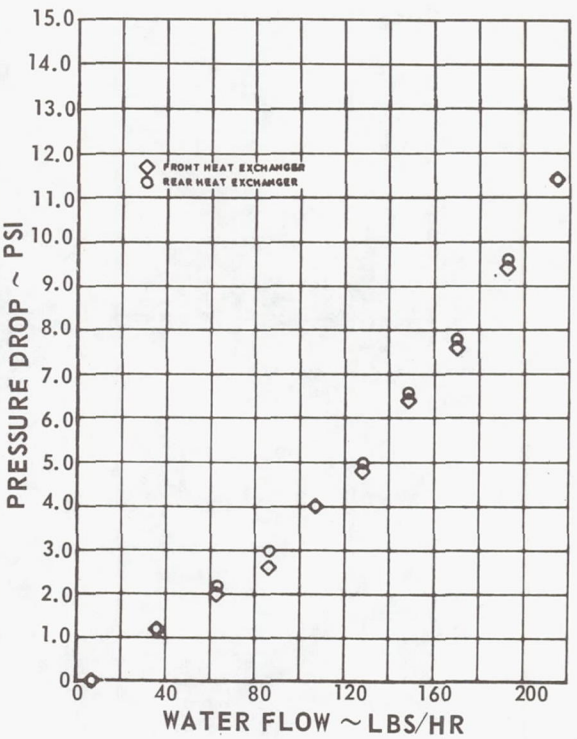

Figure 168 Second Number One Bearing Housing Pressure Drop

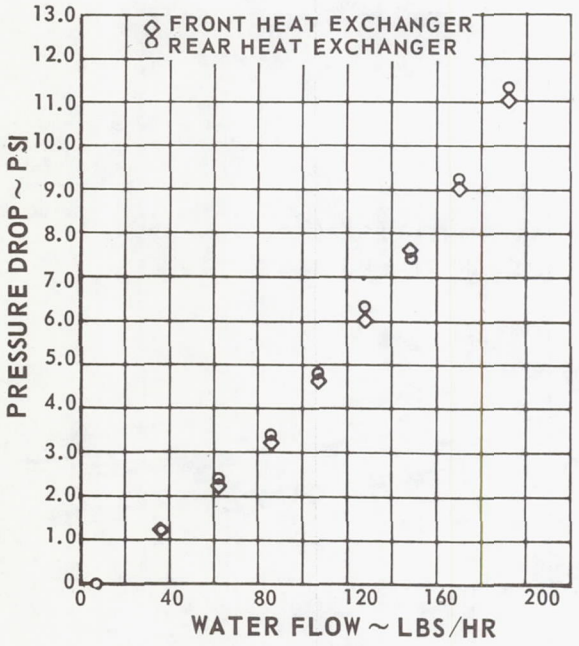

Figure 169 Number Two Bearing Housing Pressure Drop

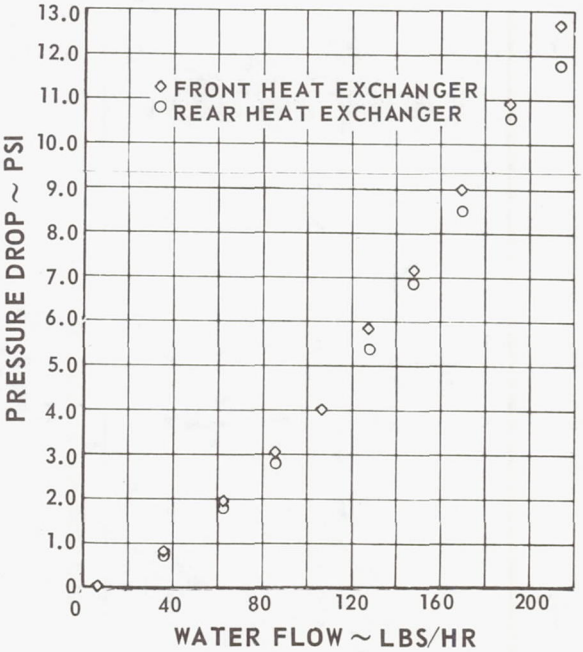

Figure 170 Second Number Two Bearing Housing Pressure Drop

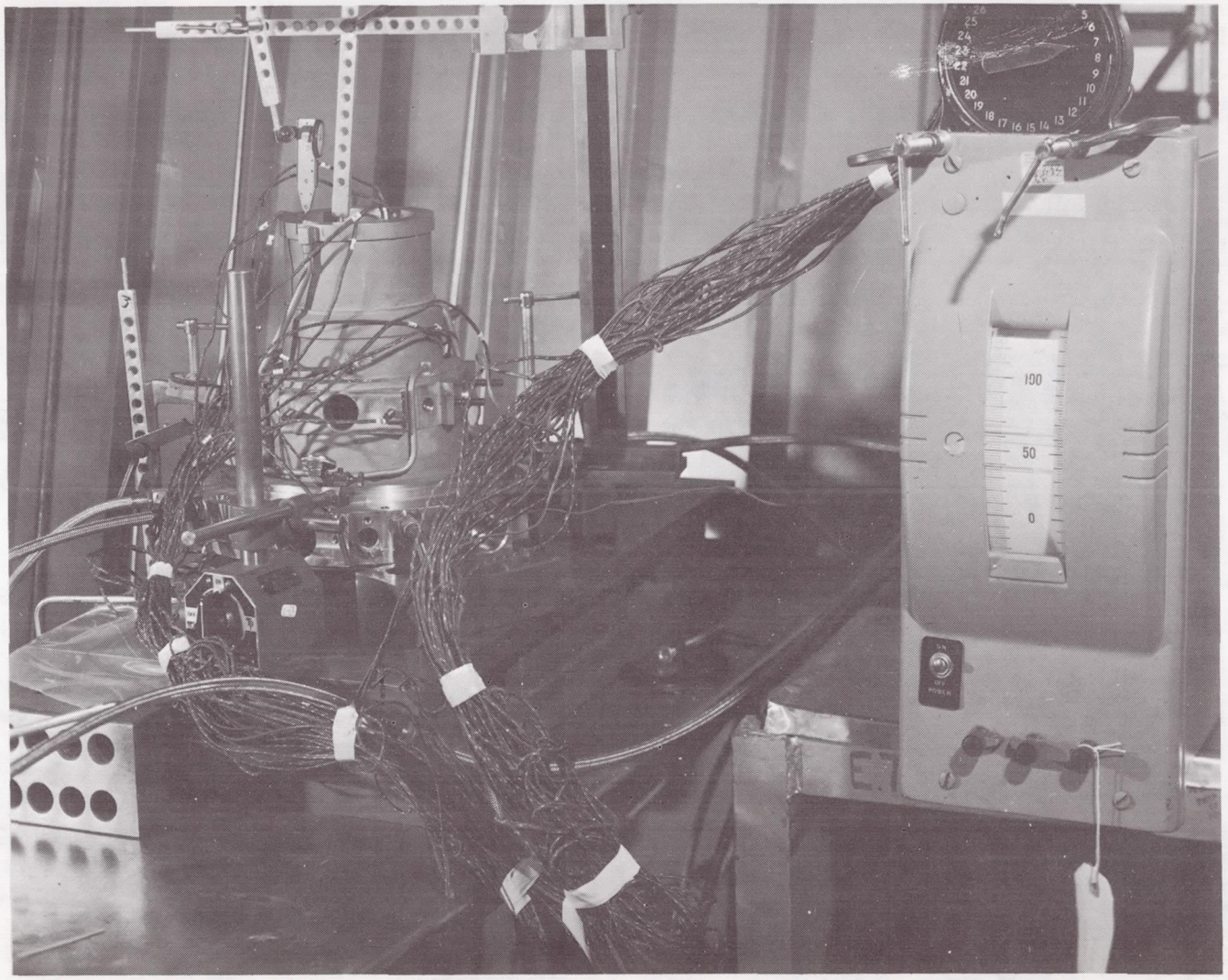

Figure 171 Thermal Distortion Test of Front Journal Bearing Mount and Heat Exchanger (X-74465)

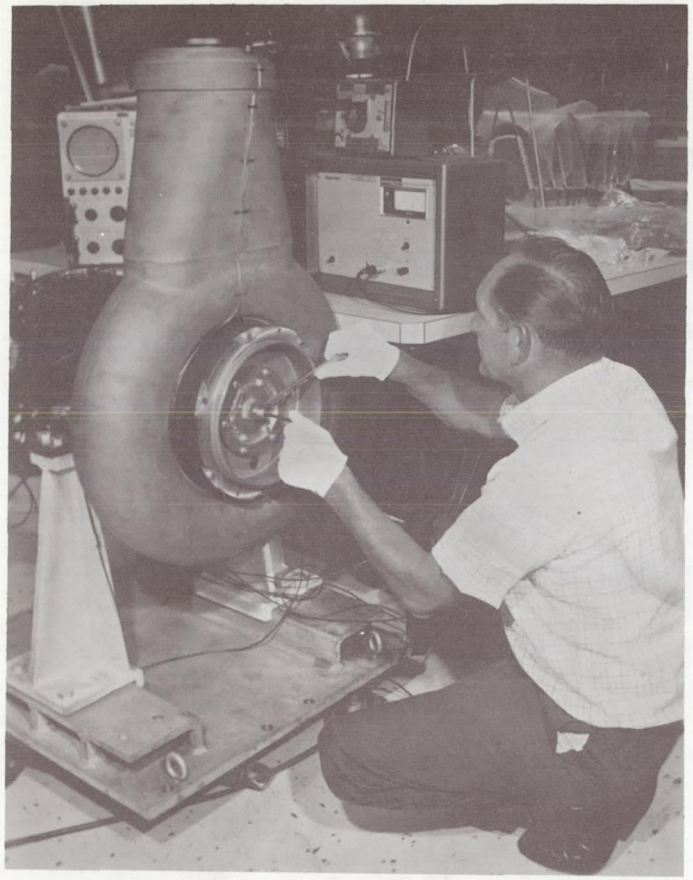

Figure 172 Adjustment of Front Shipping Fixture

(CN-10122)

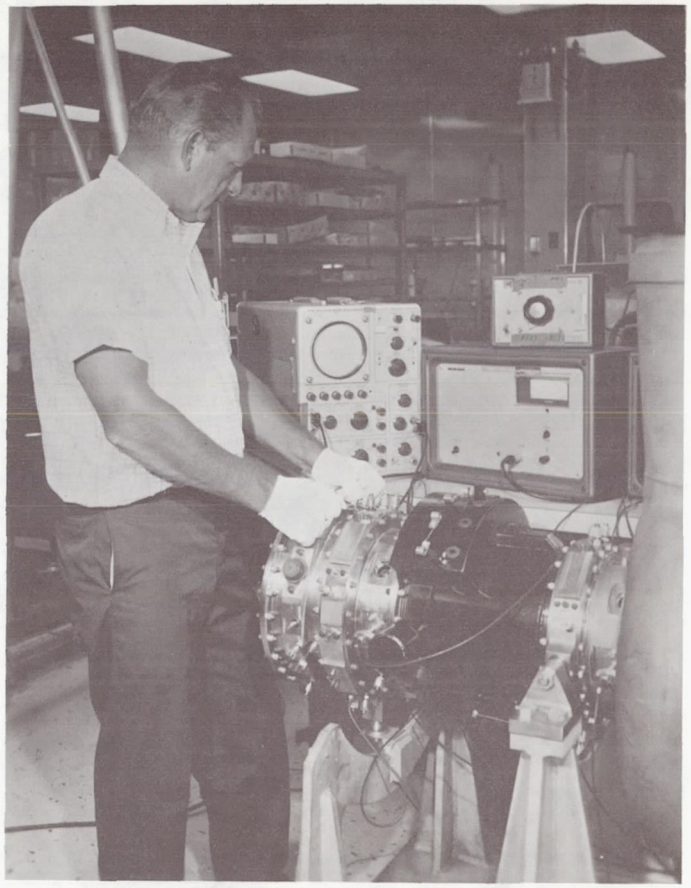

Figure 173 Adjustment of Rear Radial Shipping Fixtures

(CN-10116)

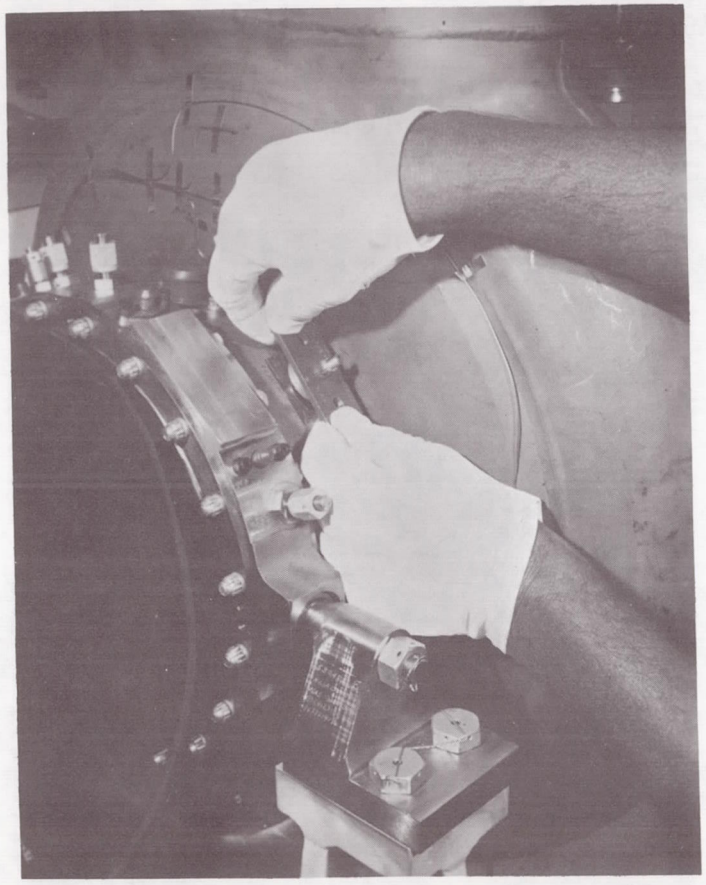

Figure 174 Shipping Fixture for Upper Journal Pads

(CN-10118)

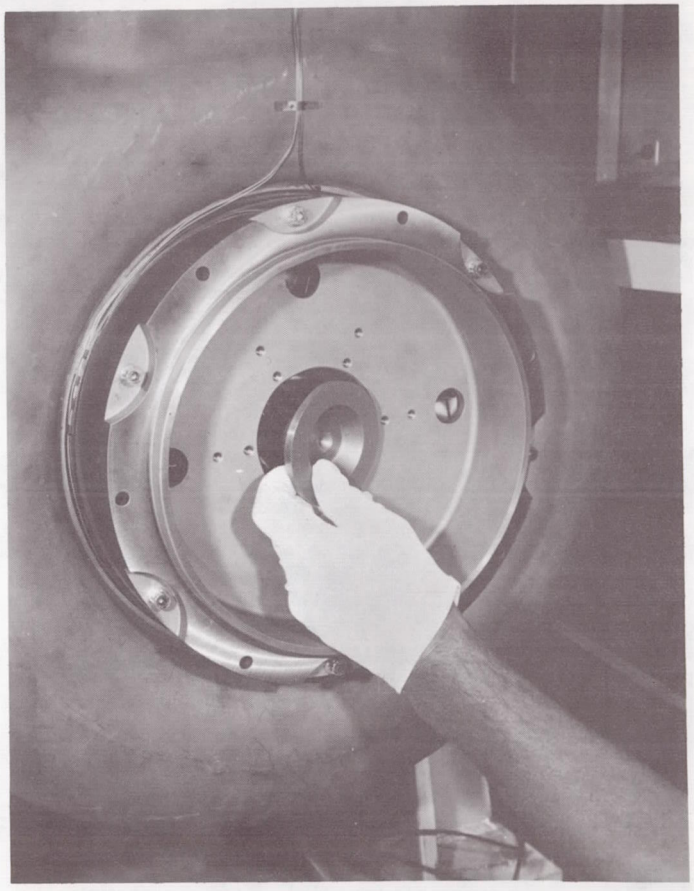

Figure 175 Installing Front Shipping Fixture Axial Load Adapter Into Turbine Wheel

(CN-10120)

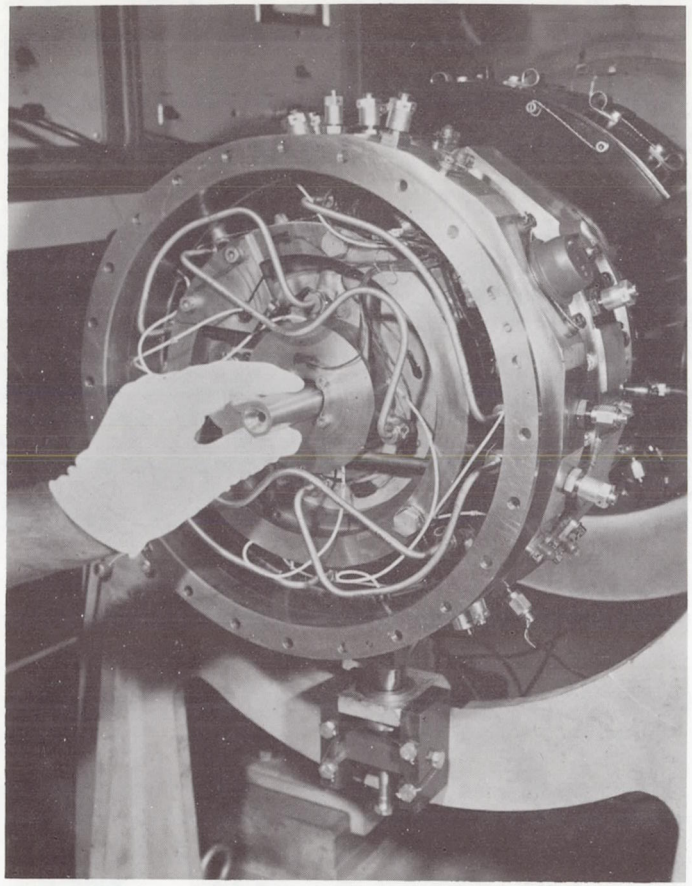

Figure 176 Positioning Rear Axial Shipping Fixture Against Thrust Runner

(CN-10119)

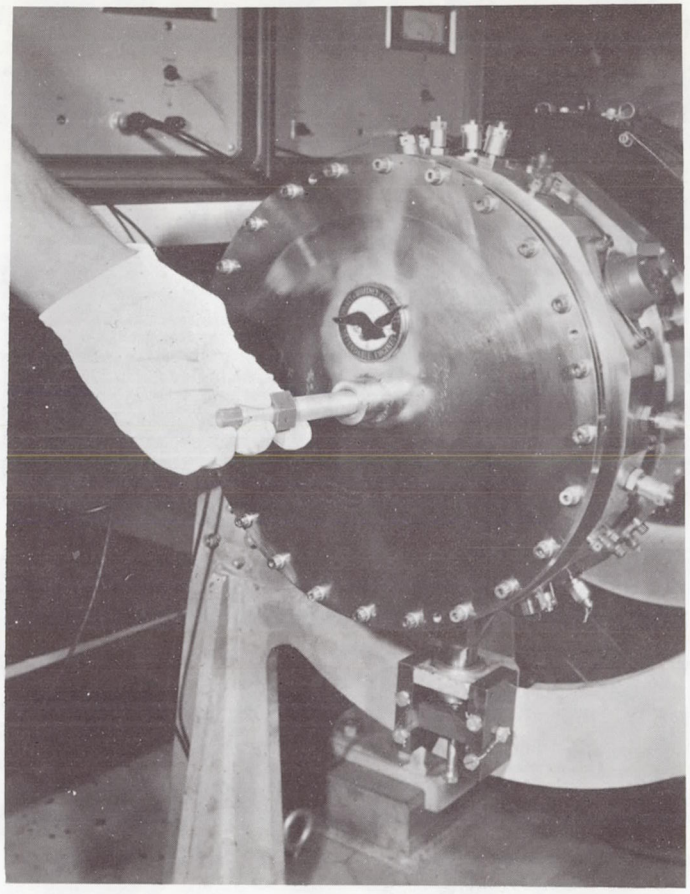

Figure 177 Rear Axial Shipping Fixture Adjusting Screw

(CN-10117)

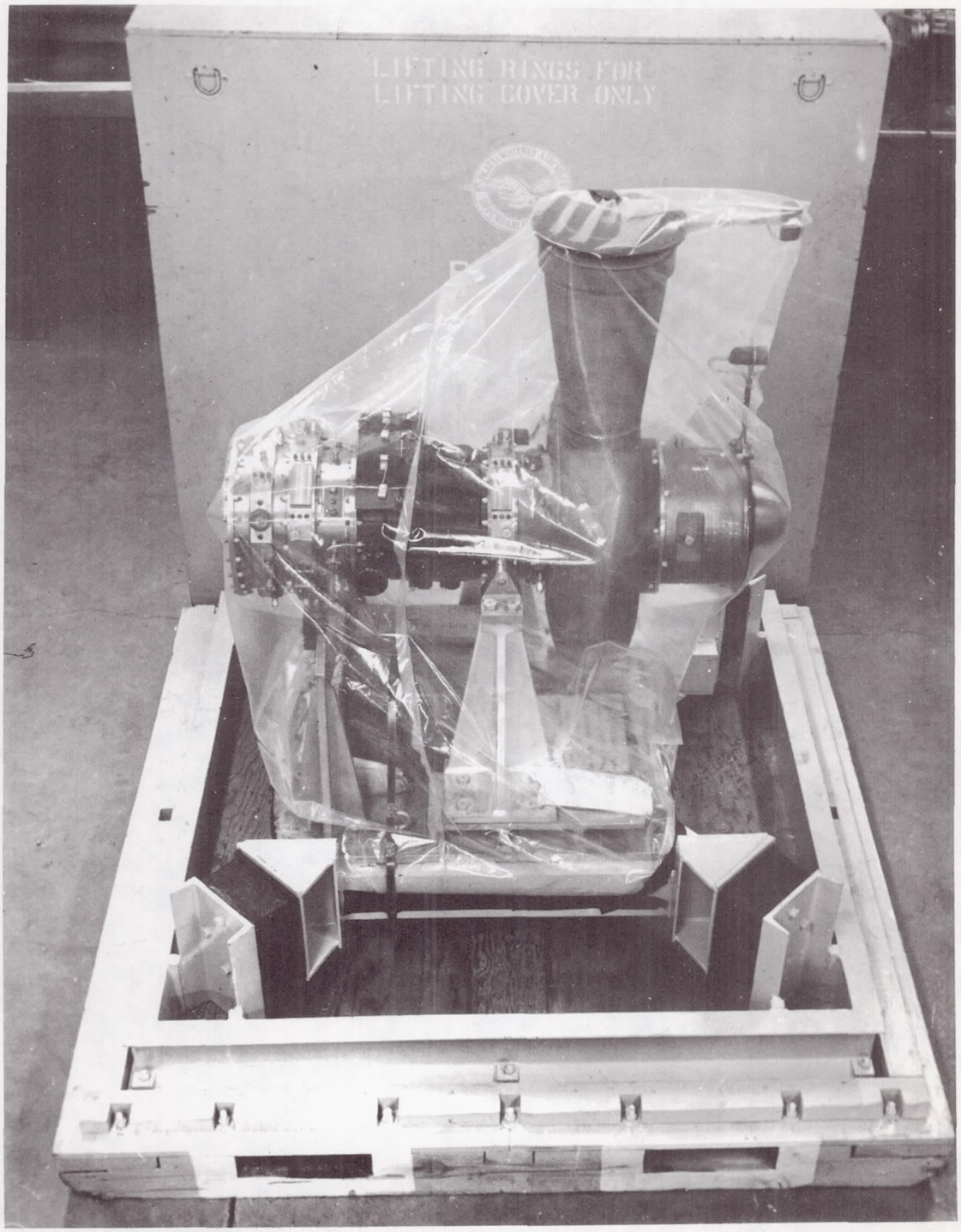

Figure 178 Turboalternator Mounted in Shipping Container (CN-10105)